Alma Mater Studiorum – Università di Bologna
in cotutela con Consiglio Nazionale delle Ricerche

DOTTORATO DI RICERCA IN

___CHIMICA INDUSTRIALE___

Ciclo __28^O__

Settore Concorsuale di afferenza: _03/C2_

Settore Scientifico disciplinare:__CHIM/04 __

PRODUCTION AND CHARACTERIZATION OF NOVEL 2D MATERIALS
FOR TECHNOLOGICAL APPLICATIONS IN COMPOSITES AND
SURFACE COATINGS

Presentata da: ____KOUROUPIS-AGALOU KONSTANTINOS_____

Coordinatore Dottorato

__Prof. Aldo Roda____

Relatore

___Prof. Loris Giorgini__

Corelatore

_Dr. Vincenzo Palermo___

Esame finale anno 2016

...To my beloved family

Acknowledgments

The way to create new knowledge is by constant and quality scientific research. This research cannot be delivered and fostered to the world without the passion and drive of people with brilliant minds and an exceptional drive to succeed. The love for curiosity to explore or discover novelties which will get us closer to a new challenge or a more sustainable living world is always the drive to keep us going and delivering. The same applies to this work and for this reason I feel grateful to all of those who mentored, guided, supported and assisted me throught my PhD with all its challenges. Whether their contribution was big or minor, everyone deserves to be thanked and acknowledged.

This work would have not been implemented or, for that matter, have achieved all the described significant results were it not for the steady, unwavering, support and engouragement from my co-supervisor Dr. Vincenzo Palermo. My thanks go to my supervisor Prof. Loris Giorgini for helping me out throughout my PhD course and supporting my work.

My graditude goes also to Dr. Andrea Liscio and Dr. Emanuele Treossi who, taught me science where I would not be able to learn elsewhere and in such perspective.

I would also like to thank my lab-colleagues Dr. Zhenyuan Xia, Dr. Alessandra Scida, Dr. Simone Ligi, Dr. Andrea Schlierf, Alessandro Kovtun, Simone dell'Elce and Nicola Mirrota for their enormous support and contribution in the lab.

Many thanks to all my friends around the world for their support and fun moments which were vital to keep me and this work going. Real friends who were always there during the good and hard times. Thanks to Dr. Michail Terzidis for his supportance, to Constantino Angelopoulos for his cheerful moments, to Alexandros Pennos who will soon complete his PhD as we started it at the same time and was always there to help me.

Finally, I am truly grateful and thankful to my beloved family for their ultimate love and unlimited support they have been showing me in all the steps of my life.

<div align="center">Thank you all</div>

Contents

Chapter 4 - Fragmentation and Exfoliation of Quasi 2D Materials: The Case of Boron Nitride

Chapter 5 - Graphene Exfoliation with Organic Dyes

Chapter 6 - Summary and Conclusions

Appendix

1D	One-dimensional
2D	Two-dimensional
2DM	Two-dimensional Materials
3D	Three-dimensional
ΔH	Denaturation Enthalpy
AFM	Atomic Force Microscopy
AlN	Aluminum nitride
Ar	Aspect Ratio
BN	Boron Nitride
CAE	Constant Analyser Energy
CCD	Cumulative Distribution Functions
$CHCl_3$	Chloroform
CNT	Carbon Nanotube
CVD	Chemical Vapor Deposition
DCB	Dichlorobenzene
DLS	Dynamic light scattering
DMF	Dimethyl Formamide
DSC	Differential Scanning Calorimetry
eV	Electronvolt
EtOH	Ethanol
FEM	Finite-Element Model
FET	Field Effect Transistor
FF	Form Factor
FLG	Few-layers Graphene
FM	Fluorescence Microscopy
FQM	Fluorescence Quenching Microscopy
FWHM	Full Width Half Maximum

GBM	Graphene Based Materials
GNP	Graphene Nanoplatelets
GO	Graphene Oxide
GOH	Graphene Organic Hybrids
GRM	Graphene and Related Materials
hBN	Hexagonal-Boron Nitride
HOPG	Highly Oriented Pyrolitic Graphite
HWHM	Half-width Half Maximum
IPA	Isopropanol
KPFM	Kelvin Probe Force Microscopy
LN	Lognormal
LPE	Liquid Phase Exfoliation
MD	Molecular Dynamics
NIBS	Non-invasive Back Scatter
NMP	N-methyl-2-pyrrolidone
OLED	Organic Light Emitting Diodes
OM	Optical Microscopy
OPV	Organic Photovoltaics
OS	Optical Spectroscopy
PAH	Polyaromatic Hydrocarbons
PALS	Phase Analysis Light Scattering
PDI	Perylene-diimide
PET	Polyethylene terephthalate
PP	Polypropylene
PVC	Polyvinyl Chloride
RMS	Route mean square
SD	Standard deviation
SEC	Size Exclusion Chromatography
SEM	Scanning Electron Microscopy

SiOx	Silicon Oxide
SLS	Static Light Scattering
STM	Scanning Tunneling Microscopy
TEM	Transmission Electron Microscopy
THF	Tetrahydrofuran
TMD	Transition Metal Dichalcogenides
TMO	Transition Metal Oxide
UV	Ultraviolet/visible absorption
XPS	X-ray photoelectron Spectroscopy
XRD	X-ray diffraction

Chapter 1

Introduction - 2D Materials

1.1. Discovery

Carbon is the basis of organic chemistry and therefore of life on earth: the reason of this extraordinary role is carbon's chemical versatility resulting in a great variety of physical and chemical properties. Atomic carbon exists in three bonding states with different geometry, shape and dimension, corresponding to sp3, sp2 and sp hybridization of the atomic orbital. These different bonds lead to diverse carbon allotrope structures, such are diamond, graphite, carbyne, fullerenes, nanotubes, polyaromatic hydrocarbons, graphene, and amorphous carbon to mention some of the most prominent forms of carbon.

Some of these different allotropes forms of carbon are the well-known materials of diamond, graphite, carbine, fullerenes, carbon onions, carbon nanotubes (CNTs), graphene and amorphous carbon. It is believed that carbon science, especially related to graphene and nanotechnologies has enormous scientific and technological potential and can provide tremendous discoveries and ultimately fascinating applications in everyday life (Again you can show data from the presentation of the new 2D journal e.g number of publications, patents etc).

Diamond for instance exhibits a typical cubic crystal structure with a repeating pattern of 8 atoms; the strong bonding leads to the highest hardness and thermal conductivity of any bulk material, determining the major industrial application of diamond in cutting and polishing tools. Graphite, in contrary, is based on sp2 hybridized carbons and has a layered, planar structure. In each layer, the carbon atoms are arranged in a honeycomb lattice with separation of 0.142 nm, and the distance between planes is 0.335 nm[1]. The two known forms of graphite, alpha (hexagonal) and beta (rhombohedral), have very similar physical properties, except that the single carbon layers stack slightly differently[2]. The layered structure of graphite and the weak forces between single carbon layers allow for application for refractories, batteries, steelmaking, brake linings, foundry facings and lubricants.

The newest and most exiting carbon allotrope, graphene, can be considered as a border case of an extended aromatic system, being a mono-atomic layer of sp^2 carbon reaching macroscopic lateral extension. As demonstrated in 2004, layers of graphene can be extracted from a graphite crystal by peeling of the sheets with simple adhesive tape.
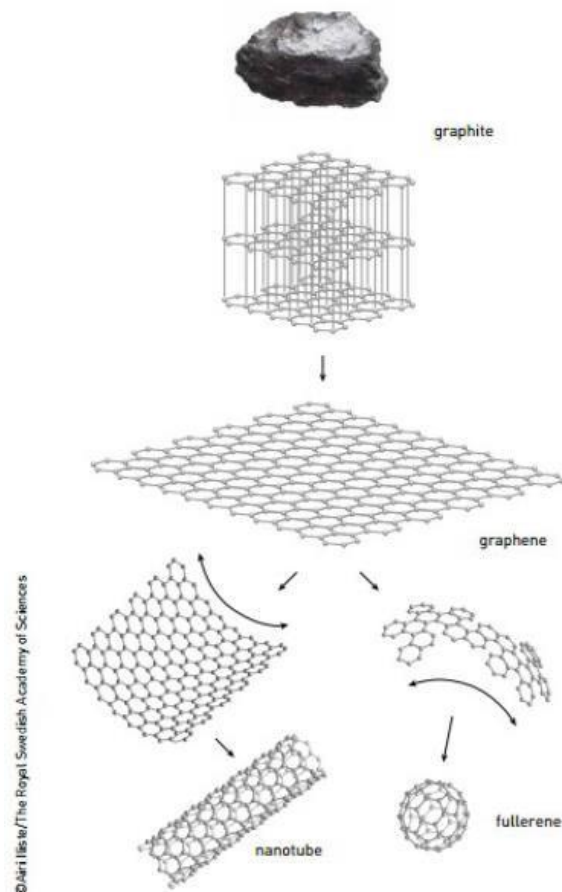
Fig. 1: Illustration of carbon allotropes derived from graphite; layered structure of graphite, single layer of graphene, carbon nanotubes and fullerenes[3].

On the very extreme of sp2 hybridized carbon systems are polyaromatic hydrocarbons (PAHs). These systems are based on a sp2 hybridized carbon backbone based on a defined number of aromatic rings, organized in a - usually planar - honeycomb network. Synthetic PAHs find application as photo-sensitizer, fluorescence markers and dyestuff, but they also appear naturally and are suspected to play a crucial role in the formation of life on our planet: According to NASA experts, more than 20% of the carbon in the universe may be associated with PAHs being possible starting materials for the formation of life. PAHs seem to have been formed shortly after the Big Bang, and are widespread throughout the universe[4]. Carbon science, especially related to nanotechnologies, has great potential and in the next years can offer more interesting discoveries and new solution, from a fundamental understanding of such new materials towards application in industry and everyday life.

1.2. Graphene Properties

Graphene research has progressively expanded the last ten years due to the relatively fast and cheap laboratory methods that enable the production of high-quality graphene. Many of the characteristics of this exceptional material are: room-temperature electron-mobility of 2.5 x 10^5 cm^{2}V^{-1}s^{-1}, a Young modulus of 1 TPa and intrinsic strength of 130GPa, very high thermal conductivity >3000 W mK^{-1}, optical absorption of exactly πα~2.3% (in the infrared limit, where α is the fine structure constant), complete impermeability to any gases, ability to sustain extremely high densities of electric current (a million times higher than copper) and can also be chemically functionalised.

However, most of the mentioned properties have been observed only for the highest-quality graphene samples. Similar characteristics have not been achieved by using techniques apart from mechanical exfoliation and graphene deposited on hexagonal boron nitride substrates, even though these methods are constantly improving.

Therefore, the big challenge that the graphene research community is facing is how to transfer the unique properties of the 'wonder material' in industrial- and mass-production levels, while keeping the outstanding performance as in the samples obtained in laboratories.

1.3. Other 2D Materials

Graphene is not the only material of the large family of 2D materials. Although it is the most famous there have been numerous others layered materials such as transition metal dichalcogenides (TMDs), transition metal oxides (TMOs) and others 2D crystals like boron nitride (BN), Bi_2Te_3 and Bi_2Se_3. TMDs are structured from hexagonal layers of metal atoms (A), sandwiched between two layers of chalcogenide atoms (B), where B can be S, Se and Te. The resulting stoichiometry is AB_2.Some examples are: Hexagonal Boron Nitride, Molybdenium Disulphide (MoS_2), Molybdenum Diselenide ($MoSe_2$), Tungsten Diselide (WSe_2), Tungsten Disulfide (WS_2),Bismuth Selenide (Bi_2Se_3), Tantalum Sulfide (TaS_2), Tin Sulfide (SnS_2), Manganese Dioxide (MnO_2). In general, van der Waals forces are keeping the layered sheets together, although the bonding within these trilayer sheets is covalent.
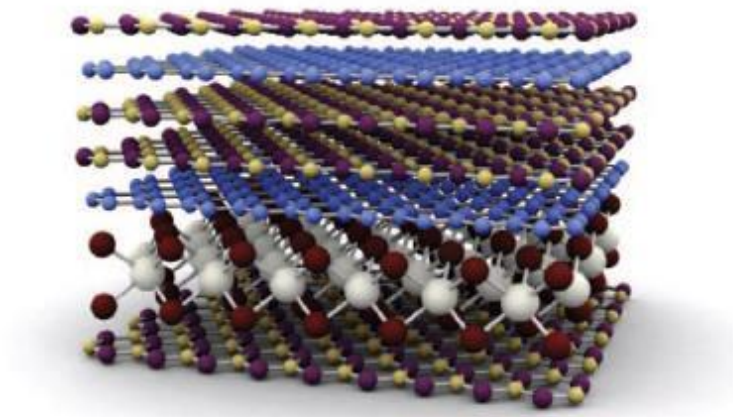
Fig. 2: A schematic representation of a 2D based heterostructure. Two graphene layers and a TMD-Molybdenium Disulfide (MoS2) are separated by several layers of boron nitride (BN), which act as a tunnelling barrier.

TMDs normally occur in forty different types depending on the combination of chalcogen and transition metal. Moreover, TMDs can be metallic, semimetallic or semiconducting, depending on the coordination and oxidation state of the metal atoms, resulting to interesting and unique properties for each of them, such as superconductivity, thermoelectricity and topological insulator effects. The common characteristic of those materials is that their properties are strongly dependent on the number of layers in the final exfoliated material.

Therefore, it is very important to study in depth how we can control the physical parameters of exfoliated 2D materials (size, shape, thickness, length, width) and hence, control the properties of the final material or the composite material that they are planned to be embedded into.
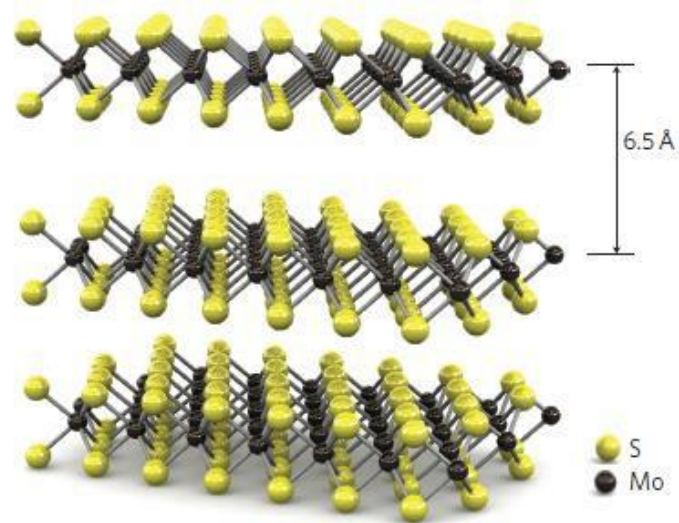
Fig. 3: Three-dimensional representation of the structure of MoS$_2$. Single layers, 6.5 Angtstrom thick can be extracted using scotch tape-based micromechanical cleavage[5].

1.4. Main production techniques

New technologies always face significant barriers in terms of cost and reproducibility as compared to the already established technologies. Therefore, low-cost production of large amounts of graphene with controlled electrical, physicochemical and structural properties is critical for graphene and 2D materials to have a technological impact on society. A big advantage of graphene is that it can be already produced by many different techniques, making it suitable for a variety of applications. Currently, there are probably a dozen methods being used and developed to prepare graphene of various dimensions, shapes and quality.
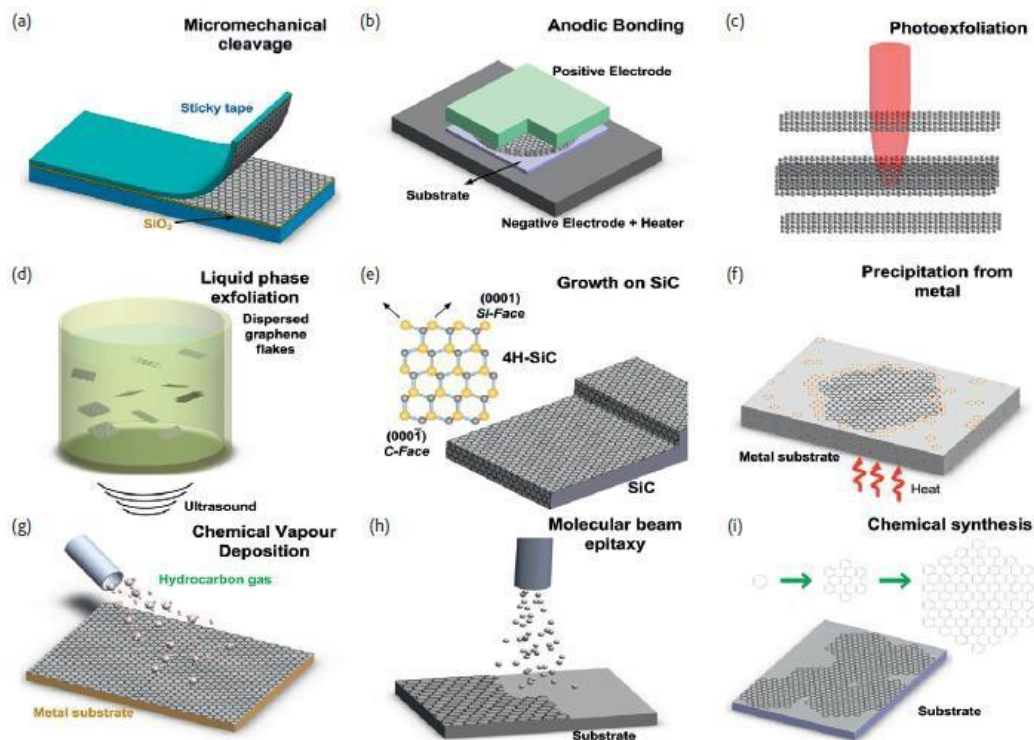
Fig. 4: Main graphene production techniques: (a) Micromechanical cleavage, (b) Anodic bonding, (c) Photoexfoliation, (d) Liquid phase exfoliation, (e) Growth on SiC, (f) Segregation/ Precipitation from carbon containing metal substrate, (g) Chemical vapour deposition, (h) Molecular beam epitaxy, (i) Chemical synthesis[6].

1.4 Mechanical exfoliation: with this method an adhesive tape is used to divide the graphene layers from the original graphite. The advantages of this technique are the high quality graphene and no need of special or expensive instruments. The main disadvantages of this method are the limitations for large-scale production, the difficulties in further processability, low yield and difficulty to detect single graphene sheets.

1.2 Chemical method: With this technique, graphene layers are produced by reducing graphene oxide (GO) usually by thermal, chemical or electrochemical methods. Graphene oxide is normally synthesized by the Hummer's method which involves the oxidation of graphite and its dissolution in water. This is feasible due to the polar groups (-OH, -COOH, -O) present on the graphene layers. The advantages of this method are that the GO is suitable for large-scale and controllable up-scaled production. Its main disadvantages are the highly defective, insulating nature of the sheets obtained, which require reduction techniques to restore electrical conductivity.

1.3 Liquid-based exfoliation: this technique involves the production of graphene layers form ultrasound sonication of the original graphite in various organic solvents. This technique normally involved three steps; 1) graphite dispersion in a solvent; the ideal solvents that can disperse graphene are the ones than can minimize the interfacial tension between the liquid and the graphene nanosheets, 2) exfoliation through ultra-sound sonication or ball milling, 3) centrifugation, where the exfoliated graphite nanosheets are separated from the non-exfoliated ones. The main advantages of this method are that is cheap and easily scalable and does not require expensive growth substrates. The downside of this approach is that the produced graphite flakes have limited size. This method is ideal for production of inks, thin films and composite materials.
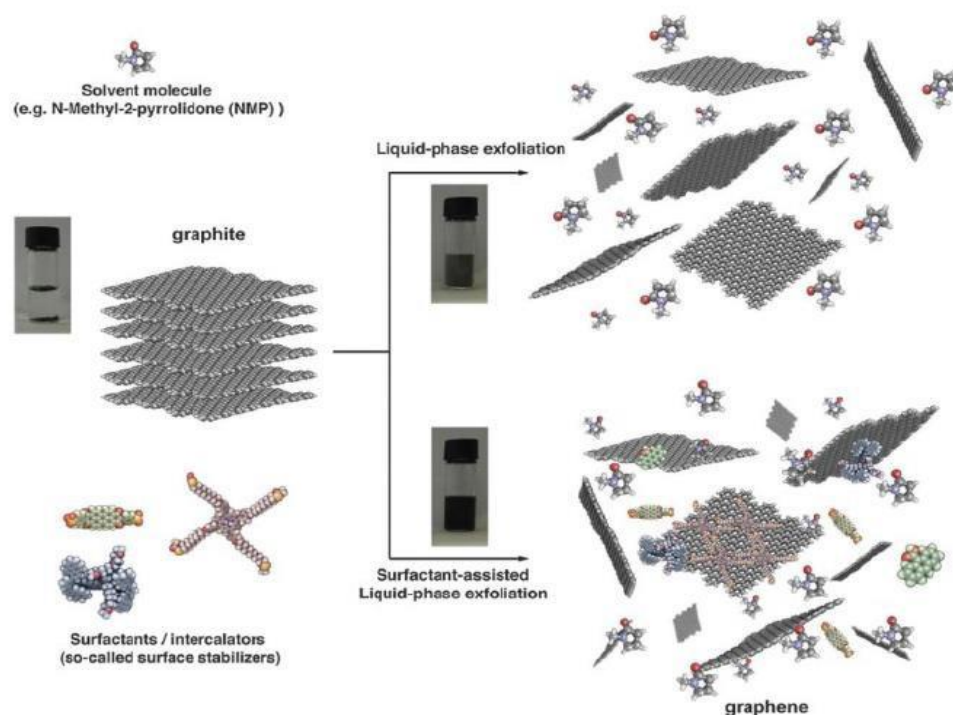
Fig. 5: Schematic representation of the liquid-phase exfoliation process of graphite in the absence (top-right) and presence (bottom-right) of surfactant molecules[7].

1.4 Growth on SiC: this technique requires thermal treatment of silicon carbide (SiC) under vacuum or in inert ambient conditions. Sublimation of silicon atoms is caused while carbon re-organizes from graphenic domains to a continuous layer. The main advantage of this technique is that it grows graphene directly on SiC, which is semi-conductive. Therefore no further transfer is needed for applications in electronics. Also, the wafers are available on different scales and the resulting graphene is of very good quality. However, the main disadvantages are that it is a high temperature process and the morphology of the resulting

layer is not controllable. Applications of this technique can be found mainly in high-frequency transistors, sensors and various fields of electronics.

1.5 Chemical Vapor Deposition (CVD): With this technique, a graphene layer is grown on a copper substrate through a carbon precursor source (e.g methane, ethylene), normally at high temperatures and in inert ambient conditions. In the process the carbon precursor dissociates at high temperature on the copper surface and the remaining carbon is dissolved in the copper and then precipitates during the cooling process. A main disadvantage of this technique is that the morphology of the resulting graphene layer is difficult to control and, for most applications, a transfer process on an insulator substrate is required after the synthesis. Some of the main applications of the method are for flexible displays, transparent conductors, sensors, solar cells, FETs and OPVs.
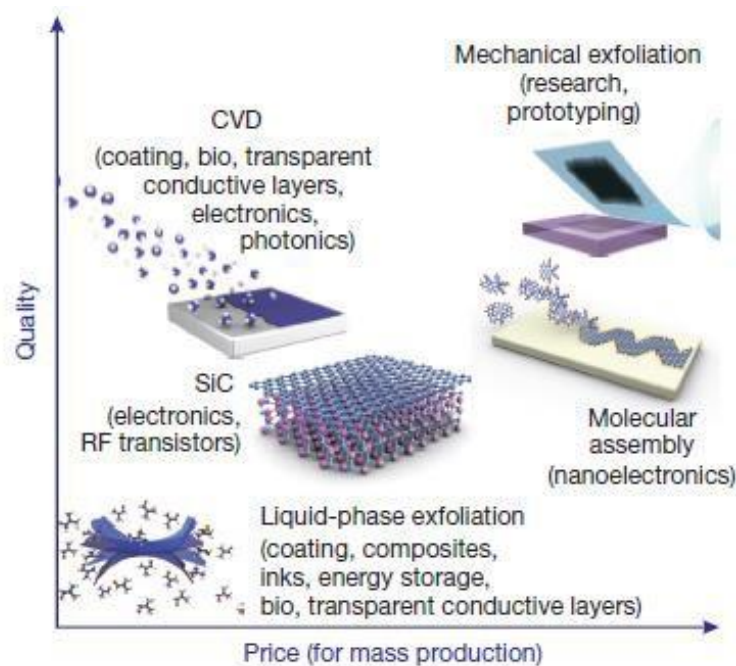

Fig. 6: The most popular methods for graphene production in terms of quality and price, which relates to their suitability for mass-production[8].

1.5. Post processing

A further step to the above production methods is the post processing of the produced graphene sheets. Until now, the most promising post processing method for graphene is the introduction of a tunable band gap into pristine graphene layers. Cutting graphene sheets into nanoribbons, and exposing or depositing graphene on various surfaces on structures could be considered as physical post processing during which the bonds in the graphene structure remain intact[9].However, a recent report on the reaction of graphene with hydrogen atoms demonstrates the feasibility of chemically post-processing graphene sheets. Interestingly, this process is reversible by annealing and suggests that graphene can serve as an atomic-scale scaffold.

1.6. Current status and trends in graphene research

Public and private investment in graphene research and innovation has been continuously growing in the last decade. The field of graphene and 2D materials is rapidly expanding, where thousands of research articles, patents and new companies appear every year. However, notwithstanding its rapid rise, graphene is facing numerous challenges and questions whether it will achieve its promising potential in the real world. In general, new technologies like graphene go through phases of great hype marked by sharp increases in expectations, interest and investment, followed by a period of uncertainty and loss. This kind of phases may eventually result in the realization of innovation advances and the scale-up of production and use, including in directions not initially expected at the beginning of the process.

In this section, a brief overview is given of the graphene trends in innovation and research. Bibliometric data on scientific publications is important in order to investigate trends and patterns in graphene publications, citations, research collaborations and focused sub-areas and emerging research topics. As illustrated in the following graph (fig. 4) there is an overall growth of graphene scientific publications, especially after the discovery of graphene. Between 2001 and 2004 there were fewer than 40 scientific papers on graphene published worldwide. In 2007, there were more than 420 papers, increasing to over 4000 in 2011-the year following the Nobel Prize award. Publication growth has continued with nearly 9,700 graphene papers published worldwide in 2014.
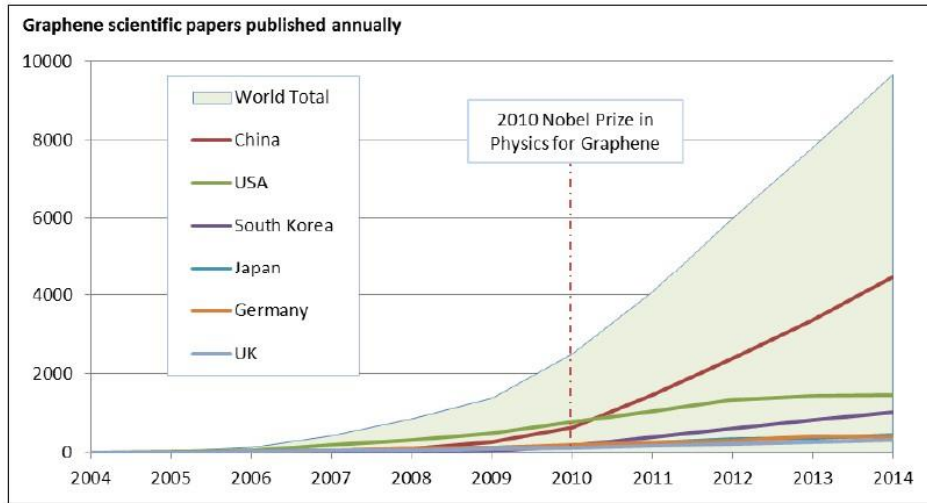
Fig. 4: Analysis of publication records, for the period 2001-2014. SCI articles and reviews with term "graphene" in title (N=32,994), country assignment based on all reported author institutional addresses[10].

Accordingly, the same trends are followed by companies that are researching on graphene new applications and patent their novel techniques. The major contributor countries in graphene patenting have been South Korea, USA and China. Fig. 5 indicates the global patent activity by geographical region.
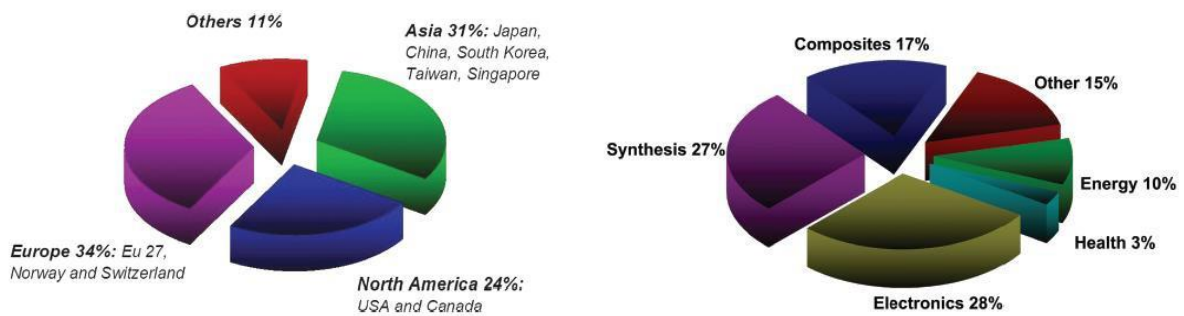
Fig. 5: Geographical distribution of scientific papers on graphene as of December 2013[8].
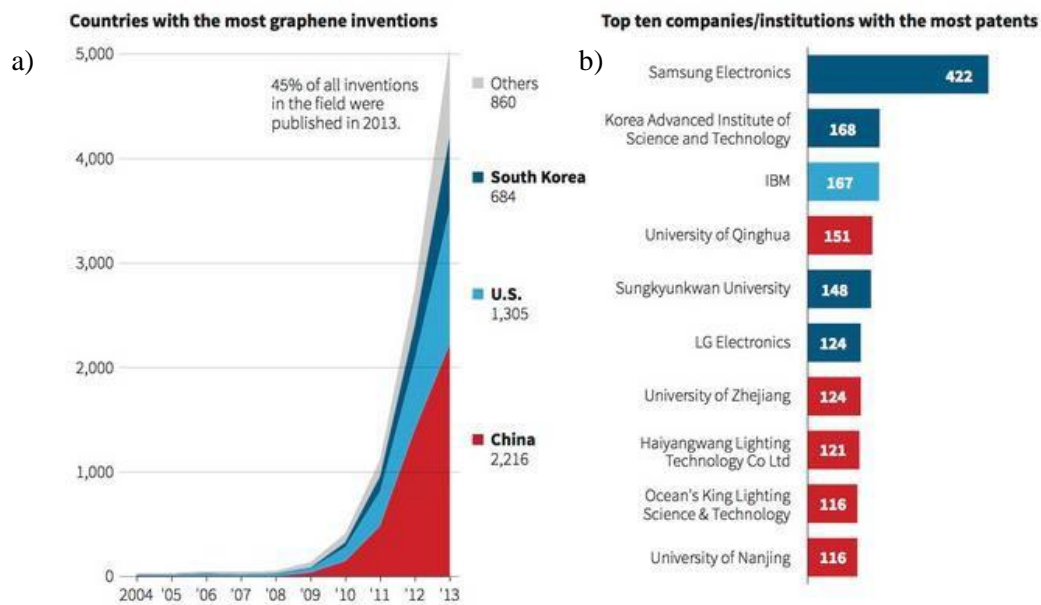
Fig. 6: a) Graph representing the countries with the most graphene inventions and b) the top ten technology companies and/or institutions with the most patents on graphene (Source: Thomson Reuters).

1.7. Applications and Current Challenges

The fast growing technological market is pushing towards transparent conductive materials which would be further used in electronic products such as touch screen displays, e-paper or organic light-emitting diodes (OLEDs). Flexible electronics is a technology where electronic circuits are assembled on flexible substrates. The advantage of such flexible technology is the ability to give new functionality to the existing electronics technology. Recently, microprocessor giant Intel at the 2015 International solid-state circuits conference (ISSCC) challenged the silicon industry which has been around our lives for nearly four decades. Intel's new 10nm manufacturing process for microchips expected in 2016-2017 will be the end of the road for silicon, and devices based on 7nm and beyond, Intel says, will require entirely new materials. One of these materials that could break the 7nm threshold could be graphene[11].

In the field of organic electronics, OLEDs are devices already being used in the current technology; Graphene is being widely studied in this emerging field for potential applications in high frequency transistors and logic transistors. Energy technologies are another area which is expected to grow from graphene's potential. In particular, graphene can be used in solar cells as an active layer or as a transparent material electrode. Energy storage

applications are another area where graphene can be used as a cathode for next-generation lithium ion batteries. An important and fast-growing area for graphene's industrial potential is the composite materials field.

The unique mechanical, thermal, chemical and gas barrier properties of it make it a strong candidate for composite materials applications. Also, the use of graphene-based paints can be used for conductive inks, antistatic, electromagnetic-interference shielding, gas barrier and anti-corrosion applications. In figure 7, the potential applications of graphene are represented in a schematic way.
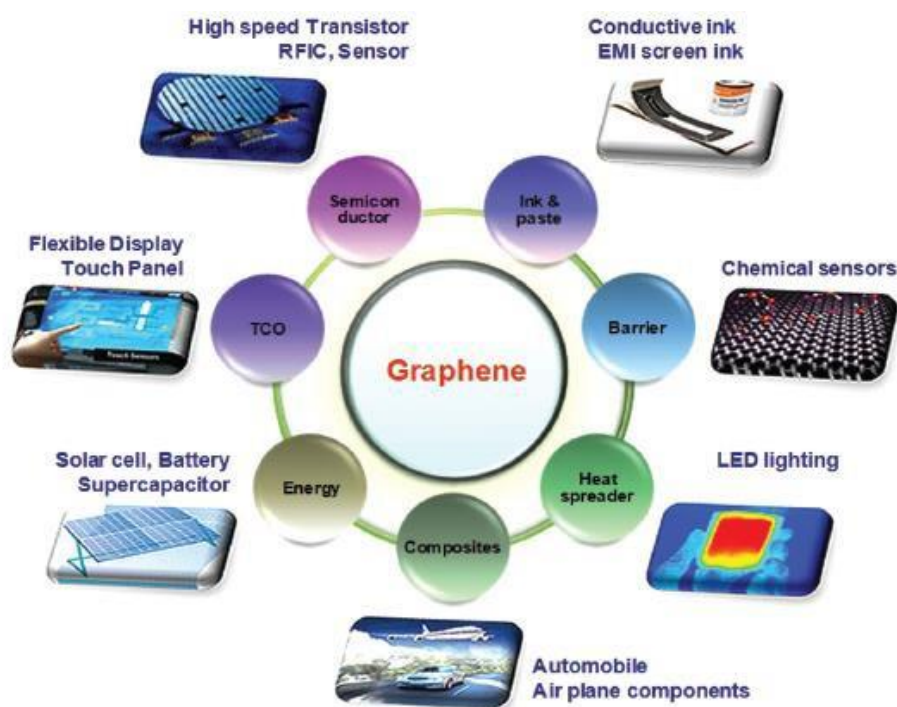
Fig. 7: Overview of applications of Graphene in different sectors ranging from conductive ink to chemical sensors, light emitting devices, composite materials, energy, touch panels and high frequency electronics[8].

How long will it take to see the first generation of graphene-based electronics in the market? That is the most fundamental question, which one may ask after learning the promising properties that graphene can offer. Even though scientific results show superb advantages of graphene for applications in super-fast electronics, the technology in this field is still not ready. One of the biggest technological challenges that graphene is facing is the hurdle of controlled production of large sheets. Therefore, solving the dilemma of mass-producing high quality graphene should be the main focus in the 2D research community. This would be the first step towards commercially-available graphene-based electronics. There have been many

different methods to produce graphene nanosheets, although the big question of reproducibility still remains.

Moreover, any of the tested methods should be competitive and/or compatible with the already successful, well-established industrial techniques (e.g. silicon in microelectronics) that are widely used in the current electronics technology. Almost all of the candidate materials to replace silicon have failed so far. While a highly convenient, widespread "killer application" for graphene is still to be inventedn, the scientific community is still exploring the unique properties of a material that continues to gives unique research opportunities and exciting, groundbreaking potential applications.

1.8. Bibliography

[1]   P. Delhaes, *Graphite and Precursors*. CRC Press, 2001.

[2]   H. S. A. R. Lipson, "A new structure of carbon," *Nature*, vol. 149, p. 328, 1942.

[3]   The Royal Swedish Academy of Sciences, *The Nobel Prize in Physics 2010*. 2010.

[4]   H. Rachel, " 'Need to Track Organic Nano-Particles Across the Universe? NASA's Got an App for That,'" *NASA*, 2014.

[5]   B. Radisavljevic, A. Radenovic, J. Brivio, V. Giacometti, and A. Kis, "Single-layer MoS2 transistors," *Nat. Nanotechnol.*, vol. 6, no. 3, pp. 147–150, 2011.

[6]   F. Bonaccorso, A. Lombardo, T. Hasan, Z. Sun, L. Colombo, and A. C. Ferrari, "Production and processing of graphene and 2d crystals," *Mater. Today*, vol. 15, no. 12, pp. 564–589, 2012.

[7]   A. Ciesielski and P. Samori, "Graphene via sonication assisted liquid-phase exfoliation," *Chem. Soc. Rev.*, 2013.

[8]   A. C. Ferrari, F. Bonaccorso, V. Fal'ko, K. S. Novoselov, S. Roche, P. Boggild, S. Borini, F. H. L. Koppens, V. Palermo, N. Pugno, J. A. Garrido, R. Sordan, A. Bianco, L. Ballerini, M. Prato, E. Lidorikis, J. Kivioja, C. Marinelli, T. Ryhanen, A. Morpurgo, J. N. Coleman, V. Nicolosi, L. Colombo, A. Fert, M. Garcia-Hernandez, A. Bachtold, G. F. Schneider, F. Guinea, C. Dekker, M. Barbone, Z. Sun, C. Galiotis, A. N. Grigorenko, G. Konstantatos, A. Kis, M. Katsnelson, L. Vandersypen, A. Loiseau, V. Morandi, D. Neumaier, E. Treossi, V. Pellegrini, M. Polini, A. Tredicucci, G. M. Williams, B. Hee Hong, J.-H. Ahn, J. Min Kim, H. Zirath, B. J. van Wees, H. van der Zant, L. Occhipinti, A. Di Matteo, I. A. Kinloch, T. Seyller, E. Quesnel, X. Feng, K. Teo, N. Rupesinghe, P. Hakonen, S. R. T. Neil, Q. Tannock, T. Lofwander, and J. Kinaret, "Science and technology roadmap for graphene, related two-dimensional crystals, and hybrid systems," *Nanoscale*, vol. 7, no. 11, pp. 4598–4810, 2015.

[9]   M. Taghioskoui, "Trends in graphene research," *Mater. Today*, vol. 12, no. 10, pp. 34–37, 2009.

[10]   F. S. Y. P. Shapira, A. Gok, "Graphene Research and Enterprise: Mapping Innovation and Business Growth in a Strategic Emerging Technology," No15/14, 2015.

[11]   Bojdys J. Micahel, "2D or not 2D-Layered Functional (C, N) Materials 'Beyond Silicon and Graphene,'" *Macromol. Chem. Phys.*, vol. 217, pp. 232–241, 2016.

Chapter 2

Metrology of Graphene and 2D Materials

2.1. Why it is important

Fragmentation is the process of disintegrating an object by multiple fracturing events. The physics of fragmentation is of interest in different fields of science and engineering: materials science, failure analysis, military applications and even astronomy. Analysing the size distribution of a fragmentation process allows understanding the underlying physics. This approach was used, as example, by Brown et al.[l] during their studies of the galaxies distribution, to demonstrate that the universe underwent a single fragmentation event (the Big Bang), separating into protogalactic volumes at a relatively early stage.

In most cases, the study of size distribution in performed on three-dimensional (3D) objects, as example powders or rocks from mining activities (or galaxies for astronomic studies). Size distribution of one-dimensional (1D) objects, in particular polymers, is also routinely measured in polymer science, as example by size exclusion chromatography (SEC). Since the first half of the 20th century, chemists were challenged to find new techniques to characterize polymers, whose exact 1D structure and macromolecular nature were then still under debate[2]. The development of new techniques to produce, analyse and process polymers led eventually to the plastic revolution. One century after, scientists are struggling to produce and characterize a further class of materials formed by repeating units not in one but in two dimensions.

Today, two-dimensional (2D) materials like graphene, boron nitride and transition metal dichalcogenides having thickness < 1 nm and sizes >1000 nm can be routinely produced on large scale with potential breakthrough applications in a wide range of sectors, from electronics to biology.[3-5] Even if the first graphene-based products composites are already commercial, we are still in a situation similar to that of polymer chemists in 1920.[6] There is an ongoing debate on how to define and measure 2D materials,[7] and a classification based on chemical composition, thickness and sheet lateral size has been proposed recently.

The size of these 2D materials is a fundamental parameter to be estimated, given that it has an impact on their performance in basically all their potential fields of applications, influencing mechanical and electrical properties in polymer composites,[9, 10] charge transport in thin conductive films,[11] gas permeation in surface coatings[12] and even biological activity such as internalization in living cells.[13]

Unfortunately, exfoliation always yields a poly-dispersed range of nanosheets thicknesses and lateral sizes because the exfoliation of 2D nanosheets starting from 3D bulk materials is a complex process based on bubble cavitation, intercalation and disruptive fragmentation.[14] When characterizing the suspensions of these 2D sheets, their size is commonly reported using a well- known couple of statistical parameters such as the arithmetic mean and the standard deviation (SD) of sheet length, in this way assuming implicitly that their length follows a Gaussian (a.k.a. "normal") distribution. However, all published experimental data show that the size distribution is non-Gaussian and highly asymmetric. Similar asymmetric distributions are commonly observed in almost all areas of science, e.g. in the length distribution of polymers, in the content of chemical elements in rocks, in the abundance of species in biology and in the distribution of galaxies in astronomy.[15]

New techniques and procedures for the metrology of 2D materials are thus needed, both for fundamental understanding of their physics and for technological developments. Thus, we developed an analysis technique to characterize large amounts of 2D monoatomic nanosheets. We used the data collected in this way to unravel the different fragmentation processes that lead to a given distribution, and propose a new parameter, in analogy with polymer metrology, to characterize the area dispersion of such 2D materials.

To understand the physics of a truly 2-dimensional fragmentation process we need an "ideal" 2D material, where the only variable parameter should be lateral size. To this aim, we chose to use water-soluble graphene oxide (GO) nanosheets obtained by oxidation and exfoliation of graphite using the Hummers method.[16] The sheets used were all monoatomic layers, completely exfoliated already at the start of our measurements, and the overall amount of material undergoing fragmentation was constant, allowing in this way to have a purely 2D fragmentation process. Thanks to their highly hydrophilic nature, these sheets were stable as monolayers in water and cold be deposited on silicon substrates up to very high surface coverage with negligible aggregation and overlap. Furthermore, the initial lateral size of these sheets (up to 100 ^m) was much larger than the one typical of 2D materials; by using sonication the average sheet size could be reduced to less than 100 nm, allowing to study the 2D fragmentation process on a wide range of scale-lengths.

2.2. Classification and Definitions

The graphene production and in general the 2D materials, requires high expectations as the properties of the exfoliated material depend strongly on its physical dimensions. This means that there is a strong need for a method or process able to control and quantify the resulted material before it is used to composites, electronics and other technological applications.
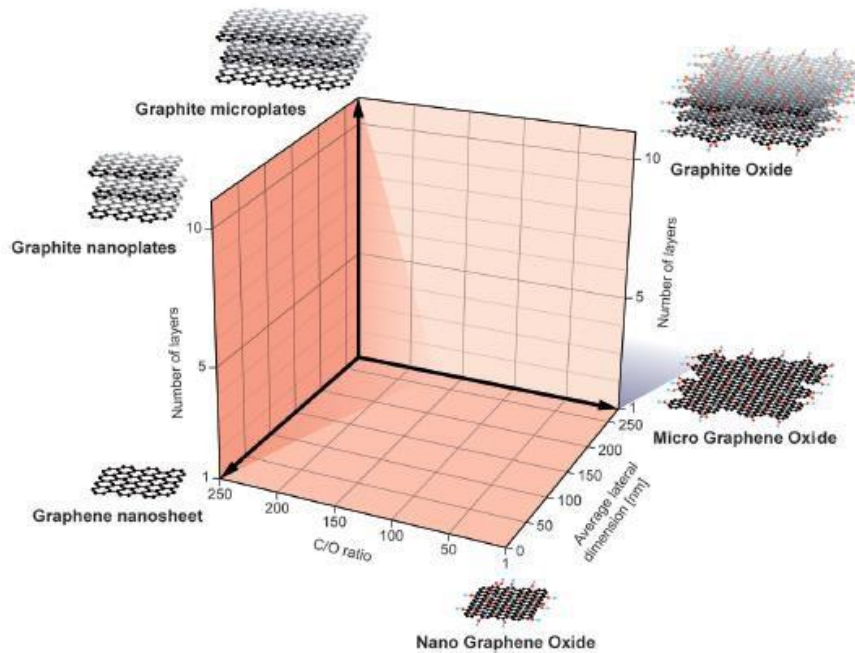

Fig. 1: A graphical grid representing the categorization of different graphene types according to three fundamental properties. Number of graphene layers, average lateral dimension, and atomic carbon/oxygen atom. The different materials drawn at the six corners of the grid represent the ideal cases according to the lateral dimensions and the number of layers reported in the literature. The values of the three axes are related to the GBMs at the nanoscale, but is feasible to expand the values to the microscale[17].

Usually the term graphene is used in a generic manner by scientist and not to describe the single graphene layer sheet as discovered by its creators and not in consistency to describe many graphene-based materials (GBMs). Therefore, there is an inconsistency in names and definition of the use of graphene but also by its reference to related 2D layers and flake carbon forms. This tells that the scientific community needs a clear, consistent and widely accepted system of describing and naming the various derivatives of the graphene-related materials. By solving this issue, we can avoid misleading understanding of definitions

amongst all the stakeholders (i.e., researchers, industry, government organisations and regulatory authorities).

One way to arrive to this clear definition is by creating a definition on its morphological descriptors such as typical dimensions like thickness (number of layers) and lateral size.

In a recent study, P. Wick et. Al., proposed a classification framework providing a starting point for the categorization of different graphene types within a grid arrangement (as show on Fig. 1) according to three characteristics which are easy to measure and to quantify. In the table below are the basic analytical techniques to measure these three fundamental characteristics for further GBM classification.

GBM-specific property and suitable analytical tools for the classification of GBMs	
Number of layers (thickness)	TEM
	AFM
	Raman Spectroscopy
	Optical absorbance measurements
Lateral size	TEM
	SEM
	AFM
Atomic C/O ratio	XPS
	Elemental analysis

Table 1: Analytical techniques for the classification of GBMs

Summarizing, there is a need for clarity in the definition of GBMs classification. This could help to avoid generalizations about the GBMs capabilities and limitations that can potentially provide false expectations and unnecessary safety concerns. Other potential benefits that could arise are;

- the improved vocabulary terminology for structural characterization

- the classification within the proposed grid prevents ad hoc naming

- better comparisons between carbon allotropes

- fitting the "molecule of interest" into the classification grid and its position determines which reference GB should be included in experiments

- Standard analytical methodology for benchmarking of materials

- Future comparative studies possible through minimal material characterization

- Aid in structure-activity analogies for predictive toxicology

- Support in peer-review process

- Clear-cut guidelines for regulatory purposes

2.3. Experimental Methods

To monitor the sheet population from the meso- to the nano-scopic scale we used a combination of different techniques (fig. 2): optical fluorescence microscopy (FM),[1] scanning electron microscopy (SEM) and atomic force microscopy (AFM). In this way we could analyse more than 2,000 sheets for each sample. The total surface areas sampled using the three techniques were: 60 mm^2 (FM), 0.1 mm^2 (SEM) and 0.01 mm^2 (AFM).
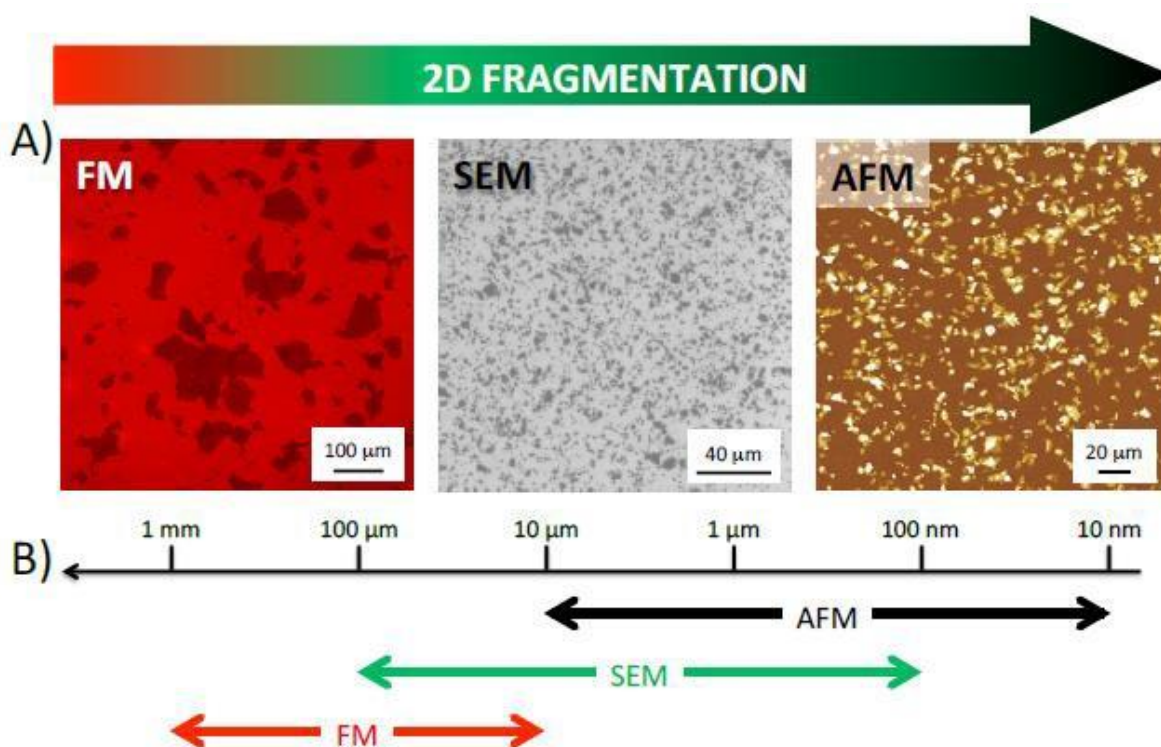
Fig. 2: A) FM, SEM and AFM images of GO sheets deposited on silicon substrate. Total surface areas sampled using the three techniques: 60 mm^2, 0,1mm^2,. B) a schematic representation of the different scale-lengths explored with the different techniques.

FM

Fluorescence microscopy (FM) images were taken in reflection mode with a Nikon Eclipse 80i optical microscope. The images were recorded with a digital color camera Nikon Coolpix 5400. Samples were prepared by spin-coating the GO sheets on 300 nm thick silicon oxide substrate that was covalently functionalised with triethoxysilane fluorescent thiophene-based dye, N-(3- (triethoxysilyl)propyl 2,2':5',2":5",2"'-quaterthiophene-5-carboxamide, as described in ref. (1).

SEM

Scanning electron microscopy (SEM) images were taken using a FEI Dual Beam system (FIB-SEM) 235 with an electron beam (1nm).

AFM

Atomic Force Microscopy (AFM) images were obtained in tapping mode by employing a commercial microscope (MultiMode Nanoscope IIIa, Bruker). The device was equipped with a J scanner, which was calibrated using the manufacturer's grating. Ultrasharp tips (RTESPA MPP- 11120, Silicon cantilevers, Bruker, typical force constant 40 N/m, resonant frequency 300 kHz) were used. Height images were flattened to remove background slopes. No other filteringprocedures were performed on the images. AFM images were analysed using SpipTM software. Detailed information about flattening procedures of the AFM images and the quantitative analysis using the frequency spectra can be found in Ref. (2).

XPS

X-rays photoelectron spectroscopy (XPS) spectra were recorded with a Phoibos 100 hemispherical energy analyser (Specs) using Mg Ka radiation (fiu=1253.6 eV). The X-ray power was 250 W. The spectra were recorded in the constant analyser energy (CAE) mode with analyser pass energies of 40 eV for the survey spectra and 20 eV for the high resolution ones. Charging effects was corrected by energy calibration on C 1s level relative to 284.5 eV. The base pressure in the analysis chamber during analysis was 3-10-10 mbar.

DLS and Zeta-potential

Dynamic Light Scattering (DLS) and Zeta-potential experiments were carried out at 25°C on a Malvern Zetasizer Nano-ZS, equipped with a helium-neon 633 nm laser and Non-invasive Back Scatter (NIBS) optics/detector at 173°. The size distribution was calculated using a built-in auto-correlation function, whereas Zeta-potential was estimated by means of the M3-PALS (Phase Analysis Light Scattering) technique, measuring the particle electrophoretic mobility in a thermostated cell.

SLS

Static Light Scattering (SLS) spectra were recorded with a Horiba Jobin-Yvon Fluoromax 4 spectrofluorimeter equipped with a 150W Xenon arc lamp, by using a synchronous scan of the emission and excitation monochromators (scan range 200-800 nm) and a right angle geometry for excitation and photon detection.

2.3.1 Sonication process

In all the samples used the sonication conditions such as the ultrasound frequency and the effective energy density transferred to the GO sheet (i.e. energy/mass) were constant.

For a typical ultrasonic power output of 120W and frequency 37 kHz, the corresponding wavelength of sound (λ) in water was ca. 4 cm. The peak pressure in the wave was of the order AP $\approx$ 1 atm corresponding to a net stress applied to GO sheet of the order $\Delta P(\text{size}/\lambda) \sim$ mPa which induces the sheet breakdown.

2.4 Image Processing

2.4.1 Definition of image

Each FM, SEM and AFM image was treated as a matrix A(i,j), where (i,j) was the 2D-position of each data-point. Each cell of the matrix for AFM images contained the height value (z). SEM and FM matrix cells contained instead the intensity of electrons and photons flux respectively.

2.4.2 Flattening procedure of an AFM image

Rough data AFM images are affected by artefacts due to piezo scanning. Piezo-electrics motors are commonly used to move the samples in sub-nanometric steps in all the Cartesian directions (X,Y,Z). For the sake of simplicity, we use the laboratory reference system (i.e.

X,Y plane defined by the surface sample and Z perpendicular). In general, the in-plane movements are decoupled: $x \neq (y,z)$, but Z-motion depends on the (x,y) position: $z = z(x,y)$. This means that the original data recorded into an AFM image of an flat surface are described by a 2D-hypersurface $z = f(x,y)$ instead of a plane $z = z_0$.

Thus, the original AFM data have to be processed and mathematical transformations applied to the image in order to minimize the artefacts are called "flattening procedures". The histogram distribution is a graph plotting for each height z the (normalized) number of points of the image having that height. It is one the most suitable parameters to monitor flattening procedure. In particular, the histogram curve Fc allows to correct the image slope because the histogram is the best indicator for the flatness of the surface. Plane surfaces are characterized by high and narrow histogram peaks and the peak width corresponds to the surface roughness in the case of Gaussian distribution.[3]

A simple scheme is shown in Fig. 3 where (a), (b) and (c) represent the raw image, an intermediate and the correct image, respectively. Each step of the flattening procedure is monitored by the histogram distribution displayed on the lower part of the figure. In particular, figure 3 shows the AFM image of GO sheets on silicon substrate at 20 hours sonication.
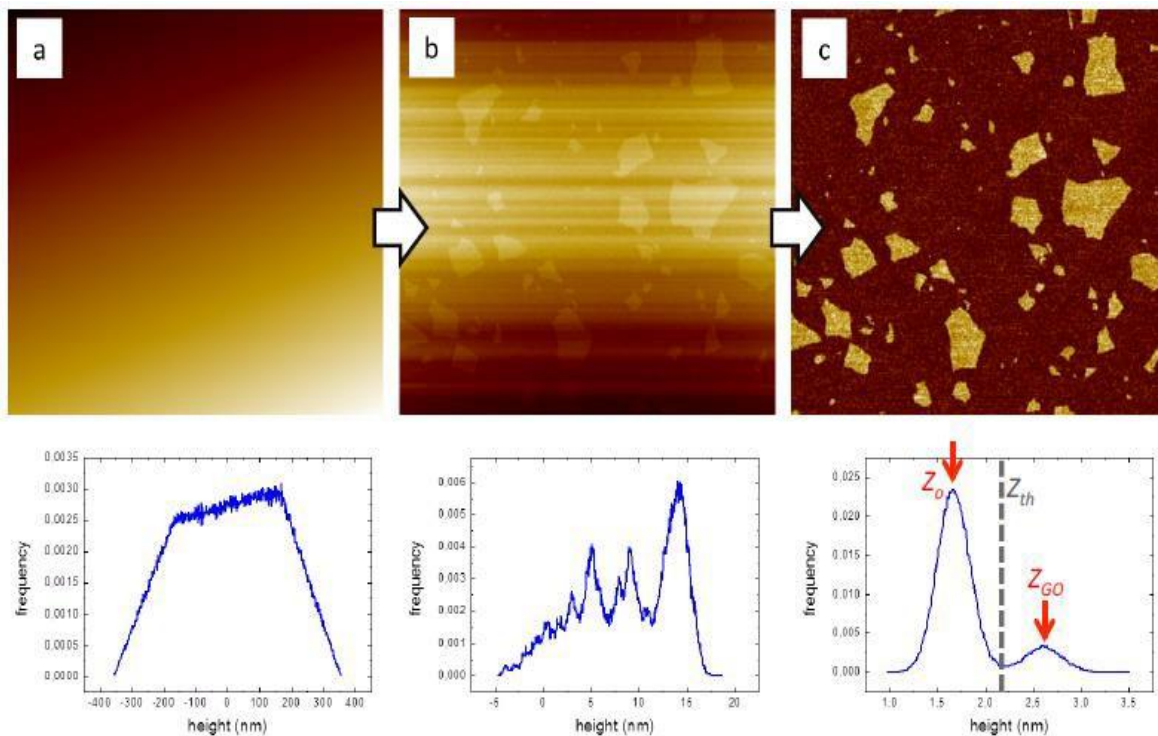
The correct (a.k.a. flattened) AFM image presents a symmetric histogram distribution well described by a Gaussian function. The peak width amounts to 3.80 ± 0.02 nm as calculated following the work of Olive et al.[4]

2.4.3 Automatic size analysis

Thanks to the flattening, bare substrate and GO sheet can be unambiguously distinguished by using a threshold value (z_{th}) defined as the mean value between the substrate Z level (z_0) and the GO height (z_{GO}): $z_{th} = (z_0 + z_{G0})/2$. All the pixels (i,j) having the corresponding z value higher than the threshold are assigned to the GO sheets.

Image analysis software recognised all the GO sheets, counted them and calculated several parameters such as area, size, perimeter, Aspect Ratio and Form Factor. Figure 4 shows the automatic analysis performed on the AFM image reported in fig 4. The different GO sheets are marked with different colours.
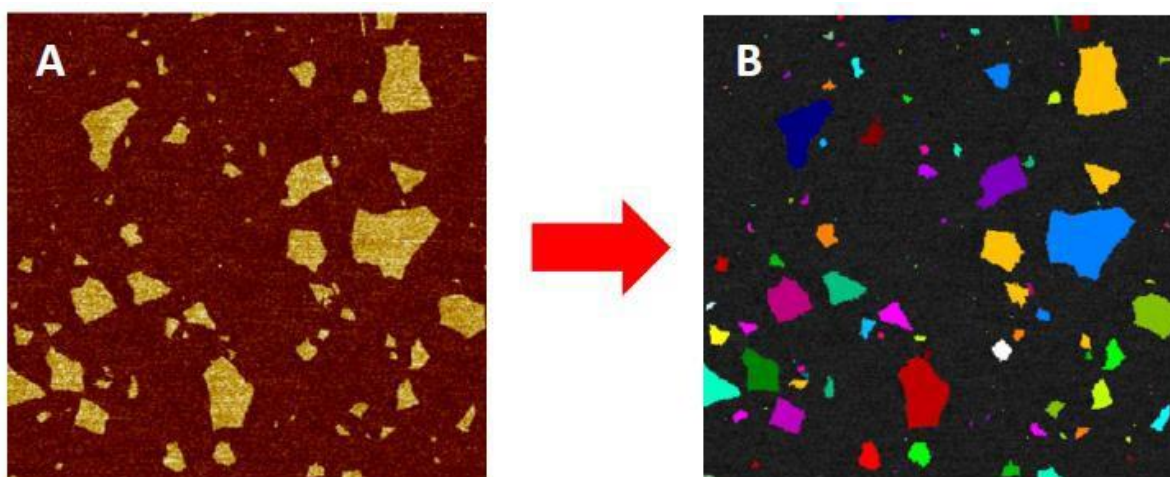

Fig. 4: a) original AFM data and b) corresponding processed image where GO sheets have been automatically identified by the software and marked with different colours.

2.4.4. Statistical parameters

Using the automatic image analysis, each image is decomposed into a set of elements. Each of them corresponds to a GO sheet and is defined by an array of six parameters: four used to

describe the lateral size and two to describe the shape of the sheet. Figure 5 summarises the information related to a single GO sheet with the size parameters such as:

- *Area* defined as the number of pixels occupied by the sheet on the surface (green region in Fig. 5 B)
- *Perimeter* defined by the length of outer contour (green contour in Fig. 5 C)
- *Length (L)* defined as the distance between the two farthest pixels of each sheet (red line in Fig. 5 C)
- *Size (s)* defined as the side length of the square having the same area of the sheet (white square in Fig. 5 B)
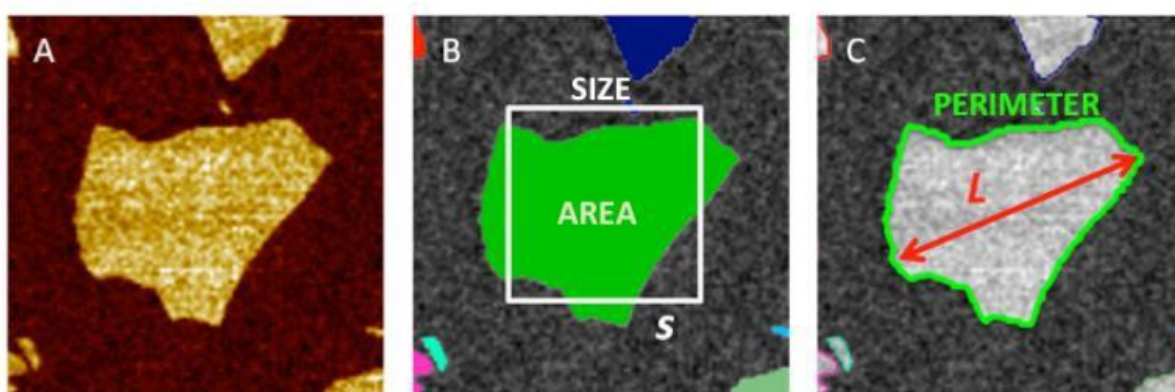

Fig. 5: Size parameters of GO sheet. a) AFM image, b) automatic recognition of GO area (green region) and corresponding c) perimeter (green line) and length (L).

For the quantitative analysis of the shape of the 2D objects, we focussed our attention on two dimensionless parameters:

i) the *Aspect Ratio (A_R)*, namely the squared length divided by the area $(A_R = L^2/A)$. The parameter describes the anisotropy of the shape considered, Ar is always $>4/\pi$ ($=4/\pi$ for circles and $=2$ for squares). ii) the *Form Factor (FF)*, which combines area and perimeter $(FF = 4\pi A/p^2)$, describing the shape irregularity: FF is always <1 ($=1$ for circles and $=\pi/4$ for squares).

2.4.5. Pixel resolution – overlapping

Image resolution basically depends on two independent factors: the lateral resolution of the experimental measurement and the pixel dimension (D_p) (a.k.a. pixel resolution). The first

factor is related to the experimental parameters such as the physical properties of the probe-sample system. Conversely, the pixel resolution, defined as the ratio between the lateral size of the acquired image and the number of pixel: $D_p = size_{image}/N_p$, can be easily tuned. The chosen pixel dimension has to be much lower than the lateral size of GO sheet in order to minimise the artefacts due to pixelization of the acquired image. All the topographic images acquired using AFM, FM and OM are obtained by scanning areas within the range between 1 am and 500 ^m. In order to compare all the collected images, we choose different pixel resolutions, as shown in fig.5, overlapping the values for the different techniques. The issue related to the pixelization

was minimised by using an iterative procedure to find the suitable pixel dimension.

For each scanned area we

i) acquired images with different D_p values,

ii) obtained the corresponding area distributions and

iii) calculated the average characteristic size (s) = sj(4).

We choose the pixel resolution value so that it was about 10 times lower than the average size of the measured GO sheets: $D_p \leq \langle s \rangle / 10$.
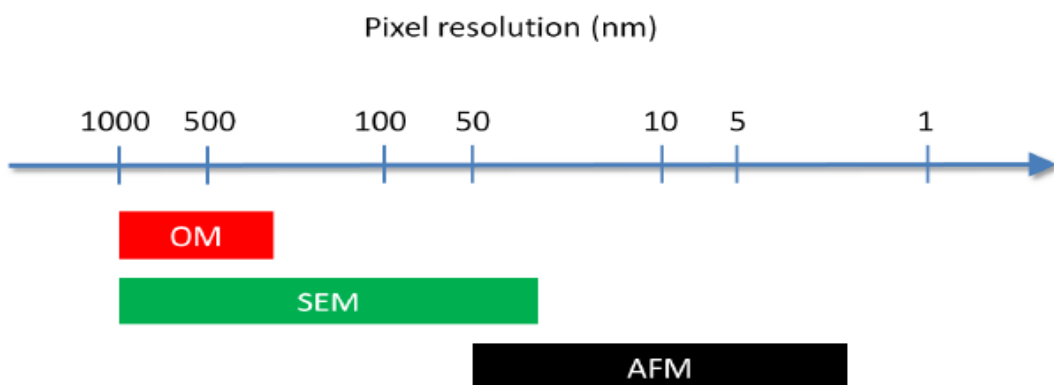

Fig. 6: Pixel resolution of all the acquired image.

2.5. Mathematical Methods

2.5.1 Discrete distributions, operative definitions

After collecting all the images, we calculated for any studied parameter *(x)* a discrete probability distribution of the sheets f_x defined as the sheet distribution normalized for the total number of sheets. In general, a distribution is described using the mean value (<x>) and the corresponding standard deviation (SD), calculated as:

$$\langle x \rangle = \sum\nolimits_{x_{min}}^{x_{max}} x_i \cdot f_x \;\; ; \qquad SD = \sqrt{\sum\nolimits_{x_{min}}^{x_{max}} (x_i - \langle x \rangle)^2 \cdot f_x} \qquad \text{with} \;\; \sum\nolimits_{x_{min}}^{x_{max}} f_x = 1.$$

These definitions can be generalised for the continuous distributions /(x) where x is a continuous random variable:

$$\langle x \rangle = \int_{x_{min}}^{x_{max}} x_i \cdot f(x) dx \;\; ; \quad SD = \sqrt{\int_{x_{min}}^{x_{max}} (x_i - \langle x \rangle)^2 \cdot f(x) dx} \quad \text{with} \;\; \int_{x_{min}}^{x_{max}} f(x) dx = 1.$$

In the case of Gaussian distribution, <x> and SD correspond respectively to the position (a.k.a. mode) and the width of the peak of the distribution. Conversely, in the case of skewed distributions this simple relationship is not valid, being <x> and SD given by a combination of the mode and the breadth of the distribution. In the case of highly skewed distributions, the standard deviation cannot be a useful parameter because it is larger than the mean value. This is a common issue related to the breadth and shape of the distributions that are usually determined most efficiently with parameters derived from the *higher* moments of the distribution. A detailed description can be found in [5].

<x> and SD are not sufficient to describe the given distribution. Fig 7, as example, shows two different discrete distributions f_x: (red) Gaussian and (blue) scattered bimodal, having the same couple of statistic parameters <x> and SD. Both distributions are normalised.
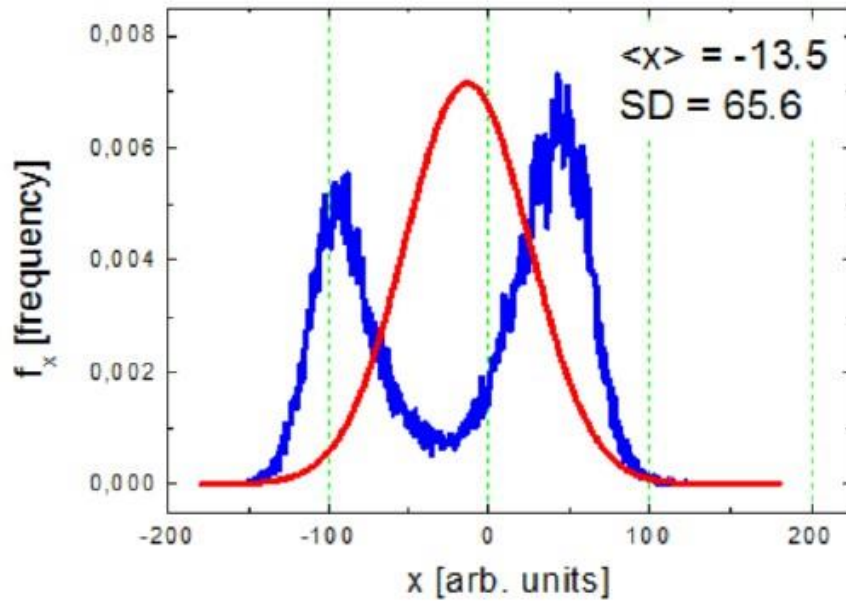

Fig. 7: Different distributions give the same couple of statistical parameters.

For the sake of simplicity, in the main text we used indistinctly the words "distribution and "function".

2.5.2 Choice of the "optimal" number of sampling points to reconstruct the distribution

The number of bins *Nb* used to buld the size distribution histogram is calculated as the ratio between the x-range and the bin width h:

$$Nb = \left\lceil \frac{x_{max} - x_{min}}{h} \right\rceil$$

where min (max) value corresponds to the smallest (largest) measured sheet, while the braces indicate the ceiling function.

The parameter h is a smoothing or localizing parameter and controls the width of the histogram bins. An h that is too large leads to very big blocks and thus to a very unstructured histogram. On the other hand, an h that is too small gives a very variable estimate with many unimportant peaks. The choice

of the "optimal" h value is not trivial and several methods are suggested.[6] We used the Scott's rule: $h = 3.49 \cdot SD \cdot n^{-1/3}$ being simple and well-founded in statistical theory taking into account the SD of the acquired dataset and the number of the measured sheets (n) [7].

2.5.3 List of used analytic continuous distributions

All the acquired area distributions were fitted with the probability distributions commonly used in fragmentation models: [8] Inverse power, Log-normal, Gamma and Exponential functions.

- **Inverse power law** describes a scale invariant (a.k.a. fractal) fragmentation, depicting a series of fragmentation processes that do not depend on the size of the fragment.

- **Log-normal distribution** describes random fragmentation processes with a random distribution of the fragment shape, and has previously been used to describe many rock crushing processes and fragmentation of 2D materials.[9]

- **Gamma function** describes the fragment distributions following a particular partition of Euclidean surfaces called Voronoi tessellation.[10] Because Gamma and Log-normal functions have very similar shapes they are often used indiscriminately, despite describing different mechanisms.

- **Exponential functions** (a.k.a. Mott functions) describe from a purely statistical point of view fragmentation given by randomly oriented cracks.

The used mathematical functions mentioned in the main text are listed below:

Distribution	Equation	$\langle x \rangle$	SD
Gaussian	$\dfrac{1}{w\sqrt{2\pi}} \cdot e^{-\frac{(x-x_0)^2}{2w^2}}$	x_0	w^2
Log-normal	$\dfrac{1}{xw\sqrt{2\pi}} \cdot e^{-\frac{(lnx-x_0)^2}{2w^2}}$	$e^{x_0+w^2/2}$	$\left(e^{-w^2}-1\right) \cdot e^{2x_0+w^2}$
Gamma	$\Gamma(\alpha) \cdot x^{\alpha-1} \cdot e^{-\beta x}$, $\alpha, \beta > 0$	$\dfrac{\alpha}{\beta}$	$\dfrac{\alpha}{\beta^2}$
Power law	$\dfrac{1}{x^\alpha}$		
Mott	$e^{-\gamma \cdot \sqrt{x}}$		

Gaussian function is a symmetric distribution where the mean value corresponds to the median and the mode, i.e. the position of the peak. The statistical parameters are calculated within the domain $x \in$ R. All the others functions are asymmetric and defined for positive variables. The statistical parameters of Log-Normal and Gamma functions are calculated within the domain $x \in (0, +\infty)$.

2.5.4 Data fit

In general, discriminating between different asymmetric distributions is not simple (see ref. (11) as example). In order to tackle this well-known problem, we studied the complementary *cumulative distribution functions:* $CCD(\xi) = 1 - \int_0^\xi f(x)dx$ together with the distribution itself $f(x)$. This function can be defined both for discrete and continuous distributions.

As example, taking into account our experimental dataset, given a certain area value *(A),* the $CCD(A_i)$ function indicates the population of GO sheets larger than A_i. For this reason it is also called *survival* or *reliability* function.

Figure 8 reports the study performed on (A) the area distribution and (B) the corresponding CCD of GO sheets after 20 sonication hours, comparing the best-fit functions obtained by using the Levenberg-Marquardt algorithm corresponding to (purple) Log-normal, (red) Gamma and (green) Mott distributions. The corresponding χ^2 coefficients are reported in table 2 (the lower is χ^2, the better is the fitting).
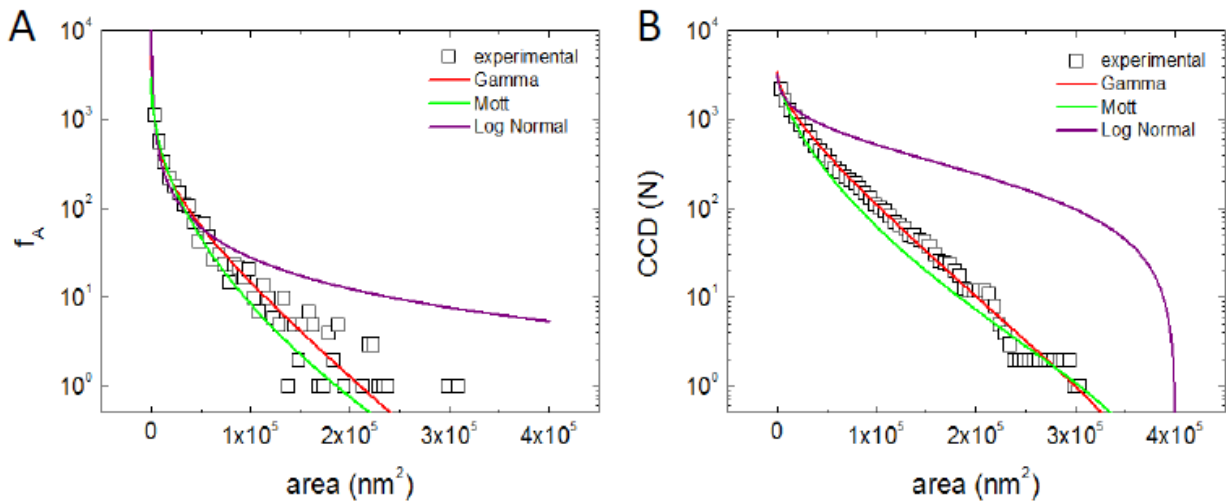
Fig. 8: Fitting analysis. (A) Distribution of GO sheets after 20 sonication hours and (B) the corresponding cumulative distribution function. The experimental distributions are fitted with (purple) Log-normal, (red) Gamma and (green) Mott distributions.

Table 2. χ^2 coefficients of best-fit.

	f(area)	CCD(area)
Log-normal	39.6	13093
Gamma	9.15	126.6
Mott	16.6	1139.7

The χ^2 coefficient of the Gamma function is the lowest, clearly evincing that this function better reproduces the measured dataset.

This procedure has been used for all the area distributions acquired at all the different sonication times. Gamma distribution always shows the lowest x^2 coefficient in the range between 0.5 hours and 40 hours sonication time.

2.6. Chemico-Physical Analysis

### 2.6.1 Monitoring of C/O ratio of the GO sheets
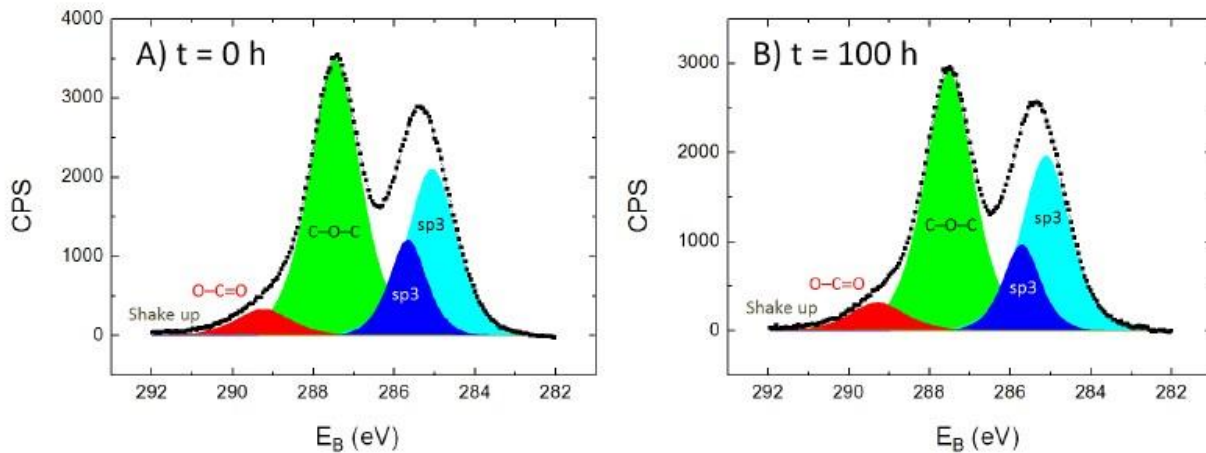
Fig. 9. High-resolution core level spectra Carbon 1s of GO sheets before (A) and after (B) 100 hours of sonication. XPS spectra have been corrected by removing the background.

The high-resolution C1s XPS spectra exhibited contributions of different C-C bonds and the presence of hydroxyl and carboxyl groups. In particular, we distinguished five components at 284.4 eV (C sp2), 285.0 eV (C sp3), 286.8 eV (C-O-C) 288.5 eV (O-C=O) and 290.8 eV (shake-up).

All the XPS spectra were obtained by subtracting the Shirley background (as displayed in Fig. 9) and then fitted with a Voigt function for each component. The Full Width Half Maximum value of all the five components is between 1.0 and 1.6 eV. We analysed three samples for each sonication time.

The oxidation degree of the GO sheets (C/O) (i.e. the ratio between the number of oxygen and carbon atoms: C/O) was calculated as a combination of the measured contribution weight by the area (A_x):

$$C/O = \frac{A_{sp2} + A_{sp3} + 2 \cdot A_{C-O-C} + A_{O=C-O}}{A_{C-O-C} + 2 \cdot A_{O=C-O}}$$

The areas of all the contributions obtained by the fit procedures are reported in the table 3.

The analysis of the relative contributions shows that the chemical functional groups and as well as the amount of carbon chemical species $(sp^2$- for graphitic clusters and sp^3 for the defects) did not change significantly. The corresponding C/O ratio amounts to 2.4 strongly indicating that the chemical properties of the GO sheets were not modified by the long sonication treatment.

Table 3. Relative composition of C1s spectra.

	C sp2	C sp3	C-O-C	O=C-O	C/O ratio
0 hours	29±2	13±1	52±1	6±1	2.38±0.08
100 hours	32±2	12±1	50±1	6±1	2.42±0.08

2.6.2 Zeta-potential analysis

GO sheets are typically functionalized with hydroxyl groups and carboxyl groups, which bear a different amount of negative charges depending on sheet composition and on pH.[12] All the samples produced showed a z-potential of -50 mV± 29 mV, independent of GO size confirming that:

i) the sheets are strongly solvated, do not interact with each other in the solution and

ii) the number of charged chemical groups present on their surface is constant.

The first point confirms the long stability of the solutions observed experimentally, while the second one indicates that the chemical properties of the GO sheets do not vary with the lateral size.
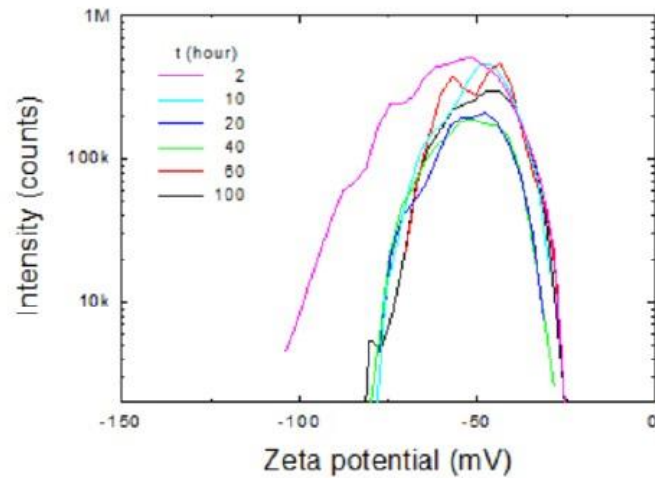
Fig. 10: Zeta potential spectra of GO in water solution acquired for different sonication times

2.7. Physical Modelling

2.7.1 Statistical analysis of the fragmentation regimes

As shown in the main text, all the area distributions calculated for the different sonication times were fitted with the analytic continuous distributions reported in the mathematical methods chapter. The study allowed to distinguish two populations of larger and smaller fragments after 40 hours of sonication, which can be modelled by Gamma and Exponential functions respectively.

Figure 10 displays the average area calculated for the two populations using the area of the fitted curves for different sonication times. The mean area value of GO sheets related to the Gamma population (red squares) decreased with time reaching an asymptotic value after 40 hours and disappearing at 100 hours. The sheet population following the exponential trend was observed from t=40 hours, and the corresponding average area value (green squares) remained constant till 100 hours.
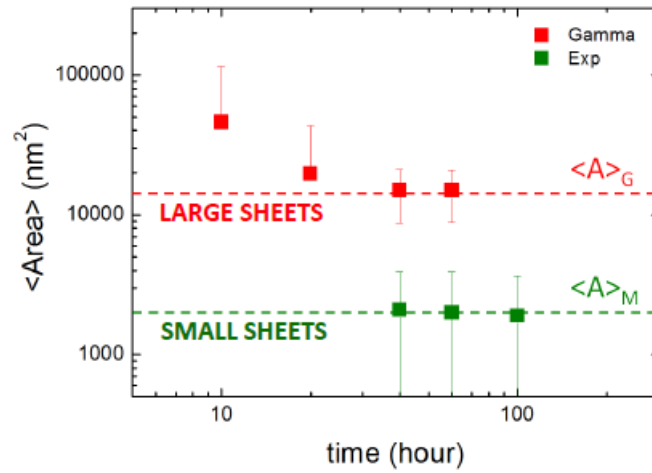
Fig. 11: Time-evolution of the areas of different population fragments (red) Gamma and (green) Mott. Dashed lines correspond to the asymptotic values

The two populations also differed in the shape of the GO sheets, as shown in Fig. 11 where the time evolution of the two shape factors is reported: A) Aspect ratio and B) Form Factor.

In particular, the shape factors of both populations do not show an appreciable variation with sonication time confirming that the changes observed are due only to the relative variation of the populations of all the fragments during the sonication.

FORM FACTOR
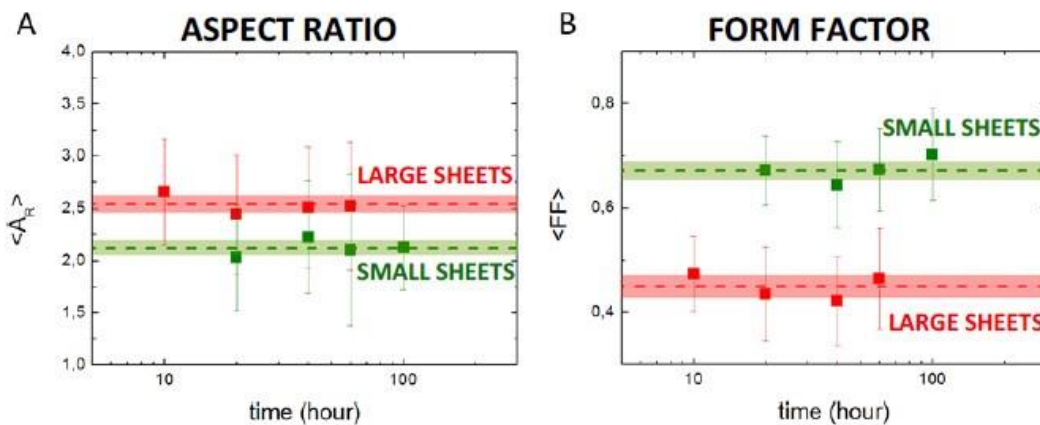
Fig. 12. Time-evolution of the shape factors: (A) Aspect ratio and (B) Form Factor of different

population fragments following (red) Gamma and (green) exponential size distribution. Coloured areas display the corresponding average values (dashed lines). The width of the shadowed area around each line corresponds to two times the standard deviation (= 2SD).

2.7.2 Bulk fragmentation - Modelling of the cavitation shear stress

XPS and Zeta-potential measurements confirm that the sonication did not affect the chemical properties of the GO sheets in solution. For this reason, any change in fragmentation mechanism was only due to the lower size of the GO sheets involved.

During sonication, the implosion of the cavitation bubbles created in the liquid imposes an inward radial fluid flow, which induces viscous forces on the graphene sheets that can thus fracture.

After multiple fractures, fragments are generated with an asymptotic area ($A_{asy,GO}$) corresponding to the smallest surface on which the viscous stress cannot generate a lateral force high enough to further break of the fragment. We here extend to GO sheets the approach proposed for nanotubes by Ahir et al.*[13]*. If a bubble of radius R implodes at a velocity R, the mass conservation law $4\pi R^2 dR = 4\pi x^2 dx$, where x is the radial coordinate, implies a fluid velocity in the form $v(x) = R^2\dot{R}/x^2$. The GO sheet is described by a characteristic lateral size s and a thickness h, as summarised in the figure 13.

COLLAPSING BUBBLE
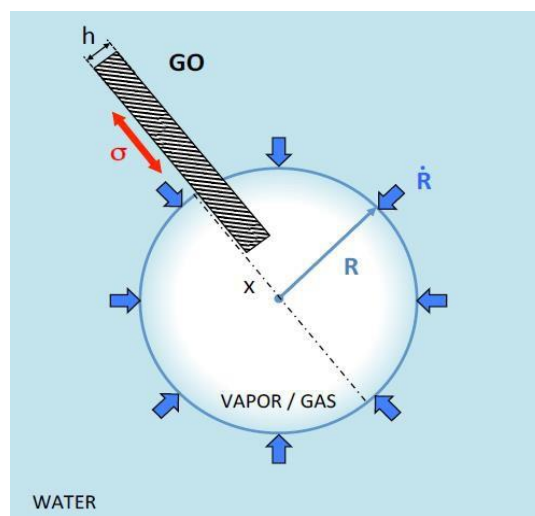
Fig. 13. Scheme of the collapsing bubble.

The dynamics of the collapsing bubble (radius and velocity) have been calculated by solving the Rayleigh-Plesset equation using the adiabatic approximation *(k = 1.4)*, considering the gas as non-condensable and as well as neglecting the thermal and the surface tension effects. A detailed description can be found in the book of Brennen (chapter 3) and reference therein[15].

2.7.3 Edge fragmentation mechanism

The mechanical stress of cavitation acts directly and indirectly on the rupture mechanisms of the GO sheets in solution. A simplified scheme is reported in figure 13.

Large fragments are directly generated by the mechanical stress of cavitation, as modelled in previous section. Stress creates large cracks on pristine sheets (fig. 14A) leading to the formation of "bulk fragments" (i.e. first generation of fragments, following Gamma size distribution) (fig. 14C).

A further mechanism has to be taken into account because unstable cracks can branch off from the main crack that generates the bulk fragments (fig. 14B).[16] This mechanism is responsible of additional edge erosion of the first generation fragments. After 100 hours sonication, bulk fragments are completely eroded leading to a new population of small GO sheets ($<s> \ll 45$ nm) whose area distribution follows an exponential curve (second generation of fragments, fig. 14D).
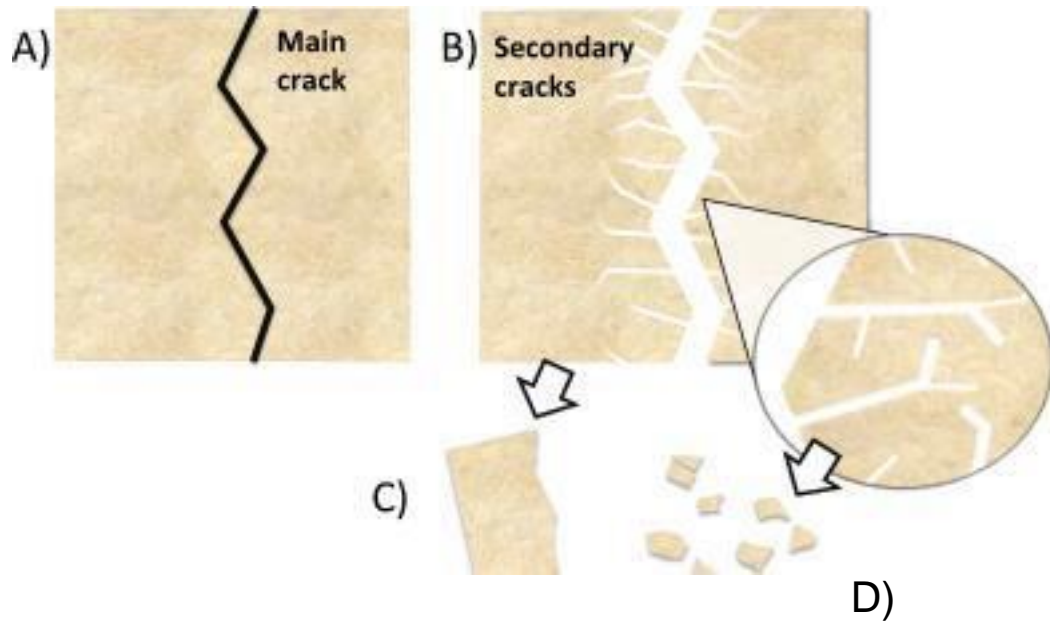
Fig. 14: Scheme of fragmentation mechanisms

2.8. Bibliography

[1] E. Treossi *et al.,* High-Contrast Visualization of Graphene Oxide on Dye-Sensitized Glass, Quartz, and Silicon by Fluorescence Quenching. *J Am Chem Soc* 131, 15576 (2009).

[2] A. Liscio, V. Palermo, P. Samori, Nanoscale Quantitative Measurement of the Potential of Charged Nanostructures by Electrostatic and Kelvin Probe Force Microscopy: Unraveling Electronic Processes in Complex Materials. *Accounts Chem Res* 43, 541-550 (2010).

[3] A. Liscio, Scanning Probe Microscopy beyond Imaging: A General Tool for Quantitative Analysis. *Chemphyschem* 14, 1283-1292 (2013).

[4] R. A. Oliver, Advances in AFM for the electrical characterization of semiconductors. *Rep Prog Phys* 71, (2008).

[5] W. J. DeCoursey, Statistics and probability for engineering applications with Microsoft Excel. (Newnes, Amsterdam ; Boston, 2003), pp. xv, 396

[6] W. Hardle, L. Simar, *Applied multivariate statistical analysis.* (Springer, Berlin ; New York, 2003), pp. 486

[7] D. W. Scott, OPTIMAL AND DATA-BASED HISTOGRAMS. *Biometrika* 66, 605-610 (1979).

[8] F. Zhang, Shock wave science and technology reference library. (Springer, New York, 2009).

[9] M. J. Monteiro, Fitting molecular weight distributions using a log-normal distribution model. *Eur Polym J* 65, 197-201 (2015).

[10] A. Okabe, B. N. Boots, K. k. Sugihara, *Spatial tessellations : concepts and applications of Voronoi diagrams.* Wiley series in probability and mathematical statistics (Wiley, Chichester, England ; New York, 1992), pp. x, 532

[11] K. Kouroupis-Agalou *et al.,* Fragmentation and exfoliation of 2-dimensional materials: a statistical approach. *Nanoscale* 6, 5926-5933 (2014).

[12] D. R. Dreyer, S. Park, C. W. Bielawski, R. S. Ruoff, The chemistry of graphene oxide. *Chem Soc Rev* 39, 228-240 (2010).

[13] S. V. Ahir, Y. Y. Huang, E. M. Terentjev, Polymers with aligned carbon nanotubes: Active composite materials. *Polymer* 49, 3841-3854 (2008).

[14] F. Hennrich *et al.,* The Mechanism of Cavitation-Induced Scission of Single-Walled

Carbon Nanotubes. *The Journal of Physical Chemistry B* 111, 1932-1937 (2007).

[15]   C. E. Brennen, *Fundamentals of multiphase flow.* (Cambridge University Press, Cambridge, UK ;New York, ed. 1st pbk., 2009), pp. 345

[16] J. A. Astrom, F. Ouchterlony, R. P. Linna, J. Timonen, Universal Dynamic Fragmentation in D Dimensions. *Physical Review Letters* 92, 245506 (2004).

[17] P. Wick, A. E. Louw-Gaume, M. Kucki, H. F. Krug, K. Kostarelos, B. Fadeel, K. A. Dawson, A. Salvati, E. Vazquez, L. Ballerini, M. Tretiach, F. Benfenati, E. Flauhaut, L. Gauthier, M. Prato, A. Bianco, Classification Framework for Graphene-Based Materials, Angew. Chem. Int Ed. 2014, 53, 7714-771.

Chapter 3

Application of Graphene Oxide in Bio-compatible Composites

3.1. Introduction

Nanofiller/polymer composites find a wide range of applications, thanks to the ability of the nanofiller to improve the mechanical, chemical, thermal and optical properties of the matrix [1,2]. Among nano-fillers, the newest and most studied class of materials is that of so-called 2-dimensional materials, such as graphene and its derivatives. While graphene can improve the mechanical, electrical and thermal properties of composites, its efficient processing and interaction with the polymer matrix is still problematic. The role of graphene as mechanical reinforcement can become all the more useful in biomaterials that have usually very poor mechanical properties or stability.

A widely used biomaterial is gelatin. Gelatin has attracted great interest due to its peculiar properties. This biopolymer is obtained by chemical-thermal degradation of collagen, which causes the rupture of the collagen triple helix into the random-coil structure characteristic of gelatin. The sol-gel transformation that takes place on cooling gelatin aqueous solutions is a conformational disorder-order transition of the gelatin chains that results in a partial regeneration of the triple helix structure [4-6]. The stiffness of gelatin gels and the mechanical properties of drawn gelatin films have been related to the renaturation level, that is the triple helix content of the protein [5-8]. Gelatin is cheaper than collagen and it does not express antigenicity in physiological conditions [9,10]. In addition, gelatin is biodegradable and biocompatible, which justifies its numerous uses in the pharmaceutical and medical fields for a variety of applications, including tissue engineering, wound dressing, drug delivery and gene therapy [11]. Moreover, gelatin-based films are thin, flexible and transparent materials widely employed in engineering food, packaging and drug recover [12,13]. However, the main drawback in the use of gelatin is related to its poor mechanical properties, which limit its range of application. The mechanical performance of the biopolymer can be improved through reinforcement with fillers. A variety of materials, including carbon fibers, clay, hydroxyapatite, have been proposed to this aim [2,14,15]. Recently, it was reported that reinforcement with graphene oxide nanoplatelets induced remarkable improvement of gelatin films mechanical properties [16].

Graphene oxide (GO) can be obtained in large quantities by chemical oxidation of graphite and processed efficiently in different solvents as single sheets with lateral size tunable from 100 μm to 100 nm, and with a nearly 100% yield of monolayers [17,18]; Furthermore, GO can be functionalized in different ways to enhance its interaction with other molecules and with the surrounding environment [19,20], displaying high Young's modulus, hardness and flexibility [21]. Whilst the positive effect of GO nano-fillers has been proved for different composite systems [22-24.] there is less evidence on what the exact failure mechanism is in these composite materials at the nanoscale [25]. Herein, we studied the mechanical properties and failure mechanism of nano-composites made of graphene oxide sheets and gelatin. We do not limit the study to bulk composite layers, but also prepare and characterize more challenging systems in which the composite is electrospun in nano-fibers. This work was made in collaboration with the groups of Nicola M. Pugno from the University of Torino and the group of Adriana Bigi from the University of Bologna.

In these systems, contrary to conventional bulk composites, the size of the nano-reinforcement (GO sheets) is comparable to the size of the nanofibers to be reinforced (≈200 nm). The electrospinning production method itself is challenging, because the fibers undergo significant mechanical and electrical stress during spinning; only highly stable and defect-free composites can be processed in this way.

Continuous electrospun nanofibers are becoming increasingly of interest in the field of functional and structural materials [26] as well as in the biomedical sector [27] due to high open porosity of the nanofibers assemblies, associated to their remarkable specific surface area and extreme flexibility. The first attempt to produce polymeric electrospun nanofibres filled with GO dates back to 2010 [28]. Very recently polymers with polar groups, thus capable of interacting with oxygen-containing hydrophilic groups located at the surface of GO - such as poly(vinyl alcohol) [29], poly(acrylonitrile) [30-32] and poly(amides) [33] - have been electrospun with GO obtaining mats with remarkably improved mechanical properties. No attempt to prepare electrospun gelatin nanofibers enriched with GO has been reported up to now.

The behaviour of these composites based on 2-dimensional nanofillers is even more complex when used in fibers and textiles, because the fiber diameter can be comparable to the size of the nanosheet. For this, we use for the first time a combination of macroscopic mechanical tests, microscopic characterization and numerical modelling to understand how the mesoscopic nanosheets are positioned into (or onto) the fibers, and how this influences the failure mechanism of the material at the nanoscale.

In these systems, the sheets can act as mechanical reinforcement of the fiber, but also as defects oriented perpendicular to the fiber axis, or can be segregated outside the fiber, thus having little effect on fiber properties. Including graphene in polymer sheets and in thin polymeric fibers is a major challenge for applications in e-textiles and bio-compatible electronics [34].

3.2. Experimental

3.2.1 Preparation of GO

Graphene oxide was prepared from graphite flakes by a modified Hummers method [17] and characterized before use by spin coating part of the solution on flat silicon wafers, and observing sheet size by Atomic Force Microscopy (AFM). As expected, the material was composed mainly by monoatomic sheets, with minimal amounts of thicker aggregates [17,18,35].

A 7.5 mg/mL GO solution in water was diluted 45 times before the characterization process. A Chemat technology spin-coater KW-4A was used for 60 s at 2000 rpm to spin-coat the GO solutions on SiO_2 films. The samples were spun in open air using 100μL of the diluted GO solutions. Spin-coating was used to make a uniform distribution of GO sheets on the substrates.

3.2.2 Preparation of gelatin-GO films

Type A gelatin (280 Bloom, Italgelatine S.p.A.) from pig skin was used. Different amounts of a 7.5 mg/mL GO solution were added, under continuous stirring, to a 10% aqueous gelatin solution at 40°C, in order to obtain films containing 5 wt% gelatin and different GO amounts (0.5, 1, 1.5, 2 wt%) in the final composition. Films were obtained on the bottom of Petri dishes (diameter=6 cm) after water evaporation at room temperature (RT) from 10 ml of solution.

The samples were labelled as F-0.5, F-1, F-1.5, F-2. Pure gelatin films were used as reference, and named F-0. Composite films containing a higher fraction of GO, 0.5 wt% gelatin and 0.5 wt % GO (Gel:GO =1:1) were also produced, and labelled as G-05 GO-05.

3.2.3 Preparation of gelatin-GO electrospun mats

Gelatin was dissolved in acetic acid/double distilled water 60/40 (v/v), at a concentration of 25% (w/v). The solution was stirred at 50°C for 60 minutes, maintained under stirring overnight and then electrospun to obtain the control mat free of GO. Different amounts of a 7.5 mg/mL GO solution were added, under continuous stirring, to aqueous gelatin solution in acetic acid/ double distilled water 60/40 (v/v) at 50°C, in order to obtain suspensions containing a gelatin concentration of 25% and a GO content of 0.5, 1 and 1.5% (wt%) in the final electrospun mat composition.

The electrospinning apparatus, made in house, was composed of a high voltage power supply (Spellman, SL 50 P 10/CE/230), a syringe pump (KD Scientific 200 series), a glass syringe, a stainless-steel blunt-ended needle (inner diameter: 0.84 mm) connected with a grounded rotating collector (length = 12 cm, diameter = 5 cm) positioned 15 cm away from the tip of the needle. The polymer solution was dispensed, through a Teflon tube, to the needle that was horizontally placed in front of the collecting mandrel. All the above described solutions were electrospun into non-woven mats by using the following conditions:

applied voltage = 20 kV, needle to collector distance = 10 cm, solution flow rate = 0.005 ml/min, at RT and relative humidity, RH = 40 ÷ 50 %. Fibers were collected with a random arrangement on the cylinder rotating at a speed of about 2 m/s. Electrospun mats were kept under vacuum over P_2O_5 at RT overnight in order to remove residual solvents. Gelatin electrospun mats were labelled as M-0 whereas gelatin-GO electrospun mats were labelled as M-0.5, M-1, M-1.5 according to GO content.

3.2.4 Morphological investigation

AFM measurements were carried out using an NT-MDT AFM in air operating in semi-contact (tapping) mode, using commercial Bruker n-doped Silicon (Si) AFM tips in a semi-contact (tapping) mode. In order to obtain quantitative results from the topographic AFM images of GO we used statistical image analysis software (Scanning Probe Image Processor, SPIP from Image Metrology and OriginPro 8.1 SR3). Morphological investigation of the composite samples was performed using a Philips XL-20 Scanning Electron Microscope (SEM). The samples were sputter-coated with gold prior to examination. The distribution of electrospun fiber diameters was determined through the measurement of about 150 fibers by means of an acquisition and image analysis software (EDAX Genesis) and the results were given as the average diameter ± standard deviation. Electrospun fibres supported on conventional copper microgrids were observed by using a Philips CM 100 Transmission Electron Microscope (TEM) operating at 80 kV.

3.2.5 Mechanical tests

Mechanical characterization was carried out on strip shaped (3x30mm, thickness around 0.12 mm, determined by micrometer) samples obtained after film immersion in H_2O/Ethanol (2/3) solution for 10 minutes and on strip-shaped electrospun mats (5 mm×20 mm, thickness ranging from 0.012 to 0.017 mm, determined by micrometer). Stress-strain

curves were recorded on dried samples using an INSTRON Testing Machine 4465, and the Series IX software package. Crosshead speed was set at 5 mm/min in the case of films and at 0.5 mm/min for the electrospun mats. The Young's modulus E, the stress at break σ_b and the strain at break ε_b of the strips were measured in a static mode.

At least ten specimens were measured for each sample type and results were provided as the average value ± standard deviation.

3.2.6 Differential scanning calorimetry (DSC)

Calorimetric measurements were performed using a Perkin–Elmer Pyris Diamond DSC equipped with a model ULSP intracooler. Temperature and enthalpy calibration were performed using high-purity standards (*n*-decane and indium). The sample weights were in the range of 3–4 mg. Samples were examined in air-dried conditions. Heating was carried out at 5°C/min from 40°C to 150°C. Denaturation temperature (T_D) was determined as the peak value of the corresponding endothermic event. The value of denaturation enthalpy was calculated with respect to the weight of air-dried gelatin.

3.2.7 Swelling

Square-shaped films ($1cm^2$) were immersed in Phosphate buffered solution (0.1 M, pH 7.4) for different periods of time. Wet samples were wiped with filter paper to remove excess liquid and weighted. The amount of adsorbed water was calculated as

$$W(\%) = 100 \frac{(W_w - W_d)}{W_w}$$

Where W_w and W_d are the weights of the wet and the air dried samples, respectively.

3.2.8 X-ray diffraction (XRD) analysis

X-ray diffraction analysis was carried out by means of a Panalytical X'Celerator Powder diffractometer. CuKα radiation was used (40 mA, 40 kV). The 2θ range was from 3 to 50° with a step size of 0.033° and time/step of 20s.

3.3. Results and discussion

In many cases, the main challenge in creating a composite material is to maximize the interaction between the two (or more) components of the material, to obtain a new product that merges together the beneficial properties of all the constituents. A major issue in composites based on graphene and graphene oxide is the re-stacking of the sheets due to poor interaction with the polymeric matrix, which creates large defects in the composite, reduces the processability and requires higher loading of graphene to obtain a significant improvement of the properties of the material.

Interestingly, the composite materials described in this work display an excellent interaction between the two different components both in the shape of films and as co-electrospun nanofibers (Fig. 1).
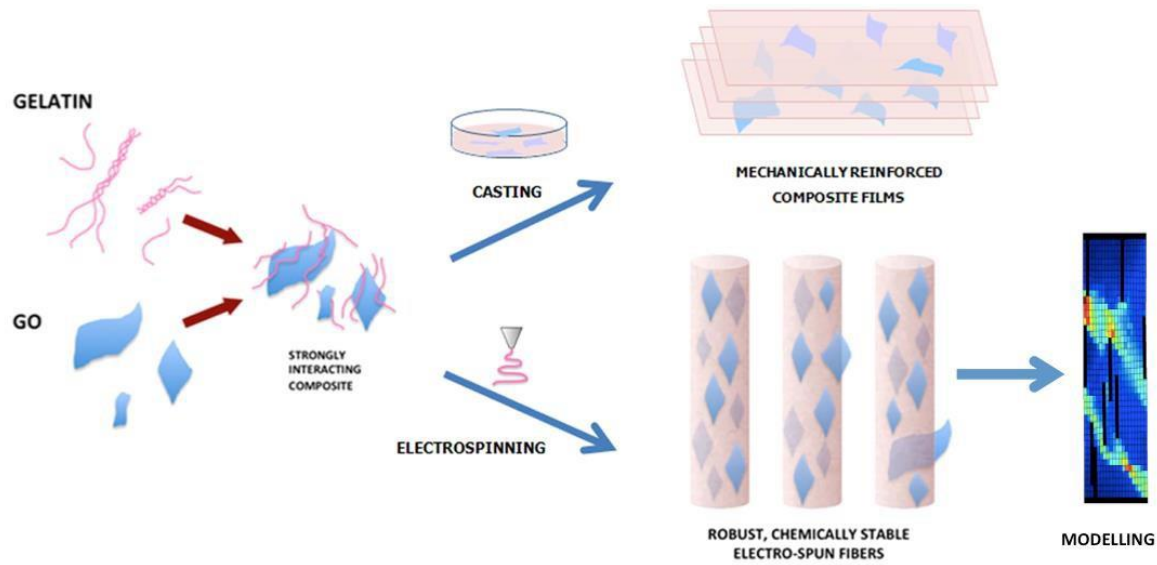
Fig. 1: Scheme of gelatin-GO composites preparation process, and numerical modelling of the gelatin-GO nanofibres at the lowest hierarchical level.

3.3.1 GO nanosheets

Fig. 2 reports the AFM image, thickness profile and statistical analysis of the GO nanosheets utilized for the preparation of the nanocomposites. Using image analysis, 2197 sheets in 4 different samples were measured. For each sheet, the length L and width W were calculated, as well as the aspect ratio L/W (Fig. 2c).
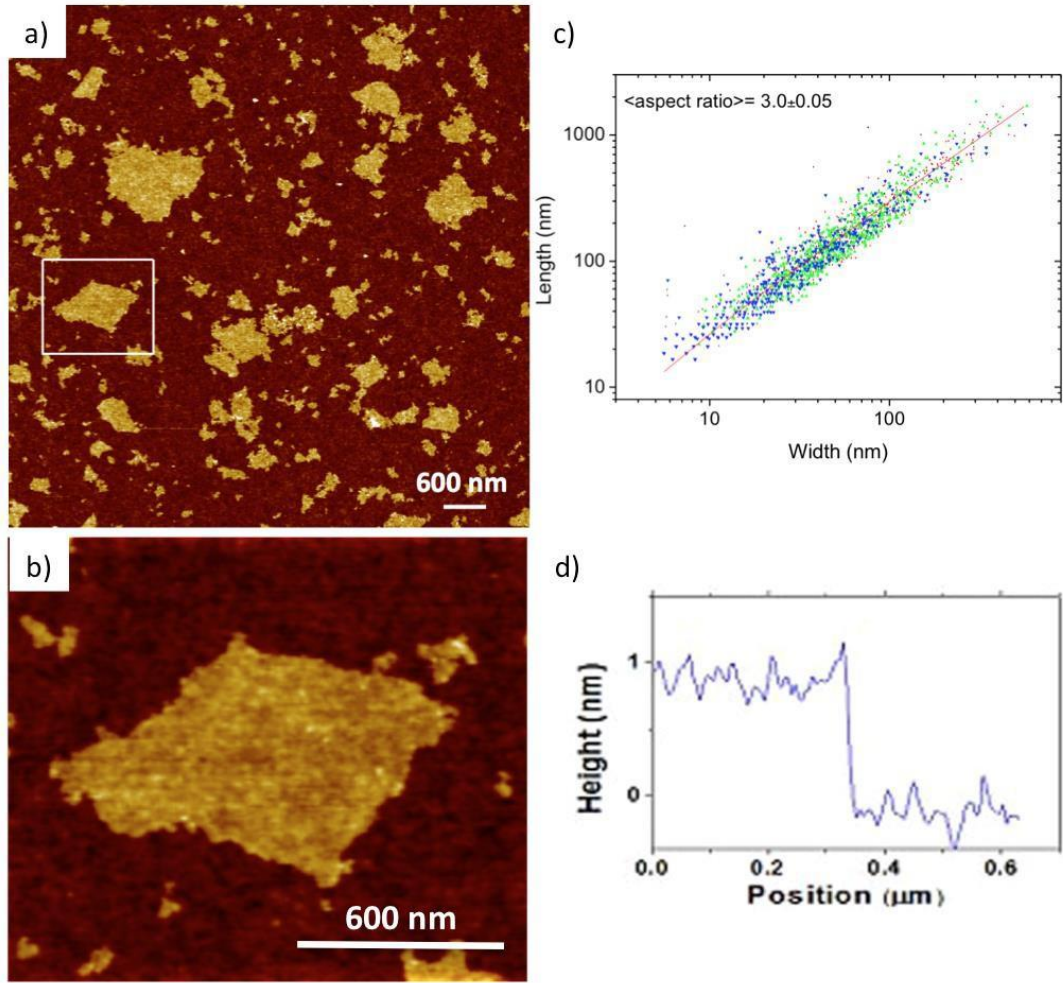
Fig. 2: a,b) AFM image of GO sheets spin coated on silicon. c) Statistical analysis of the length/width ratio of the GO sheets, in log-log scale. The different colors of the points in the plot correspond to four different samples that were analyzed. d) Height profile taken along the dashed line in b).

Given the irregular shape of the sheets, the definition of L and W is not unique. To avoid any ambiguity, we use as relevant parameter the square root of the area measured exactly for each sheet (pixel by pixel) by image analysis software: $S = \sqrt{A_{measured}}$, which has the same units of length and width. This value would correspond roughly, in the case of rectangular shapes, to the geometrical mean of the length and width. Instead, the irregular

shape of the sheets gives in all cases $S \neq \sqrt{LW}$. Thus, while L and W are arbitrary axes chosen for each flake by the image analysis software, S is an objective value directly obtained for the flake area.

Statistical analysis for this solution yields $S=84\pm66$ nm, $L=113\pm98$ and $W=56\pm44$ nm. This average must only be considered as indicative, because the size distribution does not follow a Gaussian (a.k.a. "normal") distribution, but it is strongly asymmetric and positively skewed, as typical in many poly-dispersed materials, like powders or polymer blends, giving a very high variance of the average. From the slope of the fitted line we calculated the aspect ratio of length/width that is 3 ± 0.05. The average thickness of the sheets as measured by AFM on silicon was 1.1 ± 0.3 nm.

3.3.2 Gelatin–GO Films

 Well dispersed gelatin-GO composite films were obtained using a simple assembling procedure as described in the experimental section. The good dispersion of GO inside the biopolymer is confirmed by the photographs of the films reported in Fig. 3, which show a homogeneous coloration. The intensity of the yellow/brown colour increases on increasing GO content of the composites.
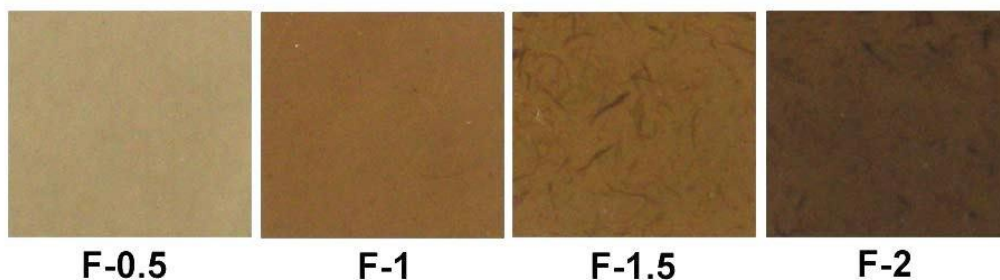

Fig. 3: Photographs of the gelatin-GO composite films at different GO content: the intensity of the yellow/brown color increases on increasing GO content.

Moreover, Scanning Electron Microscopy (SEM) images of the fractured film surfaces display a layered morphology, with the presence of GO sheets between the layers, as shown in Fig. 4 for F-0.5. The GO sheets (indicated by white arrows) appear embedded in between layers of biopolymer; although SEM does not allow the measurement of the thickness of the GO flakes, many of them appear very thin, with just occasionally some thicker platelets (an example is shown Fig. 4b). Overall, SEM data indicate a good dispersion of GO in the matrix, in agreement with XRD data (see below).
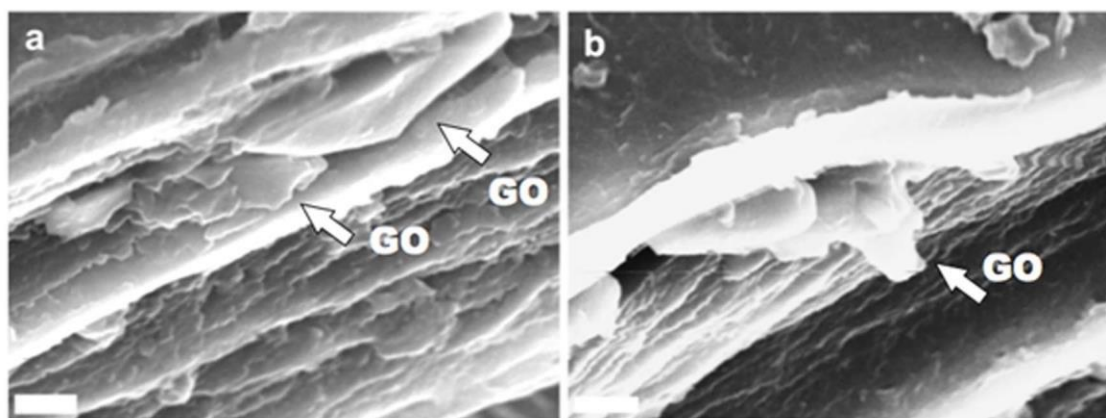

Fig. 4: a,b) Scanning electron microscopy of F-0.5 fractured surface: the arrows indicate the GO platelets which appear embedded in between the layers of gelatin. Scale bar: 5 μm.

The DSC plots of dry composites exhibit an endothermic peak due to collagen denaturation, as a consequence of the helix-coil transition. The values of denaturation temperature, T_D, and enthalpy, ΔH_D, of the films at different GO content are reported in Table 1. Contrary to T_D values, which do not show significant variations as a function of composition, the values of ΔH_D decrease on increasing GO content. Since ΔH_D is related to the relative amount of triple helical structure in the samples, these data suggest that the presence of GO during gelling interferes with the renaturation process of gelatin and reduces the triple helix content of the composite films. This finding is supported by the results of X-ray diffraction analysis (Fig. 5). The XRD pattern of gelatin shows a reflection

at about 8° of 2θ, corresponding to a periodicity of about 1.1 nm, which is associated to the diameter of the collagen triple helix, and a broad peak in the range 12°-30° of 2θ related to peptide bonds. The integrated intensity of the first reflection can be used as a measure of the degree of renaturation, or triple-helix content, of gelatin films [7]. In particular, herein the relative amount of triple helices (*X*) within the samples has been determined by dividing the integrated intensity of this reflection by that of the broad peak associated to peptide bonds [36].

Table 1: Denaturation temperature (T_D) and denaturation enthalpy (ΔH_D) of the endotermic peak event for gelatin-GO films.

| sample	T(°C)	ΔH(J/g)
F-0	94 ± 1	32 ± 1
F-0.5	91 ± 1	29 ± 1
F-1	91 ± 1	29± 1
F-1.5	91 ± 1	28 ± 1
F-2	91 ± 1	26 ± 1
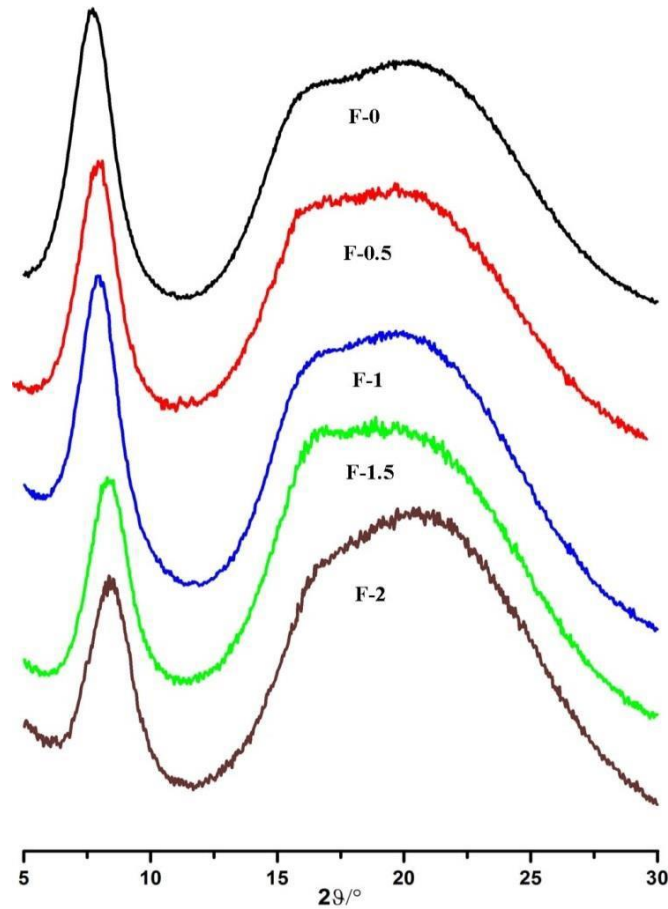
Fig. 5: XRD diffraction patterns of gelatin-GO films: the amount of GO increases from the top spectrum to the bottom one.

The comparison of the XRD patterns reported in Fig. 5 shows a decrease of the relative intensity of the 1.1 nm reflection on increasing GO content of the films. In agreement with this qualitative observation, the values of X decrease as well from 21% for F-0 to 18% for F-0.5, to 12% for the samples at greater GO content. The reduction of the triple helix content revealed by DSC and XRD results is similar to that observed on crosslinked gelatin, where the degree of renaturation of the protein decreases on increasing the degree of crosslinking [6,10]. It can be suggested that the interaction of the oxygen-rich groups on the GO surface with gelatin chains during gelling interferes with gelatin renaturation and reduces the extent of triple helix content, in agreement with previous studies [16].

The XRD pattern of GO displays a broad peak at about 10.8° of 2θ, corresponding to an interplanar distance of about 0.76 nm (Fig. 6). In contrast, the XRD patterns of gelatin/GO composite films do not exhibit any reflection due to GO, (Fig. 5), most likely because of the low GO content and/or due to the good exfoliation of GO sheets in the gelatin matrix [16,37]. In order to test this hypothesis, a few films at low gelatin concentration and at very high GO contents, up to 50 wt% have been prepared and characterized. The XRD patterns of these films display neither reflections due to gelatin nor to GO (Fig. 6), and their DSC plots do not show the presence of any endothermic peak (data not shown), confirming that GO and gelatin are interacting effectively in the composite, and that GO hinders the gelatin renaturation process. On the other hand, the absence in the XRD patterns of the GO peak at about 10.8° of 2θ and the presence of a shoulder at about 5.4° of 2θ confirms the tendency of GO to assume an intercalated structure within gelatin composites.
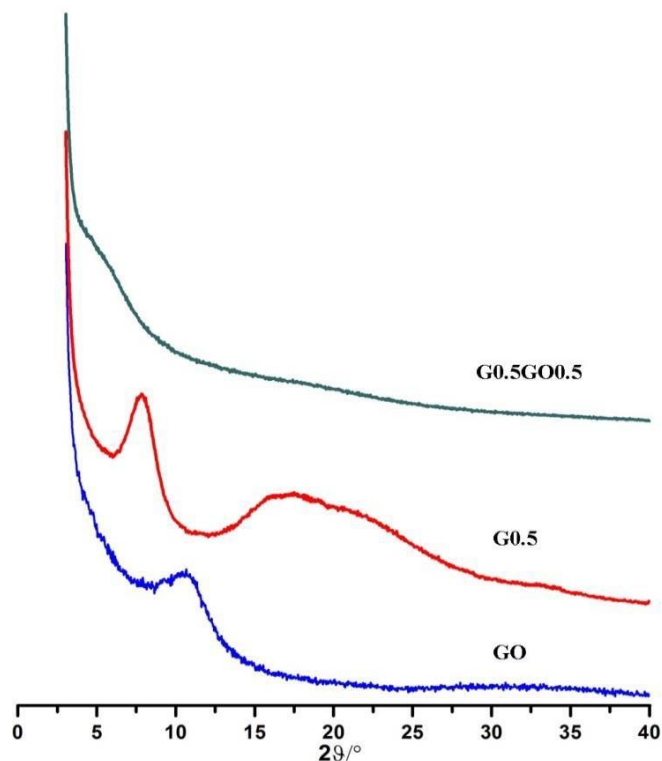

Fig. 6: XRD diffraction patterns obtained from GO powder, 0.5 wt% gelatin film (Gel), and G-05GO-05 film.

The mechanical properties of the composites improve on increasing GO content, in agreement with its reinforcement action on gelatin. Stress–strain curves recorded from air-dried samples were used to evaluate the Young's modulus, E, the stress at break, σ_b, and the deformation at break, ε_b, of the films. The results reported in Table 2 show that even a relatively low GO concentration (1 wt%) yields a remarkable increase of both E and σ_b, whereas a greater GO addition up to 2% does not cause further improvement of the mechanical parameters. The reinforcement action of the filler also reduces the degree of swelling of the composite films, as seen from the data reported in Table 3. Gelatin is highly soluble and immersion in phosphate buffer induces considerable swelling, which reaches about 900% in three hours. Gelatin films completely dissolve after 2 days. In agreement with the reinforcement action of GO, composite films display reduced swelling, F-0.5 resists up to 7 days and the dimensions of the samples richer in GO can still be measured after 2 weeks in phosphate buffer.

Table 2: Strain at break (ε_b), stress at break (σ_b), and Young's modulus (E) of gelatin-GO films. Each value is the mean of at least 10 determinations reported with the standard deviation.

sample	o (MPa)	E (GPa)	ε (%)
F-0	79 ± 9	2.1 ± 0.3	14 ± 4
F-0.5	86 ± 9	2.6 ± 0.2	18 ± 3
F-1	100 ± 4	3.1 ± 0.5	20 ± 3
F-1.5	107± 5	2.9 ± 0.2	24 ± 4
F-2	97± 5	2.9 ± 0.3	17 ± 3

Table 3: Swelling (% wt) of gelatin-GO films as a function of storage time in physiological solution. Each value was determined in triplicate.

Sample	1 min	5 min	30 min	60 min	180 min	1d	2d	7d	14d
F-0	124 ± 4	253 ± 3	562 ± 4	714 ± 3	882 ± 4	998 ±10	1470 ± 8	-	-
F-0.5	136 ± 8	264 ± 4	510 ± 3	611 ± 3	740 ± 4	960 ± 6	1200 ± 6	1416 ± 8	-
F-1	127 ± 5	240 ± 5	481 ± 5	607 ± 5	752 ± 5	971 ± 5	1040 ± 8	1280 ± 8	1692 ± 8
F-1.5	121 ± 3	236 ± 4	491 ± 4	600 ± 5	733 ± 6	880 ± 5	940 ± 5	1140 ± 5	1450 ± 8
F-2	117 ± 6	229 ± 5	491 ± 6	600 ± 4	744 ± 5	890 ± 6	920 ± 5	1040 ± 6	1200 ± 10

The stabilizing action can be explained with both a mechanical reinforcement induced by GO and with a protective effect of the large, highly anisotropic 2-dimensional GO sheets that act as a barrier to water intake into the more open, 3D porous gelatin matrix.

3.3.3 Electrospun gelatin-GO fibers

In view of the similar properties exhibited by F-1.5 and F-2, the preparation and characterization of nanofibrous gelatin-GO mats were limited to graphene oxide contents up to 1.5 wt%. The mats of pure gelatin (M-0) display bead-free and randomly arranged fibers with interconnected porosity, as shown in Fig. 7a. The nanofibers are uniform in diameter and smooth in surface, with a mean diameter of about 270 nm. The preparation of the composite scaffolds is a very delicate assembly process since the dimensions of GO

sheets are comparable to fibre diameters. Nonetheless, the presence of GO in the composite scaffolds do not seem to affect the smoothness and uniformity of the nanofibers (Fig. 7b-d), indicating a good performance of the optimized electrospinning conditions.
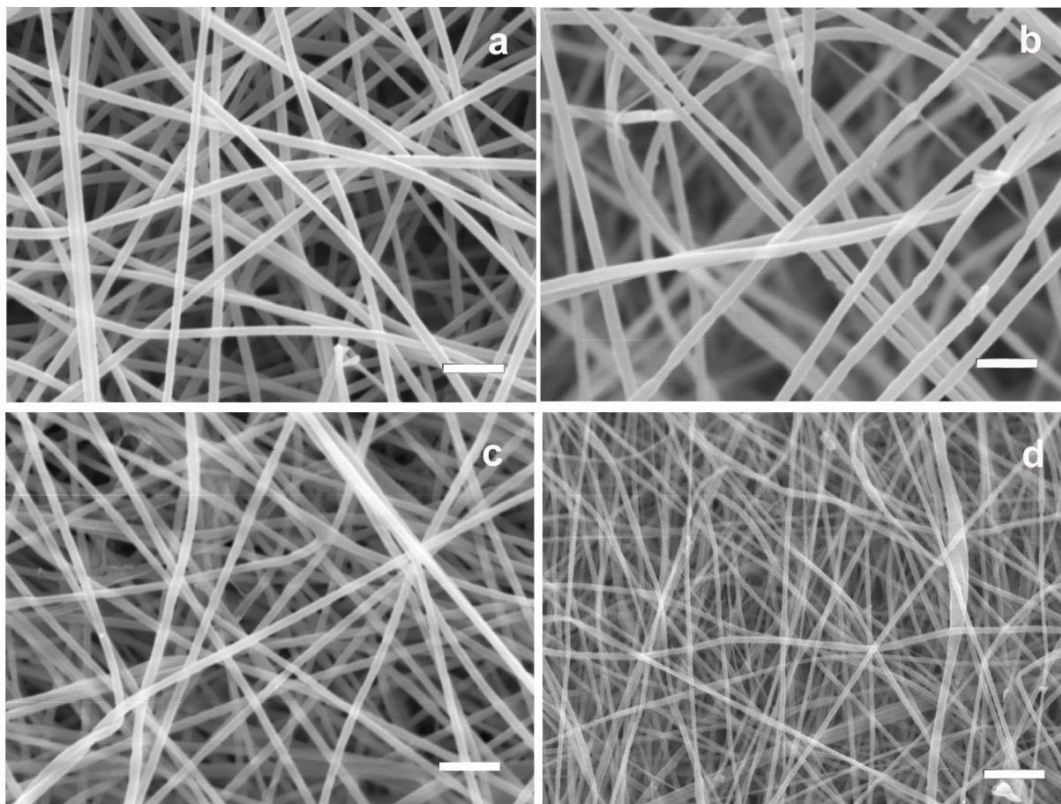

Fig. 7: Scanning electron microscopy of electrospun gelatin-GO mats a) M-0, b) M-0.5, c) M-1. d) M-1.5. Scale bar: 5 μm.

The main variation provoked by GO on fiber morphology is the reduction of the fiber mean diameter observed in the sample M-1.5, which displays a mean diameter of 150 ± 40 nm, in contrast to those of the other samples (270 ± 40 nm). Reduction of the diameter of electrospun fibers with GO content has been previously observed in different polymers and ascribed to the increase of conductivity of the electrospinning solution due to GO addition, which yields thinner fibers [30,38]. The increased conductivity has been explained in previous works as the GO reduction promoted by gelatin amino groups, which could be

oxidated to nitrite [39]. The real process is likely due to a more complex combination of causes; GO is indeed known as an insulator [40], but the presence of GO sheets having size comparable to the fiber diameter will strongly influence the viscosity and dielectric constant of the solution, changing the response to the strong electric fields (20 KV) and to the mechanical stress applied during electro spinning (typical spinning speed is 2 m/s).
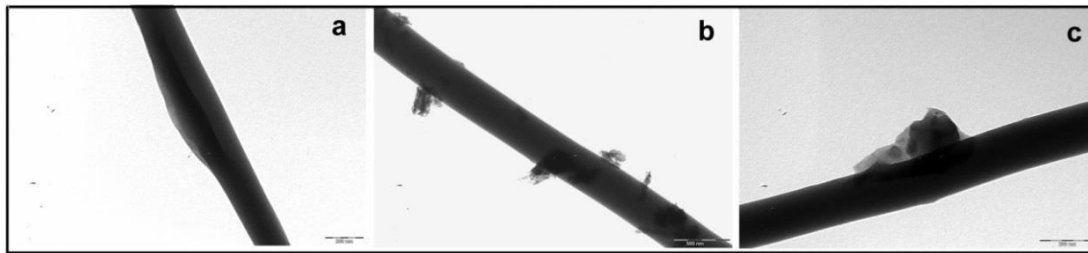

Fig. 8: Trasmission electron microscopy of electrospun M-1 mat showing GO flakes deposited b) on the surface or a,c) partially embedded into gelatin fibers. Scale bar: 200 nm a,c); 500 nm b).

TEM images show the presence of GO flakes comparable in size to the fiber diameter, onto the gelatin nanofibers (Fig. 8a), whereas further images show GO nanosheets partially embedded in the nanofibers (Fig. 8b,c). While these large flakes are clearly visible by TEM and can act as defects in the fiber, statistical analysis (Fig. 2c) shows that the majority of the flakes have a width smaller than fiber diameter (150 nm), and thus will be fully embedded into the fibers.
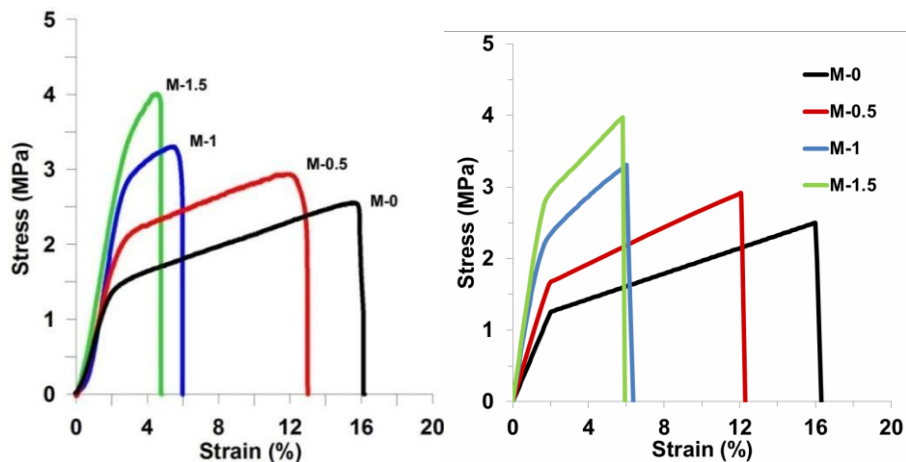

Fig. 9: a) Representative stress strain curves of gelatin-GO nanofiber mats as a function of the composition. b) Corresponding numerically calculated Stress-Strain curves.

Representative stress–strain curves of gelatin-GO nanofibers are shown in Fig. 9. The variation of the curves as a function of composition clearly shows that GO is also effective in reinforcing electrospun gelatin fibers, as previously observed for bulk films. The values of the Young's modulus, E, the stress at break, σ_b, and the deformation at break, ε_b, of the scaffolds are reported in Table 4. The deformation at break decreases for increasing GO content, and it assumes minimum values for M-1 and M-1.5, which also display greater values of σ_b than pure gelatin mats. Moreover, these same samples exhibit an increase of the value of Young's modulus of about 50% with respect to that of pure gelatin mats.

Table 4: Strain at break (ε_b), stress at break (σ_b), and Young's modulus (E) of gelatin-GO mats. Each value is the mean of at least 10 measurements reported with the standard deviation.

sample	o (MPa)	E (MPa)	ε (%)
M-0	2.5 ± 0.6	90 ± 20	17 ± 2
M-0.5	2.9 ± 0.6	92 ± 18	12 ± 2
M-1	3.4 ± 0.5	148 ± 9	5.4 ± 0.7
M-1.5	4.1 ± 0.4	141 ± 1	5 ±1

3.3.4 Numerical Simulations

To simulate the mechanical behaviour of the gelatin-GO nanofiber system, a numerical approach was used based on a previously developed Hierarchical Fibre Bundle Model [41], also employed for heterogeneous media [42, 43] and graphene composites [44], and extended here to 2-D to account for shear effects. The simulations were implemented in a hierarchical scheme in two steps: a) the GO-reinforced gelatin fibres were modelled at nanoscale using an in-house developed 2-D Finite-Element Model (FEM) formulation

accounting for elastoplastic behaviour and fracture initiation and propagation, and b) the electrospun mat geometry was modelled at micro/mesoscale using a fibre bundle model with input fibre properties (i.e. yield and fracture stresses and strains) determined from the nanoscale FEM simulations.

More specifically:

a) For the FEM simulations, representative portions of the gelatin fibres containing various GO reinforcements were discretized in a 2-D quadrilateral-element mesh, as shown in Fig.10a: each element consists of i=4 nodes, each with two degrees of freedom (u_i and v_i), with 6 inter-nodal relationships in the element. A typical mesh contains about 10^4 square elements, corresponding to approximately $2 \cdot 10^4$ degrees of freedom (accounting for common nodes between adjacent elements), with each element corresponding to an area of approximately 4.5 by 4.5 nm^2. The GO flakes are modelled with randomly varying orientation and dimensions corresponding to those reported in Fig.2c, so as to obtain an average length of about 110 nm and width of about 50 nm. The constitutive relation for the matrix is elasto-plastic and derived directly from experimental data (specimen M-0, Fig.9a). We used for the simulation an effective Young's modulus $E_{m,e}$=62.5 MPa, calculated from the linear part of the stress-strain M-0 curve in fig. 9, to account for softening effects always present before the yield point. We also used as yield strain $\varepsilon_{m,e}$ =2%, an elastic modulus (in the plastic region) $E_{m,p}$= 8.9 MPa, and fracture strain $\varepsilon_{m,p}$=16%. A perfect interface was considered between the reinforcements and the matrix, and possible failure mode are platelet/matrix debonding as well as crack propagation in the matrix .Due to the thickness of about 1 nm of the GO flakes and the larger discretization size used in the mesh to optimize computational times, for the reinforcements it was necessary to model representative GO-gelatin portions, with GO flakes constituting about 1/5th of the considered 10 nm thickness. The corresponding Young's modulus E_r was derived from the GO modulus E_{GO} = 200 GPa [45] using a rule of mixtures, thus obtaining

$E_r = 1/5 \cdot E_{GO} + 4/5 \cdot E_{m,e} = 40$ GPa. The validity of this approximation was checked and found to be responsible for only a small variation in the results (10% at most in the fracture stress). The GO flakes were assumed to be randomly oriented and randomly positioned in the matrix, with statistical variation in the size as derived from experimental data (see Fig. 2c). Due to the variation of these parameters, simulation results are statistically distributed and simulations are repeated various times to obtain the corresponding distributions in output parameters.

b) Regarding the FBM simulations, the electrospun gelatin mats shown in Fig. 7 were modelled as networks of fibres arranged in parallel and in series subjected to uniaxial tension, with statistically-distributed yield and fracture strengths, according to the input parameters from FEM simulations. We adopted an equivalent load sharing hypothesis [41], whereby when fibres fracture, stresses are redistributed uniformly among the remaining fibres in the same bundle section. Specimen dimensions were 5 mm in width, 30 mm in length, and 0.08mm in thickness, which given the measured 91 % mat porosity, 270 nm fibre diameter and assumed mean fibre length of 0.1 mm, correspond to fibre bundles of approximately 10^3 fibres in parallel. Mechanical properties of the fibres were derived from FEM simulations. In FBM calculations, the specimens were subjected to tensile loading up to failure in repeated tests to derive the corresponding macroscopic stress-strain behaviour, accounting for statistical variation, and results were compared to the experimental data.

FEM simulations show that cracks develop at nanoscale in the regions at the tips of reinforcements due to stress concentrations, but their propagation is partially neutralized by the matrix nonlinear behaviour, which concentrates deformations and failure at the initial site of the crack, thus limiting further propagation. This type of behaviour, which is shown in Fig. 10, is consistent with predictions in the literature [46].
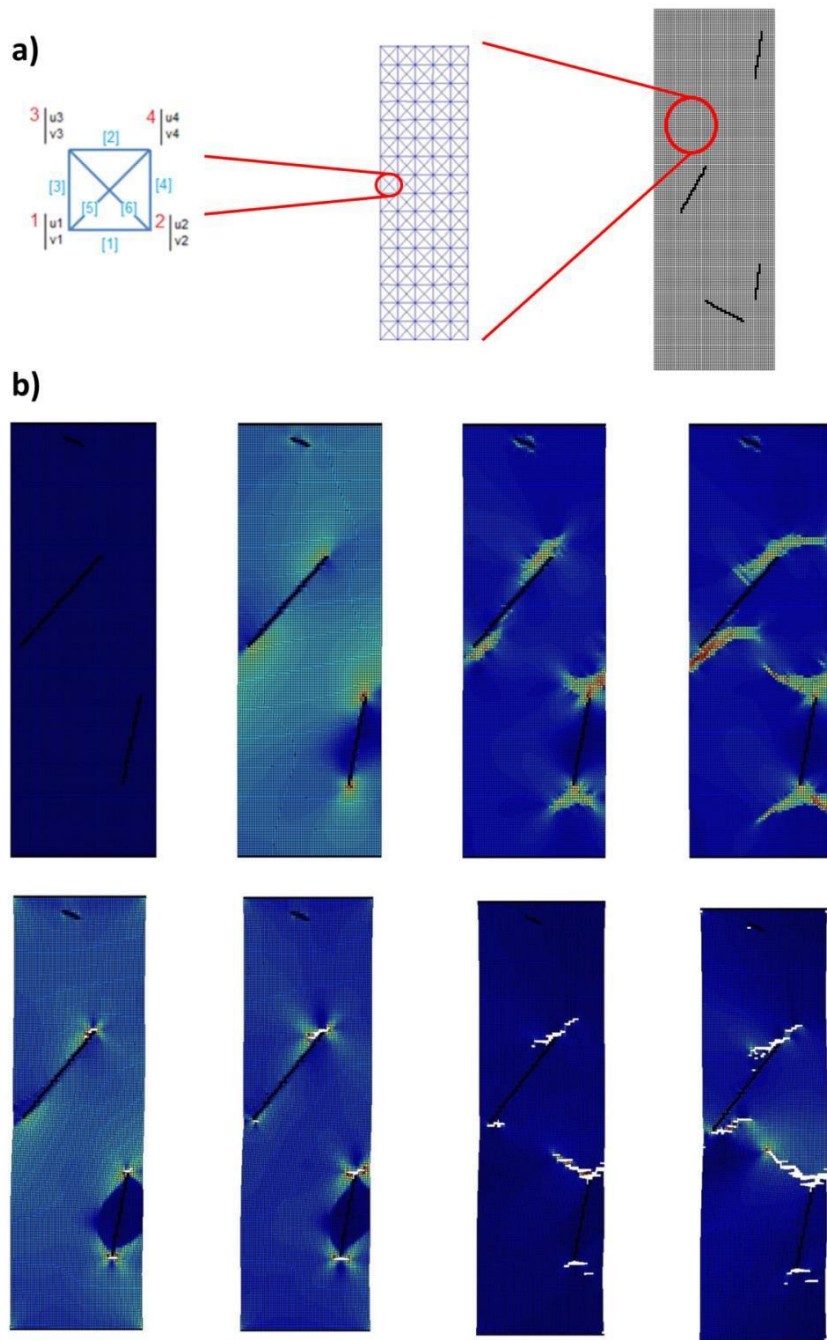
Fig. 10: a) Schematic of the quadrilateral elements used in the model and FEM mesh of a typical GO-gelatin nanofibre specimen. Nodal degrees of freedom (u_i, v_i) are also indicated; b) Development of crack propagation leading to nanofibre failure at the lowest size scale considered numerically. Successive images show stress concentrations leading first to failure in isolated areas, and finally in the whole specimen.

The resulting stress-strain curves for the different considered percentages of GO reinforcements in the matrix (M0.5, M1, M1.5) are shown in Fig. 9b. A considerable agreement is obtained with experimental curves (Fig.9a), with only a slight discrepancy in the fracture strain for the M1.5 sample Overall, simulations capture an increase of the elastic modulus both before and after the yield point for increasing GO percentages, as well as a yield stress increase. At the same time, simulations shoe that the GO-gelatin composite becomes more brittle with increasing GO content, so that fracture strain decreases.

3.4. Conclusions

The composite materials described in this work display an excellent interaction between the two different components; by mixing them together, both the renaturation of gelatin and the re-stacking of the GO sheets over each other are hindered, allowing a good mixing of the two phases. This effective interaction is even more remarkable because the building blocks of the composites have a very different nature; on the one hand we have highly polar and mechanically poor gelatin chains; on the other, we have 2-dimensional GO sheets, composed by large areas of apolar, sp^2–hybridized carbon mixed with more polar patches of sp^3–hybridized carbon, functionalized with hydroxyl, carboxyl and epoxy groups [40, 47]. The two materials have different chemical composition, shape, size and origin.

Besides XRD, DSC, SEM and TEM evidence, the successful interaction of these two materials is demonstrated by the possibility to process them not only into films, but also into nanofibers by electrospinning, a quite demanding process that applies strong electrical and mechanical forces to the material. The gelatin-GO fibers are not only produced with good yield and uniformity, but also display higher Young's modulus and stress at break as compared to pure gelatin, albeit with a smaller diameter (150 nm vs. 270 nm).

This strong interaction can be ascribed to the good quality and high hydrophilicity of the adopted GO; and the modified Hummers method applied here [17] allows to have extremely soluble sheets, which show little tendency to re-stack even when deposited on surfaces at high concentrations [18]. Under stress, cracks develop eventually at nanoscale in the regions at the tips of reinforcements, but their propagation is partially neutralized by the matrix nonlinear behaviour, which concentrates deformations and failure at the initial site of the crack, thus limiting further propagation.

While the deposition of graphene or GO sheets on flat substrates is straightforward, their incorporation into more complex, nanostructured materials is still a challenge. The results presented here demonstrate that this issue can be overcome by using suitable chemically modified graphene and appropriate techniques, and that, because of the strong interaction, high processability, and huge aspect ratio, GO can be an ideal reinforcement for bio-materials such as these gelatin fiber networks.

3.5. Bibliography

[1]   Ruiz-Hitzky E, Aranda P, Darder M, Ogawa M. Hybrid and biohybrid silicate based materials: molecular vs. block-assembling bottom–up processes. Chem Soc Rev 2011;40:801–28.

[2]   Yu G, Jialiang W, Zixing S, Jie Y. Gelatin-assisted fabrication of water-dispersible graphene and its inorganic Analogues. J Mater Chem 2012;22:17619-24.

[3]   Nicolosi V, Chhowalla M, Kanatzidis MG, Strano MS, Coleman JN. Liquid Exfoliation of Layered Materials. Science, 2013;340:1420.

[4]   Pezron I, Djabourov M, Bosio L, Leblond J. X-ray diffraction of gelatin fibers in the dry and swollen states. J Polym Sci Part B: Polym Phys 1990;28:1823–39.

[5]   Gornall JL, Terentjev EM. Helix–coil transition of gelatin: helical morphology and stability. Soft Matter 2008;4:544–49.

[6]   Boanini E, Rubini K, Panzavolta S, Bigi A.Chemico-physical characterization of gelatin films modified with oxidized alginate. Acta Bio 2010;6:383-88.

[7]   Bigi A, Panzavolta S, Rubini K. Relationship between triple helix content and mechanical properties of gelatin films. Biomaterials 2004;25:5675-80.

[8]   Yakimets I, Wellner N, Smith AC et al. Mechanical properties with respect to water content of gelatin films in glassy state. Polymer 2005;46:12577-85.

[9]   Zhang YZ, Venugopal J, Huang ZM et al. Crosslinking of the electrospun gelatine nanofibers. Polymer 2006;47:2911-17.

[10] Bigi A, Cojazzi G, Panzavolta S, Roveri N, Rubini K. Stabilization of gelatin films by crosslinking with genipin. Biomaterials 2002;23:4827–32.

[11] Mano JF, Silva GA, Azevedo HS et al. Natural origin biodegradable systems in tissue engineering and regenerative medicine: present status and some moving trends. J R Soc Interface 2007; 4:999–1030.

[12] Bergo P, Sobral PJA. Effects of plasticizer on physical properties of pigskin gelatin films. Food Hydrocolloids 2007;21:1285–89.

[13] Wang W, Wang Z, Liu Y et al. Preparation of reduced graphene oxide/gelatin composite films with reinforced mechanical strength. Materials Research Bulletin 2012;47:2245–51.

[14] Zheng J, Gao S, Li H et al. Effects of Reaction Conditions on Intercalation between Gelatin and Montmorillonite: Thermodynamical Impact. J Appl Polym Sci 2013;128:54-9.

[15] Bigi A, Panzavolta S, Roveri N. Hydroxyapatite-gelatin films: a structural and mechanical characterization. Biomaterials 1998;19:739-44.

[16] Wan C, Frydrych M, Chen B. Strong and bioactive gelatin–graphene oxide nanocomposites. Soft Matter 2011;7:6159-61.

[17] Treossi E, Melucci M, Liscio A, Gazzano M, Samorì P, Palermo V. High-Contrast Visualization of Graphene Oxide on Dye-Sensitized Glass, Quartz, and Silicon by Fluorescence Quenching. J Am Chem Soc 2009;131:15576-77.

[18] Liscio A, Veronese G P, Treossi E, Suriano F, Rossella F, Bellani V, et al. Charge transport in graphene–polythiophene blends as studied by Kelvin Probe Force Microscopy and transistor characterization. J Mater Chem 2011;21:2924-31.

[19] Melucci M, Durso M, Zambianchi M, Treossi E, Zia ZY, Manet I, Gianbastiani G, Ortolani L, Morandi V, De Angelis F, Palermo V. Graphene–organic hybrids as processable, tunable platforms for pH-dependent photoemission, obtained by a new modular approach. J Mater Chem 2012; 22:18237-43

[20] Melucci M, Treossi E, Ortolani L, Giambastiani G, Morandi V, Klar P, Casiraghi C, Samorì P, Palermo V. Facile covalent functionalization of graphene oxide using microwaves: bottom-up development of functional graphitic materials. J Mater Chem 2010; 20: 9052-60

[21] Park S, Ruoff RS. Chemical methods for the production of graphenes. Nat Nanotechnol 2009;4:217-24.

[22] Cano M, Khan U, Sainsbury T, O'Neill A, Wang Z, McGovern IT, Maser WK, Benito AM, Coleman JN. Improving the mechanical properties of graphene oxide based materials by covalent attachment of polymer chains. Carbon 2013; 52:363-71.

[23] Bortz DR, Heras EG, Martin-Gullon I. Impressive Fatigue Life and Fracture Toughness Improvements in Graphene Oxide/Epoxy Composites. Macromolecules 2012; 45:238-45.

[24] Shin MK, Lee B, Kim L, Lee JA, Spinks GM, Gambhir S, Wallace GG, Kozlov ME, Baughmann RH, Kim SJ. Synergistic toughening of composite fibres by self-alignment of reduced graphene oxide and carbon nanotubes. Nature Communications 2012;3:650-55.

[25] Young RJ, Kinloch IA, Gong L, Novoselovb KS. The mechanics of graphene nanocomposites: A review. Composites Science and Technology 2012; 72:1459-76.

[26] Zucchelli A, Focarete ML, Gualandi C, Ramakrishna K. Electrospun nanofibers for enhancing structural performance of composite materials. Polym Adv Technol 2011;22:339-49.

[27] Agarwal S, Wendorff JH, Greinier A. Use of electrospinning technique for biomedical applications. Polymer 2008;49:5603-21.

[28] Bao Q, Zhang H, Yang JX et al. Graphene–Polymer Nanofiber Membrane for Ultrafast Photonics. Adv Funct Mater 2010;20:782–91.

[29] Wang C, Li Y, Ding G et al. Preparation and Characterization of Graphene Oxide/Poly(vinyl alcohol) Composite Nanofibers via Electrospinning. J Appl Polym Sci 2013;127:3026–32.

[30] Papkov D, Goponenko A, Compton OC, An Z, Moravsky A, Li XZ et al. Improved Graphitic Structure of Continuous Carbon Nanofibers via Graphene Oxide Templating. Adv Funct Mater 2013; DOI: 10.1002/adfm.201300653.

[31] Wang Q, Du Y, Feng Q et al. Nanostructures and Surface Nanomechanical Properties of Polyacrylonitrile/Graphene Oxide Composite Nanofibers by Electrospinning. J Appl Polym Sci 2013;128:1152–57.

[32] Matsumoto H, Imaizumi S, Konosu Y, Ashizawa M, Minagawa M, Tanioka A et al. Electrospun Composite Nanofiber Yarns Containing Oriented Graphene Nanoribbons. ACS Appl Mater Interfaces 2013;5:6225−31.

[33] Pant HR, Park CH, Tijing LD, Amarjargal A, Lee DH, Kim CS. Bimodal fiber diameter distributed graphene oxide/nylon-6 composite nanofibrous mats via electrospinning. Colloids Surf A 2012;407:121–25.

[34] Yun YJ, Hong WG, Kim WJ, Jun Y, Kim BH. A Novel Method for Applying Reduced Graphene Oxide Directly to Electronic Textiles from Yarns to Fabrics. Adv Mat 2013; 25; 40: 5701–5705.

[35] Perrozzi F, Prezioso S, Donarelli M, Bisti F, De Marco P, Santucci S, et al. Use of Optical Contrast To Estimate the Degree of Reduction of Graphene Oxide. J Phys Chem C 2013;117:620-25.

[36] Zaupa A, Neffe AT, Pierce BF, Nochel U, Lendlein A. Influence of Tyrosine-Derived Moieties and Drying Conditions on the Formation of Helices in Gelatin. Biomacromolecules 2011;12:75–81.

[37] Yang XM, Tu YF, Li L, Shang SM, Tao XM. Well-Dispersed Chitosan/GrapheneOxide Nanocomposites. ACS Appl Mater Interfaces 2010;2:1707-13.

[38] Qi YY, Tai ZX, Sun DF et al. Fabrication and Characterization of Poly(vinyl alcohol)/Graphene Oxide Nanofibrous Biocomposite Scaffolds. J Appl Polym Sci 2013;127:1885-94.

[39] Liu K, Zhang JJ, Cheng FF et al. Green and facile synthesis of highly biocompatible graphene nanosheets and its application for cellular imaging and drug delivery. J Mater Chem 2011;21:12034–40.

[40]   Mattevi C, Eda G, Agnoli S, Miller S, Mkhoyan KA, Celik O, et al. Evolution of Electrical, Chemical, and Structural Properties of Transparent and Conducting Chemically Derived Graphene Thin Films Adv Funct Mat 2009;19:2577–83.

[41] N. Pugno, F. Bosia, A. Carpinteri, Multiscale stochastic simulations for tensile testing of nanotube-based macroscopic cables, Small 2008;4:1044-1052.

[42] F.Bosia, T.Abdalrahman, N. Pugno. "Investigating the role of hierarchy on the strength of composite materials: evidence of a crucial synergy between hierarchy and material mixing", Nanoscale 2012;4:1200-7.

[43] N. Pugno, F.Bosia, T.Abdalrahman. "Hierarchical fibre bundle model to investigate the complex architectures of biological materials", Physical Review 2012;E 85:1080-83.

[44] F. Bosia, N.Pugno. "In silico tensile tests of graphene fibres", Physica Status Solidi B 2013;250:1492–1495.

[45] Y. Gao, L.Q. Liu, S.Z. Zu, K. Peng, D. Zhou, B.H. Han, and Zhong Zhang, "The Effect of Interlayer Adhesion on the Mechanical Behaviors of Macroscopic Graphene Oxide Papers" ACS Nano 2011;5: 2134-2141.

[46] H.Gao, B. Ji, I.L. Jäger, E.Arzt, P.Fratzl, Materials become insensitive to flaws at nanoscale: Lessons from nature. PNAS 2003, 100:10:5597-5600

[47] Erickson K, Erni R, Lee Z, Alem N, Gannett W, Zettl A. Determination of the Local Chemical Structure of Graphene Oxide and Reduced Graphene Oxide. Adv Mat 2010;22:4467-72.

Chapter 4

Fragmentation and Exfoliation of Quasi 2D Materials: The Case of Boron Nitride

4.1. Objective of this work

In this chapter we used automatized image processing of Atomic Force Microscopy (AFM) data, described in Chpater 2, to measure, one by one the exact shape and size of thousands of nanosheets obtained by exfoliation of a model 2D material, Boron Nitride. This material is intensively studied for applications in electronics and composites. We used different statistical functions to model the asymmetric distribution of nanosheets sizes typically obtained by the standard production techniques, i.e. sonication and ball milling. We find that the size distribution of the sheets at a given time follows a log-normal distribution, indicating that the exfoliation process has a "typical" scale length that changes with time and that exfoliation proceeds through the formation of a distribution of random cracks that follow Poisson statistics.

4.2. What is Boron Nitride

Boron Nitride is a ceramic material with exceptional properties. It does not occur naturally. It is thermally stable at temperatures up to 2,370 C, is a good electrical insulator, and has a high thermal conductivity coupled with excellent thermal-shock resistance. It is also chemically inert. Even though Boron Nitride was synthesized as early as in the mid-nineteenth century, its industrial path started after the first hot pressed sintered Boron Nitride parts became available (Carborundum Co., US-Patent 2808314, 1957).

BN exists in three basic structures which are h-BN (hexagonal), β-BN (sphalerite structure) and BN wurtzite structure as shown in figure 1. The most stable crystalline form is the hexagonal one. Hexagonal BN has a microstructure similar to that of Graphite. In both materials this structure made up of layers of tiny platelets, is responsible for excellent machinability and low friction properties.
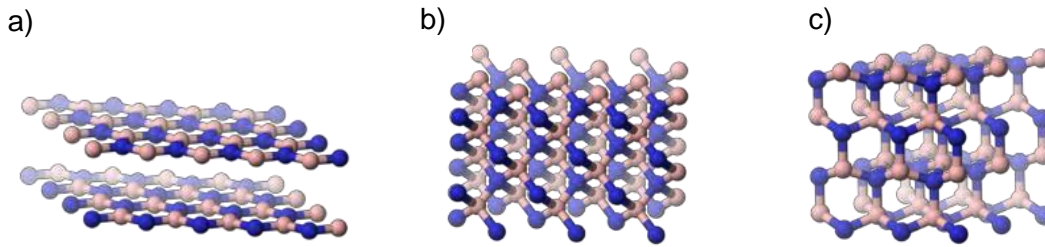
Fig. 1: a) Hexagonal-Boron Nitride (h-BN), b) sphalerite-Boron Nitride (β-BN), c) wurtzite Boron Nitride.

4.2.1 BN applications and market

Global BN market has been growing over the years at a steady pace. The world market for Boron Nitride is forecast to reach 3.1 thousand metric tons by the year 2017. The major growth of the overall market is due to its unique features such as thermal conductivity, high-temperature lubricity and electrical insulation. According to production Turkey is the single largest boron producer, garnering a substantial chunk of the world production, followed by Argentina, Chile, Russia and Peru. Some leading players profiled in the report of Global Industry Analytics Inc. by San Jose include Ceradyne Inc., ESK Ceramics GmbH & Co. KG, Denki Kagaku Kogyo Kabushiki Kaisha, Electro Abrasives Corporation, H.C. Starck Gmbh & Co KG, Momentive, Mudanjiang Jingangzuan Boron Carbide Co. Ltd., Saint-Gobain Advanced Ceramics Corp., Shin-Etsu Chemical Co., Ltd., Showa Denko KK, Sumitomo Electric Hard Metal Corp., and Washington Mills Electro Minerals Company.

4.2.2 Hexagonal Boron Nitride (hBN)

Hexagonal Boron Nitride has a microstructure similar to that of Graphite. In both materials this structure made up of layers of tiny platelets, is responsible for excellent machinability and low friction properties. However, while Graphite is black, Boron Nitride is white in colour. There are other important differences
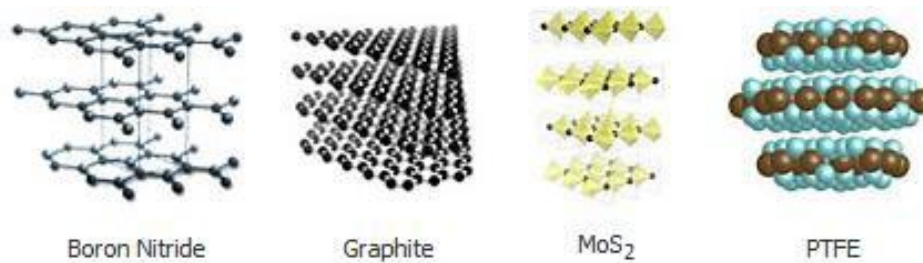
Fig. 2: Microstructures of a) h-BN, b) Graphite, c) Molybdenium Disulfide (MoS$_2$) and d) PTFE

Both Graphite and Boron Nitride have good thermal conductivity, but Graphite is an electrical conductor whereas BN is an excellent electrical insulator, both in its pure form and as a constituent of ceramic composites. Moreover while Graphite needs humidity to act as a lubricant, BN is an excellent dry lubricant which will maintain its low coefficient of friction up to 900 C in air and at even much higher temperatures in a vacuum or under protective atmosphere.

4.2.3 Hexagonal Boron Nitride and its preparation

Hexagonal boron nitride is produced by the nitridation or ammonolysis of boron trioxide. h-BN parts can be made by hot-pressing with subsequent machining. Thin films of boron nitride can be obtained by CVD from boron trichloride and nitrogen precursors. Industrial production is based on two methods: one involves the reaction of molten boric acid with ammonia, the other that of boric acid or alkaline borates with urea, guanidine, melamin or other suitable organic nitrogen compounds in a nitrogen atmosphere. Combustion of boron powder in a nitrogen plasma at 550 C yields ultrafine boron nitride for lubricants and toners.

Boron Nitride is made of Boron (B) and Nitrogen (N). In the periodic table these elements are located to the immediate left and right of Carbon (C). Carbon and Boron have identical outer electron shells, but while the outer electrons of carbon are mobile, those of boron are bound firmly by the nitrogen in the Boron Nitride molecule. Just as Carbon there exist two allotropic

modifications of Boron Nitride, a hexagonal form which corresponds to Graphite, and a cubic form analogous to Diamond.
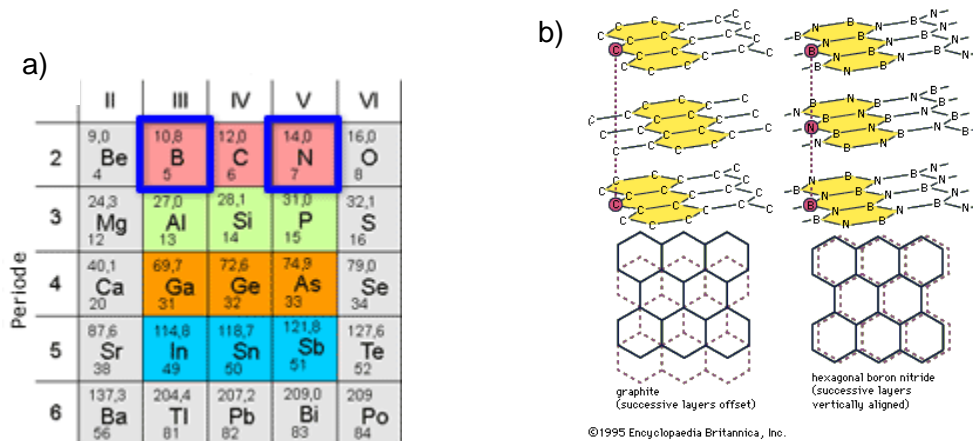

Fig. 3: a) Part of the periodic table where elements Boron (B) and Nitrogen (N) are located left and right of Carbon (C), b) Stacking sequence difference between Graphite (left) and hexagonal Boron Nitride (right).

4.2.4 Crystallography

The structure of BN in its cubic form is similar to diamond the hexagonal form is similar to graphite, with a hexagonal-layer structure. Therefore, its properties should be highly anisotropic. The bond strength within the rings is strong. The planes are stacked and held together by weaker bond forces. Similarly to graphite and molybdenum disulfide, this allows for easy shearing of the planes when a force is applied parallel to the plane. The ease of shear provides the expected friction reduction and resulting lubrication. Concurrently, the high bond strength between boron and nitrogen within the hexagonal rings provide the high load-carrying capability that is necessary maintain metal-metal separation of the substrates. Similar to MoS_2, boron nitride has intrinsic lubrication properties. Boron nitride effectively lubricates in a dry as well as a wet atmosphere. It is very resistant to oxidation, more so than either graphite or MoS_2, and maintains its lubricating properties up to its service-temperature limit.

The thermodynamically stable crystal structure of carbon at room temperature is graphite, shown in the figure below. The lattice is hexagonal with four atoms per unit cell. The structure of hexagonal boron nitride thermodynamically stable at room temperature is closely related to graphite. The atoms occur in hexagonal sheets, but the sheets are stacked directly above one another along so that the stacking sequence is described as AAAAA…, with unlike atoms above one another n consecutive layers. In any one sheet there are equal numbers of B and N atoms arranged so that B and N alternate around any one atomic hexagon. At room temperature the B-N separation in the sheets is 1.45 Å and the separation between the sheets is 3.33Å.
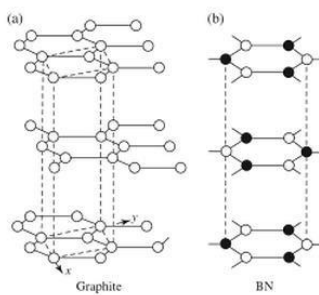
Fig. 4: Crystal structures of a) Graphite and b) BN.

Hexagonal boron nitride adopts a typical layer structure where, within one layer each boron atom has three nitrogen neighbors and vice versa, all with equal B-N distances of 145pm. B-N bonding proceeds via the sp2 hybrid and the π orbitals. The layers are held together by van der Waals contacts. In every other layer the boron and nitrogen atoms are exchanged; that is, the layers rotate at 60° to each other such that each boron atom has a nitrogen neighbor above and below, as would be expected by electronegativity considerations.

h-BN is a white solid that does not conduct electricity. It has a very bad wettability by metal melts (e.g., Al, Mg, Zn, Pb, Cu) slags as well as salt melts, and is therefore an excellent material for crucibles and reaction vessels. Boron nitride is stable in air up to ca. 1000 C and has good thermal shock stability. Today, due to the platelet-like crystal shape, h-BN is applied to various cosmetic powders.

4.3. General properties of BN

Commercial grades are available in a variety of purities and particle sizes. These varieties influence the degree of lubrication provided by BN since particle size affects the degree of adhesion to substrate, burnishing ability BN offers a unique combination of properties that cannot be found in any other material.

Property	Value
Molecular weight	24.83
Density	2.27 g/cm^3
Crystal structure	Hexagonal
Color	White
Dielectric strength	35KV/mm
Dielectric constant	4.2
Coefficient of friction	0.2-0.7
Service temperature	1200°C (oxidizing atmosphere)
Thermal conductivity	55 W/mK
Practice size	1-10 micron grade

Fig. 5: Table with the main properties of hexagonal Boron Nitride

- Low density (approx 2,2 g/cm^3)
- High thermal cycling resistance
- High thermal conductivity
- Resistance to most acids and melts
- Electrical insulation
- Very high oxidation resistance
- Low coefficient of friction
- And excellent machinability

4.3.1 Temperature resistance

In air, BN is useable to temperatures as high as 950 ^{o}C. In inert or vacuum conditions, to temperatures in excess of 2500 ^{o}C.
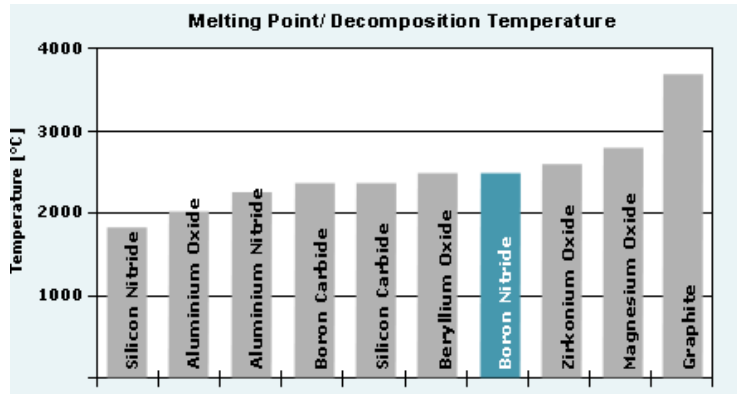
Fig. 6: Graph indicating the different melting point temperatures for different ceramic materials. The blue bar is for the Boron Nitride (2500 ^{o}C)

4.3.2 Thermal shock resistance

Like all nitrides, BN has a very low coefficient of thermal expansion, similar to that of graphite. Thermal expansion of BN may vary in accordance to production methods and composition.
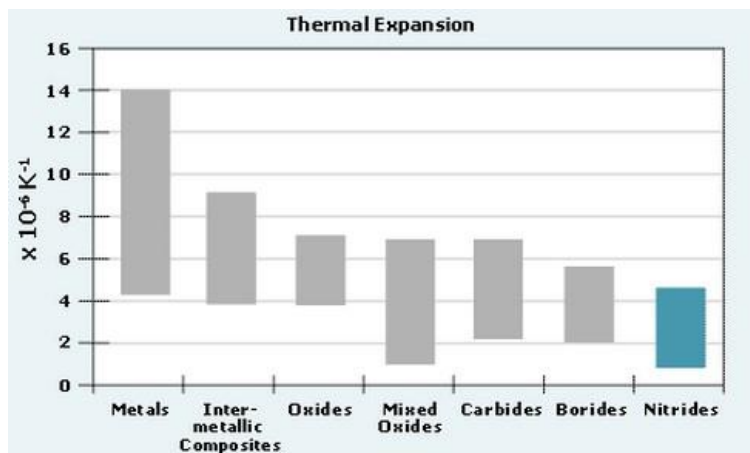
Fig. 7: Graph indicating the different coefficients of thermal expansion for materials with similar to graphite

As a result of its low thermal expansion, the resistance of BN to thermal shock is superior to that of other high temperature ceramic materials.

4.3.4 Density

BN has the lowest density of all ceramic materials:
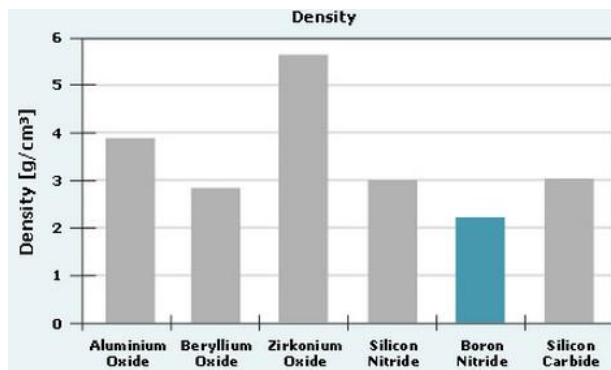
Fig. 8: Graph indicating the different densities of ceramic materials. The blue bar is for Boron Nitride.

Owing to its low density and excellent machinability BN is the ideal material for light components in aerospace applications, providing solutions for a variety of technical problems.

4.3.5 Important parameters

As is the case with Graphite, BN powders can be characterized by six interrelated parameters:

Structurally, hBN is very similar to Graphite. However, because the Nitrogen effectively binds the outer electrons firmly to it, hBN is superior to Graphite in the following areas

- Electrical Insulation and Thermal Conductivity
- Dry Lubrication Properties
- Oxidation Resistance and Chemical Resistance

- WettabilityUses of hexagonal Boron Nitride (hBN)

Boron nitride is a ceramic lubricant with interesting and unique properties. Its use as a solid lubricant is typically for niche applications when performance expectations render graphite or molybdenum disulfide unacceptable. The most interesting lubricant feature of boron nitride is its high-temperature resistance. Boron nitride's service temperature of $1200^{o}C$ in an oxidizing atmosphere makes it desirable for applications that require lubrication at very high service temperatures. Graphite and molybdenum disulfide cannot approach that high of a service temperature and still remain intact. Boron nitride also has a high thermal conductivity property, making it an excellent choice for lubricant applications that require rapid heat removal.

- hBN powder is used as a lubricant additive and can be dispersed in Lubricating Oil, Grease, Water and Solvents. When mixed with water and binders, it can also be applied as paint (for lubricity coating).
- Due to strong thermal resistance hBN is used as an additive for high temperature lubrication.
- hBN powder can be sprayed (similar to sand blasting) or can be sprinkled on hot surfaces (hot forging dies) to provide dry lubricity. Used in extrusion of Aluminum.
- Electrical Insulators: Due to high dielectric breakdown strength and resistivity, hBN is used as an electrical insulator in electronics as substrate for semiconductors, microwave transparent windows, seals, electrodes and catalyst in fuel cell and batteries. It is used as filler for insulation and heat radiation material.
- Due to Chemical inertness, hBN is used in manufacture of crucibles, boats, molten metal carrier pipes, pumps, thermocouple protection sheaths and lining for reaction vessels.
- hBN being a good thermal conductor, it is used as an additive to various types of heat radiation material.
- Due to high lubricity hBN is used as mold release agent for Plastic Injection and Metal Injection Molds. hBN coating is used in refractory molds for glass forming and Titanium forming.

- Due to Non-Wetting property, hBN is widely used in glass manufacturing process.
- hBN powder can be mixed with ceramics, alloys, resins, plastics, rubbers and other material for self-lubricating properties.
- hBN is also used in manufacture of Cosmetics, Paints, Dental Cements, Pencil Leads etc.
- Due to high temperature stability, hBN is used in many Aeronautic and Space applications.

4.4. BN fillers for electrically insulating and thermally conductive polymers

An innovative way to produce functional, thermally conductive parts is the use of heat conducting polymers. Hexagonal Boron Nitride meets the requirements of a heat conductive filler for polymers like no other. Polymers including hBN can be used for insert moldings to achieve best contact and mechanical fixing of the heat generating part. Heat can be conducted out of such assembles much more effective because many functions are incorporated at once:

- Form closure
- Thermal energy transfer to the heat sink
- Electrical insulation
- Protection towards the environment (moisture, vibration, dirt)

Additional the superior lubricating properties of hBN increase the speed of production and reduce the wear of the production equipement. BN also increases the the lubricity and wear resistance of the final polymer parts. Especially its lubrication makes it superior to common fillers like alumina or aluminium nitride (AIN) by:

- Filling the mold cavities prior to the freezing of the polymer,
- Allowing higher pressures despite of higher viscosities, and
- Shortening production cycles.

Due to the platelet structure of BN particles an orientation during molding takes place, thus leading to a higher thermal conductivity 'in plane' than 'through plane' in order of times 2. This is of advantage for heat dispersion and discharge, e.g. at the base of cooling fin

4.5. Introduction

The huge scientific and technological interest for graphene has triggered in last years the development of a wide range of techniques to produce and process nanosheets that, having nanometric thickness and mesoscopic lateral size, shall be considered as *quasi* 2-dimensional (2D) objects. Besides their novel properties, even the way these 2D sheets are produced in solution, by exfoliation, [1]is an original process, still not completely understood.

The exfoliation of a 2D object from a 3D bulk material is a process spanning from nano- to meso-scale due to bubble cavitation, intercalation and disruptive fragmentation, as we described in recent work. Exfoliation always yields a poly-dispersed range of nanosheets thickness and lateral size. When characterizing these 2D sheets solutions, their average size and size standard deviation are commonly reported, in this way assuming that their size follows a "Gaussian" (a.k.a. "normal") distribution. Conversely, the experimental data show that the size distribution of these materials is highly asymmetric and non-Gaussian.

Noteworthy, this asymmetry in size distribution shall be observed in very different systems such, as example, the distribution of chemical elements in rocks, the species abundance in biology, the lengths of latent periods of infectious diseases in medicine, the distribution of galaxies in astronomy (Fig. 1). [2], [3]
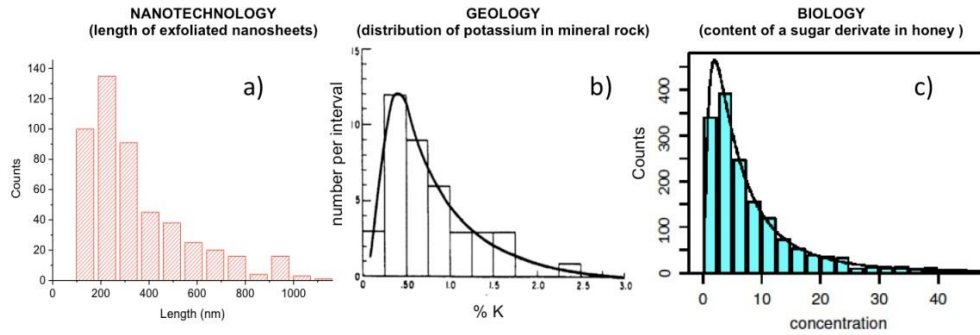
Fig. 1 Comparison of the typical size distribution obtained by exfoliation with other distributions observed in 2D materials, geology and biology. a) Histogram of length distribution of BN nanosheets length obtained by liquid phase exfoliation. b) Distribution of potassium in mineral rock.[2] c) content of hydroxymethylfurfurol in honey.

A better modelling of the size distribution of 2D materials is needed both from a fundamental point of view (to understand the exfoliation mechanism) and a technological point of view (to improve the metrology of 2D materials for applications and quality control). Here, we used image processing of Atomic force Microscopy (AFM) images to study the exfoliation and fragmentation process of a well-known 2D material, Boron Nitride (BN, Fig. 2) exfoliated in solution with two technologically relevant techniques: ultrasonication and ball milling. Exfoliated BN nanosheets are deposited on silicon and their size distribution is measured by AFM and an image analysis software, performing in this way statistics on *all* the sheets present on the surfaces, for a total of >6000 sheets, as compared to the tens of sheets analysed by manual TEM statistics typically used for this task.[4] Being the resolution of AFM much larger than the average sheet size, the exact shape of each sheet shall be included in the statistics, allowing to cross-relate the length, the area and length/width ratio of each sheet in each sample.[5]

By using a large statistical population we are confident to discriminate the most suitable analytic function able to reproduce the achieved fragment size distribution. As example, studying the galaxy distribution Brown *et al.* demonstrated that the universe underwent a single

fragmentation event, separating into protogalactic volumes at a relatively early stage after the Big Bang.[6]

As test material, we chose not to use the well-known graphene but used Boron Nitride, a relatively less studied 2D material which has anyhow huge scientific and industrial interest, because it can be used as a monoatomic insulating layer for graphene-based electronic devices,[8, 9] or as a bulk additive in polymers.[10]

Fig. 2 shows Scanning Electron Microscopy (SEM) images of typical BN flakes, and solutions obtained from such flakes by sonication or ball milling in isopropyl alcohol (IPA). The solutions obtained are stable for more than 6 months. BN solutions show a whitish colour and a strong light scattering (Fig. 2b), due to the presence of the BN nanosheets.

4.6. Exfoliation methods

Two different techniques (sonication and ball milling) were used to prepare the samples, with two different conditions each (high and low power, see table 1).

Table 1: Exfoliation techniques used (see text for more details)

Procedure	High Power	Low Power
Sonication	220 W (effective power)	66 W (effective power)
Ball milling	450 rpm (rotation speed)	200 rpm (rotation speed)

Sonication is a process in which sound waves are used to agitate particles in solution. Such disruptions can be used to mix solutions, speed the dissolution of a solid into a liquid (like sugar into water), and remove dissolved gas from liquids.

4.6.1 Liquid-phase exfoliation

Liquid phase exfoliation of layered materials has been found to have great potential for the scalable production of the 2D nanosheet-based materials. Layered materials can be exfoliated to monolayer and few-layer 2D nanosheets in various organic solvents via sonication. However the concentrations of the resulting BN suspensions are very low for large-scale applications. In addition the solvents used are expensive, toxic, requiring special care during handling and have high boiling points which make them difficult to remove.

The liquid exfoliation process generally involves two steps: the thinning of layered materials into small individual 2D nanosheets, and then further dispersion of these nanosheets in solvents. The solvents used for dispersion are required to be capable of preventing the aggregation of 2D nanosheets driven by their high surface energy. Moreover, it would be better if the solvents are volatile (easy to be removed), cheap, and eco-friendly.

For sonication test, suspensions were prepared at same starting concentration (3 mg/ml) in IPA and sonicated at different times (20, 40, 60 and 80 hours) using an Elmasonic P70 Ultrasonic Bath at 220W or 66W of effective power.
A planetary ball mill (Retsch PM100) with a 50 ml Zirconium dioxide grinding jar and $\approx$1300 zirconium oxide balls (3 mm in diameter) was used to mill BN powders in IPA at different times (from 1 to 60 hours) and rotation speeds (200 and 450 rpm). After the exfoliation, a centrifuge Heraeus (Omnifuge 2 RS) was used to remove the larger, mesoscopic BN particles.

Upon exfoliation, BN solutions show a whitish colour and a strong light scattering (Fig. 2c), due to the presence of the BN sheets. At difference with graphene, that is exfoliated using high boiling solvents, we exfoliated BN using as solvent isopropanol (IPA) which is a low boiling point solvent (b.p.=82 $^{\circ}$C), quick to volatilize and easy to remove after BN processing on surfaces or in composites, thus minimizing processes of flake aggregation. Exfoliation in IPA yields stable solutions of BN.

4.6.2 Ball milling

Ball milling can generate two forces on layered materials, shear force and compression force. The shear force can cleave layered materials from their outer surfaces while the compression force peels off thin 2D nanosheets from the edge of layered materials. The relatively straight edges of the big sheet indicate that it has mainly experienced tearing rather than vertical impact on the in-plane surface during ball milling, resulting in no major destructions of the crystal structure*. The observed curled edge is usually found in ultrathin graphite or graphene as curling can reduce the free surface and dangling bond energies.

Efficient mechanical cleavage while retaining the in-plane crystal structure can be achieved under the following selected milling conditions. First, a suitable type of ball mill needs to be chosen. Most types of high-energy ball mills employ strong collisions or vertical impacts to fracture particles and even destroy crystalline structures to amorphous or non-equilibrium phases*. A planetary mill, allows controlling balls in rolling actions that apply only shear force on the milling materials. Second the use of small steel balls also helped to minimise the damage to in-plane crystal structure and the relatively large number of these balls make the milling more efficient. Third, a liquid controlling agent is essential in milling as it acts as a lubricant to make the shear force much gentler to further reduce the damage to the structures and also to prevent welding effect*. Under the gentle shear force, preferential that the thin BN layers were able to be mechanically peeled off from the hBN particles.

Comparing to other milling agents i.e. water, ethanol and dodecane, benzyl benzoate gave the best peeling results because of the high viscosity of benzyl benzoate and its similar surface tension to hBN, which prevents the newly peeled-off BN sheets from agglomerating and also enhances exfoliation.

The low energy ball milling does not cause damage to the in-plane structure of 2D nanosheets and generates fewer defects and impurities in contrast to sonication. However, most ball milling treatments are violent processes which destroy or disorder the crystal structure and introduce a

great number of defects. The three parameters in a ball milling process which are affecting the exfoliation results are (Burmeister):

1. Rotational speed
2. Time of milling
3. Number of milling balls in the jar.

The exfoliation of hBN is more difficult compared to that of graphite because of the slight ionic bonding*. The controlled ball milling could be a process to supply a large quantity of high-quality BN nanosheets.

Both in ball milling and sonication mechanical forces act on the material; however, these forces have a different origin and work on different scale lengths. In ball milling, the exfoliation is due to compression or shear forces caused by the movements of the balls, that in our case have a macroscopic diameter (3 mm). In sonication, the mechanical action arises from cavitation bubbles, with radius of about one hundred of μm, that generate high strain rates in the surrounding liquid upon implosion. [7]–[9]Fig. 7 in main text shows the typical effects of treatment by sonication (Fig. 7b,c) and milling (Fig. 7d,e) on BN.

Sonication reduces the size of mesoscopic flakes, but does not change significantly their morphology. We previously studied the effect of sonication on materials by monitoring the evolution of surface roughness on bulk graphite sonicated in a solvent commonly used for graphene production, *N,N'*-dimethylformamide;[9] in these conditions exfoliation proceeds on a layer-by-layer basis; only the upper part of the graphite is interested, and the process is slow, requiring several hours to have visible effects on the substrate roughness.

In case of milling, instead, the effects of shear and compression action of the milling spheres is visible on several flakes, with BN stacks shifted over each other, showing folds not only on the surface of the platelets (Fig. 7d, white arrows) due to the shear force of balls rolling over the top surface of the particle, but also *inside* the platelets, (Fig. 7e, white arrows) due to the

compression force of milling balls colliding with the edge of the particle and then sliding over it, in agreement with the results obtained in ref.[10].

Both milling and sonication yield a large number of BN sheets after spin coating on silicon oxide substrates. The amount of exfoliated material estimated by AFM is found to be roughly proportional to BN concentration in solution. By assuming for BN an extinction coefficient α=2367 ml/mg/m measured at 300 nm, [1]an estimated concentrations up to 0.04 mg/ml, comparable to 0.06 mg/ml obtained by extensive sonication could be estimated; however, the presence of significant light scattering due to the large size of the sheets does not allow to use optical absorption data to estimate exfoliation yield.

The absorbance A of all solutions showed a power-law dependence of A on light wavelength λ ($A \propto \lambda^{-n}$), indicative of strong light scattering, in agreement with what observed in ref.[1]. The sheet morphology, as measured by AFM, is the one expected for layered materials, with linear edges and sharp corners (Fig. 2d), but the sheets have a wide distribution in lateral size (from tens of nm to more than 1 μm) and thickness (up to 10 nm, with no large macroscopic aggregates). It is thus difficult to discriminate any difference just by visual comparison of the AFM images. After exfoliation, the nanosheets were spin coated on silicon and measured by AFM (Fig. 2c,d).
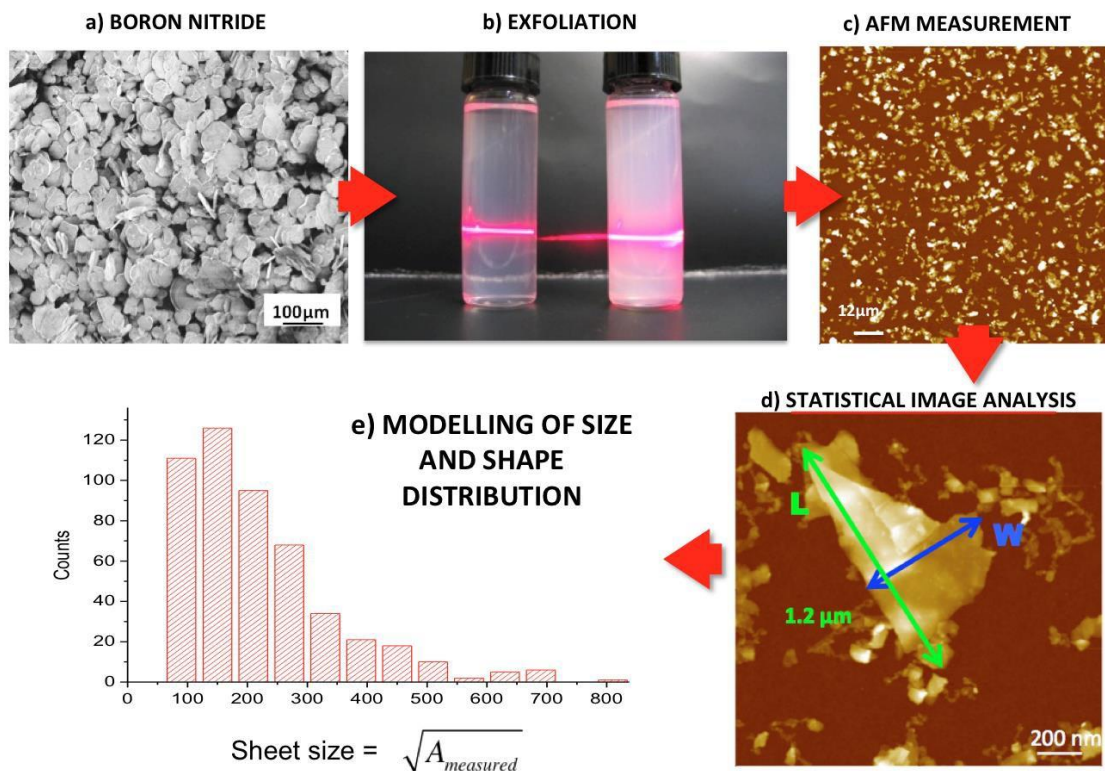
Fig. 2 a) SEM image of the pristine BN flakes used for exfoliation. b) Exfoliated solutions of BN in isoproanol, showing strong scattering due to the dispersed flakes. c) AFM image of BN nanosheets spin coated on silicon oxide substrates. d) Zoom-in of a single nanosheet, showing the typical, non-exact way to estimate of its length and width. e) Histogram distribution of sheet size obtained instead measuring precisely the area of each sheet.

To quantify the sheet size obtained with different techniques, we used image analysis software able to detect automatically individual sheets and measure their area and lateral size (Fig. 2e). [11]While AFM can easily give high-resolution images of the flakes and allow manual measurements of their size, several steps (image flattening, threshold selection, etc.) and careful analysis are required to obtain quantitative results.

4.7. Image analysis procedure

To characterize and define effectively nano-materials is a major metrological problem; as example, the exfoliation of the same starting solution shall give different yields of solubilized material and monolayers fraction if centrifuged at different speeds,[12] or purified using different washing procedures.[13], [14] It is fundamental to quantify not only the average size of the sheets obtained, but their size distribution as well; in this, 2D materials have some analogy with what is done routinely to characterize poly-dispersed, 1D polymers. [15]

For this, statistical analysis is needed to characterize the poly-dispersed sheets. This is commonly done through one-by-one localization and analysis of exfoliated sheets with Transmission Electron Microscopy (TEM). This approach, besides bring tedious and cumbersome, is also not fully objective, because smaller sheets shall escape from the TEM grid thus over-estimating the mean sizes of the exfoliated flakes and making the related statistics inaccurate. For example, the measurement uncertainty depends on the square root of the number of the detected sheets in case of ensembles following Poisson statistics. Thus, a sample population of 100 measured sheets is associated with 10% of intrinsic error. The operator as well shall sometime focus on examining the most interesting (i.e. thinner) sheets while missing larger aggregates. Furthermore, sheets aggregation, restacking and folding on the TEM grid during solvent evaporation makes the analysis of size and shape of the sheets difficult. The number of sheets localized and measured by TEM can be very low, even below ten for a given nanosheet type, and even partially folded or overlapping sheets should be measured to improve the statistics.[16]

Thus, it is fundamental to complement published results obtained by TEM with more detailed studies, performed at the nanoscale and on large statistical data (see also section dedicated to Dynamic Light Scattering in the following text). Atomic Force Microscopy (AFM) can be used to characterize the size distribution of thousands of nano-sheets, to automatically detect and analyze the length, area and surface density of them, and to compare the obtained results with

more macroscopic characterization techniques such as optical spectroscopy and dynamic light scattering.

To quantify the sheet size obtained with different techniques, we used an image analysis software able to detect automatically individual sheets and measure their area and lateral size[11]. In this way we could also remove noise and grains crossing the image edge, and plot the statistical distribution of the different observables measured. While AFM can easily give high-resolution images of the flakes and allow manual measurements of their size, several steps are required to obtain quantitative results on a statistical base.

a) Use of a flat substrate allowing a fast and unambiguous discrimination of the flakes from the surrounding bare substrate. This primary condition was satisfied by spin coating BN on atomic flat silicon substrate because the height of the single sheet (about 1 nm thick as measured by AFM) is significantly larger than the root mean square roughness (RMS) of the substrate which amounts to 1.8 Å.[17]

b) Use of the correct flattening procedure to remove the AFM artefacts due to sample tilt, always present, and non-linearity of the piezoelectric scanner.[18], [19]Dedicated flattening procedures based on local mean or local standard deviation (SD) of the height values shall be used in case of irregular surfaces.[11] The first method simply subtracts the mean value of the pixels in the local neighbourhood of each pixel. The SD equalization scales the height values by a factor given by the standard deviation of the global image, divided by the local mean of the standard deviation. The efficiency and the reliability of the flattening procedure were monitored step-by-step by histogram analysis, plotting the frequency distribution in z of all the pixels of each image. In case of relatively flat substrates, the better is the flattening, the narrower is the measured height histogram, with a peak-width close to silicon roughness. The used procedure removes the artifacts in few steps and the measured substrate roughness rapidly converges in the range of values between 0.15 and 0.20 nm, in good agreement with the values reported in literature.

c) Once the image is flattened, a suitable height threshold is used to discriminate flakes from background. A binary condition selection is used: only the pixels above the threshold are

considered belonging to a flake, while the rest is disregarded. Anything having a height lower than the threshold will be counted as background, and not included in the statistics. We choose 0.5 nm as a suitable threshold, a value half the thickness of a typical sheet and more than two times larger than the substrate RMS roughness.

d) A further filter shall also be applied. The filter will simply exchange small "ridge pixels" with interpolated values if the slope on the ridge is smaller than the given percentage of the maximum slope. We define a ridge pixel as a pixel having a value that is either larger or smaller than its four next-neighbour pixels. In contrast to other filters, this filter will only affect the smaller corrugations. To eliminate larger noise peaks a Local Mean filter could be applied (see above).

e) Recognise connected or partially overlapping flakes by finding local minima, even above the threshold, that will be considered as flake edges.
Even if the software performs automatically all these operations, the parameters used for each operation (threshold height, noise filter, etc.) should be carefully tuned and cross-checked for reproducibility and reliability. However, the automatic detection of flakes is pretty robust and not so sensible to fine-tuning of these parameters, given that the flakes are usually deposited on very flat silicon substrates and that the lateral resolution of AFM is much larger than the average sheet size. In particular, we have found that the method is very suitable to analyze structures having a lateral size of tens of nanometers and uniform thickness, such as flakes of graphene, BN or other 2D materials. More details on the flake detection procedure shall be found in ref.[11].

The first output of the AFM statistical analysis is simply the amount of sheets obtained for each process and treatment time, expressed in terms of number of sheets per square micron plotted in Fig. 3. Insets in Fig. 3 show the typical AFM images obtained at initial and final stages of the exfoliation, where the image analysis software has automatically identified and assigned a different colour to each BN sheet.
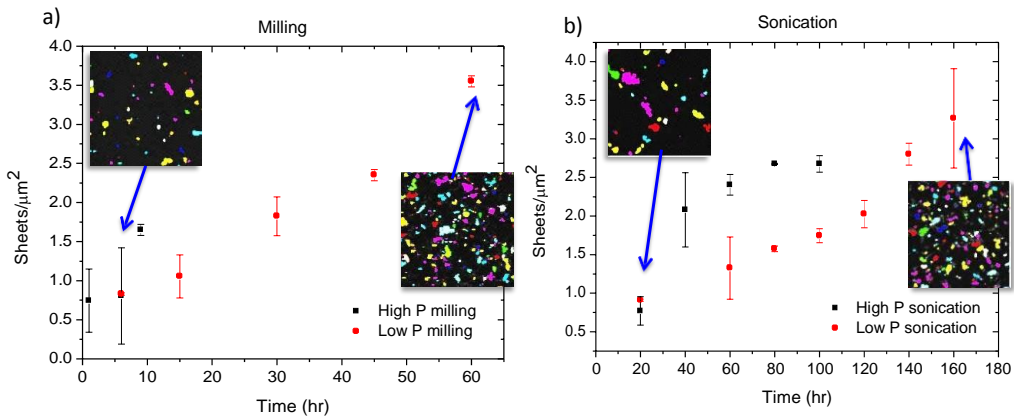
Fig. 3 Graphs representing the number of sheets counted per μm² for a) sonication and b) ball milling. Inside the graphs we also show typical processed images from the AFM analysis of the BN samples at lowest or highest concentrations.

Of course, the most interesting output of the analysis is not the simple number of sheets, but their lengths and area (or size) distribution that was already discussed in main text.

We tried to use statistical histogram analysis to measure as well the AFM thickness of the sheets, as previously done with organic self-assembled monolayers and with mono-atomic graphene oxide sheets. [20]However, the height histograms obtained did not yield well-defined peaks corresponding to the different BN layers, due to the strong dependence of this measurement on the roughness of the sheets, which often show the presence of partial folds and nano-debris. Thus, the thickness was measured manually by profile analysis of different AFM scans, showing a skewed distribution similar to the ones observed for length (fig. 4).
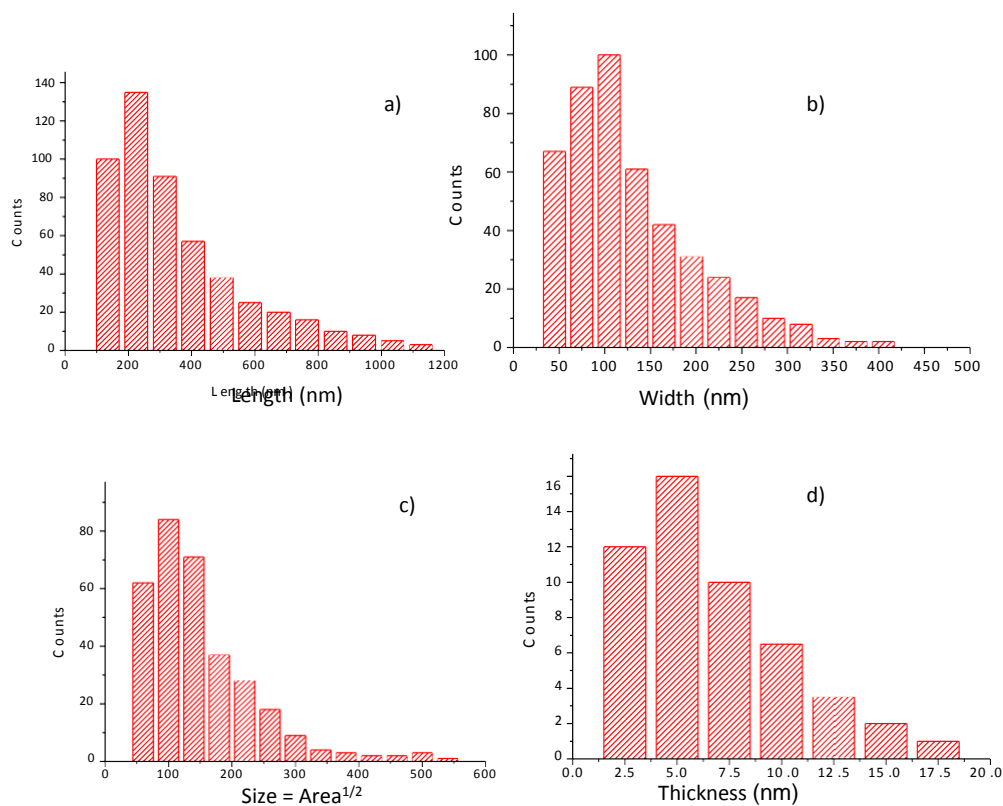
Fig. 4 Typical histogram distributions of various physical quantities of the nanosheets obtained by AFM image analysis, all featuring a highly skewed shape.

The thickness shows a decreasing trend (Fig. 5) similar to what observed for lateral size, with most of the material present as multi-layered sheets, and with all the samples distribution approaching an asymptotic average thickness of $\approx$ 6 nm; the values of average final thicknesses measured by AFM were: 8±4 nm (High P. sonication), 6±3 nm (Low P. sonication), 6±3 nm (high P. Milling), 6±3 nm (low P. milling). As mentioned in main text, we should keep in mind that these average values will not correspond to the median or to the highest peak of the size distribution $N(s)$, because they are not Gaussian.
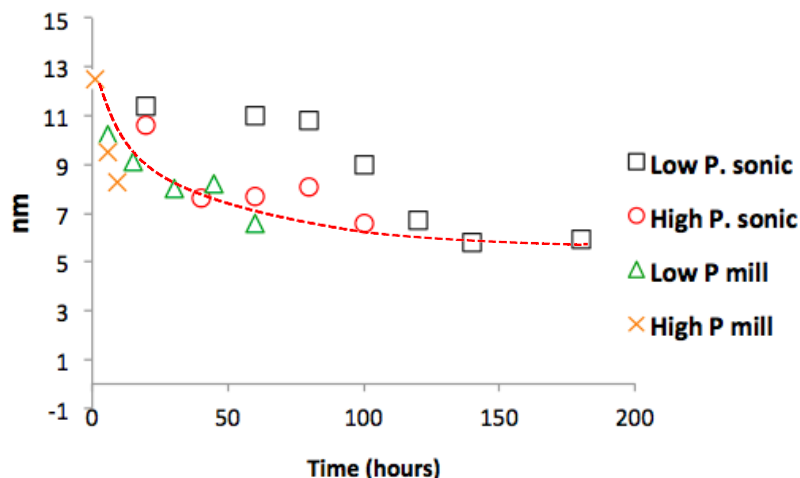
Fig. 5 Evolution of BN nanosheet thickness exfoliated by sonication and Ball milling in solution, measured by AFM. The lines are just a reference for the eye.

By using this approach, we could detect and digitalize hundreds of flakes having thickness down to 1 nm, deposited on areas of 1 - 400 μm^2.

4.7.1 Definition of sheet sizes

A particular issue in characterizing 2D nanosheets is to define the "size" of the sheets, because they have highly irregular shapes; we shall define for each sheet a given length L, measured along the main axis, and a width W measured perpendicular to it (Fig. 2d).

For perfectly rectangular sheets the area A would be simply $L \cdot W$. This is not true for irregular shapes such as the ones typically obtained by exfoliation of 2D materials. However, the image analysis software allows to measure pixel by pixel the area of each sheet, and use this as the relevant parameter to monitor exfoliation.

To have a reliable parameter, not depending on a particular shape, we thus used as relevant "size" of the sheets the square root of the sheet area, measured pixel by pixel: $s = \sqrt{Area_{meas}}$. In

case of perfectly rectangular shapes, this would be simply $s = \sqrt{L \cdot W}$; for irregular sheets, this has the same dimensionality but is a more reliable parameter than length L. Differently from L, s does not depend on sheet shape, but only on the exact area.

4.7.2 Modelling of fragmentation processes

Fig. 3 shows that the statistical distributions of sheet sizes obtained with either sonication or ball milling do not follow a Gaussian (a.k.a. "normal") distribution, but are strongly asymmetric and positively skewed, with a tail due to the presence of larger sheets in all samples. All the physical dimensions of the exfoliated sheets (length, width, area, thickness) show the same asymmetric, non-Gaussian distribution

Table 2: Statistical distributions

	Equation $f(x)$	Reliability $N(x)$	Mean μ	Variance σ^2
Gaussian	$\dfrac{1}{w\sqrt{2\pi}}e^{-\frac{(x-x_0)^2}{2w^2}}$	$\dfrac{1}{2} - \dfrac{1}{2}\,erf\left\{\dfrac{x-x_0}{w\sqrt{2}}\right\}$	x_0	w^2
Log-normal	$\dfrac{1}{xw\sqrt{2\pi}}e^{-\frac{(\ln x - x_0)_2}{2w^2}}$	$\dfrac{1}{2} - \dfrac{1}{2}erf\left\{\dfrac{\ln x - x_0}{w\sqrt{2}}\right\}$	$e^{x_0 + w^2/2}$	$\left(e^{w^2}-1\right)e^{2x_0+w^2}$
Weibull	$\dfrac{k}{\lambda}\left(\dfrac{x}{\lambda}\right)^{k-1}\cdot e^{-(x/\lambda)^k}$	$e^{-(x/\lambda)^k}$	$\lambda \cdot \Gamma\left(1+1/k\right)$	$\lambda^2\cdot\Gamma\left(1+2/k\right)-\mu^2$
Gamma	$\Gamma(\alpha)\,x^{\alpha-1}e^{-\beta x}$	$\dfrac{1}{\Gamma(\alpha)}\gamma(\alpha,\beta x)$	$\dfrac{\alpha}{\beta}$	$\dfrac{\alpha}{\beta^2}$

note:

error function: $erf\{z\} = \dfrac{2}{\sqrt{\pi}} \displaystyle\int_0^z e^{-t^2}\, dt$

lower incomplete Γ function: $\gamma(\alpha, x) = \displaystyle\int_0^x t^{\alpha-1} e^{-t}\, dt$

In general, skewed functions are the most general case to describe the asymmetric distribution of a physical observable (e.g., the size particle in powders or polymer blends). As example, one of the most used distribution is the Poisson one, a discrete distribution that estimates the probability of a given number of events occurring in a fixed interval of space (distance, area or volume) and/or time if these events occur with a known average rate and independently from each other.[21] Poisson distribution is asymmetric and represents a very general case containing the well know and commonly used Gaussian distribution which is obtained as a limit of the Poisson one in the case of the total number of events $N \to \infty$.

The Gaussian is a continuous symmetric distribution with the domain defined at all $\Re$; in particular the position of the peak (mode) coincides to the mean value (μ) and the median and the peak width are directly correlated with the standard deviation (σ); for these reasons, the Gaussian function is widespread and is commonly used to model several kinds of real distributions.

Given a distribution $f(\mu, \sigma)$, where μ is the distribution average and σ the distribution standard deviation, the Gaussian is a good approximation for $\mu/\sigma \gg 1$. This condition is not satisfied for the measured length, width and size distribution of the BN sheets. Moreover, the studied observables cannot be negative and the Gaussian distributions cannot be used to reproduce the measured ones.

For exfoliated 2D nanosheets the mean value will not correspond to the median or to the highest peak of the size distribution, and the standard deviation will not be proportional to the half width of the distribution peak.

On the mathematic side, the importance of the Gaussian function is due to its role in the Central Limit Theorem, which loosely says that the *sum* of a large number of independent quantities tends to have a Gaussian form, independent of the probability distribution of the individual measurements. This is the case, as example, of the distribution of the *x,y,z* coordinates of particles diffusing in a solvent, coming from the sum of random scattering events.

When, instead, the final size is the result of the *product* of many independent, identically distributed actions, the final result is a highly skewed log-normal distribution. The skewed shape obtained in all exfoliation processes can thus be explained as the result of a more general fragmentation process,[2] where the size *s* of a sheet changes at each "cutting" event *i* as $s_i = s_{i-1} / c$.

In order to find the most appropriate analytic function to model exfoliation, we compared three continuous probability distributions commonly used to study the fragmentation processes: (*LN*) *Log-normal, (W) Weibull and (G) Gamma function*. A comparison of the properties of these functions is reported in Table 2.

LN function represents the distribution of a random variable whose logarithm is normally distributed. If the random variable *x* is log-normally distributed, then $X = \log(x)$ has a Gaussian distribution. LN is characteristic of a random multiplicative process, and has previously been used to describe many rock crushing processes.

Weibull function was the first function applied by Rosin & Rammler in 1933 to describe a particle size distribution.[13] W function describes the size distribution given by a series of fragmentation events which are not constant and whose rate is proportional to a power of size: $\tau = s^k$, where *k* is the exponent of the power law.

Gamma Function is the generalization of the Maxwell-Boltzmann distribution and it is used to study the collisional fragmentation problem.[22] Moreover, G distribution functions are known to provide a very good fit to the distribution of cell sizes in Voronoi textures (i.e area in 2D partitioned Euclidean spaces).[23]
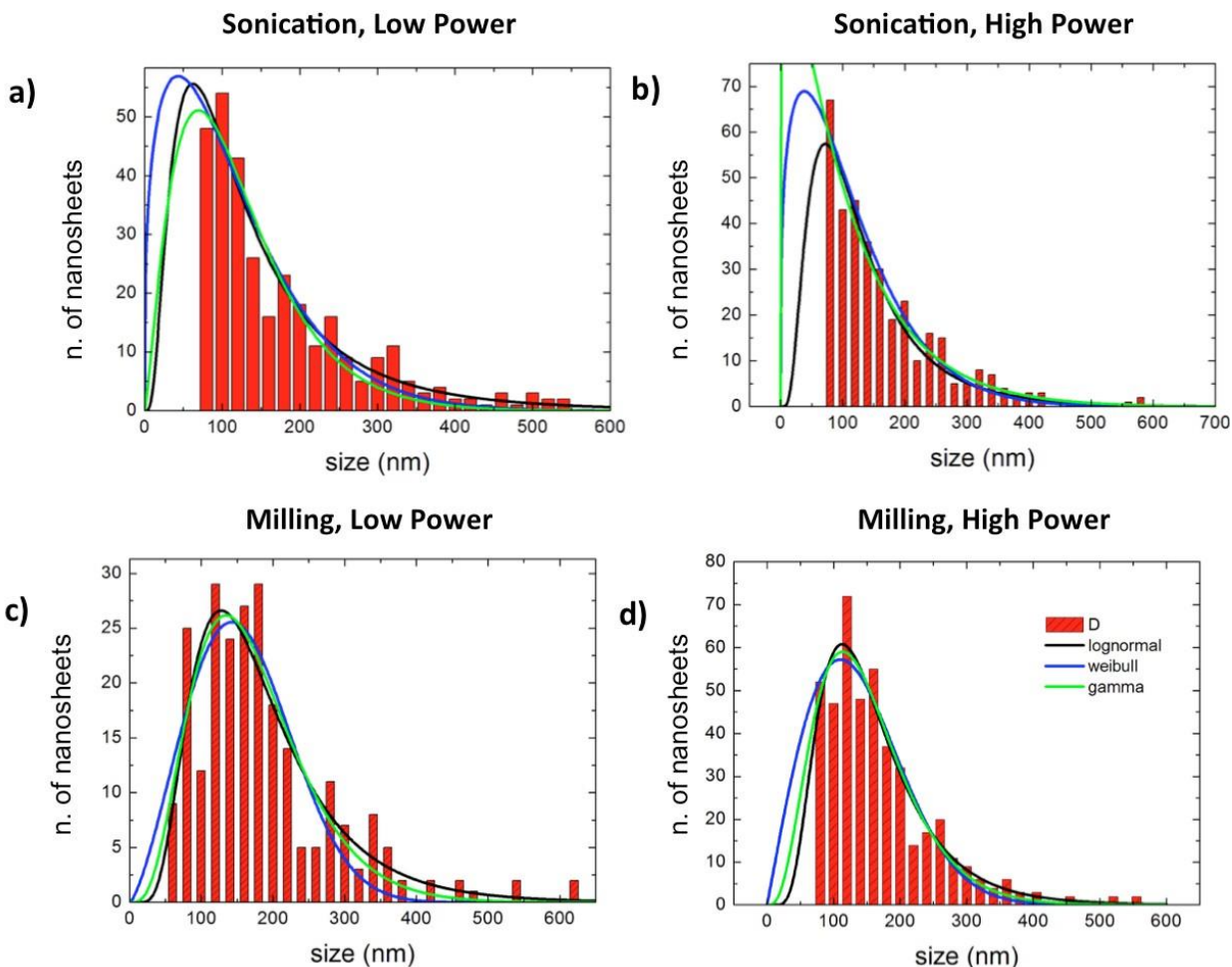
Fig. 6 Nanosheet size distribution obtained with sonication and ball milling, using different preparation conditions. A fit of the experimental data using Lognormal, Weibull or Gamma distributions is also reported in black, blue, green lines respectively.

Fig. 6 shows the measured size distribution of sheet size *f(s)*, obtained by sonication and ball milling with high and low power (see SI for details). To avoid any artefacts we used for the fit only sheets having *s>50* nm, significantly larger than AFM resolution. Experimental data have been fitted using different statistical distributions: LN (black line), W (blue line) and G (green line).

In general, it is difficult to discriminate between the Lognormal, Weibull and even Gamma distributions in particle size distribution curves as evident from the figure; the coefficient of

determination (R^2) is 0.93 – 0.94 for all the three curves (the closer is R^2 value to 1, the better is the fitting).

In order to overcome this well-known problem (see[24] as example), we studied the complementary cumulative distribution functions: $N(s) = N(s_{TOT}) - \int_0^s f(x)dx$, calculated by the best fits of three curves. Given a size *s*, *N(s)* function indicates the number of sheets *larger* than *s*, for this reason it's also called *survival* or *reliability* function.
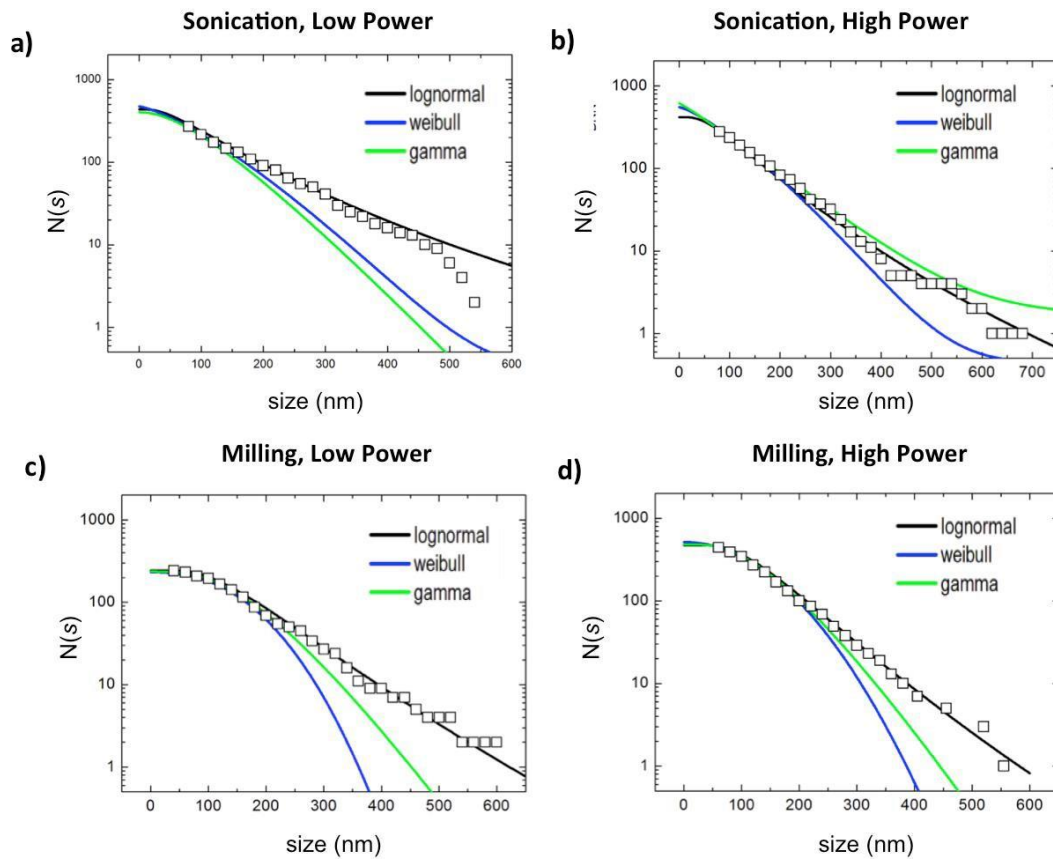
Fig. 7: Survival distribution functions (empty squares) corresponding to the data shown in fig. 6. A fit of the experimental data using Lognormal, Weibull or Gamma distributions is also reported in black, blue, green lines respectively.

The measured distribution and the calculated curves are displayed in Fig. 7 using a semi-log scale visualization. The comparison between all the curves shows clearly that the experimental distribution *N(s)* of sheet sizes follows a Lognormal curve. Sheet distribution obtained with very different methods (sonication and ball milling) can thus be fitted using the same model, suggesting that the sheet size distribution does not depend on the details of the preparation methods, but is instead a common feature in the exfoliation of 2D materials. This kind of "universal behaviour" is not surprising, and has been observed in different disciplines.[3] The presence of lognormal behaviour is characteristic of a random multiplicative process; it indicates that exfoliation follows a linear fragmentation model, i.e. a process where the fragmentation is only driven by external source (in this case, ultrasounds or milling balls) and where the repeated collisions between fragments can be neglected. [25]According to Kolmogorov theory[26] the LN distribution represents the final size distribution in the limit of small BN fragments originated by a "mother cluster" which broke into random-sized fragments through a stochastically determined process (Markov process). The regime of limit of small fragments corresponds to the case in which the fragmentation is completely described by rupture-like breakup events while the erosion-like events (described by a size distribution with bimodal shape) can be completely neglected.

Not only many different variables distributions follow a lognormal behaviour, but even the width of these lognormal distributions (calculated as the variance of the normalized unit $S = \ln s \,|_{s_{mode}}$) range from about 0.2 to 0.5 in several different cases in literature.[27]

We calculated the effective distribution widths V_{Eff} for all our samples (fig. 8); while, as could be expected, variance increases slightly with processing time, all values found lay within the range 0.2-0.5 indicating that the fragmentation event is nearly binary, i.e., one flakes is divided in two flakes, with no "multiple fragmentation" events. [27]In simpler words, in the assumed fragmentation $s_i = s_{i-1}/c$ we have *c≈2.*
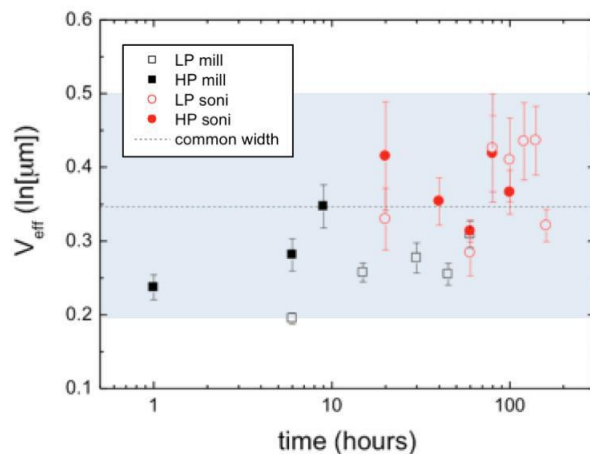
Fig. 8 Effective variance of the lognormal distribution observed for all samples. The shaded area indicates the 0.2-0.5 "universal" variance observed in several different cases in literature. [27]

Last but not least, it can be seen that the distribution decay is linear for large s, indicating that the exfoliation proceeds through the formation of a distribution of random cracks that follows Poisson statistics.[6], [28]

4.7.3 Shape analysis of the exfoliated sheets

Using image processing of the AFM images, we could also calculate the length/width aspect ratio for all the samples. We found that, even if the sheet's size spans over nearly two orders of magnitude (within the range between 30 and 1000 nm), the overall length/width (*L/W*) ratio is fairly constant, being ≈*2.8* for sonication and ≈*2.6* for milling (see Fig. 10; all graphs showing the data points analysed are shown in Fig. 9).
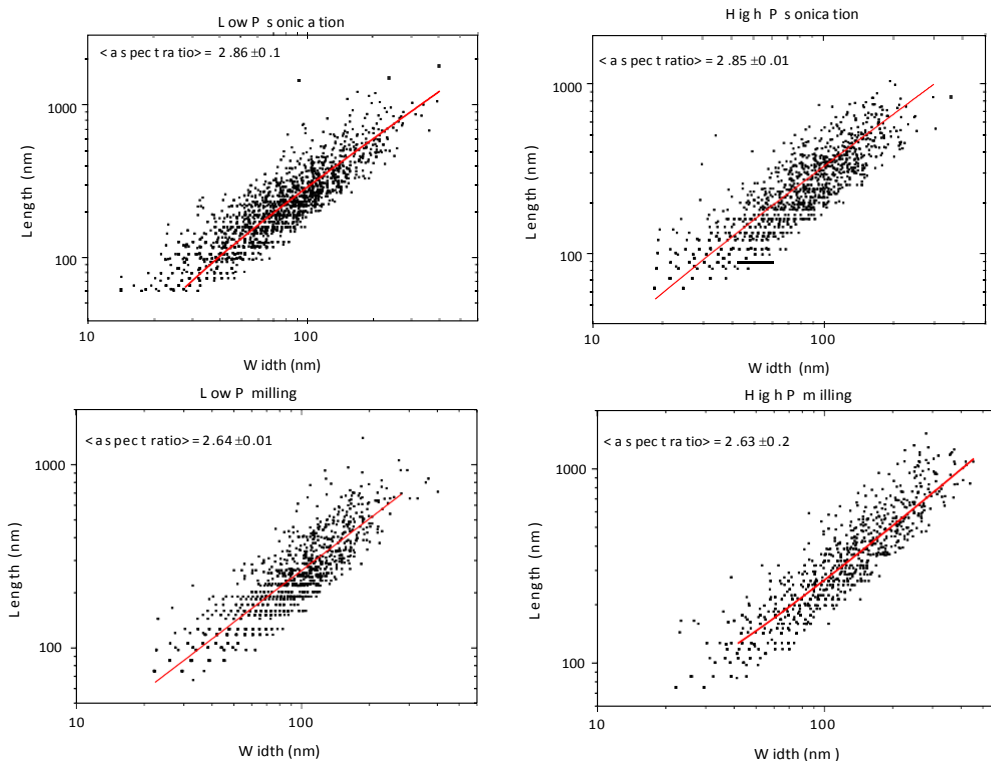
Fig.9 Aspect ratio of length to width for all the BN samples exfoliated by milling and sonication, plotted in log-log scale. Red lines show the best linear fitting of the data points. The average slope is reported with its standard error in the inset of each graph.

Summarizing, (*L/W*) ratio only depends on the fragmentation technique, but does not show any appreciable variation on the processing time and/or processing conditions.
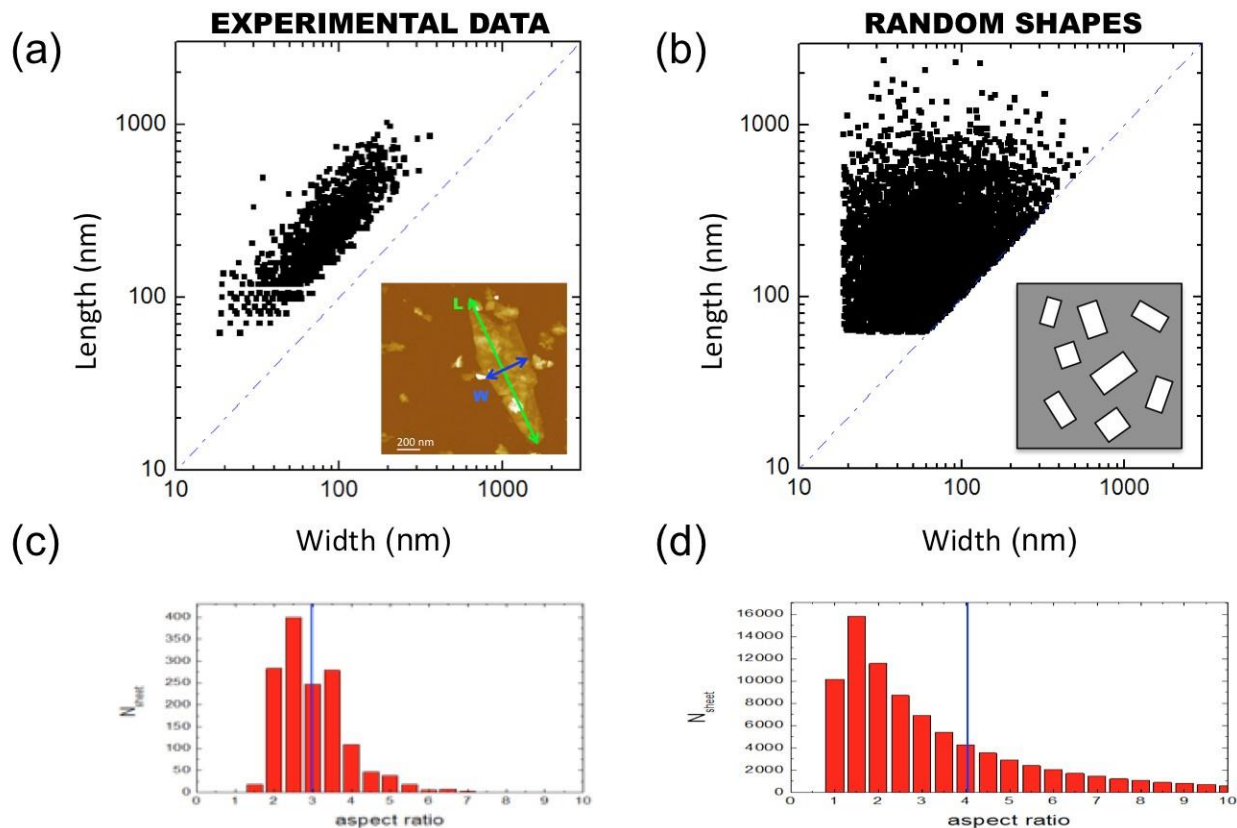
Fig. 10 Length/width plots of BN sheets (a) measured in the case of High power Sonication and (b) calculated by random distributions, plotted in log-log scale. Blue dash-dot line represents the case of aspect ratio = 1. (c,d) Corresponding L/W ratio distributions (red bars) (c) measured in the case of High power Sonication and (d) calculated by random distributions. Blue vertical lines show the mean values.

To understand if this ratio is simply due to a random distribution of sheets' shape, we compared it with the *L/W* ratio of computer-generated rectangles having random sides *a* and *b* spanning the same size range observed for real nanosheets. Fig. 10 shows length vs. width plots obtained by experimental data (Fig. 6a) or by assuming random, uncorrelated length and width (Fig. 10b). The experimental data are based on the analysis of more than 1400 sheets obtained with sonication and ball milling at different times. For the calculation we used an array of several thousands of random numbers couples generated from the lognormal distribution with mean values and standard deviations that mimicked the ones measured experimentally for *L* and *W*. The calculated distributions clearly show different behaviours respect to the measured ones and

as well a *L/W* ratio=4.0±0.1, significantly larger than that obtained from the measurements. The experimental length and width of sheets are thus correlated, as visible in Fig. 6 and Fig. S2, and their ratio is not a random value. This suggests that the shear stress of 2D sheets along different directions yields fracture probability of sheets having a preferred *L/W* aspect ratio. This ratio is slightly larger for sonication (*L/W≈2.8,* likely due to the aligning effect of collapsing cavitation bubbles,[7]) than in ball milling, (*L/W≈2.6),* where shear force can cleave the BN flakes from their outer surfaces, while the compression force can crush and delaminate thin nanoplatelets acting on their edge.[29] Scanning Electron microscopy (SEM) images of BN mesoscopic flakes cleaved by different shear forces are shown in Fig. 11.
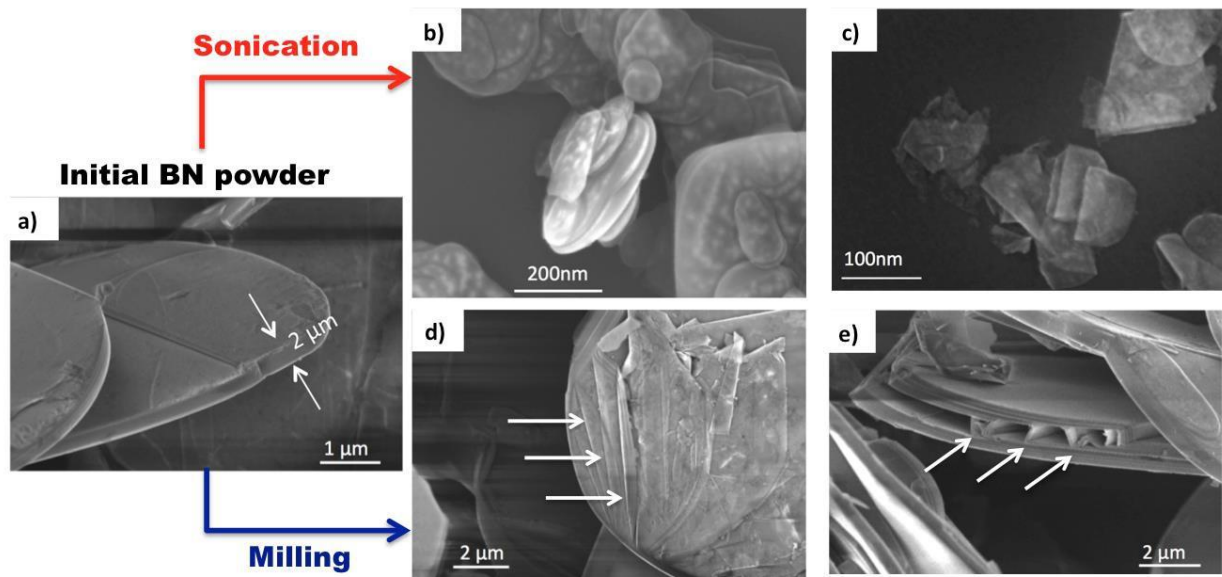
Fig. 11 SEM images showing the effect of different forces in BN exfoliation by milling and sonication

The effects of shear and compression action of the milling spheres is visible on several flakes, with BN stacks shifted over each other, showing folds not only on the surface of the platelets, due to the shear force of balls rolling over the top surface of the particle, but also *inside* the platelets due to the compression force of milling balls colliding with the edge of the particles [10]

4.8. Sheet size evolution with time

We studied the evolution of average size at increasing processing times, that we call $s_{mean}(t)$. As mentioned above, we should keep in mind that this average value will not correspond to the median or to the highest peak of the size distribution $N(s)$, because it is not Gaussian.

This AFM size analysis, performed on surfaces at the nanoscale, gives similar results to macroscopic DLS measurements performed in solution, but with an offset (DLS gives an estimated size that is larger than the AFM measured one of ca. 20%, see SI for more details). LN distribution is observed for all the used fragmentation procedures and for different times. This uniformity is predicted by the Kolmogorov model. Hansen et al.[30] observed that the size scales with time as an inverse power-law: $s_{mean} \propto t^{-1/\lambda}$
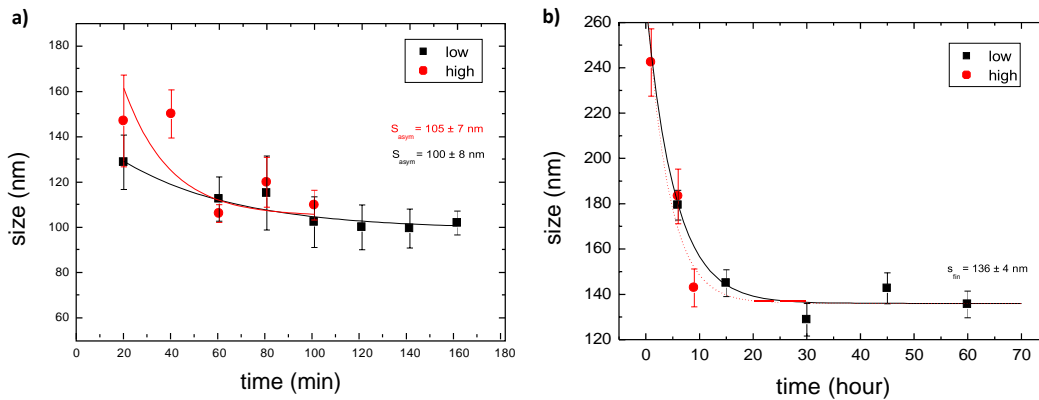
Fig. 12 Evolution of BN nanosheet size exfoliated by ultrasonication and Ball milling measured on a surface by AFM. All the data-set are fitted with exponential curves.

(Fig. 12) where λ is the exponent of the overall rate of breakup (a.k.a. homogeneity index). A similar inverse power-law dependence (with $\lambda=2$) as been recently reported by Khan et al.[25] exploiting a theory previously involved to reproduce the length distributions of sonication of 1D nanotubes[21] to model the size reduction of sonicated graphene sheets.

We note that the application of models developed for 1D objects to 2D shapes is not straightforward. A 1D nanotube can be defined with a single dimension L and can broken in just

one direction, perpendicular to its long axis; conversely, a 2D sheet can be broken in different directions, shall have different length/width ratio, and thus have a different evolution of the average area or average lateral size with processing time. Moreover, the power law should depend on the power dissipated during the fragmentation events.

Using the inverse power-law to fit the sonication data we obtain an exponent value of 4.5±0.6 (8±1) for high (low) power. This difference agrees with the Scaling theory fragmentation where a lower value of λ indicates that the fragmentation rate is less dependent on the sheet size. At sufficiently high shear rates, the probability of rupture is more uniform for sheet of any size. Consequently, the homogeneity index will be zero in this case. A lower value of λ is therefore expected when the acoustic power of the sonicator increases.

Finally, the statistical procedure described here was used to compare the average size of BN sheets obtained by high sonication and milling. The asymptotic values are 105±7 nm and 100±8 nm, for high and low power sonication, while for milling we obtain 142±8 nm and 136±4 nm, respectively for high and low power. We underline that (differently from size distributions discussed above) these numbers are not universal results but depend on the exfoliation conditions used such as processing conditions, time, solvent, etc.

To test the processability of the obtained materials, we used them to produce BN paper membranes by filtering the solution on filter paper. Upon removal of the filter, we obtained uniform membranes of BN, robust enough to be handled and further processed (Fig. 13).
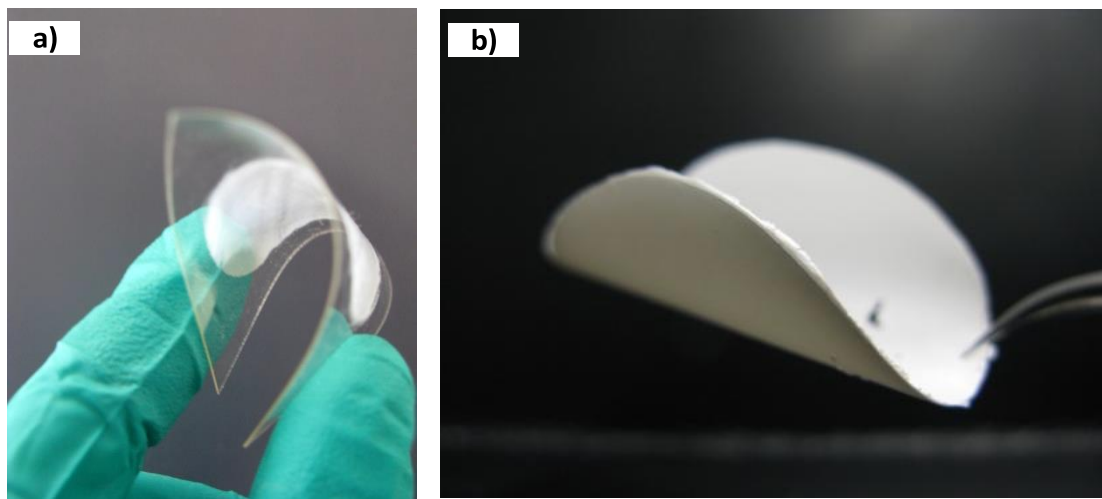
Fig. 13 a) BN membranes prepared from the BN solutions. a) thin layer deposited on PET. b) BN self-standing thick membrane.

4.9. Comparison of sheet size on surfaces and in solution

Statistically efficient techniques, able to estimate particle size quantitatively on large scale and in solution are light scattering techniques, [31]such as dynamic light scattering (DLS) that has already been used to quantify the size and shape of graphene or graphene oxide (GO) sheets in solutions. [32][33] A recent work has demonstrated that there is an empirical relationship between the sheet size measured by TEM and by DLS that, even if having relative errors up to 40%, shall be used to give a quick estimate of the average size of solubilized sheets.[16]

DLS measurements are affected by two key properties: solvation and sample shape. While the first kind of overestimation can be simply neglected for mesoscopic objects, the second point is not trivial. The DLS measurement is based on the assumption that all particles undergo Brownian motion in the solution and diffuse in the liquid like spherical particles; instead, 2D anisotropic sheets have different diffusion coefficients, and thus one could not assume *a priori* that DLS will give the right measurement. [32], [33]

For a perfect sphere, Brownian motion is the same in all directions; for a linear nanostructure (like a nanotube), Brownian mobility is larger along the optical axis. For 2D sheets the large optical anisotropy shall align the flake orthogonal to the light polarization, with increased fluctuations in both longitudinal and transverse directions due to a higher contribution from rotational motion with respect to nanotubes, as demonstrated for graphene by Ferrari and co-workers.[34]

The size evolution observed by AFM was thus compared with measurements performed in solution by DLS. The correspondence between the two techniques shall never be straightforward: AFM measures the sheets one by one, with high resolution, on a solid surface whereas DLS measures thousands of sheets at once, while floating in solution.
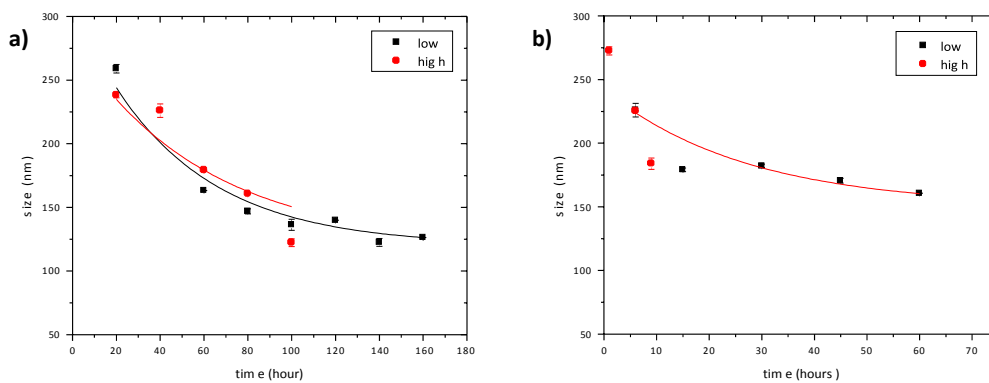
Fig. 14 Evolution of BN nanosheets size exfoliated by ultrasonication and Ball milling measured in solution by DLS. Lines show the corresponding exponential fit of the data.

Fig. 14 compares the BN sheet size as measured by AFM and DLS. We see that both AFM and DLS techniques give a similar trend in size evolution, but with an offset between the measured s. A recent work by Coleman and coworkers[16] reports for 2D materials an empirical power law correlation between the graphene nanosheets length, measured by TEM, and the first peak of the particle size distribution $a_{DLS} \propto L^{2/3}$. In our case, this empirical finding does not apply because we were interested in the original size distribution and did not perform any sorting of nanosheets

size by centrifugation. Finding the right correlation between DLS signal and the "true" size of flexible, monoatomic, 2-Dimensional objects in solution will require much more experimental and theoretical work, and is out of the scopes of this paper. All we shall safely say is that, averaging on all samples, DLS gives an estimated size that is larger than the AFM measured one of ca. 20%. The 20% difference we observed between the size of a 2D sheet measured on surface and in solution can be due to the complex hydrodynamic radius, the folding and the unknown refractive index of these 2D sheets in solution, that does not allow to use the Mie theory commonly used in DLS to infer the particles' radius from the scattering spectrum.

4.10. Raman analysis

Raman spectroscopy is a standard way to measure the number of layers on exfoliated graphite. For this reason we employed Raman spectroscopy to identify the number of hBN layers exfoliated by sonication and milling. In graphene, the number of layers can be easily identified by their optical contrast and Raman signatures.

However, hBN has zero opacity (the band gap is larger than 5eV). On a standard SiOx wafer with a thickness of ~300nm, BN monolayers show white-light contrast of <1.5% which makes them undetectable by human eye[35]. Figure 15 shows representative spectra of hBN on SiOx .The first two peaks are from SiOx and the third one is from hBN. The position of the Raman peak for hBN was noticed at ~1366cm^{-1} that is due to the E_{2g} phonon mode analogous to the G peak in graphene[35]. We tried to measure with a blue (λ=450nm) and red laser (λ=620nm) but no differences were observed. Normally, the peak should become progressively weaker as the number of layers is increasing. Also the Raman peak is usually shifted upwards in monolayers downwards in bilayers. Unfortunately, in our case we did not observe any monolayers or bilayers.
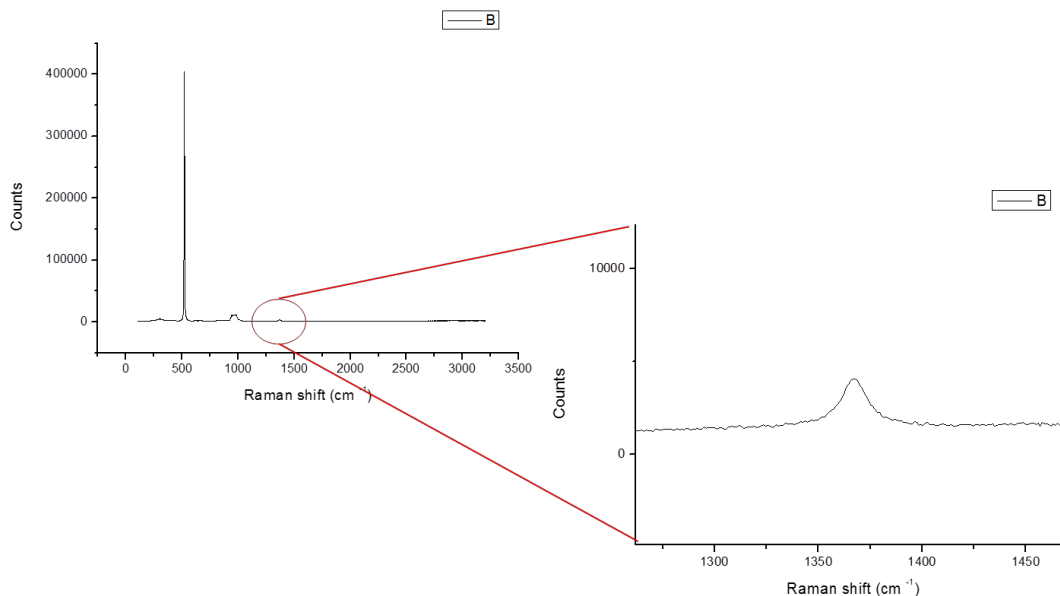
Fig 15 Representative Raman spectra taken on SiOx substrate containing exfoliating BN nanosheets on its surface.

A small shift of the position of the peak was noticed between sonicated and milled samples. Although, that difference is very close to the error of the laser. Other differences were on the sharpness and width of the peak and this was because of the amount of the materials that was spotted by the laser each time. The analysis of the width (HWHM) of the Raman peaks was made by Lorentzian fit on the Origin software.

a)

b)
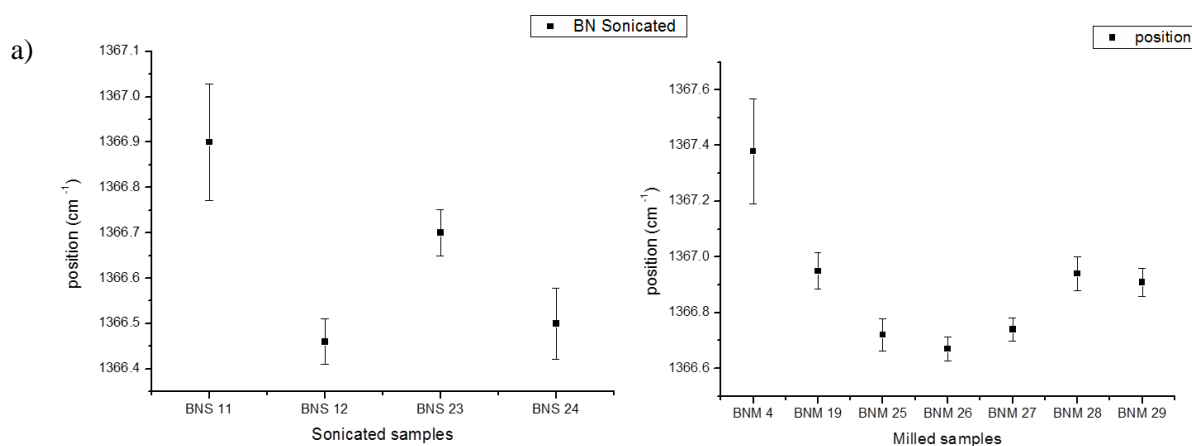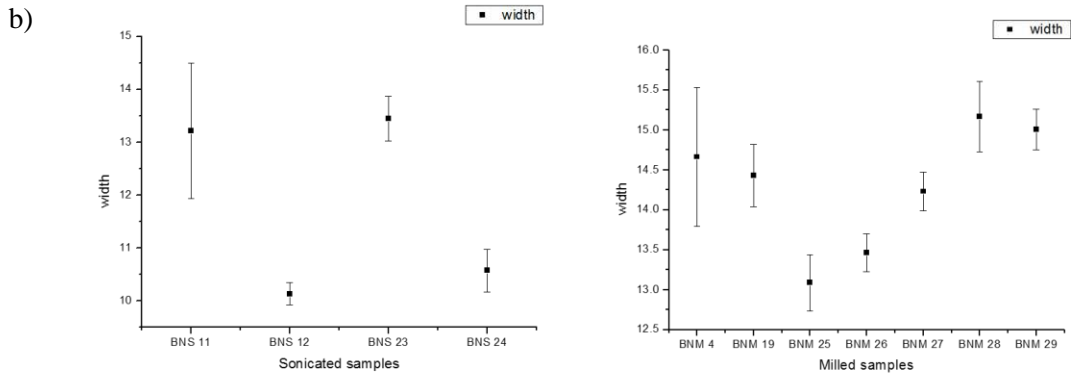
Fig 16: Raman statistics, monitoring the change of the a) position of the peak and b) the width of the peak.

4.11. X-ray Photoelectron Spectroscopy (XPS)

We employed XPS to understand if there is a change in the chemical structure of the Boron Nitride crystal being affected by the extensive sonication. Two different samples were tested, one which was sonicated for 20 hours and another been sonicated for 320 hours. The results, as shown in the spectra below, indicated no change in their structure.
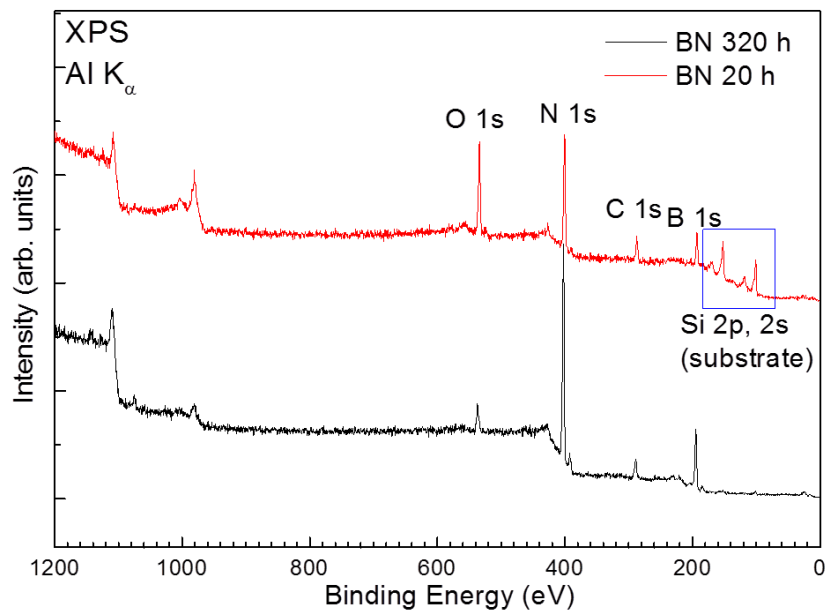
Fig. 19: XPS spectra for BN sonicated at 20 hours (red line) and BN sonicated at 320 hours (black line).
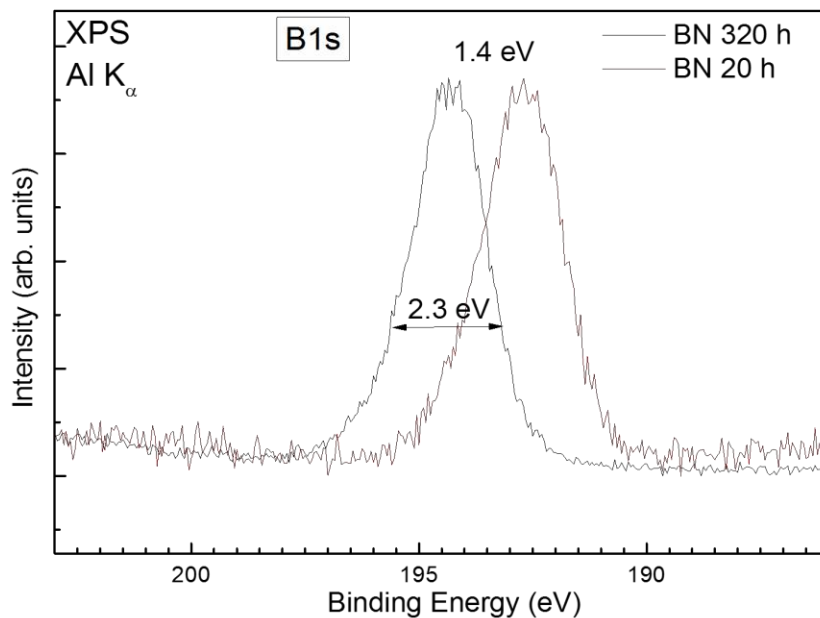
Fig. 20: Magnification from full-range spectrum (fig. 19) on the Boron (B1s) peak.

The 2.3eV shift of the peak Fig. 20) is because the sample gets charged due to the X-ray flux, thus the energy shift is not related to the properties of the BN sample. The same applies for the Nitrogen peak (fig. 21).
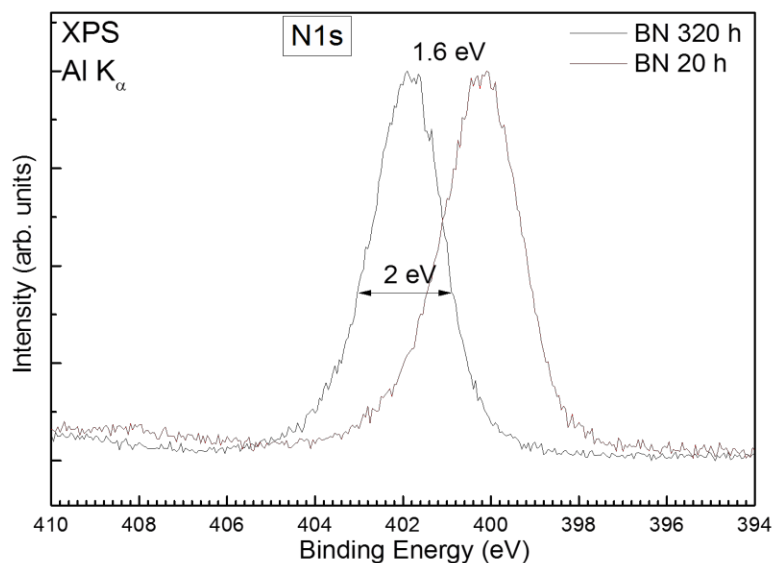
Fig. 21: Magnification from full-range spectrum (fig. 19) on the Nitrogen (N1s) peak.

4.12. Final remarks: which is the best nanosheet shape for composites?

In a draft experiment that we settled to create a BN membrane we used an un-centrifuged solution of BN exfoliated by ball milling after 9 hours at 450 rpm speed. The membrane was created by filtration using a filter paper of 2 μm porous size. For the filtration we used 6mL of solution which were filtered and dried immediately. The final BN membrane was removed from the filter paper after putting it in the oven for a few seconds in order to take the bending shape that we see on the image below. The thickness of this membrane was measured 30 μm and the weight of it 35.8 mg which means that the concentration of the solution that was initially filtered was 5.96 mgr/mL. Mechanically, the membrane was very stiff and brittle which let us think to reinforce it with a polymer in order o improve its mechanical properties.
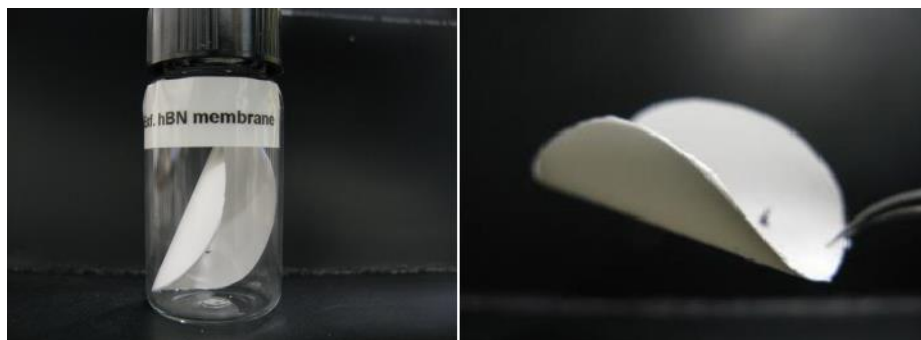
Fig. 23: The BN membranes created after filtration of the exfoliated material

On a second experiment we tested a different solution of BN that was milled for 6 hours at 450 rpm but this time we centrifuged our solution before filtering at 500rpm for 5min in order to remove all the big particles from it. Then removing the supernatant we filtered 20 mL of solution using a 2μm porous size filter paper and let it dry overnight. The final membrane had a thickness of 100μm and weighed 85.5 mgr which means that the concentration of the solution that we initially filtered was 4.27 mgr/mL. On figure 24, we can see the membrane that was created after filtration. On the left we have the half part of the membrane that was cut and put in the oven after drying for 1 hour at 800°C but we didn't see any differences in the mechanical stiffness compared to the other one that was not heated in the oven. Again, both parts were very stiff and brittle.
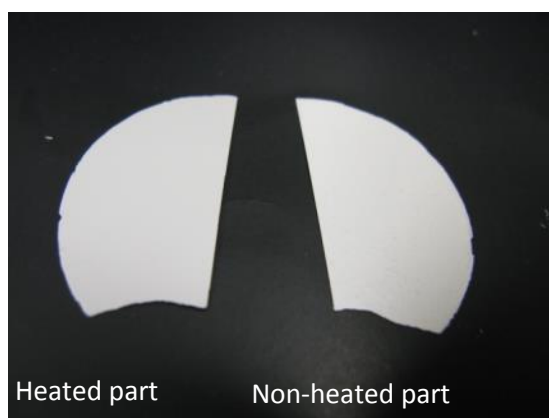
Fig. 24: the membrane that was created after filtration. On the left we have the half part of the membrane that was cut and put in the oven after drying for 1 hour at 800°C.

The above experiments were made in order to let us understand how we want to proceed with further experiments with BN membranes. It is interesting to point out that from both experiments for every mL of solution we use we get a 5µm thick membrane. So, for instance if we want to create 1mm thick membrane we will need a 200 mL of BN solution.

4.13. Conclusions

Overall, the statistical comparison of the samples indicates that the four different techniques give comparable results, with a lateral sheet size between 116 and 136 nm (as measured by AFM) and an average thickness of 6 nm, with a lateral size/thickness aspect ratio ≈20. The relevant size that should be monitored depends on the final application of the material; in general, for composites applications, both length and width are relevant and should be optimized. In particular, in order to produce stronger composites, the load transfer must be maximized and this would correspond to have a length larger than a critical minimal value (along the applied load) of the flake $L_{min} \approx \sqrt{thE/G}$, where h is the thickness of the interface between matrix and the few layer graphene flake, t is its total thickness, E is the Young modulus of graphene and G is the shear modulus of the interface[36]. In order to have all the graphene mass working in the composite this minimal length is also the optimal one. However, because of the random orientation of the sheets, load transfer will take place along all sides of the sheets, and thus the size distribution of both L and W should be taken into account; maximizing both length and width means maximizing the average area of the sheet, to give a very good interaction with the surrounding matrix.

We characterized the size distribution of BN nanosheets produced in solution by sonication and ball milling. In all the different samples tested, the cumulative size distribution of the sheets at a given time follows a log-normal distribution. We did not observe a power-law distribution of sizes that would imply a scale-invariant exfoliation process. The failure of the power-law curve indicates that the exfoliation process does not follow fractal law, but rather has a "typical" sheet scale length.

The Lognormal best-fit curves obtained show a very good linearity in semi-log scale (black lines in Fig. 7) within the data range ($R^2 = 0.9936$) This behaviour corresponds to the simplest case of the empirical Rosin-Rammler equation,[37] indicating that for both sonication and ball-milling techniques, exfoliation proceeds through the formation of a distribution of random cracks that follow Poisson statistics.[6], [28] The fragmentation can be simply described as process mainly driven by external source and completely described by rupture-like breakup events.

4.14. Bibliography

[1]   J. N. Coleman, M. Lotya, A. O'Neill, S. D. Bergin, P. J. King, U. Khan, K. Young, A. Gaucher, S. De, R. J. Smith, I. V Shvets, S. K. Arora, G. Stanton, H. Y. Kim, K. Lee, G. T. Kim, G. S. Duesberg, T. Hallam, J. J. Boland, J. J. Wang, J. F. Donegan, J. C. Grunlan, G. Moriarty, A. Shmeliov, R. J. Nicholls, J. M. Perkins, E. M. Grieveson, K. Theuwissen, D. W. McComb, P. D. Nellist, and V. Nicolosi, "Two-Dimensional Nanosheets Produced by Liquid Exfoliation of Layered Materials," *Science (80-.).*, vol. 331, no. 6017, pp. 568–571, 2011.

[2]   E. Limpert, W. A. Stahel, and M. Abbt, "Log-normal distributions across the sciences: Keys and clues," *Bioscience*, vol. 51, no. 5, pp. 341–352, 2001.

[3]   L. H. Ahrens, "The lognormal distribution of the elements," *Geochlmlca Coemoehlmlca Acta*, vol. 5, pp. 49–73, 1957.

[4]   Y. Hernandez, V. Nicolosi, M. Lotya, F. M. Blighe, Z. Y. Sun, S. De, I. T. McGovern, B. Holland, M. Byrne, Y. K. Gun'ko, J. J. Boland, P. Niraj, G. Duesberg, S. Krishnamurthy, R. Goodhue, J. Hutchison, V. Scardaci, A. C. Ferrari, and J. N. Coleman, "High-yield production of graphene by liquid-phase exfoliation of graphite," *Nat. Nanotechnol.*, vol. 3, no. 9, pp. 563–568, 2008.

[5]   J. Russier, E. Treossi, A. Scarsi, F. Perrozzi, H. Dumortier, L. Ottaviano, M. Meneghetti, V. Palermo, and A. Bianco, "Evidencing the mask effect of graphene oxide: a comparative study on primary human and murine phagocytic cells," *Nanoscale*, vol. 5, no. 22, pp. 11234–11247, 2013.

[6]   W. K. Brown, R. R. Karpp, and D. E. Grady, "FRAGMENTATION OF THE UNIVERSE," *Astrophys. Space Sci.*, vol. 94, no. 2, pp. 401–412, 1983.

[7]   F. Hennrich, R. Krupke, K. Arnold, J. A. R. Stutz, S. Lebedkin, T. Koch, T. Schimmel, and M. M. Kappes, "The mechanism of cavitation-induced scission of single-walled carbon nanotubes," *J. Phys. Chem. B*, vol. 111, no. 8, pp. 1932–1937, 2007.

[8]   U. Khan, H. Porwal, A. O'Neill, K. Nawaz, P. May, and J. N. Coleman, "Solvent-Exfoliated Graphene at Extremely High Concentration," *Langmuir*, vol. 27, no. 15, pp. 9077–9082, 2011.

[9]   Z. Y. Xia, S. Pezzini, E. Treossi, G. Giambastiani, F. Corticelli, V. Morandi, A. Zanelli, V. Bellani, and V. Palermo, "The Exfoliation of Graphene in Liquids by Electrochemical, Chemical, and Sonication-Assisted Techniques: A Nanoscale Study," *Adv. Funct. Mater.*, vol. 23, no. 37, pp. 4684–4693, 2013.

[10]   L. H. Li, Y. Chen, G. Behan, H. Z. Zhang, M. Petravic, and A. M. Glushenkov, "Large-scale mechanical peeling of boron nitride nanosheets by low-energy ball milling," *J. Mater. Chem.*, vol. 21, no. 32, pp. 11862–11866, 2011.

[11]   "Scanning Probe Image Processor, version 2.0000, Image Metrology A/S, Lyngby, Denmark." .

[12] U. Khan, A. O'Neill, H. Porwal, P. May, K. Nawaz, and J. N. Coleman, "Size selection of dispersed, exfoliated graphene flakes by controlled centrifugation," *Carbon N. Y.*, vol. 50, no. 2, pp. 470–475, 2012.

[13]   A. Schlierf, H. F. Yang, E. Gebremedhn, E. Treossi, L. Ortolani, L. P. Chen, A. Minoia, V. Morandi, P. Samori, C. Casiraghi, D. Beljonne, and V. Palermo, "Nanoscale insight into the exfoliation mechanism of graphene with organic dyes: effect of charge, dipole and molecular structure," *Nanoscale*, vol. 5, no. 10, pp. 4205–4216, 2013.

[14]   H. Yang, Y. Hernandez, A. Schlierf, A. Felten, A. Eckmann, S. Johal, P. Louette, J. J. Pireaux, X. Feng, K. Muellen, V. Palermo, and C. Casiraghi, "A simple method for graphene production based on exfoliation of graphite in water using 1-pyrenesulfonic acid sodium salt," *Carbon N. Y.*, vol. 53, pp. 357–365, 2013.

[15]   V. Palermo, "Not a molecule, not a polymer, not a substrate... the many faces of graphene as a chemical platform," *Chem. Commun.*, vol. 49, no. 28, pp. 2848–2857, 2013.

[16] M. Lotya, A. Rakovich, J. F. Donegan, and J. N. Coleman, "Measuring the lateral size of liquid-exfoliated nanosheets with dynamic light scattering," *Nanotechnology*, vol. 24, no. 26, p. #265703, 2013.

[17]   P. Gentile, J. Eymery, F. Gustavo, P. Mur, J. M. Hartmann, and P. Besson, "STM study of ultra-thin (< 2 nm) silicon oxide," *J. Non. Cryst. Solids*, vol. 322, no. 1–3, pp. 174–178, 2003.

[18]   A. Liscio, "Scanning Probe Microscopy beyond Imaging: A General Tool for Quantitative Analysis," *ChemPhysChem*, vol. 14, no. 6, pp. 1283–1292, 2013.

[19]   M. Morita, T. Ohmi, E. Hasegawa, M. Kawakami, and M. Ohwada, "GROWTH OF NATIVE OXIDE ON A SILICON SURFACE," *J. Appl. Phys.*, vol. 68, no. 3, pp. 1272–1281, 1990.

[20]   A. Liscio, G. P. Veronese, E. Treossi, F. Suriano, F. Rossella, V. Bellani, R. Rizzoli, P. Samorì, and V. Palermo, "Charge transport in graphene-polythiophene blends as studied by Kelvin Probe Force Microscopy and transistor characterization," *J. Mater. Chem.*, vol. 21, no. 9, pp. 2924–2931, 2011.

[21]   J. Frederick, *Statistical Methods In Experimental Physics (2Nd Edition)*. Singapore: World Scientific Publishing Co Pte Ltd, 2006.

[22]   M. Kostoglou and A. J. Karabelas, "A study of the collisional fragmentation problem using the Gamma distribution approximation," *J. Colloid Interface Sci.*, vol. 303, no. 2, pp. 419–429, 2006.

[23]   M. A. Fortes and P. N. Andrade, "A MODEL OF FRAGMENTATION BY

NONINTERSECTING CRACKS," *J. Appl. Phys.*, vol. 64, no. 10, pp. 5157–5160, 1988.

[24] G. M. Kondolf and A. Adhikari, "Weibull vs. lognormal distributions for fluvial gravels," *J. Sediment. Res.*, vol. 70, no. 3, pp. 456–460, 2000.

[25] Z. Cheng and S. Redner, "Scaling Theory of Fragmentation," *Phys. Rev. Lett.*, vol. 60, no. 24, pp. 2450–2453, 1988.

[26] N. A. Kolmogorov, "Uber das Logarithmisch normale Verteilungsgesetz der Dimensionen der Teilchen bei Zerstuckelung," *Dokl. Akad. Nauk. SSSR*, vol. 31, 1941.

[27] K. Hosoda, T. Matsuura, H. Suzuki, and T. Yomo, "Origin of lognormal-like distributions with a common width in a growth and division process," *Phys. Rev. E*, vol. 83, no. 3, 2011.

[28] D. L. Turcotte, "FRACTALS AND FRAGMENTATION," *J. Geophys. Res. Earth Planets*, vol. 91, no. B2, pp. 1921–1926, 1986.

[29] Y. G. Yao, Z. Y. Lin, Z. Li, X. J. Song, K. S. Moon, and C. P. Wong, "Large-scale production of two-dimensional nanosheets," *J. Mater. Chem.*, vol. 22, no. 27, pp. 13494–13499, 2012.

[30] S. Hansen, D. V Khakhar, and J. M. Ottino, "Dispersion of solids in nonhomogeneous viscous flows," *Chem. Eng. Sci.*, vol. 53, no. 10, p. 1803–+, 1998.

[31] S. Los, L. Duclaux, L. Alvarez, L. Hawelek, S. Duber, and W. Kempinski, "Cleavage and size reduction of graphite crystal using ultrasound radiation," *Carbon N. Y.*, vol. 55, pp. 53–61, 2013.

[32] A. Catheline, L. Ortolani, V. Morandi, M. Melle-Franco, C. Drummond, C. Zakri, and A. Penicaud, "Solutions of fully exfoliated individual graphene flakes in low boiling point solvents," *Soft Matter*, vol. 8, no. 30, pp. 7882–7887, 2012.

[33] C. J. Shih, S. C. Lin, R. Sharma, M. S. Strano, and D. Blankschtein, "Understanding the pH-Dependent Behavior of Graphene Oxide Aqueous Solutions: A Comparative Experimental and Molecular Dynamics Simulation Study," *Langmuir*, vol. 28, no. 1, pp. 235–241, 2012.

[34] O. M. Marago, F. Bonaccorso, R. Saija, G. Privitera, P. G. Gucciardi, M. A. Iati, G. Calogero, P. H. Jones, F. Borghese, P. Denti, V. Nicolosi, and A. C. Ferrari, "Brownian Motion of Graphene," *ACS Nano*, vol. 4, no. 12, pp. 7515–7523, 2010.

[35] P. B. R. V. Gorbachev, I. Riaz, R. R. Nair, R. Jalil, L. Britnell, B. D. Belle, E. W. Hill, K. S. Novoselov, K. Watanabe, T. Taniguchi, A. K. Geim, "Hunting for Monolayer Boron Nitride: Optical and Raman Signatures," *Small*, vol. 7, no. 4, pp. 465–468, 2011.

[36] N. M. Pugno, "The design of self-collapsed super-strong nanotube bundles," *J. Mech. Phys. Solids*, vol. 58, no. 9, pp. 1397–1410, 2010.

[37]   J. J. Gilvarry, "Fracture of Brittle Solids. I. Distribution Function for Fragment Size in Single Fracture (Theoretical)," *J. Appl. Phys.*, vol. 32, no. 3, p. 391, 1961.

Chapter 5

Graphene Exfoliation with Organic Dyes

5.1. Introduction
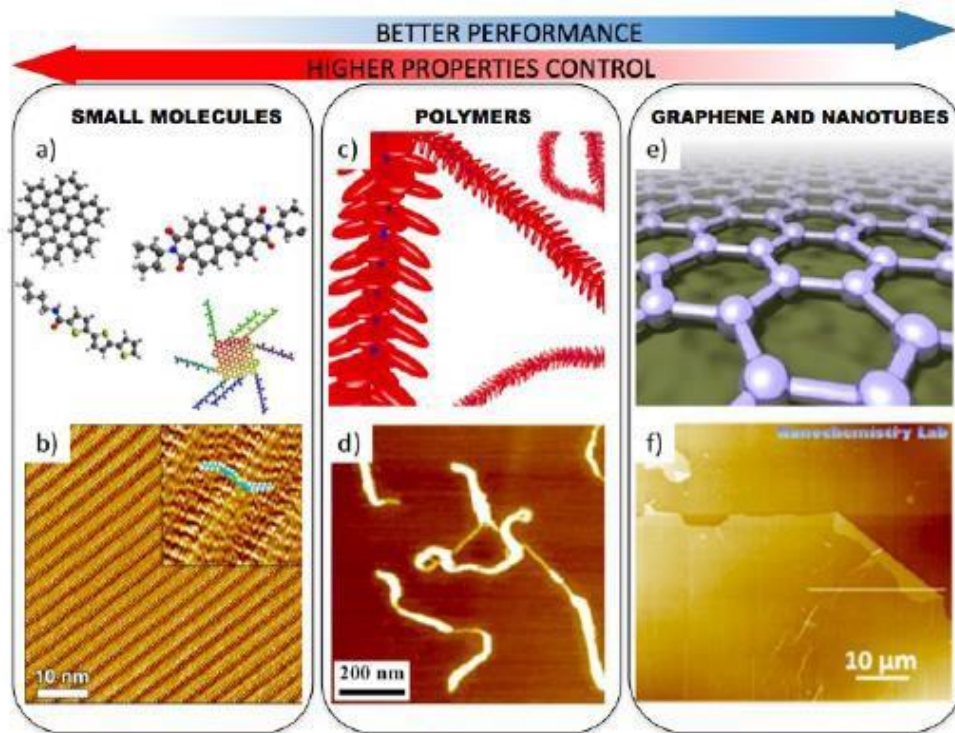
Fig. 1: Schematic representation and scanning probe microscopy images of different classes of carbon-based materials for (opto)electronic applications: a, b) small molecules[1], c, d) polymers[2], e, f) Graphene[3], [4].

A main advantage of graphene as compared to other nano-fillers like carbon nanotubes is that it can be produced in different ways, using top-down as well as bottom-up approaches[5]. Bottom-up, atom-by-atom growth of high quality graphene can be obtained by chemical vapour deposition (CVD) of hydrocarbons on copper or nickel[6]. Wafer-scale production of graphene in this way is now routinely achievable.

Graphene dispersions shall instead be obtained at low cost and kilograms scale by liquid exfoliation of graphite (LPE), as recently demonstrated by Coleman and co-workers [7]. This method is the most promising one for industrial applications, as example to produce graphene as

nano-additive in polymer composites,[8], [9] or ultra-light foams as electrodes for energy storage or catalysis[10].

The principle of LPE is simple: just add graphite powder to the right solvent and apply ultrasound or high-speed mixing for enough time. The effect of cavitation bubbles or mixing will create shear forces able to detach graphene sheets from the graphite powder;[11] at the same time, molecules present in solution will adsorb on the graphene sheets, stabilizing them and avoiding restacking[12]. A wide range of different molecules has been used up to now for LPE. These shall generally be divided in two main classes:

A) organic solvents, whose surface tension matches the surface energy of graphite. [13] The most suitable media for liquid formulations used at the moment are high-boiling solvents such as dimethylformamide (DMF) and *N*-methyl-2-pyrrolidone (NMP), which are though difficult to remove from the polymer composite, in this way affecting its properties.

B) water-based surfactants that have amphiphilic behaviour, i.e. have an hydrophilic head, which favours solubility and an hydrophobic tail, which favours adsorption on graphene.[2], [3] Besides the use of "conventional" aliphatic surfactants, stable dispersions of graphene in water have also been obtained using small polyaromatic surfactants, molecules featuring a hydrophobic, aromatic core, able to interact with graphene through π-π stacking, and hydrophilic side groups[12], [14], [15]. A major advantage of this approach is that it shall use, as surfactants, cheap dyes that are already well established for the large-scale compounding of polymers, such as industrial additives and colorant dyes, able to exfoliate and stabilize graphene in water. Noteworthy, these molecules demonstrated to exfoliate effectively not only graphene but also a wide range of different 2-dimensional materials (2DM) such as boron nitride, tungsten disulfide and molybdenum sulphides, selenides and tellurides[16].

Water, even if being the most common and less polluting solvent commonly used, is not the ideal solvent for all kinds of applications. Its boiling point is much lower than the one of DMF (b.p.=153°C) or NMP (b.p.=202°C), but it is anyhow difficult to remove quantitatively. It shall

remain in traces, creating, as example, charge traps and oxidative defects in materials for electronics;[17]in composites application, water-based dispersions are not miscible with the great majority of common polymers e.g. polypropylene (PP), polyethylene terephthalate (PET), polyvinyl chloride (PVC) etc.

Alternatives to NMP and DMF have been demonstrated to process graphene with semiconducting polymers, as example exfoliating graphene with dichlorobenzene (DCB), but this solvent has anyhow a boiling point of 189°C[18]. For an effective, technologically competitive application of 2DM as additives in composites for electronics or mechanics it will be needed to process graphene in low-boiling volatile solvents that are commonly used in organic synthesis labs and in polymer processing for organic electronics or composites such, as example, chloroform (CHCl3) or tetra-hydro-furan (THF). The use of amphiphilic surfactants is not suitable to solubilize graphene in organic solvents, whose polarity is typically low. Thus, we explored a different strategy using molecules that feature an extended polyaromatic core to have π-π interactions with graphene, and flexible side groups with low but tunable polarity that makes these molecules soluble in a wide range of organic solvents (fig. 2).
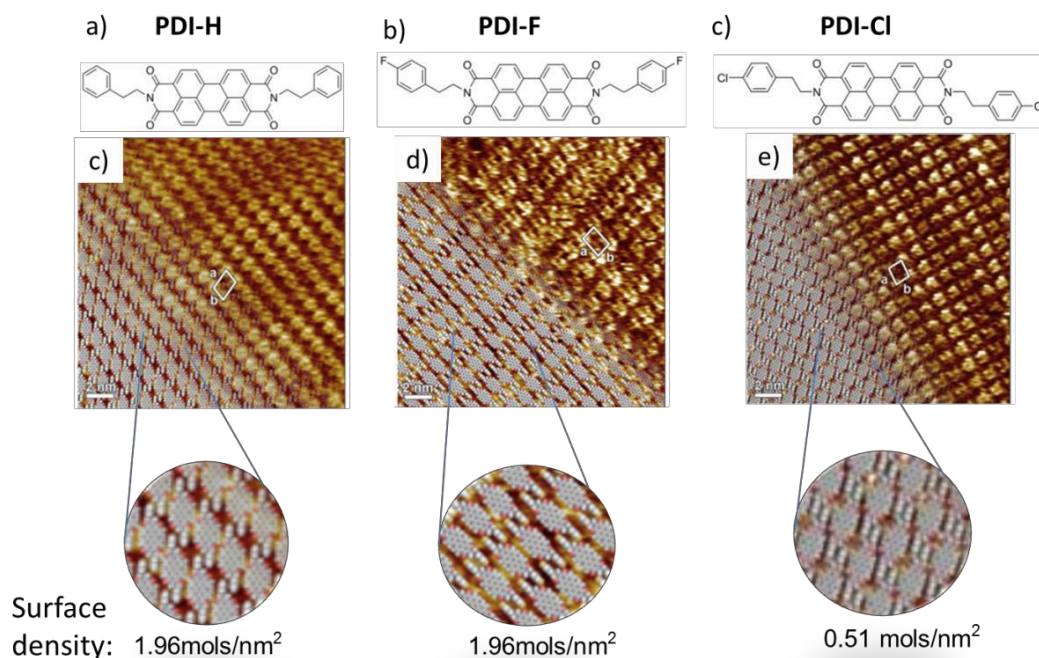
Fig.2: Molecular structures of a) PDI-H, b) PDI-F, c) PDI-Cl along with their STM images where highly ordered 2D supramolecular architectures are formed on HOPG surface.

As aromatic core we used a perylene dimide (PDI) dye, a standard building block of organic semiconductors used in electronics and photovoltaics applications,[19]–[26] and also a widely used dye for textile applications, industrial paints as well as protein tagging[27].

As side groups we used relatively flexible phenylethyl moieties that are able to render the perylene core soluble in many organic solvents. Due to the complex interplay of supramolecular interactions of the molecules with the solvent and with each other[28], the self-assembly and the solubility of the molecules can be tuned significantly already changing one single atom of the phenyl ring.

Thus, we performed a study on the exfoliation of graphene by systematic comparison of different exfoliating molecules. The only difference among the molecules tested was one single atom in the molecular structure. In particular, we used a perylene core with side ethyl-phenyl groups, where the side groups had a single hydrogen, or fluorine, or chlorine atom in *para* position.This single change of molecular structure is enough to tune the polarity of the flexible side chains and its self-assembly and solubility behaviour without perturbing the optoelectronic properties of the perylene core.

We demonstrate that all the molecules tested are able to stabilize few layers of graphene flakes in dispersion to give graphene-organic hybrids (GOH). Their different supramolecular behaviour influences significantly their interaction with graphene, yielding anyhow GOH with good stability on high- and low-boiling solvents, and good processability with polymers as electrically conducting additives.
The materials and molecules studied have been extensively characterized at the nanoscale using scanning tunnelling microscopy (STM), Atomic Force Microscopy (AFM) and scanning electron microscopy (SEM). The details of PDI-graphene interaction at atomic scale were also modelled by force-field calculations, to estimate the contributions of the different parts of the molecules to the interactions, and the effects of the single atom differing in all the molecules.

The stability of such GOH in volatile solvents allows an easier use for typical target applications of graphene-based materials. To demonstrate this, we used the GOH as thin conductive coatings on the surface of polymer sheets or as active layers field-effect transistors based on the GOH.

5.2. Experimental details

All molecules used are commercial, and were obtained from Sigma Aldrich. for simplicity, the molecules are termed as PDI-H, PDI-F and PDI-Cl, where PDI stands for the perylene diimide core and the letter corresponds to the final end atom of the phenylethyl sidegroups.

Detailed chemical formulas of the molecules used are: 1,3,8,10(2*H*,9*H*)-Tetraone, 2,9-bis(2-phenylethyl)anthra[2,1,9-*def*:6,5,10-*d'e'f'*]diisoquinoline, named for simplicity PDI-H. 2,9-Bis[2-(4-fluorophenyl)ethyl]anthra[2,1,9-*def*:6,5,10-*d'e'f'*]diisoquinoline-1,3,8,10(2*H*,9*H*)tetrone , named for simplicity PDI-F. 2,9-Bis[2-(4-chlorophenyl)ethyl]anthra[2,1,9-*def*:6,5,10-*d'e'f'*]diisoquinoline 1,3,8,10(2*H*,9*H*)tetrone, named for simplicity PDI-Cl.

Graphite powder and PDI were purchased from Sigma Aldrich and used as received. Graphite suspensions were prepared with the same initial concentrations (3 mg/mL) and dissolved in 0.1 mg/mL the perylene solutions. The solutions were sonicated for 4.5 hours at medium power in a temperature-controlled sonication bath (Elmasonic P70). In order to prevent any evaporation from the low-boiling point solvents as the temperature inside the sonication bath was kept fixed at $50^{o}C$ during sonication. After sonication process, the dispersions were centrifuged at 2200 rpm for 45 minutes in a Heraeus centrifuge (Omnifuge 2 RS) in order to eliminate the macroscopic, non-exfoliated graphite particles. Absorption measurements were recorded using an Agilent Cary 7000 Universal Measurement Spectrophotometer (UMS) in a wavelength range of 300-800 nm. The studied dispersions were then spin-coated on SiOx substrates using a Laurell WS-650MZ-23NPB Spin Coater. Before use, the SiOx substrates were sonicated at $60^{o}C$ for 15 min in Acetone and Isopropyl alcohol (IPA), followed by treatment in a Diener Plasma Cleaner to remove any remaining organic material on the SiOx surface.

AFM Topography measurements were performed using a Digital Instruments AFM (NT-MDT), using cantilevers in a semi-contact (tapping mode), (model RTESP, material: 1-10 Ohm cm phosphorus (n) doped Si, f0: 27-309kHz, k: 20-80 N m^{-1}; from Bruker). Kelvin Probe Force Microscopy (KPFM) images were taken using an NT-MDT instrument, the samples were fixed using silver paste to Silicon substrates, equipped with a spring to provide electrical contact. Images from Scanning Electron Microscopy were taken with a ZEISS 1530 instrument. The Scanning Tunnelling Microscopy (STM) study of the self-assembly in two dimensions was performed using a Veeco scanning tunnelling microscope (multimode Nanoscope III, Veeco) at the interface between highly oriented pyrolitic graphite (HOPG) and a supernatant solution. Dispersions of investigated molecules were applied to the basal plane of the surface. For STM measurements the substrates were glued on a magnetic disk and an electric contact was made with silver paint (Aldrich Chemicals). The molecules were dissolved in chloroform and then diluted in 1-phenyloctane 0.08 mM; a drop of solution was casted on the sample just before the measurement.

The STM tips were mechanically cut from a Pt/Ir wire (90/10, diameter 0.25 mm, commercially available from Goodfellow.uk). The raw STM data were processed through the application of background flattening (2nd degree least square polynomial fitting on both X and Y directions) and the drift was corrected using the underlying graphite lattice as a reference. The latter lattice was visualized by lowering the bias voltage to 20 mV and raising the current to 65 pA. All of the models were minimized with Chem3D at the MM2 level and subsequently rendered with QuteMol.[M. Tarini, P. Cignoni, C. Montani, Leee T Vis Comput Gr 2006, 12, 1237.]

Commercial, PVC sheets and rubber wires were used to create the G-PDI-x composites. The PVC sheets were cut in 3x3 cm dimensions. The membranes swelled in a bath of 8 ml of Chloroform. During the swelling process, the bath was sealed to prevent any evaporation of the solvent that could modify the parameters of the process. The same procedure was followed for the Rubber composite, although this time the dimension of the rubber was at 6x1cm and it swell at a constant volume of 10 mL.

The adsorption of PDI molecules on the graphene surface was performed using MM/MD simulation methods. The GROMACS molecular dynamics package was used for all the calculations described in this study. The simulated model system was built by placing a single molecule on an infinite graphene surface within a simulation box, which was then with solvent molecules.

Fluorescence Quenching Microscopy (FQM) was performed on a Nikon TE2000-U inverted fluorescence microscope with the Exfo X-cite illumination system using an ET-GFP filter cube (FITC/Cy2, Chroma Technology Corp.). The images were taken by a monochrome interline CCD camera (Photometrics, CoolSNAP HQ^2).

5.3. Results

Fig. 2a, b, c shows the molecular structure of the molecules under study. We know from previous works that a key stage of graphite exfoliation by any kind of surfactant is the adsorption of the molecule on the graphene surfaces, to stabilize them in solution[29]. Thus, this stage was studied at atomic, nanometric and macroscopic scale.

5.3.1. Modelling of PDI-graphene interactions at atomic scale

The adsorption of single molecules on a graphene sheet was first studied using force fields simulations (see SI for details). Each of the three molecules was positioned on the surface of graphene in a box of solvent molecules modelled explicitly, and simulated for a total of 105 ns. Chloroform was chosen as a model solvent.
Fig. 3a,b,c shows some snapshots, taken from simulations of PDI-F on graphene, and the statistics showing the average distance between the phenyl rings and the graphene for the different PDI.
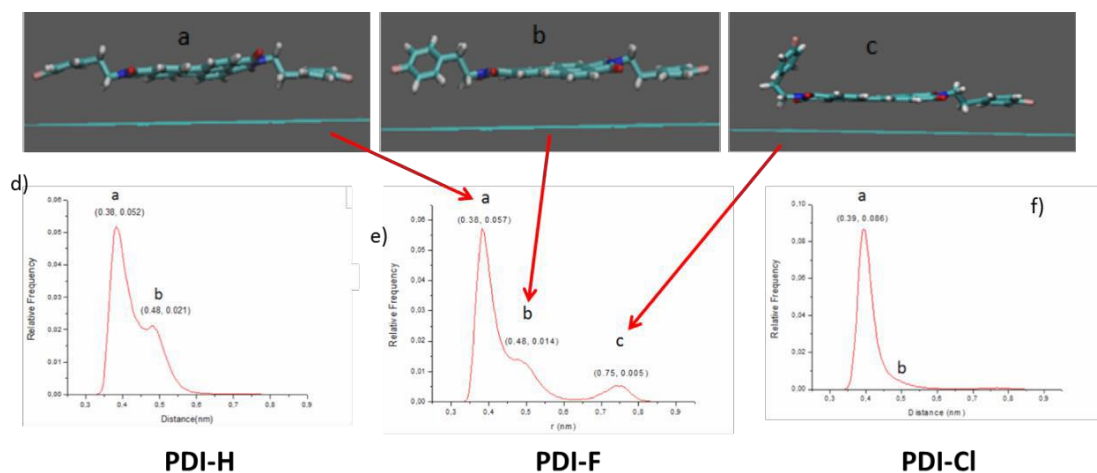
Fig. 3: Population distribution of conformers for PDI-F on graphene in chloroform when a) is parallel to graphene, b) the phenyl rings rotate perpendicular to the graphene surface and c) the phenyl ring folds onto the PDI core. d,e,f) Histogram distribution of the average distance from graphene of the side-groups, measured for each molecule. Numbers in parenthesis show the dihedral angles ϕ and φ of the sidegroups.

5.3.1.1 Conformation Analysis

To study the conformational dynamics of PDI molecules on the surface of graphene, the equilibration of PDI molecules on the surface of graphene, in chloroform, was simulated using force field method. The configuration of the molecules on a surface can be defined by the relative orientation of the different parts of the molecules with respect to the surface. In a previous MD simulation we have observed that the perylene core of the molecules remains, essentially, parallel to the graphene surface, while the two benzene fragments and the alkyl linkers (-CH_2CH_2)- are relatively flexible and change their orientations.

To get the prominent equilibrium conformations of the molecules, the simulations for each molecule were started from three different configurations on the surface, which were achieved by considering the anti and syn conformers of the PDI molecules in respect of the two alkyl linkers. Keeping the perylene core parallel to the surface, the syn conformer can be placed on the surface either with both alky groups pointing down towards the surface (syn-down) or both pointing up away from the surface (syn-up), while for the anti-conformer there is only one way in which one alkyl group points towards the surface while the other away (see the structures in Figure 4).

These orientations also result in that the benzene groups on the other end of the alky linkers going closer towards the surface or away. The other option that the alkyl group be horizontal with respect to the surface-with the perylene core parallel-are ruled out again because optimizations of the structures on the surface of graphene have shown that the perpendicular conformations are more stable. Hence, there were three possible starting conformers taken for the simulations here after named as Syn-up, Anti and Syn-down.
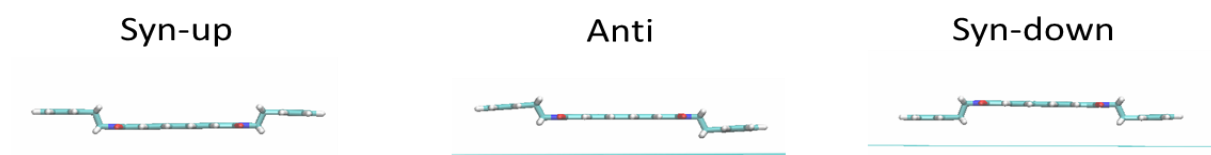
Fig 4: The three starting configurations of the PDI molecules for the MD simulations.

Long MD simulations (105 ns) were performed on these structures in chloroform and the conformation of the molecules due to the alkyl rotation was analyzed. This was done by following the evolution of the torsional angle along the bond connecting the alkyl group with the perylene core (Figure 5). Due to the presence of the surface, equal-magnitude rotations in opposite directions-from zero-of this dihedral no more result in equivalent structures. They can mean either going to wards or away from the surface-two different operations. To distinguish between the two operations, we fixed different signs for the torsional rotations that would result in each operation. This was achieved by taking the measurement of the torsional angle from a fixed direction at a fixed orientation of the molecule (Figure 5). When the main axis of the molecule is perpendicular to the screen (Figure 5 (b)), the measurement of dihedral angle is taken only from the carbon atom of the left carbonyl group of the perylene core to the first carbon atom of the alkyl linker. This way the angle becomes positive only when the alkyl goup is above the plane of the perylene core, and negative when bellow.

ψ_1

ψ_2

+ve

-ve

(a)

(b)
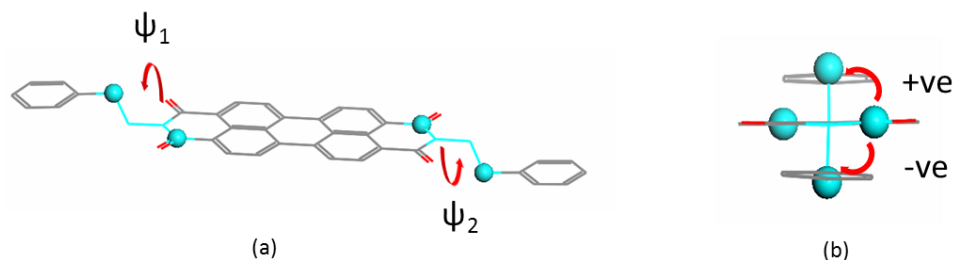
Fig 5: Schematics showing the torsional angles taken for the conformational analysis of the PDI molecules with respect to the alkyl linkers (a) and an orthographic front view, with the main axis of the PDI molecule perpendicular to the screen, showing the measurement protocol (b). A dihedral angle is measured between the carbon atom of the left carbonyl group (when the molecule is in the (b) alignment) and the second carbon atom of the alkyl linker which are shown by blue spheres.

While the PDI molecules may land on the graphene surface in the three different configurations, in respect of the alkyl linkers, the benzene fragments may assume different possible alignments with respect the surface. For example, in the Anti configuration one benzene ring should be closer to the surface than the other one, while in the Syn-up configuration both may be, more or less, at the same distance. In addition, the benzene fragments can rotate along the alkyl linkers and attain different orientations with respect to the perylene core and the graphene surface. To get a complete picture of the conformations of the PDI molecules, the orientations of each benzene fragment were analyzed by following the rotation of the ring along the bond connecting it with the alkyl linker and along the C-C bond of the linker defined by the torsional angles ϕ and φ respectively (see Figure 6). The dihedral angle ϕ controls the rotation of the plane of the benzene ring along a horizontal axis which may results, for example, in a parallel or tilted orientation with respect to the graphene surface. The other angle φ controls the rotation along a vertical axis which results in the cis-trans orientation of the benzene fragment with respect to the perylene core. The analyses on all the dihedral angles mentioned above were made only for the last 20 ns frames of the simulations.

Fig 6: Schematics showing the torsional angles which were analyzed to follow the orientation of the benzene fragments.

To identify the prominent equilibrium conformation of the PDI molecules in respect of the alkyl linkers, the statistical distribution of the two dihedral angles ψ_1 and ψ_2 were plotted. The resulting 2D distribution plots are given in Figure 6.

According to the definition of the angle measurement, a negative sign indicates that the alkyl and the benzene fragments are closer to the surface (pointing down) and an angle with positive sign indicates they are away from the surface (pointing up), i.e.; a point in the distribution plots with (-,+) or (+,-) represents an Anti configuration, (-,-) represents a Syn-down configuration and (+,+) represents a Syn-up configuration. From the distribution plots it can be seen that for all molecules the angles are localized in narrow regions which shows that there were no major orientational change of the alkyl groups during the last 20 ns period of the simulations, indicating the relative stability of the resulting conformers. However, some of these resulting structures are different form their corresponding starting structures. For all the three molecules, the Syn-down configuration is not observed in the resulting structures. The starting Syn-dow configuration turns to the Anti configuration. In the case of PDI-H and PDI-F molecules the Anti and the Syn-up configurations did not change throughout the MD simulations whereas for PDI-Cl the Anti starting configuration results in the Syn-up configuration while the Syn-up one remains the unchanged. The results may indicate that the Syn-down configuration is the list stable for all the three molecules, while the Syn-up and Anti configurations may exist in dynamic equilibrium for the PDI-H and PDI-F molecules. It was also observed that in the case of PDI-Cl, the Anti to Syn-up transition happens at the early stage of the MD simulations, which may suggest that the Syn-up configuration is the most favored for PDI-Cl.

The statistical distributions of the two torsional angles ϕ and ϕ were also plotted to identify the possible orientations of the benzene rings. The analyses were made on the already identified prominent configurations, in respect of the alkyl linkers, of the PDI molecules discussed above. For PDI-H and PDI-F, the Anti and Syn-up configurations were taken, while for PDI-F only the Syn-up configuration is taken.
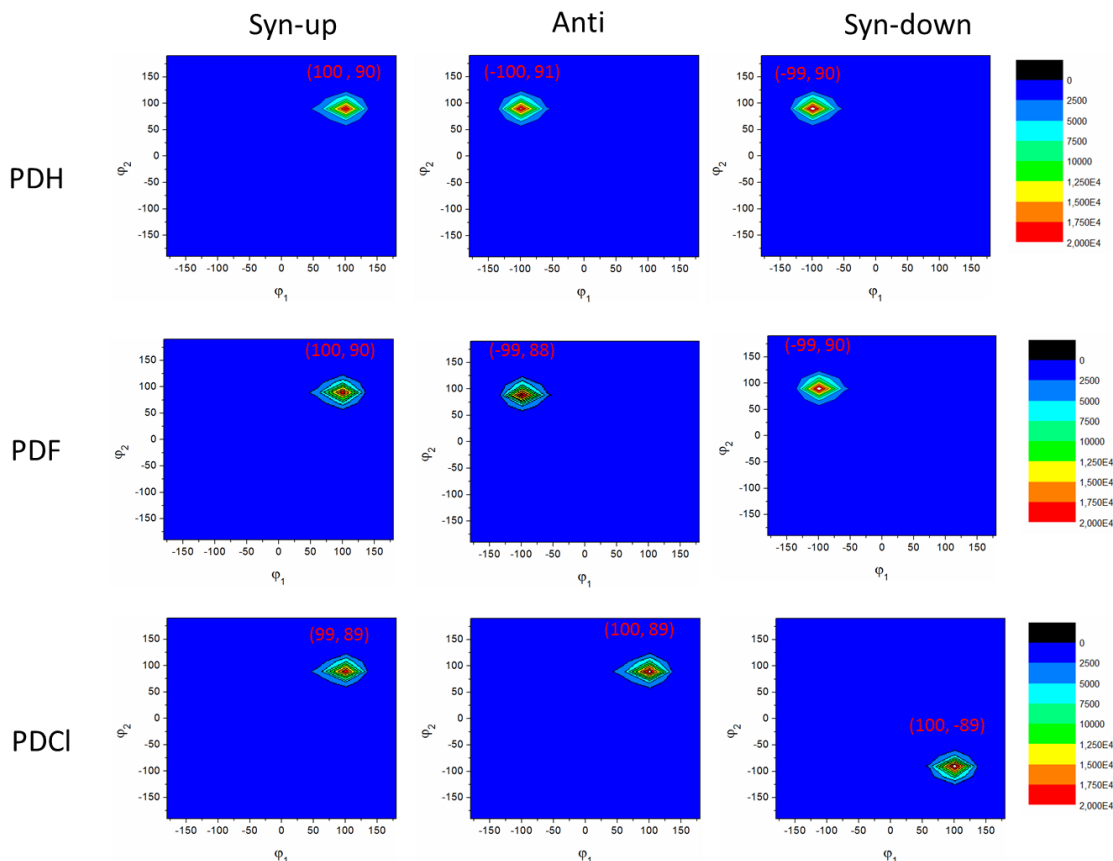
Fig. 7: 2D distribution plots of the torsional angles ψ_1 and ψ_2 of the PDI molecules computed from the resulting structures of the last 20 ns period of the MD simulations done on three starting structures of each molecule (indicated by the names on the top of the plots).

In the case of the Anti configuration of PDI-F, three typical conformations with respect to the benzene rings were identified-a,b and c. The four bright red regions, shown by letter a, in the 2D distribution for the benzene on the upward pointing linker (Fig. 8 (A) Ring-up) are structurally equivalent. They are rotational mirror images. They correspond to the parallel alignment ($\phi \sim$ 90°) of the benzene ring with respect to the surface which results in a structure like a (Figure. 8

(B)). The light green regions, shown by letter b, indicate significant deviation from parallel orientation of the benzene ring with respect to the surface to result in a tilted orientation as in structure b in Figure. 8 (B). For structures like a and b the torsional angle ϕ has values $170° \pm 20°$ (-170° and 170° are structurally equivalent, and also 190° is equivalent to 170°) which indicates more or less trans conformations, in respect of the benzene ring and the perylene core, along the alkyl linker. The light blue regions around (-70, -70) and (110, -70) indicate that at these conformations, the benzene ring is closer to a syn alignment with respect to the perylene core. In such structures the benzene ring is aligned almost above the pyrylene core and further from the surface as in structure **c** in Figure 8 (B). The population of such conformations, however, is much less than the other two indicating its unfavorableness. The distribution of the torsional angles for the ring closer to the surface (Figure 8 (A) Ring-down) has also four bright regions. The values for ϕ are localized around 93° and 89° which indicates a more or less parallel alignment of the ring with respect to the surface. But, the opposite sign angles for ϕ indicate that the ring is flipping up-side-down during the dynamics.
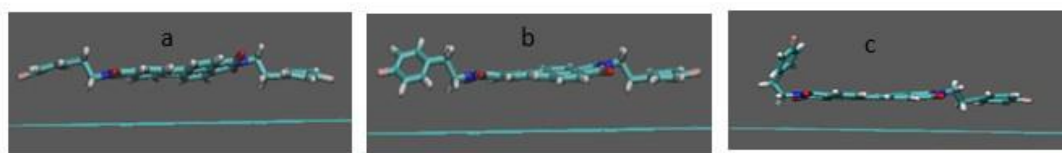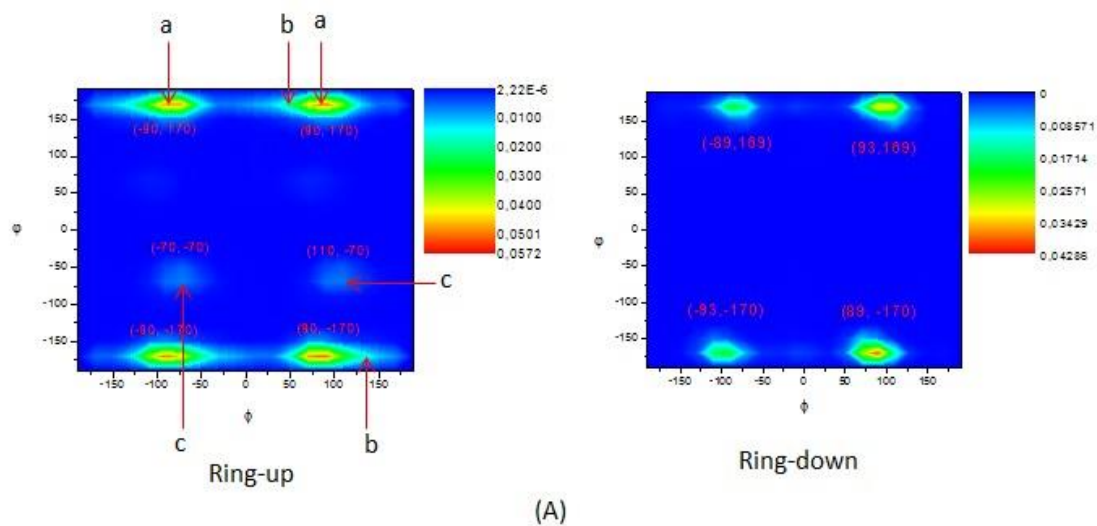
Fig. 8: Population distribution of conformers for PDI-F in respect of the benzene rings at the Anti configuration. (A) 2D distribution of the angles ϕ and ϕ, (Ring-up for the ring further from the surface and Ring-down for the one closer) (B) snapshots of prominent conformers).
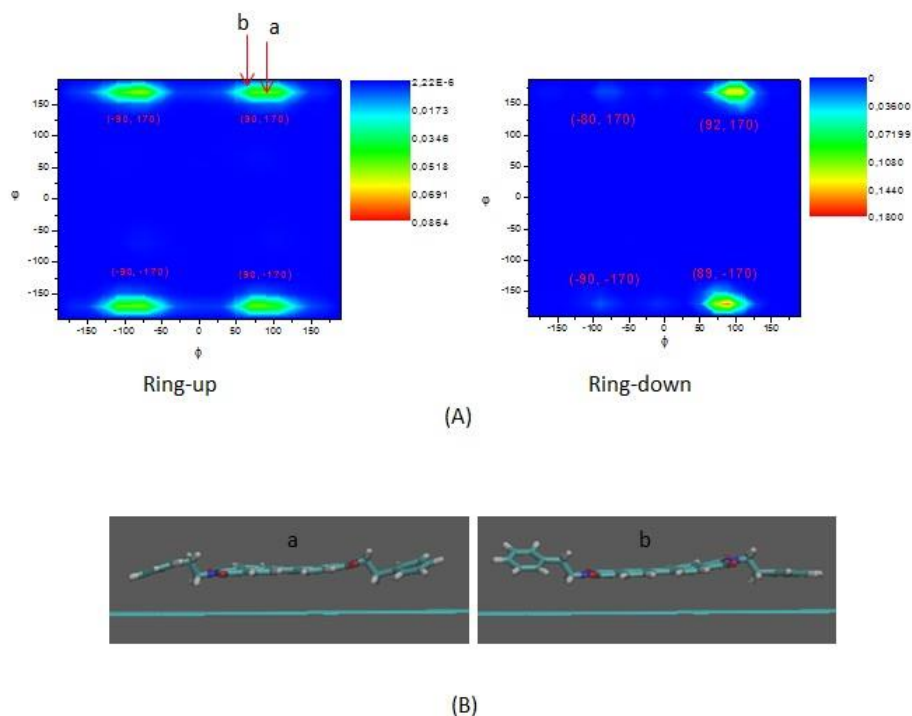
Fig. 9: Population distribution of conformers for PDI-H in respect of the benzene rings at the Anti configuration. (A) 2D distribution of the angles ϕ and φ, (Ring-up for the ring further from the surface and Ring-down for the one closer) (B) snapshots of prominent conformers).

Similarly, for the Anti configuration of PDI-H, the values for ϕ is predominantly occur around 90°, which indicates a more less parallel orientation of the benzene ring, with respect to the surface, like in structure a of Figure 9 (B). The next predominant structures at tilted orientations are also observed. However, unlike in the case of PDI-F, the least favored syn conformation of the benzene with respect to the perylene core is not observed. The ring closer to the surface stays almost parallel to the surface, like in the case of PDI-F, but with little frequency of up-side-down flipping.

In all the molecules, for the Syn-up configurations, the two benzene rings are seen to attain the predominant parallel and tilted orientations leading to structures with the two benzene rings at parallel-parallel, parallel-tilt and tilt-tilt orientations with respect to the surface (see Figures 10 through 12). In case of PDI-F and PDI-H, one of the rings attains the syn conformation with respect to the core, but again, with reduced probability.

Ring-I   (A)   Ring-II

(B)
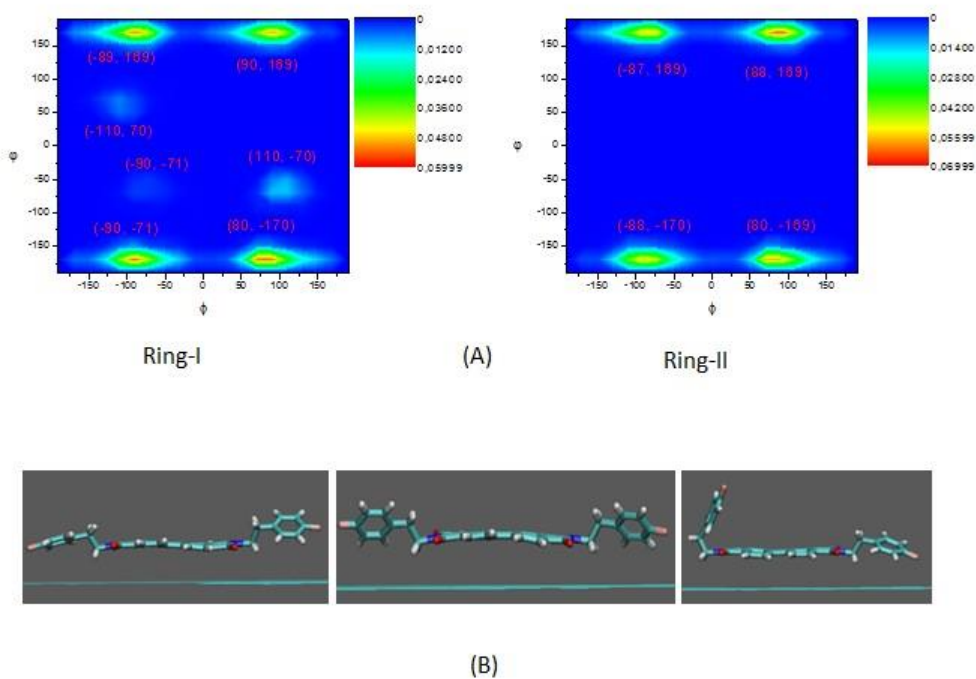
Fig. 10: Population distribution of conformers for PDI-F in respect of the benzene rings at the **Syn-up** configuration. (A) 2D distribution of the angles ϕ and ϕ, for the two rings. (B) Snapshots of prominent conformers.
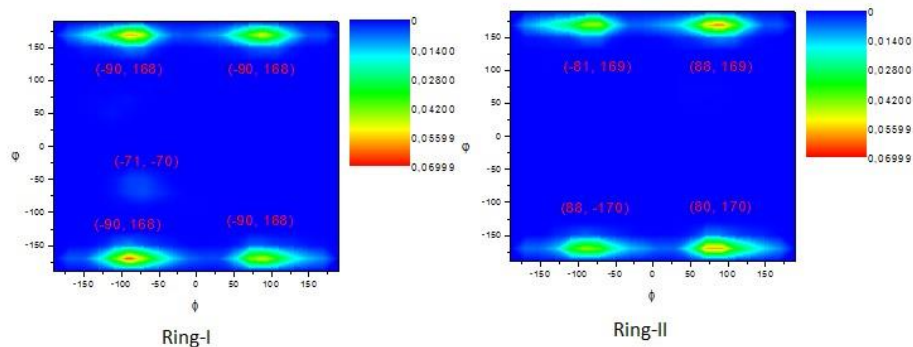
(A)
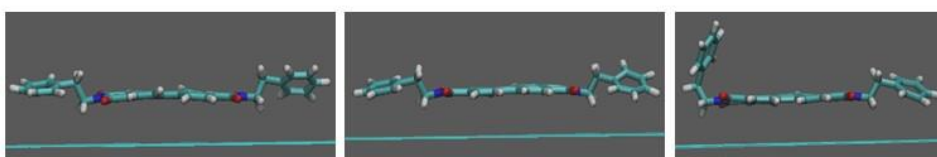
(B)

Fig. 11: Population distribution of conformers for PDI-H in respect of the benzene rings at the Syn-up configuration. (A) 2D distribution of the angles ϕ and ϕ, for the two rings. (B) Snapshots of prominent conformers.
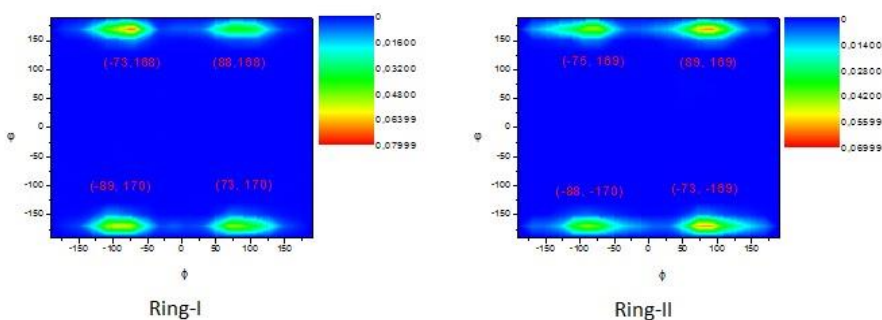
(A)
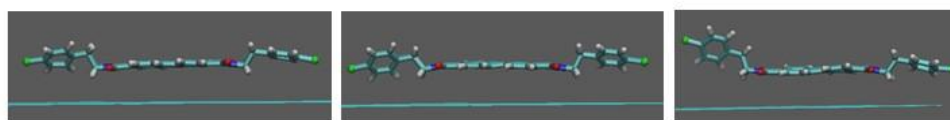
(B)

Fig. 12: Population distribution of conformers for PDI-Cl in respect of the benzene rings at the Syn-up configuration. (A) 2D distribution of the angles ϕ and ϕ, for the two rings. (B) Snapshots of prominent conformers.

Fig. 13 reports the calculated interaction with both the solvent and the graphene surface and the adsorption energy for each of the PDIs.
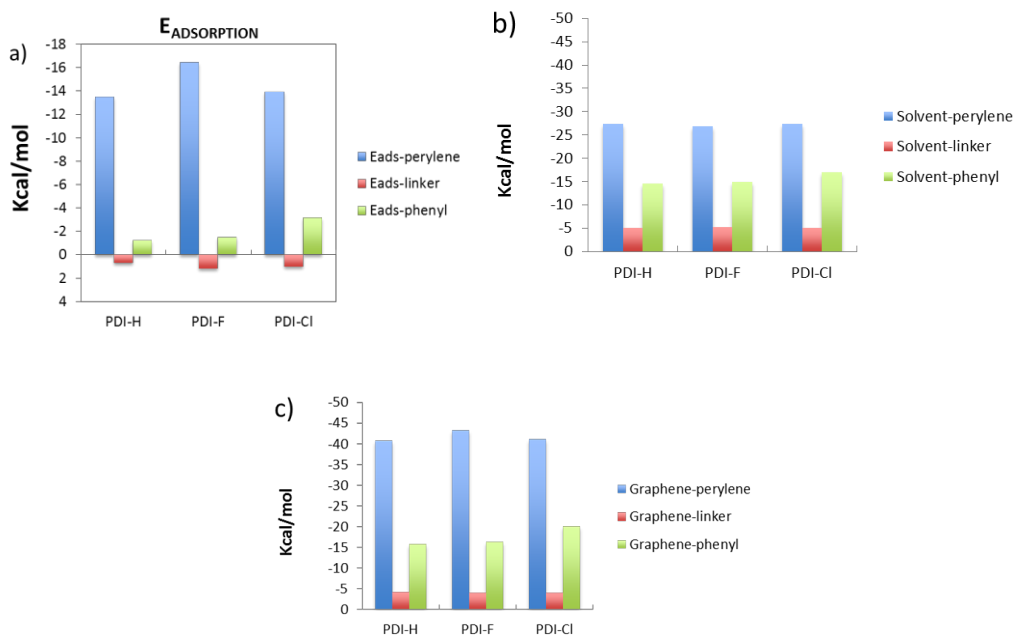
Fig.13: Different energy contributions for PDI-graphene and PDI-Chloroform interactions obtained from force-field calculations. Energies are given in kcal/mol.

Table 1 below reports the calculated interactions, due to Van der Waals or electrostatic interactions, of different parts of the molecules with graphene.

Molecules	Interaction	Solvent-perylene	Solvent-linker	Solvent-phenyl	Total
PDI-H	Van der Waals	-25,92 ± 2,16	-4,54 ± 0,65	-13,86 ± 1,45	-44,32
	Coulomb	-1,40 ± 0,48	-0,44 ± 0,27	-0,76 ± 0,50	-2,60
	Total	-27,32	-4,98	-14,62	-46,92
PDI-F	Van der Waals	-25,41 ± 2,1	-4,70 ± 0,65	-14,22 ± 1,47	-44,33
	Coulomb	-1,33 ± 1,18	-0,46 ± 0,24	-0,68 ± 0,54	-2,47
	Total	-26,74	-5,16	-14,90	-46,80
PDI-Cl	Van der Waals	-25,96 ± 2,14	-4,52 ± 0,64	-16,39 ± 1,58	-46,87
	Coulomb	-1,31 ± 1,04	-0,51 ± 0,26	-0,50 ± 0,41	-2,32
	Total	-27,27	-5,03	-16,89	-49,19

Table 1: Different energy contributions for PDI-graphene and PDI-Chloroform interactions separately from force-field calculations. Energies are given in kcal/mol.

The adsorption energies were estimated by taking the energy difference between two separately simulated systems which differ only in the relative position of the PDI molecule w.r.t. the graphene surface. In one of the systems the PDI was placed on the surface (adsorbed molecule), while on the other it was restrained in the solvent at a distace far enough to avoid its interaction with the surface (desorbed molecule).

As could be expected, all the molecules adsorbed preferentially with the perylene core flat on the substrate, while the side phenyl groups could assume more irregular, tilted configurations. However, the single differing atom in the side groups gave significantly different behaviours already for a single, isolated molecule adsorbed on graphene. Most of the interaction is due to the aromatic core, but the single differing H, F and Cl side atoms give also different adsorption energies on graphene for the side groups.

The phenyl rings interact significantly with graphene, and spend most of their time close to the surface, parallel to it, with an average distance of ~0.38 nm between graphene and the molecule

center of mass (peak *a* in fig. 3). In case of hydrogen (PDI-H) and fluorine (PDI-F) terminations, it is possible for the phenyl rings to rotate perpendicular to the surface increasing the distance to 0.48 nm (peak *b*); in particular, in PDI-F, the phenyl ring shall fold onto the PDI core (peak *c*). A more detailed description of the modelling results is available in Supporting Information (SI). Chlorine terminated rings interact much strongly with graphene, staying flat on the surface. Calculated interaction energy between side groups and graphene is 16.89 Kcal/mol for PDI-Cl, significantly larger than in the case of PDI-H and PDI-F .

5.3.2. PDI adsorption on graphite at nanometric scale

The study of single molecules adsorbed on graphene can be useful to understand basic behaviour and interactions, but cannot give insight into the collective behaviour of these self-assembling molecules.
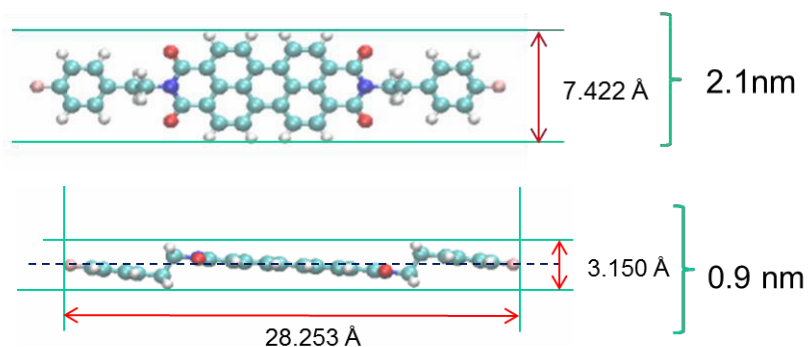
Fig. 14: Computational representation of a PDI molecule showing its width, length and height.

Thus, we studied the adsorption of the molecules on bulk graphite substrates using STM at the solid liquid interface. STM shows that all the molecules used are able to form a tightly packed, ordered lattice on graphite (Fig. 2 d,e,f and table 2). The packing of PDI-H (1.96 ± 0.16 nm^2/molecule) and PDI-F (2.1 ± 0.16 nm^2/molecule) is comparable, while PDI-Cl shows a significantly denser packing (1.67 ± 0.13 nm^2/molecule).

molecule	a (nm)	b (nm)	α (deg)	Area (nm²)	Surface density =1/A) mols/nm²
PDI-H	1.7	1.2	107	1.96	0.51
PDI-F	1.7	1.26	97	2.1	0.48
PDI-Cl	1.4	1.2	95	1.68	0.60

Table 2: Parameters of crystalline 2D packing of the three PDI on graphite as measured by STM

This denser packing is not due to steric hindrance, given that the chlorinated groups are larger and more bulky than the hydrogenated and fluorinated ones. This could be due to the different polarity of the chloro-phenylethyl moiety (2.56 Debye) that is significantly higher than the one of fluoro-phenylethyl (2.23 Debye) and of the non-functionalized one (0.42 Debye). However, PDI-F and PDI-H shows a similar packing on graphene even if the of the former has highly polar side groups and the latter has not. The different packing of PDI-Cl could be explained by a stronger interaction of the chlorinated side groups with graphene, in good agreement with the force fields calculations, which pushes towards having more molecules adsorbed on the surface regardless of the increased steric hindrance.

Overall, STM data show that all three molecules are able to interact strongly with graphite, forming ordered monolayers on it, even if with slightly different behaviour. Unfortunately, STM at the solid-liquid interface can only be performed in high-boiling solvents, so it is not useful to demonstrate interaction of molecules with graphite or graphene in, as example, low boiling solvents.

To overcome this issue, we studied interaction of the three PDIs with graphite in chloroform and THF using a "dye capture" technique already successfully used for water solutions [15], [29]

5.3.3. PDI adsorption on graphite at macroscopic scale

In this experiment, we studied the relative removal of the different dyes from solution when incubated with increasing amounts of graphite powder. Our approach is similar to what used in the measurement of Brunauer–Emmett–Teller (BET) specific surface area of materials, monitoring the change of pressure in a gas due to adsorption on the surface, and in tests for water purification using organic dyes in water[30].

Typically, in this latter approach the concentration of dye in the water is varied while keeping constant the amount of available sample surface (e.g. graphite). This can give spurious effects in our case due to concentration-dependents aggregation of these self-assembling dyes, such as the formation of H- or F-aggregates[27]. For this reason, in our experiment we varied the amount of graphite powder while keeping fixed the PDI concentration.

We underline that, at this stage, no sonication was applied to the system and no exfoliation process took place, so the experiment is a plain measure of the relative affinity of the different molecules with graphite[12]. Given that all these dyes adsorb strongly in the visible, the amount of molecules adsorbed on graphite surface could be measured very precisely by monitoring the decrease in optical absorption of the solution (Fig. 15).
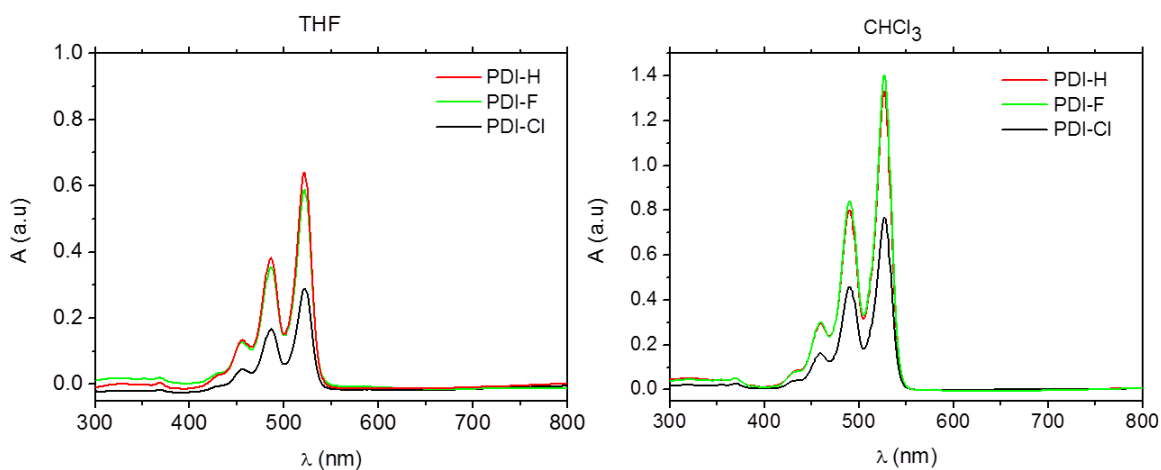
Fig. 15: Comparison of the absorption spectroscopy of the three PDIs in chloroform and THF. The highest values were collected at 521nm for THF and at 527nm for chloroform.

Fig. 16 shows the amount of molecules adsorbed on graphite N_{ADS} vs. the available area of graphite S_A. For all molecules and for both solvents tested N_{ADS} increases with S_A, eventually reaching a plateau in the left part of the graphs, when S_A is large enough to capture all the molecules present (≈ 3.25 x 10^{16} in our experiment). This data representation allows to compare the ratio between N_{ADS} and A (measured at ensemble level, in bulk solutions) to the molecular footprint of the molecules on graphite as measured by STM (measured at molecular scale in fig. 2).
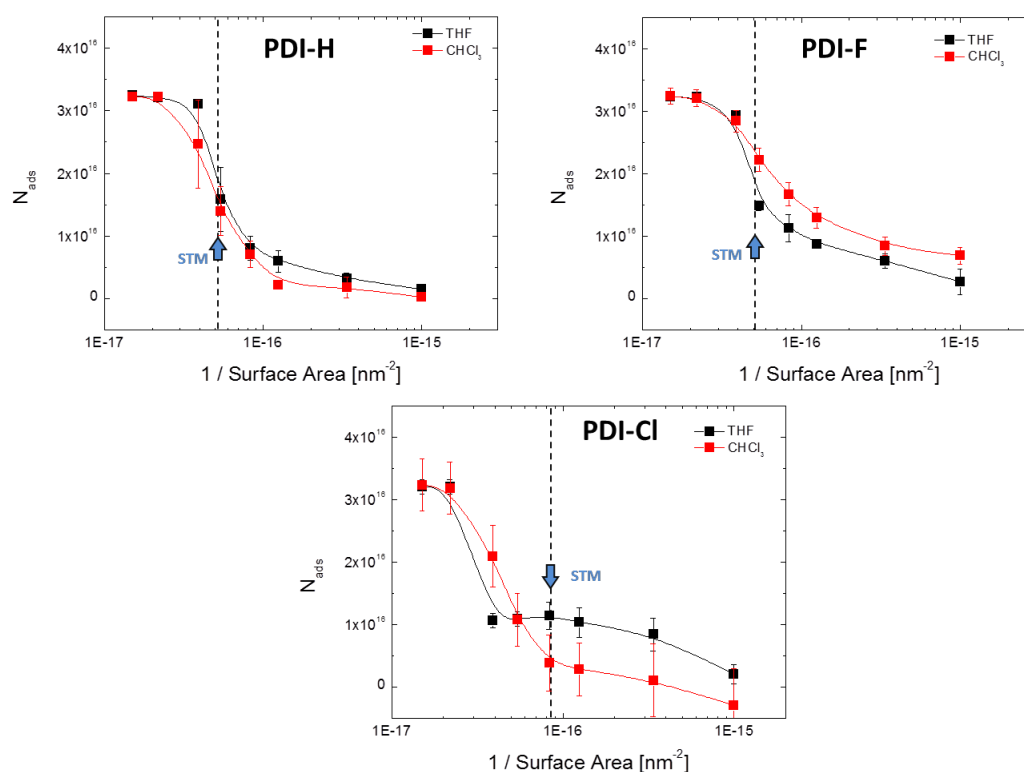
Fig. 16: Amount of molecules adsorbed varying the available graphite for the three molecules studied, in THF.

The values expected for "ideal" monomolecular, highly ordered coatings as calculated by STM (1.96 nm^2/mol for PDI-H and PDI-F; 1.67 nm^2/mol for PDI-Cl) are shown for comparison in fig. 16. In all cases PDI adsorption becomes relevant only when the available surface S_A reaches a value similar to the one calculated by STM; this suggests that also in bulk solutions of THF and

chloroform all molecules tend to form monolayers with packing similar to what shown in fig. 2. However, some deviations are observed depending on the molecule and solvent used. In particular, PDI-Cl shows a more irregular adsorption behaviour, likely due to the denser packing and strong interaction with graphite shown by modelling.

5.3.4. Graphite exfoliation in different solvents

After studying the interaction of the PDI with bulk graphite, we proceeded to study the exfoliation mechanism itself. The three molecules were dissolved in a wide range of organic solvents with different polarity and increasing surface tension: Ethanol (EtOH), Isopropyl alcohol (IPA), Tetrahydrofuran (THF), Chloroform (CHCl₃), Toluene, Dichlorobenzene (DCB), Dimethylformamide (DMF) and N-Methyl-2-pyrrolidone (NMP). The molecules showed different solubility in the different solvents, with PDI-H having the worse solubility, as visible also by naked eye (fig. 17 a,b,c).
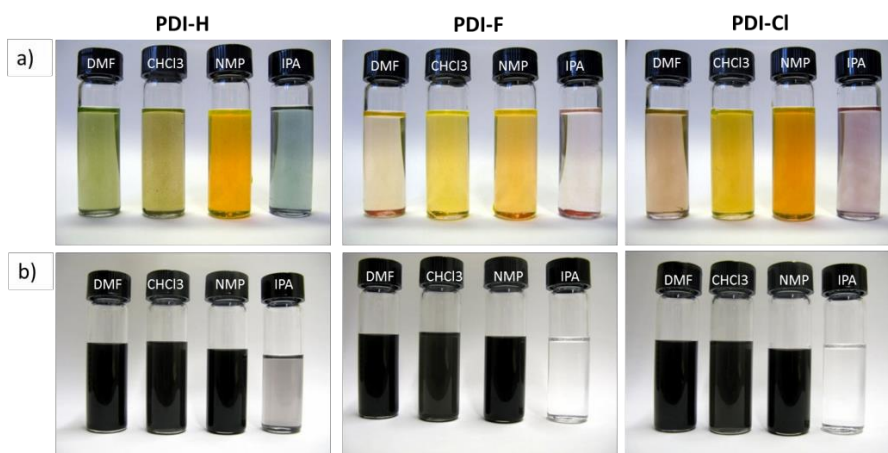
Fig. 17: Dispersions of a) PDI-H, b) PDI-F and c) PDI-Cl in some of the different organic solvetns tested. The same solutions after addition of graphite powder, sonication and centrifugation for d) PDI-H, e) PDI-F and f) PDI-Cl.

Each molecule showed significantly different absorption spectra in different solvents, due to different self-assembly properties and influence of the solvent. This changes in optoelectronic

properties of PDI in solution have been extensively studied in previous work, and will not be discussed here; for more details see as example[31] and references therein.

Graphite powder was then added and the solutions were thoroughly sonicated, following well-established standards[1]. After sonication, the dispersions were centrifuged and the supernatant was taken for further analysis, with no further purification step. Fig. 17 d,e,f shows photographs of the resulting dispersions.

We can notice that in some cases (e.g. in IPA) the only visible effect of the treatment was removal of the dyes leading to clean solvent purification, similar to the "dye capture" experiments, performed without sonication, described in the previous section. In most cases, however, dispersions of black graphitic material and PDI (named G-PDI) were obtained after centrifugation. The dispersions were stable after several months. The amount of dispersed material was precisely measured using optical absorption spectroscopy (OS) of diluted dispersions (see an example in Fig. 18).
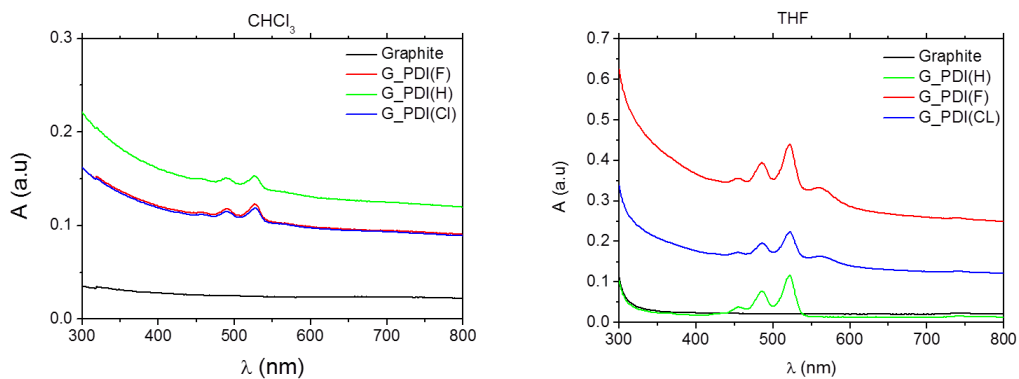
Fig 18: Typical absorption spectra of Graphene exfoliated with three PDIs in a) Chloroform and b) THF.

Fig. 19a shows a plot quantifying the amount of dispersed graphitic material, for different solvents, for different PDI molecule added to the solvent. Results obtained with no PDI, in pure solvent, are also shown (dark blue bars).
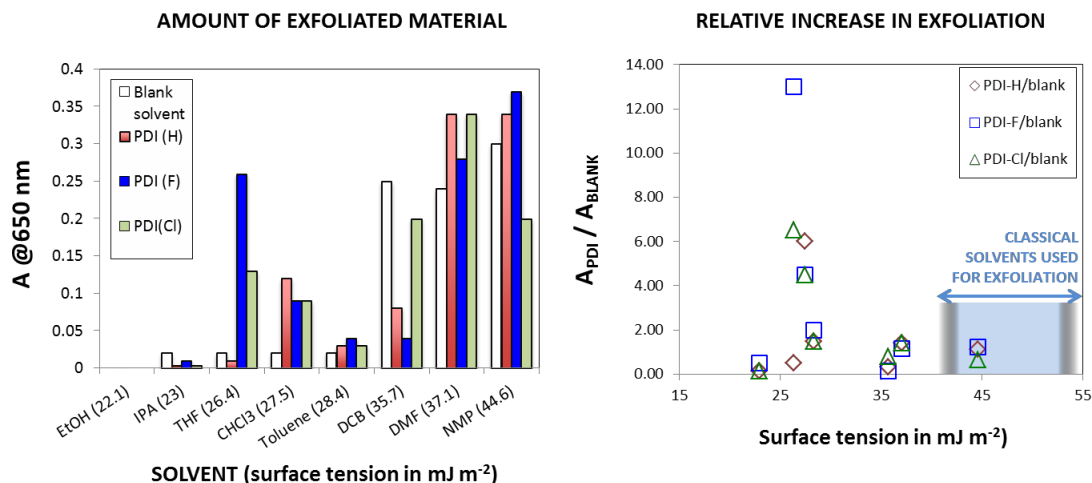
Fig. 19: Plots of Graphene-PDIs exfoliated in different solvents related to a) mass of exfoliated material and b) relative increase as compared to exfoliation in pure solvent. The shadowed area indicated the surface tension of solvents used typically for graphene exfoliation.

From the plot, we shall distinguish three different groups:

1) High-boiling solvents (DCB, DMF, NMP), having a high surface tension >35 mJ m^{-2} that yield high concentrations already in the blank sample (coloured dark blue in the graph). This result could be expected, because solvents like DMF and NMP with a surface tension of 40-50 mJ m^{-2} are the best ones to match graphite surface energy[1]. DCB has also been used successfully to exfoliate graphene, as example in ref. [18]. In this case, the addition of the PDIs can give either an increase or a decrease of the amount of dispersed material.

2) Low-boiling, highly polar solvents such as EtOH and IPA having a surface tension <25 mJ m^{-2} where graphene is poorly soluble, regardless the presence of surfactants. Even the solubility of PDIs was low in these solvents.

3) Low boiling solvents, with average surface tension of 25-30 mJ m^{-2} (THF, chloroform, toluene). Sonication of graphite in these solvents yields typically very low concentrations. However, adding to these solvents the PDI molecules increases greatly the amount of dispersed material.

Noteworthy, the efficiency of PDI as dispersing agents does not seem to be related to the strength of interaction with graphene; PDI-Cl, the molecule with highest adsorption energy and packing density on graphene, did not give the best results.

The relative improvement in exfoliation and dispersion due to each PDI (as compared to blank solvent) is plotted in fig. 19b vs. the surface tension of each solvent. We can see that in some cases a significant improvement is observed (e.g. 1300% for PDI-F in THF). In general, strongest effects are observed for solvents with surface tension between 25 and 30 mJ m^{-2}. These values are significantly lower than the ones considered, up to now, ideal for graphene exfoliation, i.e. 40-50 mJ m^{-2} [1].

Optical absorption measurements of these dispersions showed a spectrum similar to what previously observed in graphene-pyrene composites, with well-defined adsorption peaks due to the PDI aromatic core, and a slowly decaying absorption component typical of graphene (fig. 18). The different optical properties of graphene and organic dyes in G-PDI allow estimating their ratio by measuring optical absorption at different wavelengths. Concentration of exfoliated graphene can be estimated by optical spectroscopy (OS), measuring the absorbance of graphene at 650 nm (where PDI does not absorb), using the molar extinction coefficient reported in ref. [1].

 Concentration of PDIs can be obtained measuring absorption at the PDI strongest absorption wavelength (527 nm in CHCl$_3$ and 521 nm in THF), after subtracting the contribution of graphene by mathematical deconvolution procedures. The molar extinction coefficient of each PDI was measured experimentally by using solutions of known concentration. For the concentration calculations, the molar extinction coefficient (ε) for each PDI was calculated from the slope of the linear line presented on the figure below.
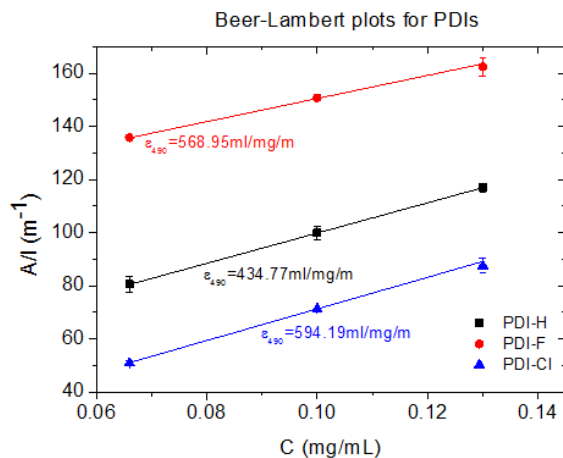
Fig. 20: Molar extinction coefficients (ε) for the three PDIs

Tables 3-4 show the estimated amounts of dispersed few-layers graphene (FLG) and PDI obtained in each case, and the ratio R between the two (expressed in graphene carbon atoms present in dispersion / PDI molecule present in dispersion).

Table 3: Amount of PDI and FLG solubilized in THF, estimated by optical absorption spectroscopy (OS). The amount of carbon atoms (from graphene sheet) solubilized vs. amount of PDI molecules is also reported.

Solvent: THF	PDI conc.	Graphene conc.	G/PDI ratio R
Units	*(mg/L)*	*(mg/L)*	*C atoms/PDI molecule*
PDI-H	70.78	1.58	1
PDI-F	74.00	31.63	22
PDI-Cl	39.31	15.87	22

Table 4: Amount of PDI and FLG solubilized in CHCl₃, calculated by optical absorption spectroscopy (OS). The amount of carbon atoms (from graphene sheet) solubilized vs. amount of PDI molecules is also reported.

Solvent: CHCl₃	PDI conc.	Graphene conc.	G/PDI ratio R	Ideal G/PDI ratio (calculated from STM)
Units	*(mg/L)*	*(mg/L)*	*C atoms/PDI molecule*	*C atoms/PDI molecule*
PDI-H	**12.36**	**15.50**	**62**	**37**
PDI-F	**11.14**	**11.71**	**55**	**38**
PDI-Cl	**9.42**	**11.55**	**68**	**32**

We can see that, for "bad" surfactants (as example, PDI-H in THF) the material dispersed in the solvent is mostly PDI ($R<2$). Conversely, for systems where the PDI seems to have a positive effect (e.g. in chloroform), R is <50. Noteworthy, in chloroform the highest values of dispersed material are obtained for the combination of FLG with the least soluble molecule (PDI-H).

An exact estimate of the actual coverage of the PDI on the exfoliated flakes cannot be done, because exfoliation always yield a poly-dispersed material featuring a range of different thicknesses, with different fractions of mono, bi- and thicker layers[12], [32]. The final *R values* obtained are higher than the "ideal" ones (reported in the last column of table 2 calculated from the STM measurements of fig. 2). This can be explained by the certain presence of graphene multilayers that increases the number of carbon atoms in the dispersion.

The systems showing the highest improvement in exfoliation as compared to blank solvent (PDI-F and PDI-Cl in THF, table 3 and fig. 17a) show a lower *R*, because together with large amounts of flakes, they have also a high concentration of PDI remaining in the dispersion, likely in the form of thick layers existing on the surface of the flakes. Presence of thick aggregates is also suggested by the onset of a new absorption band at 565 nm (fig. 16a), in agreement with what reported in previous work[22], [33].

Overall, the strongest improvements were obtained using PDI-F/THF, together with high concentrations of PDI that need further steps to be purified[12]. Dispersions in chloroform gave as well significant improvements, but also a lower content of PDI and highest values of R, due also to an effective removal of the PDIs by dye capture from graphite.

The flakes obtained were characterized by AFM and SEM after spin coating on silicon (fig. 21). Both techniques show a uniform distribution of platelets of typical thickness ≈5 nm and lateral size of few hundreds nanometers.
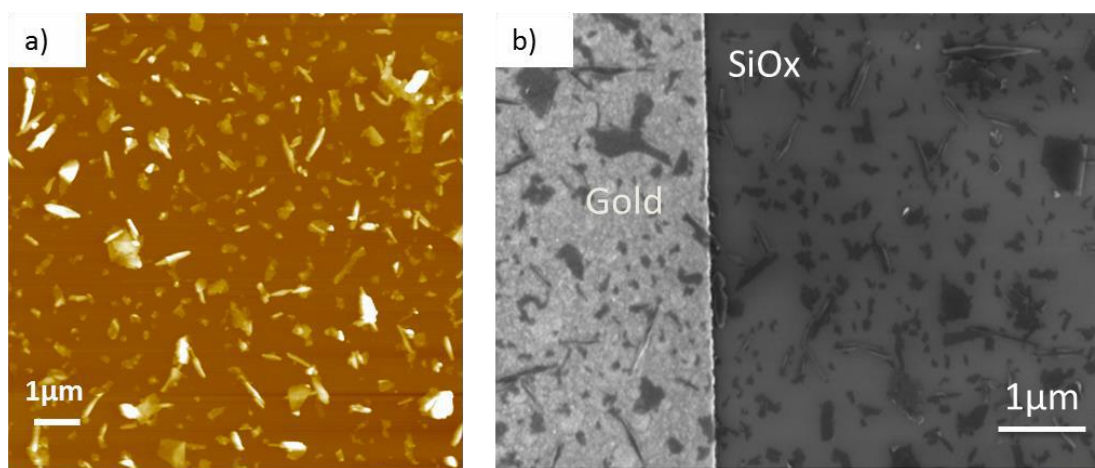
Fig. 21: a) Representative AFM image of the exfoliated graphene solutions with PDI-Cl in Chloroform on SiOx surface and b) SEM images on a SiOx surface. A gold electrode is visible on the left part of the image.

SEM images were taken on exfoliated graphite flakes on SiOx surface in order to observe the effect of exfoliation, post to sonication and centrifugation process, as seen on figure 22.
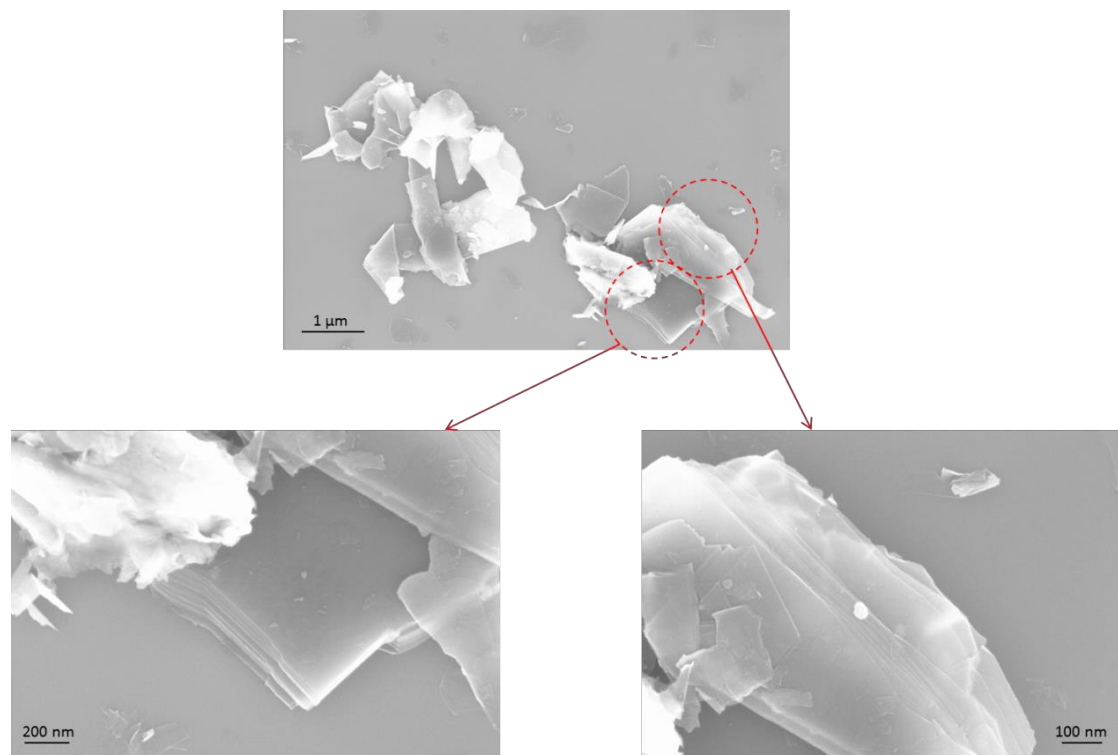
Fig. 22: SEM images on exfoliated graphite flakes under PDI-x presence

The measured thickness is well above the theoretical thickness of a single-layer (0.33 nm), likely due to incomplete exfoliation, and to the presence of residual molecules on the flakes; a similar result was obtained for dispersions of graphene exfoliated in water using pyrenes[29] where, even if sheet thickness measured by AFM was ~5 nm. Further AFM images were taken in order to observe the morphology of the PDIs alone without graphene as shown on figure 22.
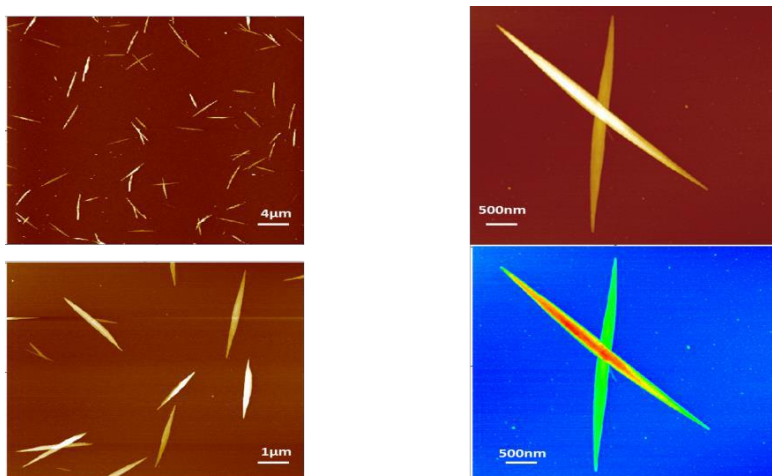
Fig. 23: AFM images on PDI-F molecules, forming crystals since deposited on a SiOx surface.
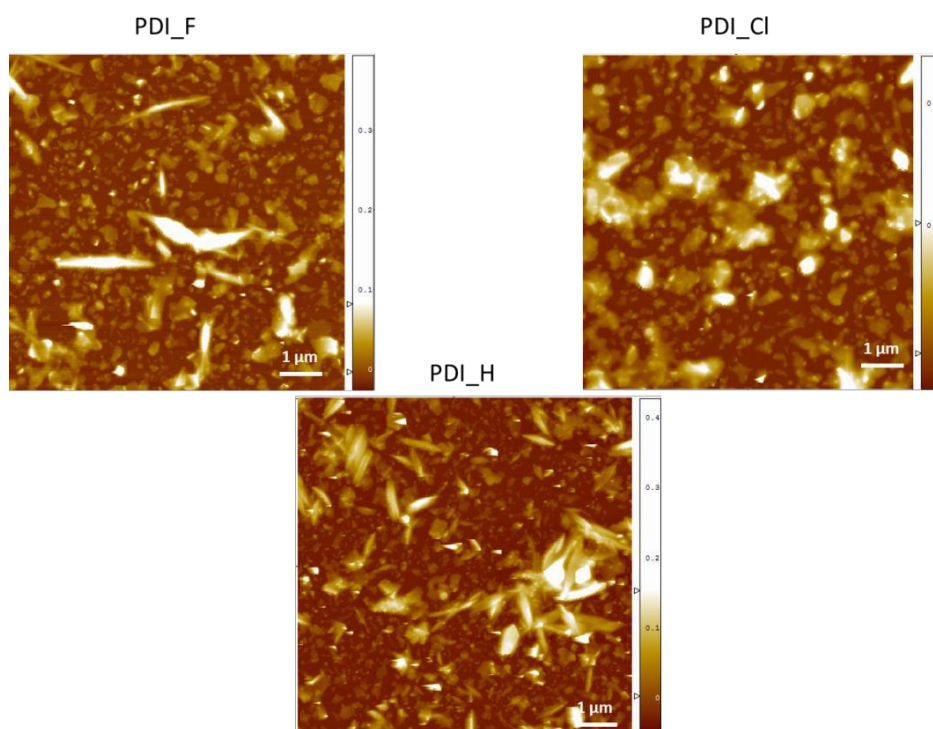
Fig. 24: AFM-topography images on PDI molecules creating aggregates on a SiOx surface.

a)

b)
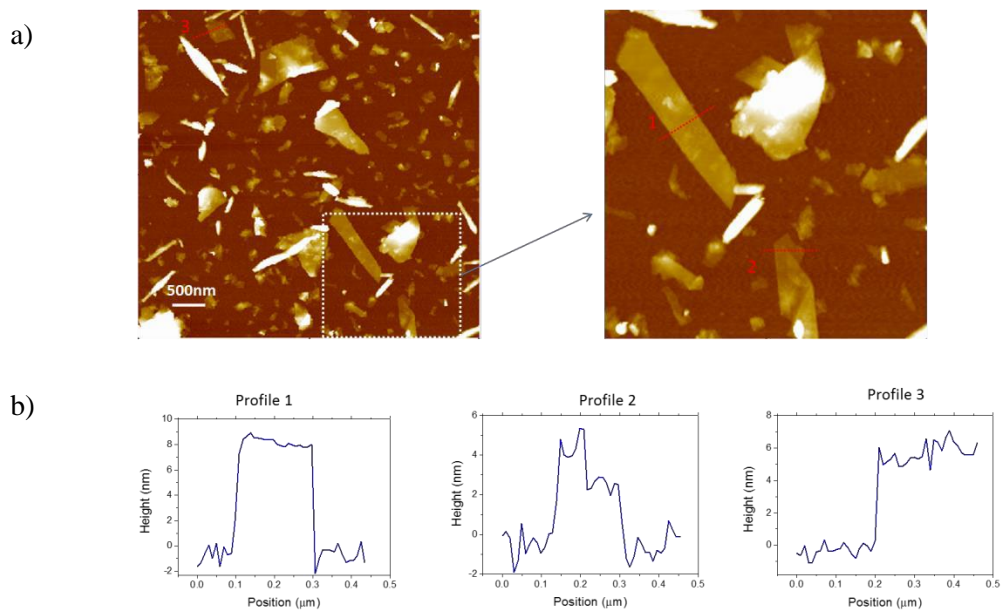
Fig. 25: a) AFM images and b) profile lines taken on several graphite flakes, confirming the number of few layers exfoliated with PDIs.

5.3.4.1 Optical and Fluorescence Microscopy
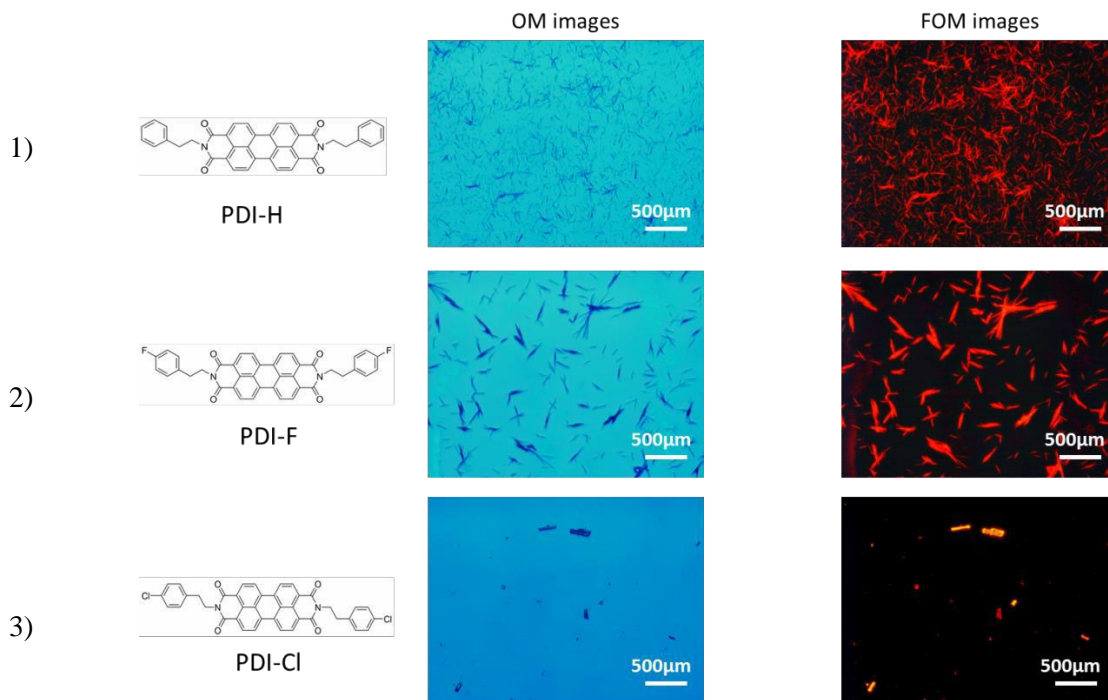
Fig. 26: Images taken under an optical microscope (OM images) and under a fluorescence optical microscope (FOM images) in the same area for the three PDIs used 1) PDI-H, 2) PDI-F, 3) PDI-Cl.
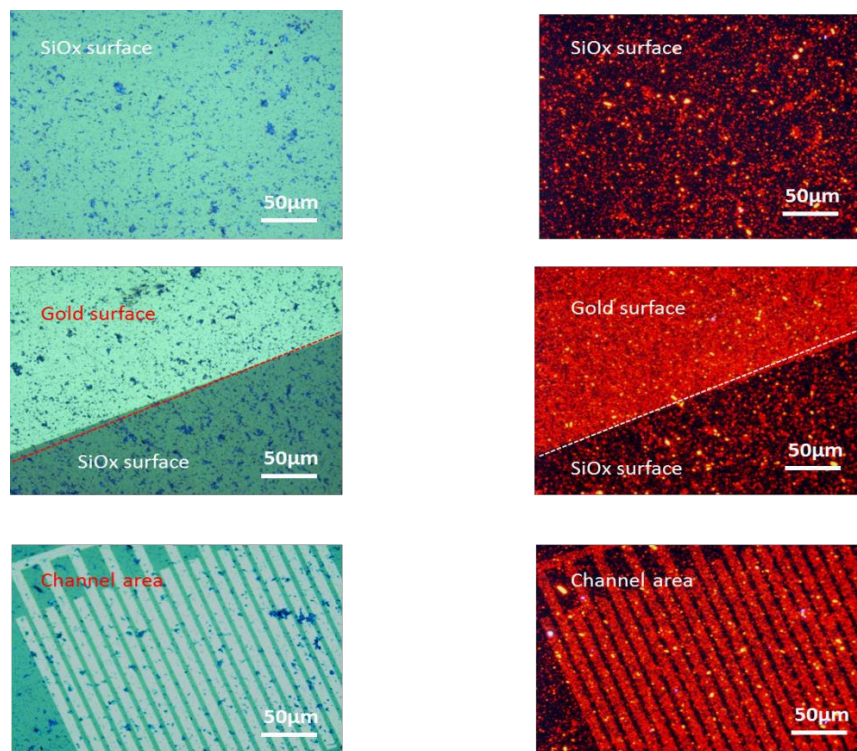
Fig. 27: OM and FOM images from SiOx with exfoliated graphene in PDI-H covering different areas on a FET substrate.

5.3.4.2 Raman analysis

Raman spectroscopy is a fast and non-destructive method for the characterization of graphene. As a process, Raman spectroscopy is a surface sensitive method that probes the inelastic scattering of monochromatic light on at the sample we need to test. When light hits the sample, the beam can be scattered elastically (Rayleigh scattering), without a change in energy, or inelastically: As the incident laser light is not only scattered in this case, but interacts with molecular vibrations, phonons or other excitations of the sample, the energy of the laser photons being shifted up or down. This shift in energy in respect to the incident light gives information about the vibrational modes in the system. A Raman vibration is active and can be detected only if the polarizability of the system has changed (during the normal vibration). In general, molecular vibrations that are symmetric with respect to the centre of symmetry are allowed in Raman, resulting in an active Raman band[34].This selection rule makes Raman a particularly

informative method in characterizing sp2 carbon backbones as are found in chromophores, nanographenes, graphene-organic hybrid materials or polymers.

Raman spectra of graphene samples typically contain two main features; the G peak, corresponding to the E2g phonon mode at the Brillouin zone center, at 1580 cm^{-1} and the 2D peak, which is activated by two-phonons intervalley assistes Raman scattering, at 2700 cm^{-1}. Since this work deals with liquid phase exfoliated graphene, typically this gives a wide variety of mono- and few-layer graphene flakes. Normally, we observe the appearance of a D peak in our Raman spectra. The D peak is caused by breathing-like modes corresponding to the transverse optical phonons near the K point[35].
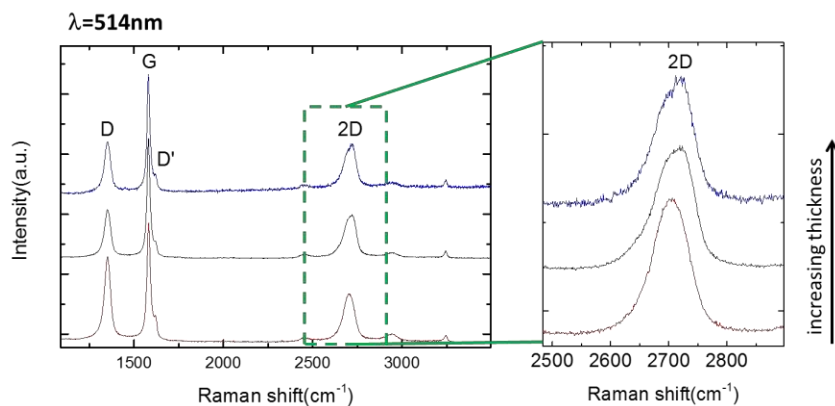
Fig. 28: Raman features observed with exfoliated graphite with PDIs at 514nm excitation.

The samples have a distribution of graphene thickness with prevalence of few-layer graphene flakes (<10 layers), based on the analysis of the 2D peak line shape. The 2D peak can be used to identify graphene layers[36]. When there is a graphene monolayer then we get a single and sharp peak. Few- or multi-layer graphene flakes show a broad and up-shifted 2D peak, which in first approximation can be fitted with two peaks. The 2D peak shape quickly evolves with the number of layers. When we have more than 8-10 layers of graphene, then it is very hard to distinguish the spectra from the one of a bulk graphite[36].
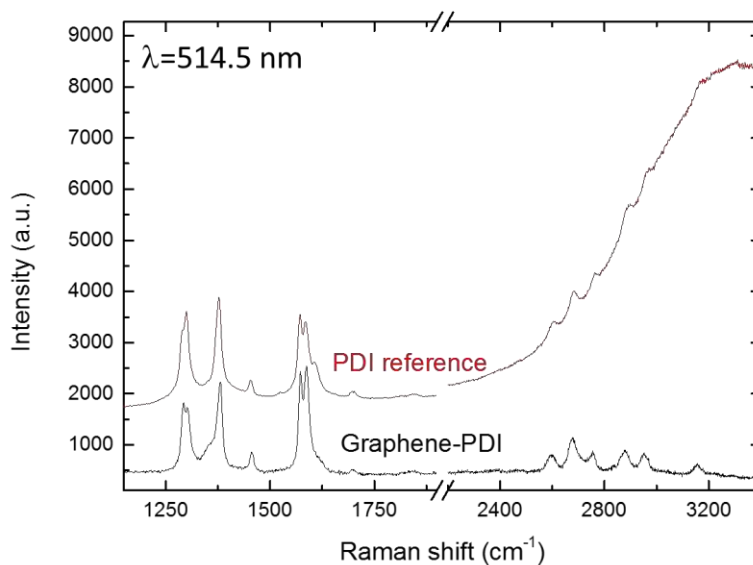
Fig. 29: Representative Raman spectrum (black curve) of a Graphene-PDI sample deposited on Si, measured after three washing steps in Chloroform. The red sample deposited on Si, measured after three washing steps in Chloroform. The red spectrum was taken on a sample with bare PDI deposited on Si, for comparison. The balck curve has been extracted from a statistics performed on over 100 points.

Raman analysis confirmed that 50-60% of the sheets were 2-7 layers thick, with a 10-20% fraction of monolayers , the rest being >7 layers[12]. Unfortunately, we could not use Raman spectroscopy to analyse the thickness of the samples obtained with PDIs, because Raman peaks of graphene were overshadowed by the presence of intense PDI Raman features. Due to the high thickness measured by AFM and the lack of Raman signal, the GOH obtained shall not be considered graphene but rather few layers graphene (FLG).

In general, exfoliation with organic molecules never gives a high yield of monoatomic sheets, differently from exfoliation proceeding by chemical or electrochemical oxidation[11]. Purification of the monolayers shall be achieved by centrifugation steps[37], [38] or by chromatography[39] for applications such as transparent conductors, where monolayers are requested.

Here instead we used these materials with no purification, as additive in composites or in electronics to enhance the electrical properties of polymer in thin layers or in bulk matrix[14],

[40], [41]. In such applications the coating of organic semiconducting dyes enhances the interaction with the matrix, low cost and high processability are key factors, and recent results indicate that FLG is better than pure monolayers for applications in polymer composites[42].

5.3.4.3 XRD Analysis

X-ray diffraction is a method of determining the distances between the atoms in a substance. The reason that solely x-rays are used in these measurements is that they have the wavelengths that cover the range of the typical distances between atoms in a crystal lattice. The calculations for the distance (*d*) between the atoms is based on Bragg's law[43]. This law states that

$$n\lambda = 2d \sin\theta$$

where θ is the angle between the layer and the approaching x-ray when there is a constructive interference as shown in Figure 30, *n* an integer and λ the wavelength. At these angles, the intensity of x-ray reflected will be significantly higher. As the x-ray leaves the x-ray tube, a filter will ensure that the rays departing are all of approximately the same wavelength and in the same phase. Thus when the x-ray hits a crystal material, the first crystal plane will reflect some of the beams, while others will pass through. Reflection will occur at the planes below and the reflected rays will partly reach the x-ray detector. If the rays that reach the detector are in phase, they will have a constructive interference and thus a very high intensity. Let us consider only the rays that have been reflected on the first and the second layer. Since the rays that have been reflected at the second layer has travelled further than those that have been reflected on the first layer, this extra distance needs to be a multiple of the wavelength for the waves to be in phase. This extra distance is obviously a function of the distance between the layers. Because the x-ray is sent in an angle to the layer, the extra distance travelled is twice the sine of that angle times the distance between the layers.
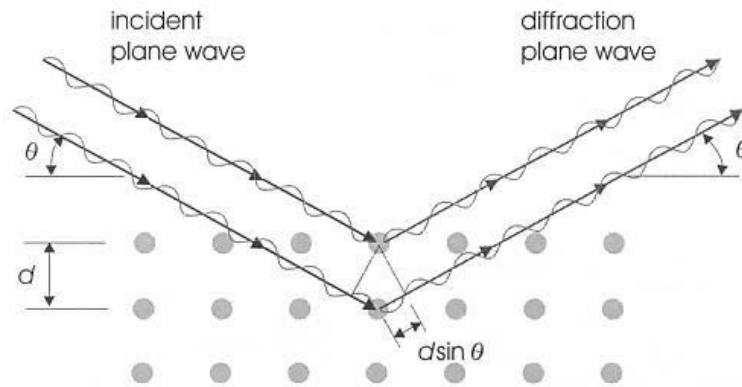
Fig. 30: X-rays reflecting off layers of a crystal material

5.3.4.4 XRD on exfoliated Graphene with PDIs

There are two types of structures for solids, amorphous and crystalline. Crystalline structures are such where atoms arrange themselves in distinct patterns. Graphite is a good example of a crystalline structure. A definition of a crystalline material is that if looking into the same direction from any unit cell (one or more atoms forming a group, the structure of which is identical to other unit cells) it would look the same. But even in this definition, there are two different types of crystals. There is the polycrystals, which is made up of many small crystals, each oriented to a different direction, with light reflecting boundaries between. There is also the single crystalloids, such as diamond, which are made of one large crystal and so do not have internal boundaries. Different from a crystalloid, an amorphous material does not have any patterns. However, the atoms inside such a material are still likely to be ordered so that they are approximately the same distance away.
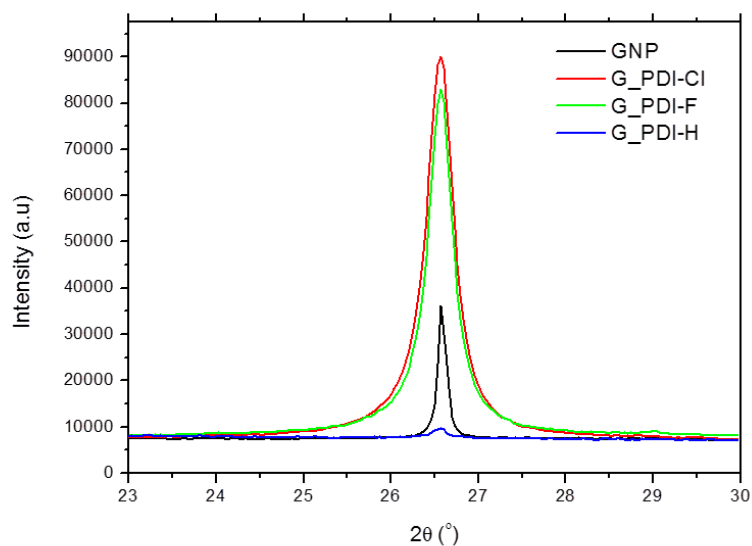
Fig. 31: Where GNP represents the exfoliated graphite flakes in CHCl3, G-PDI-Cl & F are the exfoliated graphite flakes in Chloroform with the presence of PDI-F and PDI-Cl respectively, and G-PDI-H is the exfoliated graphite flakes in Chloroform with PDI-H.

Table 5: The calculated the domain of the exfoliated material present on a SiOx surface after a spin-coating deposition, as summarized below:

	GNP	GPDI-H	GPDI-F	GPDI-Cl
FWHM (deg.)	0.13	0.21	0.34	0.38
Size (nm)	78	45	28	25

The domain size or crystal size can be estimated by the Scherrer formula from the FWHM value. The value refers to the domain in the direction perpendicular to the considered plane. If we consider the reflection at 26.5 deg for graphite, it is the plane parallel to the hexagonal rings. So the domain size refers to the direction normal to the plates. It is of the interest for internal comparisons and it represents a good value when the FWHM is not too similar to the instrumental broadening.

$$D = \frac{K\lambda}{\beta \text{Cos}\,\theta}$$

5.3.5. Processing of G-PDI materials in polymer composites

Processing of graphene and related materials with polymers is a major issue hindering widespread commercialization of graphene-based products. Processing of graphene composites by extrusion and solvent casting, molding, etc. needs careful tuning of the processing conditions and of the nanosheets structure. Incorrect processing can lead to aggregation of the nanosheets, yielding mechanical defects and poor electrical percolation in the final composite, and modifying the rheology of the matrix and the final performance of the material.

Recently, Coleman and coworkers have demonstrated a new way to embed graphene into rubber stripes already formed[44]. In this approach, the rubber stripes were swollen in a dispersion of graphene and NMP. The swelling allowed the dispersion and the graphene sheets to penetrate in depth into the rubber, yielding conductive graphene-rubber composites.

This swelling-deposition approach is industrially interesting because, being a post-processing step, it does not require to modify the production setup, and ensures a more uniform distribution of graphene in the matrix. Here, we demonstrate that a similar approach shall be used not only with elastomers like rubber but also with thermoplastic polymers using the G-PDI composites described in the previous sections.

5.3.5.1 Rubber swelling process

First, we repeated the experiments described in ref.[44] soaking natural rubber in a G/PDI dispersion. The rubber was soaked for 12 hours in a G-PDI-F dispersion in chloroform and dried for another 12 hours in open air. After this process, the rubber showed measurable electrical conductivity that changed with rubber stretching, going from 300 kΩ to 3.7 MΩ upon 300% of elongation. More details on this can be found in ref. [44].

Similar experiments performed using G-PDI in THF, instead, led to the complete dissolution of the polymer.
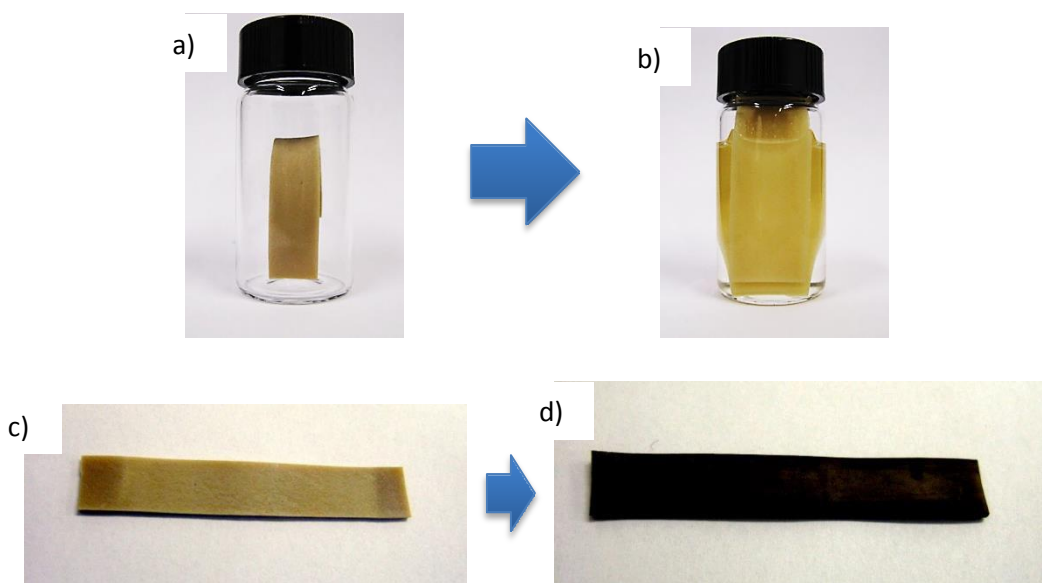
Fig. 32: Images taken from a) an unprocessed commercial rubber, b) when the rubber gets swollen upon entering a chloroform solution. Last images show how the unprocessed rubber (c), can really change when rubber is wollen in a cholorofrom solution and the graphene-PDI materials penetrate into the surface of the rubber.
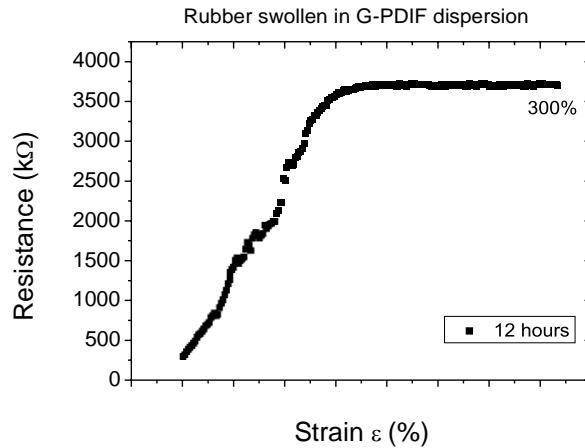
Fig. 33:Resistance versus applied strain. The resistance reaches a treshold upon a specific strain. This suggests that while the rubber network is deforming, the flakes are seperating from each other and therefore loosing the resistance signal.
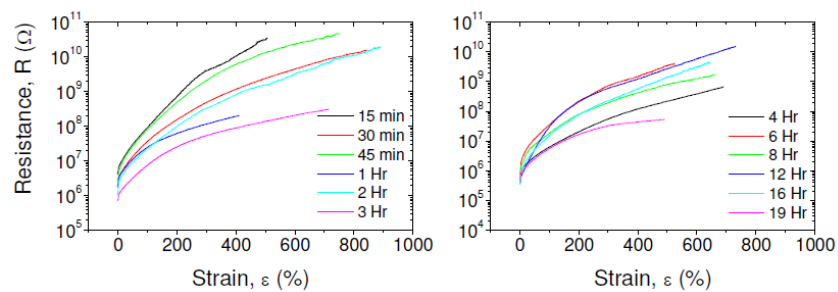

Fig. 34: Resistance versus applied strain as demonstrated from Boland et. al. [44]. It is clearly reprisented how the resistance is strongly depended on the strain applied.

As shown in figure 34, the resistance is highly depented on the applied strain of the graphene-processed rubber.This suggests that while the rubber polymeric chains are streched, the graphene flakes that are attached or penetrated between them are loosing contact from each other and therefore the resistance is lost as no electricity can be transferred through them. Although, this makes these materials a very good candidate for dynamic strain sensing, as shown by Boland et. al.[44]. As seen on figure 35, graphene-processed rubbers were attached on different parts of the

body to monitor the change of movement , speech and blood pressure de to their high strain sensitivity.
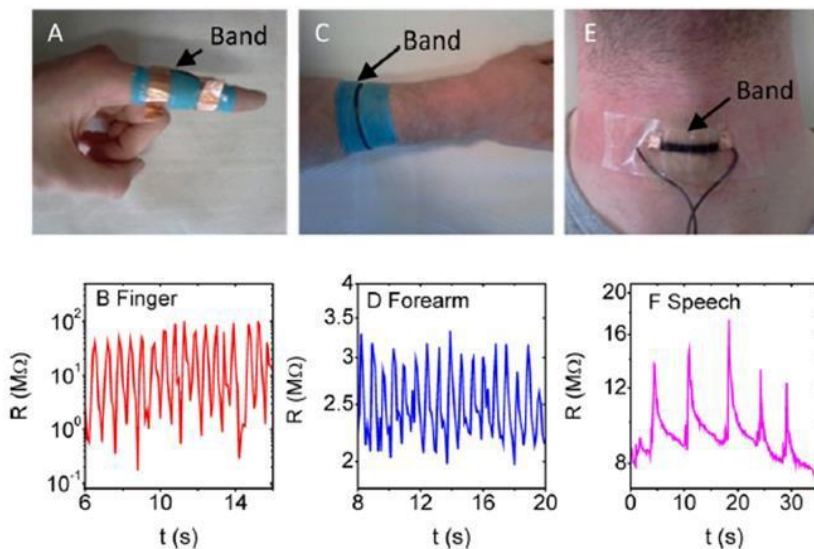

Fig. 35: Photo of a graphene-processed rubber attached on a finger (A), a forearm (B) and on the neck (E), as body monitors of movement, speech and breathing monitoring the change of resistance[44].

We then chose poly-vinyl chloride (PVC) as a test polymer, because it is one of the most technologically relevant polymers, used extensively for pipes, cables, building, clothing, etc. Transparent sheets of PVC were dipped into chloroform dispersions at room temperature, and then dried in air, to let the chloroform evaporate. The swelling process was completed in less than 3 minutes (fig. 38), and gave an increase of ≈80% in volume. No further change to the swollen area/size was observed when the polymer films were left in the dispersions for more than 3 minutes. After the swelling treatment, the PVC samples showed a dark colour due to the presence of the G-PDI complex. The presence of PDIs rendered also the polymer fluorescent.

5.3.5.2 PVC swelling process

We chose poly-vinyl chloride (PVC) as a test polymer, because it is one of the most technologically relevant polymers, used extensively for pipes, cables, building, clothing, etc. Transparent sheets of PVC were dipped into chloroform solutions for 3 min at room temperature, then dried in air, to let the chloroform evaporate. The time of 3 minutes was the maximum amount of time needed for the PVC films to swell at their maximum quantity (fig. 38). No further change to the swollen area/size was observed when the polymer films were left in the dispersions for more than 3 minutes. It was also noted that the polymer films increased 80% from their original size during the swelling process. In chloroform the PVC did not dissolve but swelled.
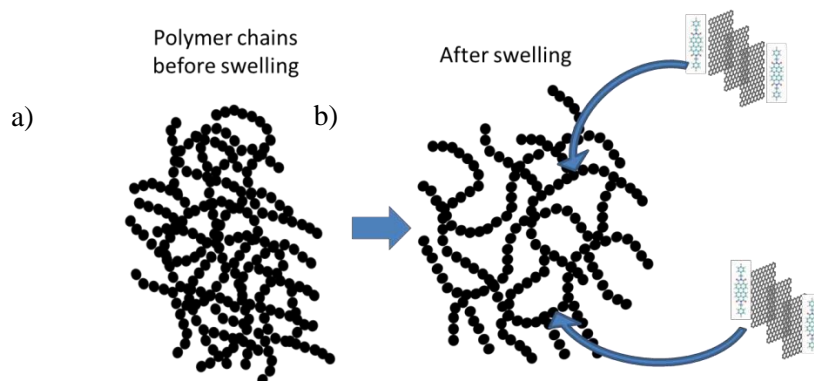

Fig. 36: Polymer chains in a) a normal situation and b) when inserted in a solvent that favors swelling which loses the polymer chains and allows penetration of the exfoliated graphene and molecules between the chains.

Cross-linked polymers swell significantly when exposed to chemicals having similar solubility-parameter values[45]. A cross-linked polymer when placed in a good solvent, rather than dissolving completely, will absorb a portion of the solvent and subsequently swell. The extent of swell represents a competition between two forces. The free energy mixing will cause the solvent to penetrate and try to dilute the polymer solution. This entropic increase may be enhanced by increasing the temperature. As the polymer chains in the crosslinked polymer network begin to

elongate under the swelling action of the solvent, they generate an elastic retractive force in opposition to this deformation. The volumetric swelling reaches steady state when the two forces balance each other [46]. Solvents like THF which are proton acceptors can dissolve PVC which is a proton donor (as illustrated in section 3.5.4). Whereas solvents like Chloroform which is proton donor can only swell it[47]. In the swelling of a cross-linked polymer an additional free-energy change, arising from the elastic extension of the three-dimensional molecular network has to be taken into account[48]. The swelling can be rather extreme when the solubility parameter difference between polymer and solvent is small[45]. On the table below we can see how this is confirmed related to Chloroform and THF that the PVC membranes were tested and how they compare to natural rubber that has been previously tested[44].

Table 6: Hansen solubility parameter values (δ_D, δ_P, δ_H and δ_{total}) for the materials tested on the swelling process.

	δ_D (Mpa$^{1/2}$)	δ_P (Mpa$^{1/2}$)	δ_H (Mpa$^{1/2}$)	Total (δ)
Graphene	18	9.3	7.7	21.6
THF	8.2	2.8	3.9	9.1
Chloroform	17.8	3.1	5.7	19.0
Natural rubber	17.4	3.1	4.1	18.1
PVC	18.2	7.5	8.3	21.3

After the swelling deposition, the dark colour due to G-PDI complex is visible by eye (fig. 37). The presence of PDIs was also confirmed by fluorescence images (fig. 38). Optical absorption spectra of the G-PDI-PVC multilayer show spectral signature of both graphene and PDI, in analogy with what observed in solution. Coleman et. al. [44] suggests that due to similar solubility parameters of rubber (PVC in our case) and toluene ($CHCl_3$ and THF for us) the polymer is swelling and hence letting the nanoparticles to penetrate inside the polymer chains.
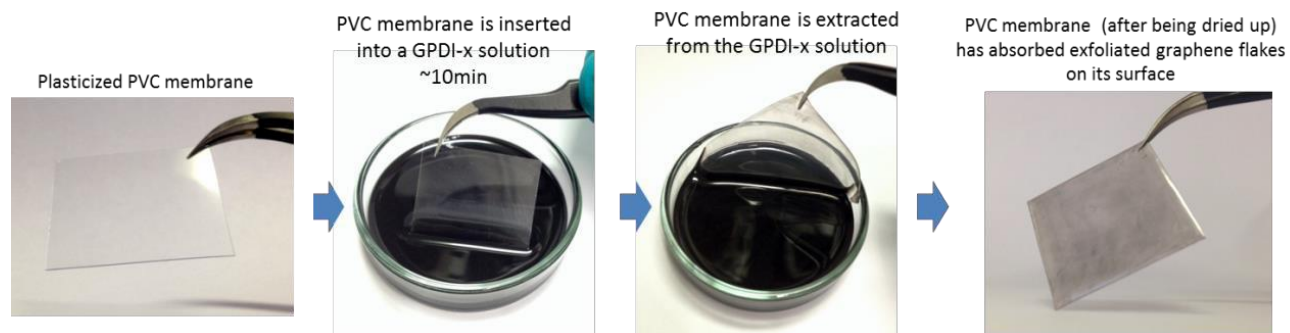
Fig. 37: Process followed from the point when a blank PVC film is inserted in a graphene-PDI-x solution for ~10 minutes, then extracted from the solution, dried in open air and then the processed PVC film with graphene and PDI molecules attached on its surface.
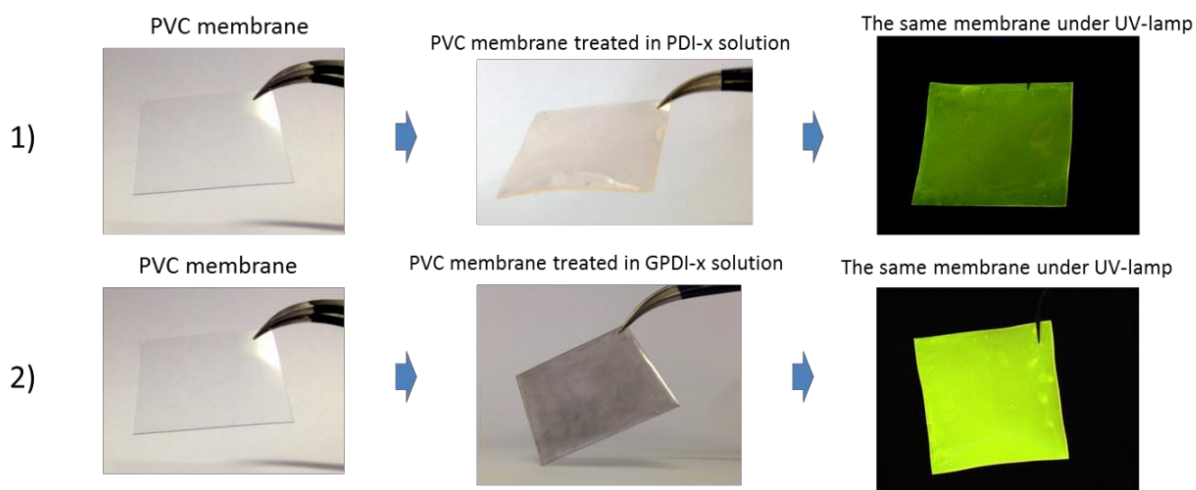

Fig. 38: Two blank PVC films treated in a 1) PDI-x solution and 2) in a graphene-PDI-x solution. The final images were taken under a UV lamp to confirm the presence of molecules attached with graphene on the PVC surface.
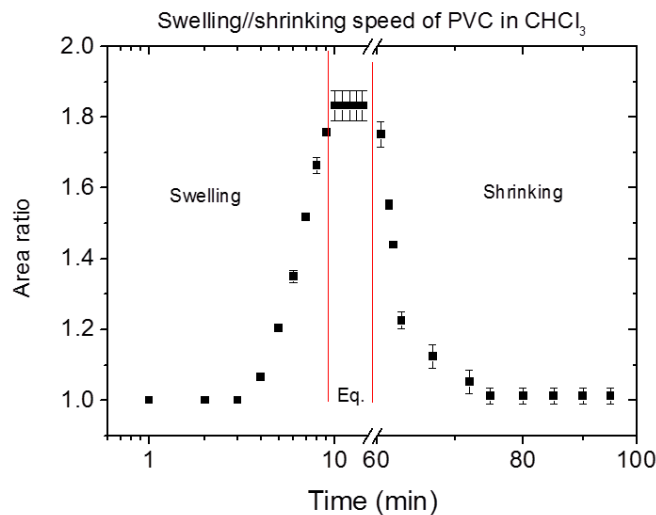
Fig. 38: Graph illustrating the swelling and shrinking speed of a PVC substrate after being inserted in a chloroform solution. The PVC film is increasing 80% of its initial size/area when inserted in chloroform and then returns back to its initial dimensions when exits the solution and the solvent has evaporated.
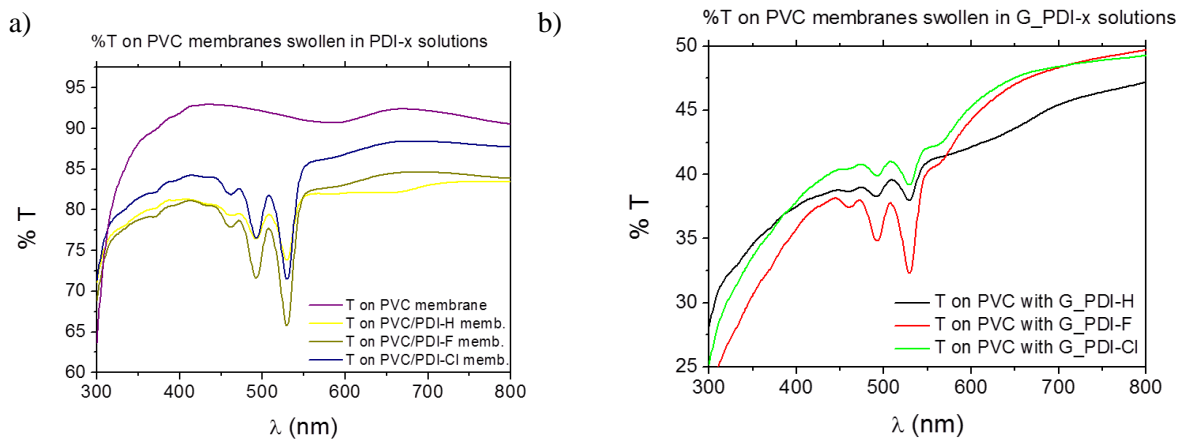

Fig. 39: Transmittance spectra on PVC samples when treated in a) just PDI-x solutions and b) when treated in exfoliated graphite-PDI-x solutions.
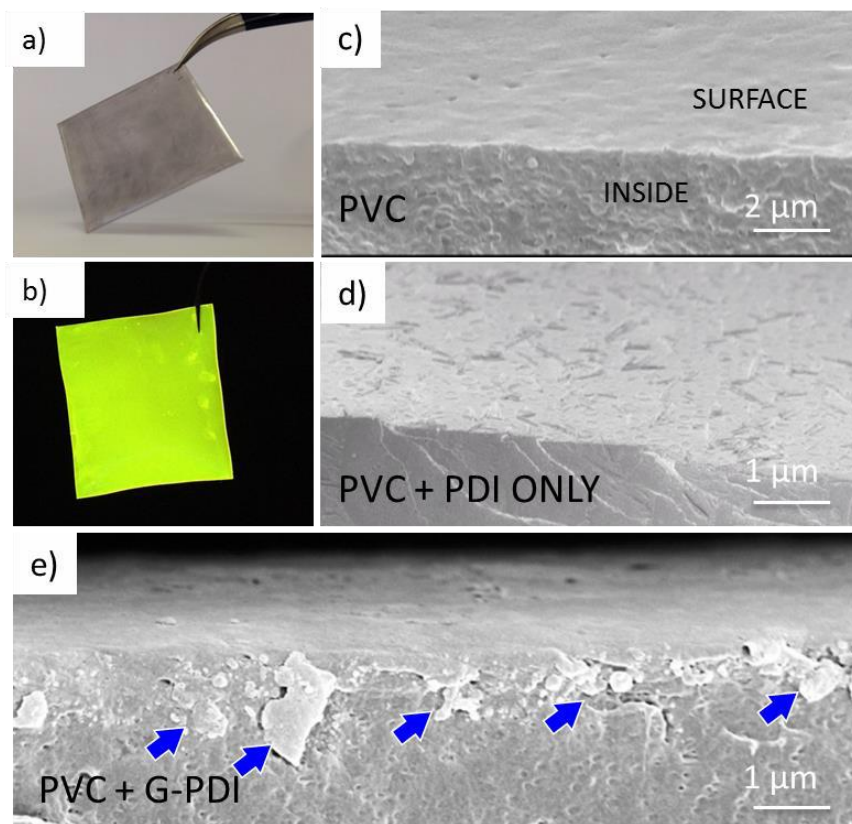
Fig. 40: a) Representative image of a PVC membrane after the swelling process in a Graphene-PDI-F dispersion in Chloroform. B) the same PVC membrane under UV light, revealing the presence of uniformly distributed PDI molecules. c, d, e) cross-section SEM images on; c) an untreated PVC film, d) treated only in a PDI solution and e) treated in a G-PDI dispersion, confirming the presence of intercalated graphene sheets and molecules.

AFM and KPFM images were taken on the PVC surface in order to confirm the presence of graphene and the uniformity of them penetrated into the polymer chains (fig. 41). Optical absorption spectra of the G-PDI-PVC multilayer showed spectral signature of both graphene and PDI, in analogy with what observed in dispersion (fig. 42). No shift in absorption was observed between the PDIs in dispersion, when mixed with FLG and after insertion in PVC, indicating that there is no significant molecular aggregation during processing[22].
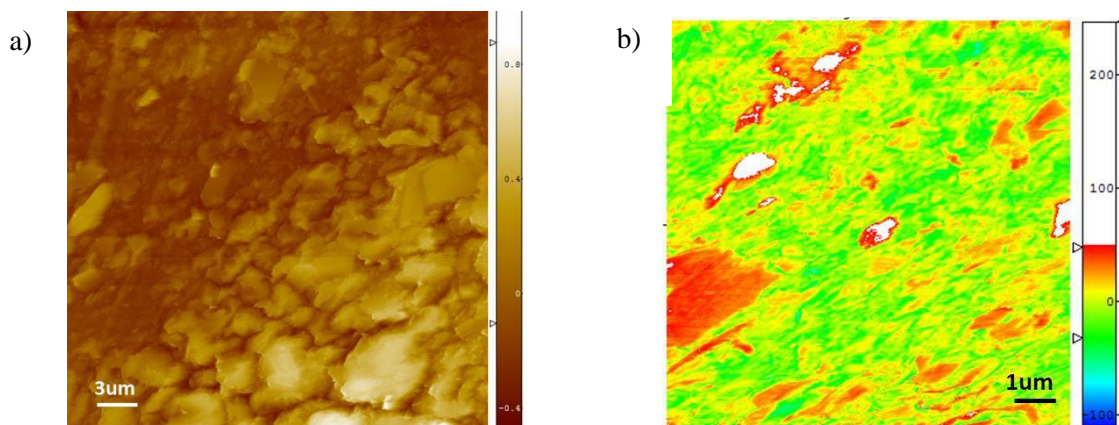
Fig. 41: a) AFM topography image on a PVC film surface after treatment in a G-PDI-x solution and b) Kelvin Probe Force Microscopy surface potential difference map indicating the presence of graphene flakes.
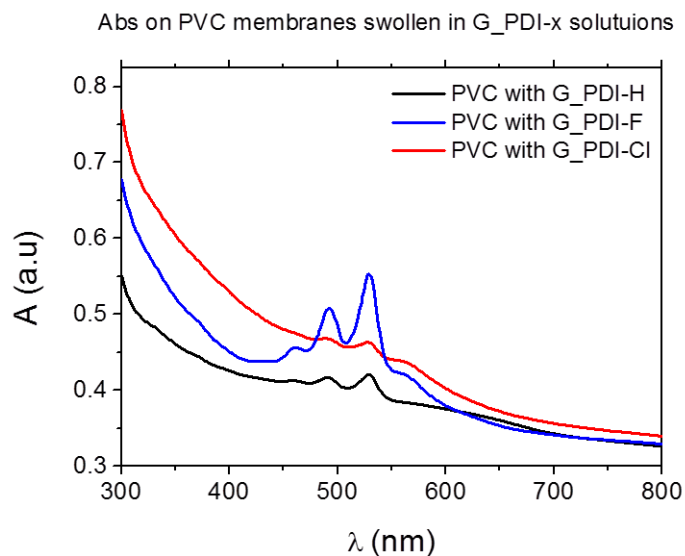

Fig. 42: Absorption spectroscopy of PVC membranes swollen in different G-PDI solutions in Chloroform.

The sheets seem well adhering to the PVC, and could resist to washing and scratching. To confirm that they are truly embedded into the polymer and not just adsorbed on it, cross-section SEM images were performed. The initial PVC (fig.8c) appears uniform. Upon swelling in a

dispersion of chloroform with pure PDI, some molecular PDI crystals of elongated structures grow on the surface (see fig. 8d and fig. 43), but the surface remains electrically insulating.
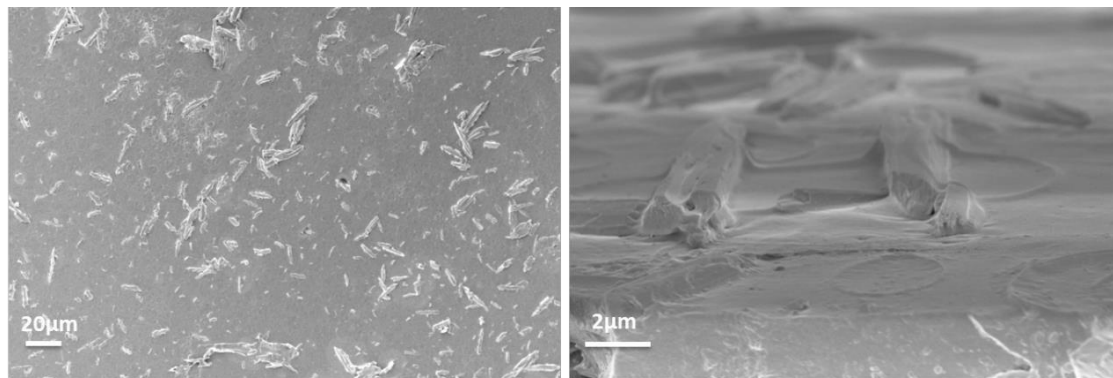

Fig. 43: SEM on PVC samples swollen in solutions of pure PDI-F in chloroform and no presence of graphene layers.

By swelling a PVC membrane in G-PDI-F dispersions in chloroform, the SEM images show instead a dense coating of rectangular and polygonal shapes covering the surface (fig. 44 a,b). The sheets are not just deposited on the surface, but are embedded into it, in some case reaching some microns in depth, as visible in fig. 8e.

AFM images (fig. 44 c) show the fine details of the structure, with folds and flat sheets visible on the otherwise rough surface.
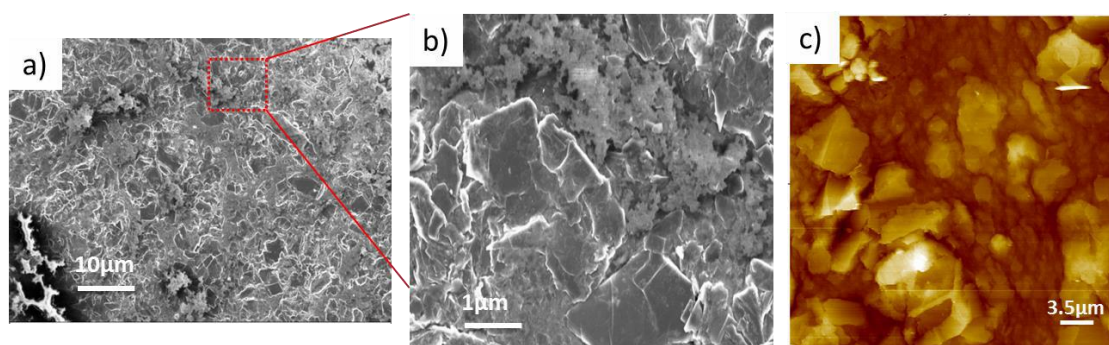

Fig. 44: a, b) SEM and c) AFM images from the surface of a PVC film, treated in a G-PDI-F dispersion. Typically, 2D sheets end up laying flat on a substrate, when deposited by conventional solution processing[49]–[51]. Due to the swelling, instead, it is clearly observable by SEM that the sheets

penetrate into the polymer, in some cases protruding out of the surface (fig. 14). Polymer swelling procedure could be used to include the material in PVC using all the tested PDIs.
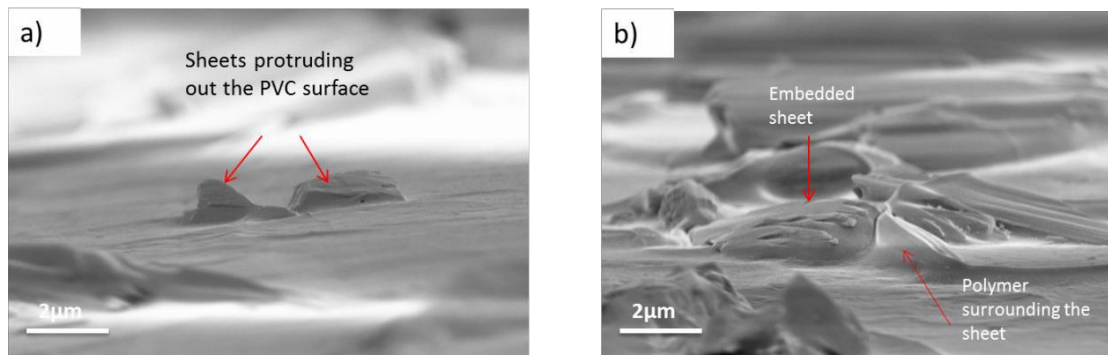

Fig. 45: SEM images of PVC membranes swollen in solutions of G-PDI-F in Chloroform

5.3.5.3 Contact angle measurements

A strong improvement of material hydrophobicity by 41,7% was observed in all cases, with water contact angle increasing from 72° (blank PVC) to 103°±2 when treated with PDI-H and PDI-F and 101°±2 when treated with PDI-F.
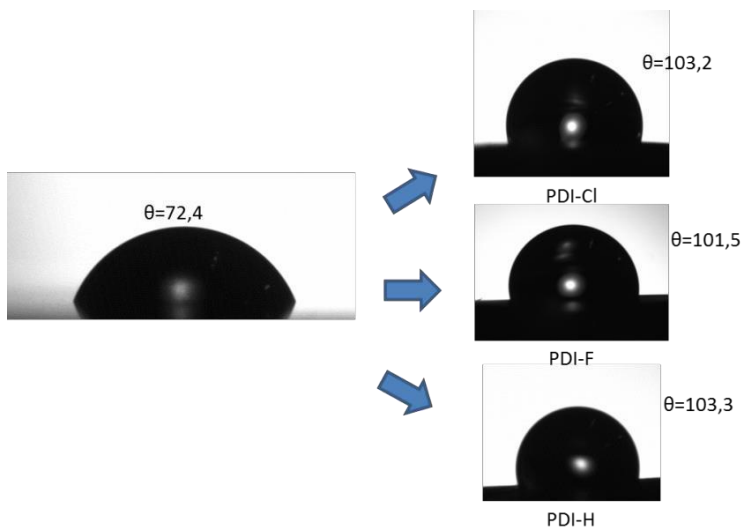

Fig. 46:Illustration of the change of the contact angle of a water drop when deposited on a PVC surface, before and after treatment with G-PDI-x solutions.

5.3.5.4 Electrical measurements

The embedded sheets form a continuous, micron-thick layer (fig. 14) on the surface of the otherwise insulating PVC. Electrical conductivity was measured on different areas of each sample using a four probe Van der Paw setup.; sheet resistance of ca.10^2 $\Omega/\square$ was measured on all the samples, a value useful for antistatic coatings.

The most conductive coatings on PVC were obtained using G-PDI-H (3.0 ± 1x 10^5 $\Omega/\square$) while G-PDI-F gave values of 4.14 ± 1 x 10^5 $\Omega/\square$ and G-PDI-Cl values of 4.83 ± 1x 10^5 $\Omega/\square$. Given the irregular rough surface of PVC, it was not possible to calculate the bulk conductivity of the G-PDI coating on the polymer.

5.3.5.5 Raman mapping on PVC conductive membranes

The PVC membranes that were fabricated and processed with the above method, after swelling in choroform solutions, where then characterized by Raman creating a map of the distribution of the exfoliated graphite flakes.
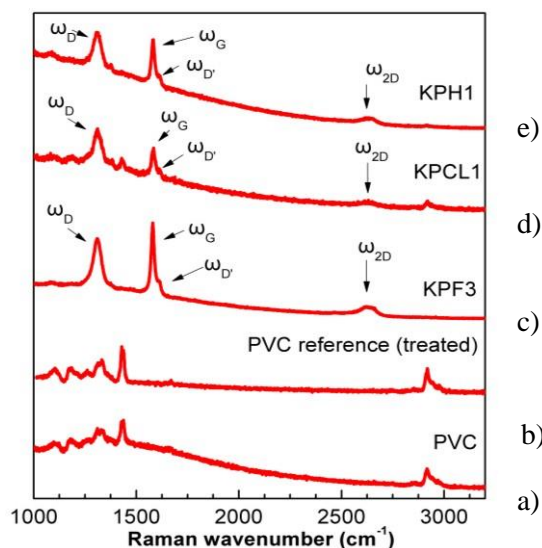

Fig. 48: Raman spectra collected at 785 nm on a) a PVC untreated film, b) PVC film treated in chloroform, c) PVC film treated in G-PDI-F dispersion, c) PVC film treated in G-PDI-Cl dispersion c) PVC film treated in G-PDI-H dispersion.

Raman spectra were collected at 785nm (1.58eV) excitation, the laser was focused on the sample by means of 100xobjective and the laser power was kept below 2.5mW on the sample to eliminate laser-heating effects on the probed materials.

The indicated samples are: KPF3=0.27±0.01MΩ, KPH1=0.3±0.01MΩ, KPCL1=0.9±0.1kΩ.
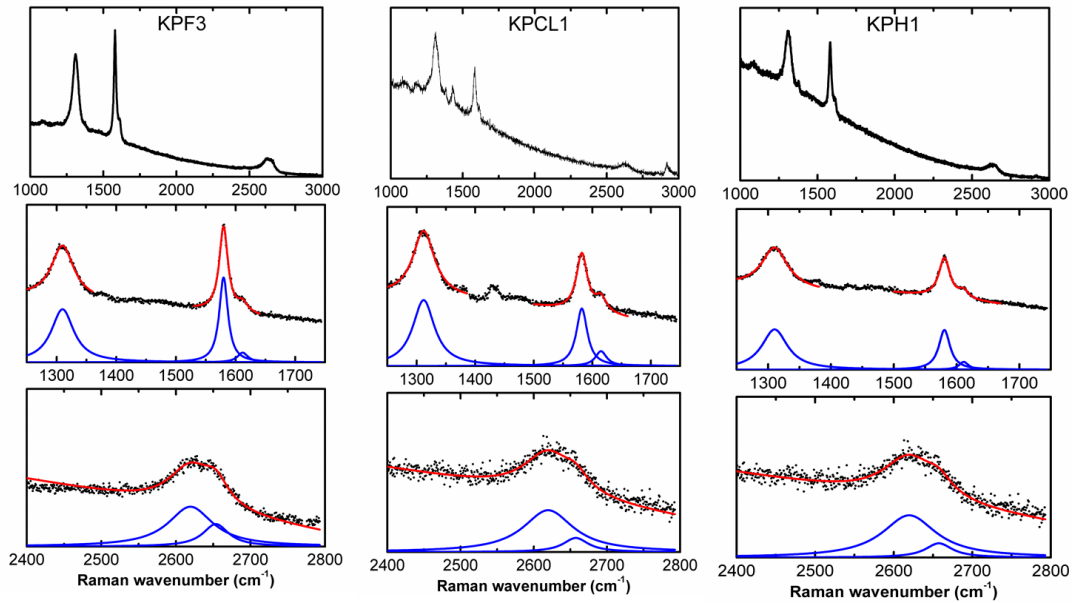
Fig. 49:Raman spectra on different samples indicating a strong presence of ω_G influenced by the weak presence of ω_D

All examined samples appeared to have strong presence of ωG influenced by the weak presence of $\omega_{D'}$ (~1611 cm^{-1}) which attributed to the presence of defects. The presence of defects/edges are reflected also via the strong presence of ω_D. The assymetric presence of ω_D confirms the presence of graphite (fitted with two Lorentzian curves).
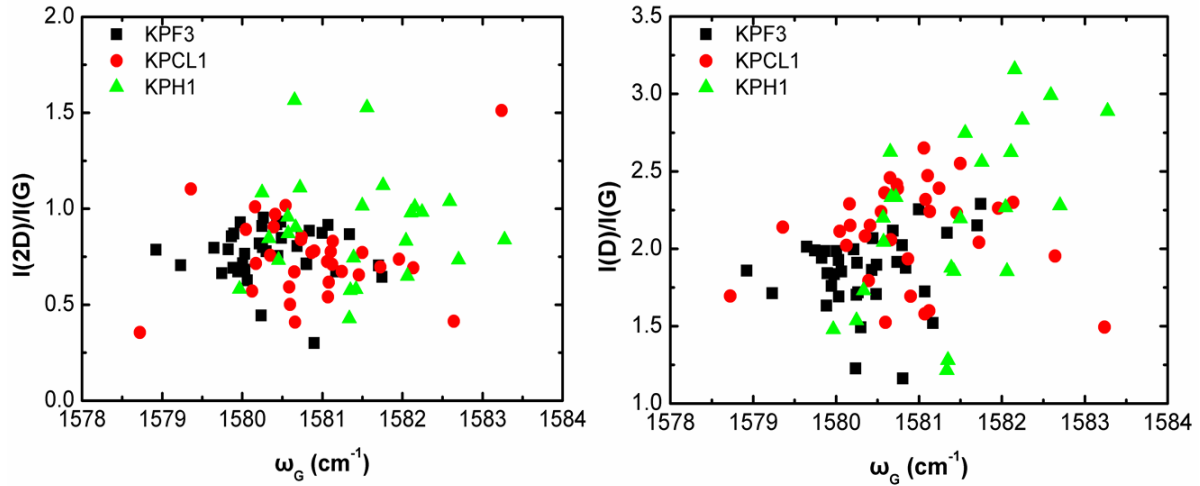
Fig. 50: I(2D)/I(G) as a function of the G peak position.

Initially a mapping area of $10 \times 10 \mu m^2$ with a step of $2\mu m$ was scanned at all samples. The plot of I(2D)/I(G) as a function of PosG shows a variation with doping (I(2D).(I(G)<1) for the majority of the examined points at all samples. Similarly, the plot of I(D)/I(G) with PosG indicated relative high amount of disorder.

Table 6:Summarizing table with all the above measured parameters

Sample	Average ω_D (cm^{-1})	Average FWHM ω_D (cm^{-1})	Average ω_G (cm^{-1})	Average FWHM ω_G (cm^{-1})	Average $\omega_{D'}$ (cm^{-1})	Average FWHM $\omega_{D'}$ (cm^{-1})
KPF3	1310.0±2.0	45.5±4.0	1580.4 ± 0.6	19.2±1.1	1612.2±1.0	19.4±3.0
KPCL1	1310.0±3.1	47.7±5.7	1580.9±0.9	21.1±1.8	1613.0±1.4	27.0±4.2
KPH1	1307.0±3.8	51.1±5.4	1581.4±0.9	25.2±3.1	1613.4±1.5	16.3±5.7

5.3.5.6 Unaxial tension using Raman spectroscopy and measuring specific electrical resistivity via the Van der Pauw method.
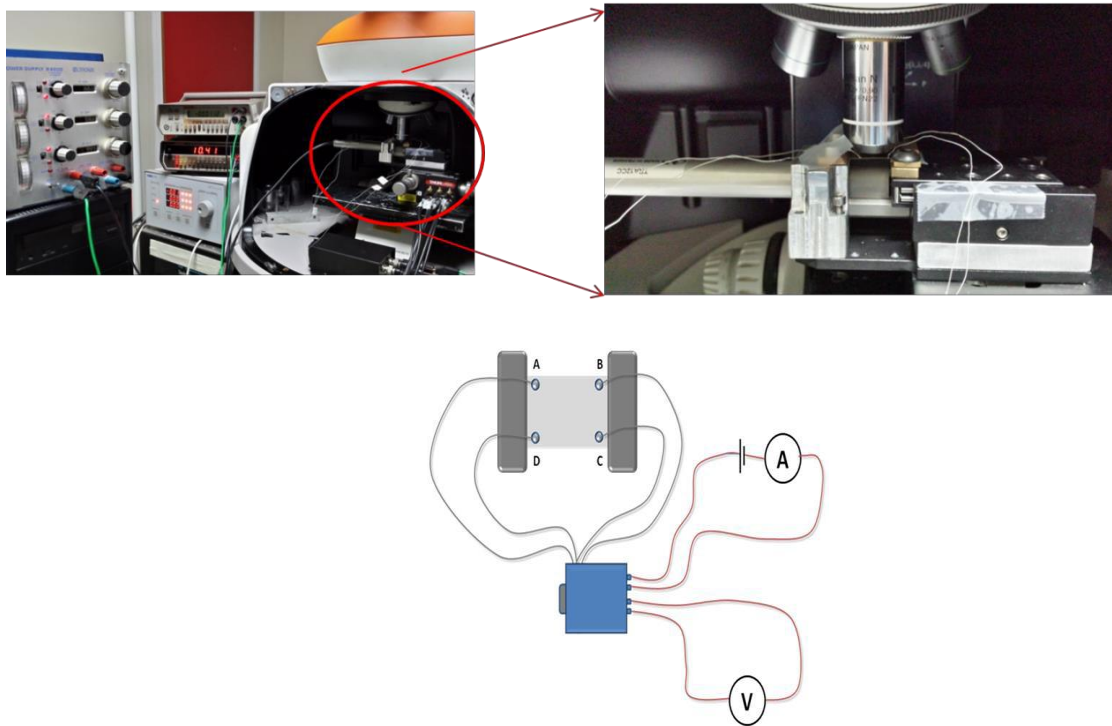

Fig. 51: Representation of the applied van der Pauw method that was used to characterize the PVC films as described below

The sample was placed in the automated tensile frame, four contacts were placed in the circumference of the sample and secured using a tiny amount of silver paste. The successive contacts A, B, C and D were connected in order to measure the resistivity $R_{AB,CD}$. Similarly was measured the resistivity $R_{BC,AD}$. The actual circuit contained a switch which alterned the A and C cables making it easier to switch the circuit between measuring the $R_{AB,CD}$ and the $R_{BC,AD}$. Finally, the specific resistivity of the samples was calculated using the values of $R_{BC,AD}$, $R_{AB,CD}$ and the thickness of the sample.

$$\rho = \frac{\pi d}{\ln 2}\left(\frac{R_{AB,CD} - R_{BC,AD}}{2}\right) f\left(\frac{R_{AB,CD}}{R_{BC,AD}}\right)$$
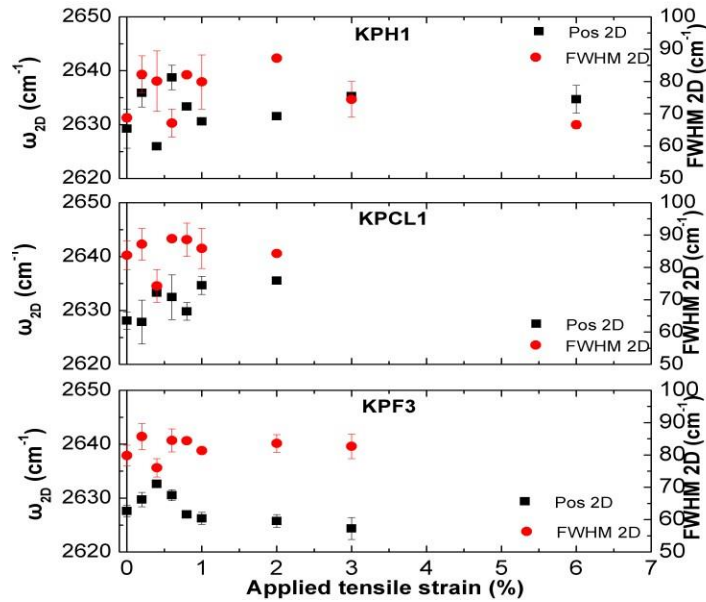
Fig. 52:Monitoring the position of the 2D peak (black dots) –for higher strain levels there is no response. The FWHM 2D (red dots) broadens initially and afterwards remains constant.

All samples appeared to have a rather compressive response (2D shifts to higher values) to the applied strain (up to 0.8%). For higher strain levels there is not any response (constant behaviour)
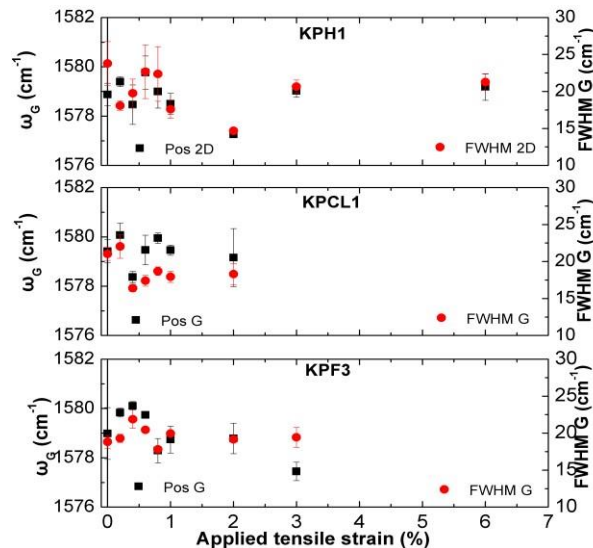
Fig. 53: Monitoring the position of the G band (black dots) due to small shifts for the tested samples.The FWHM G (red dots) broadens initially and afterwards remains constant.

There is a very small shift to higher values (~1.5cm^{-1}) of G band for all samples up to 0.8%. for higher strains, a constant behaviour is monitored. Similar FWHM G broadens initially and afterwards remains constant.
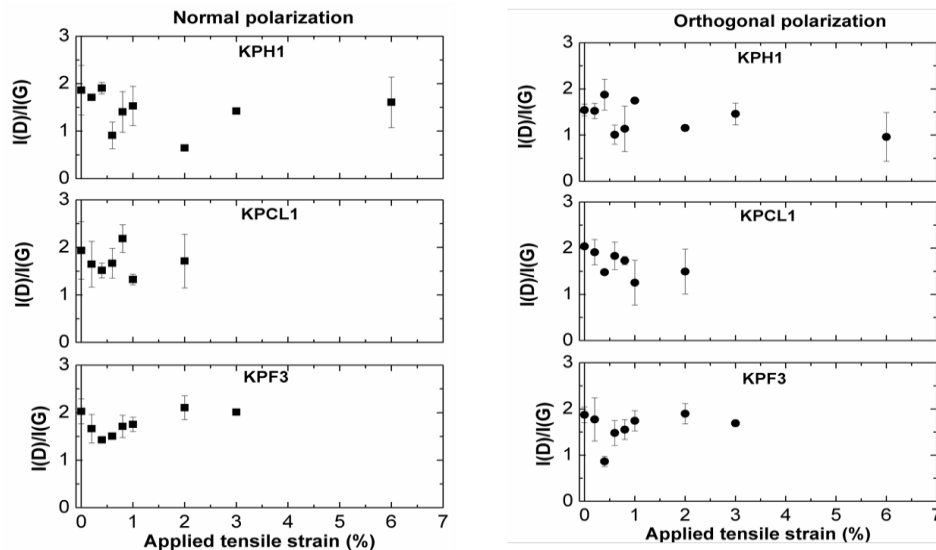
Fig. 54:Graphs indicating the measured specific resistivity via the van der Pauw method for the described samples in normal polarization (left side) and orthogonal polarization (right side).

There is a decrease of disorder with the applied strain for all samples up to 1%. Similar results were obtained in orthogonal polarization.
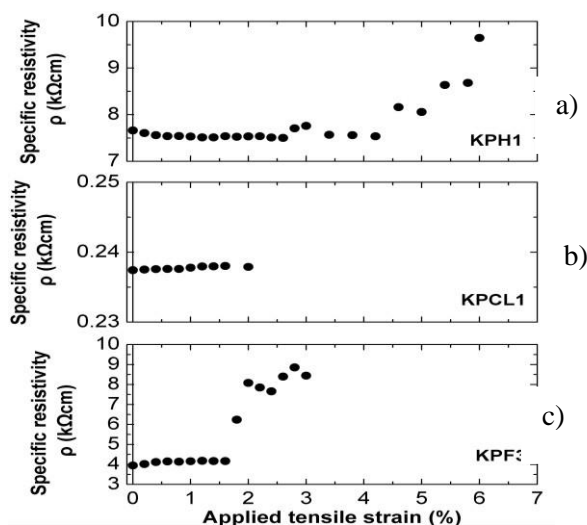
Fig. 55:Specific resistivity versus applied strain for PVC membranes treated in a) g-PDI-H , b) G-PDI-Cl and G-PDI-F solutions.

In figure 55a, an up to 4.2% of strain was applied and the specific resistivity is stable and varies between the value of ~7.5kΩcm. For higher strain levels, the specific resistivity increases rapidly. In figure 55b, we noticed constant values of specific resistivity up to 2%. For higher strains, the electrodes were detached from the sample. In graph 55c for an up to 1.6% of applied strain the specific resistivity was stable again and varied between the value of ~4.0kΩcm. For higher strain levels, it increases rapidly.

To conclude, since the size of the distributed graphene nanoplatelets are less than 5μm, there is no sufficient transfer length for stress transfer. Thus, no significant shift is observed for both examined bands (2D, G). The specific electrical resistivity measurements showed that the corresponding values assume a constant value up to 2-4% of applied strain. For higher strain levels, the specific electrical resistivity increases rapidly which indicates that an internal failure takes place within the material.

5.3.5.7 Field Effect Transistors (FETs)

Graphene based materials are not only good as electrically conductive additives, but can also be used to enhance the charge mobility of organic semiconducting molecules in field effect transistors (FET)[40], [52]. Perylene molecules are well-known organic semiconductors, used in transistors and solar cells[20], [21], [53], [54], thus the G-PDI composites were also tested as active layer in transistors.

They were used as prepared, spin coated on a silicon oxide/silicon substrate, acting as the gate, in between two gold electrodes acting as source and drain. Unfortunately, most of the devices resulted unstable. Interesting results were obtained anyhow in the case of PDI-H devices, where addition of small amounts (4μg/mL) of G-PDI improved the charge mobility of 2 orders of magnitude (from 10^{-5} cm V^{-1} s^{-1} to 10^{-3} cm V^{-1} s^{-1}) while maintaining a good on/off ratio (see a typical transfer curve in fig. 56). Overall, though, the performance of the devices was not

satisfying, likely due to the poor initial charge mobility of the perylene dyes used here as semiconductors.
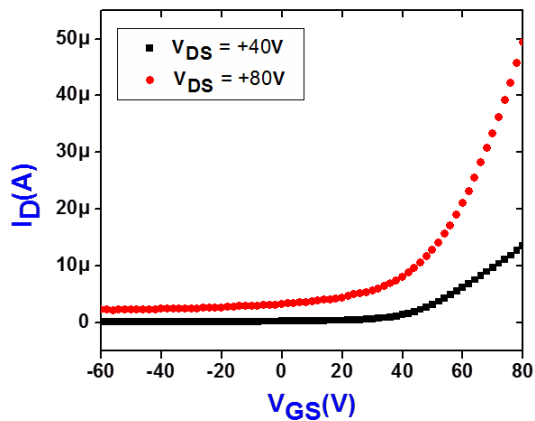
Fig. 56: Improved transfer curve from increasing G-PDI amount.

5.4. Conclusions

All results obtained to date for LPE relied on the use of organic solvents having a high surface tension, between 40 and 50 mJ m^{-2} following the seminal paper of Coleman et al.[1]. However, solvents featuring such a high surface tension also feature a high boiling point, and pose some limitations to the use of graphene (e.g. toxicity, or compatibility with industrial standards). As mentioned in the introduction, the graphene dispersions actually available at academic of commercial level shall be classified in two main groups: water/ surfactant and high boiling solvents.

In this chapter, we demonstrate that it is possible to use a hybrid approach, combining the use of organic solvents and the use of organic surfactants to obtain dispersions of FLG in solvents where graphene would not be stable on its own. The results described here demonstrate that few-layer graphene flakes can be stabilized in organic solvents by adding small amounts of suitable molecules, in a way similar but different to what typically done by soaps in water. The composite

materials obtained in this way can be included in a straightforward way in elastomer or thermoplastic materials rendering them conductive. Processing in transistors for microelectronics was also tested, even if results were unsatisfying and required the use of different molecules, or better optimization.

Exfoliation in liquids using solvents is one of the most promising techniques to mass-produce graphene and process it into useful materials. Even if graphene produced in this way is already commercially available on industrial scale[55] its penetration in the market of advanced materials is still shallow[56]. Main challenges to be overcome are the improvement of the quality and reliability of the materials produced (larger sheet size, lower average thickness, lower density of defects etc.) and the development of procedures to process graphene in a way compatible with actual production standards (compounding with polymers, coating on metals and surfaces, integration with silicon-based electronics etc.). Expanding the range of solvents usable for graphene processing could be a major step towards this direction.

5.5. Bibliography

[1]   Y. Hernandez, V. Nicolosi, M. Lotya, F. M. Blighe, Z. Y. Sun, S. De, I. T. McGovern, B. Holland, M. Byrne, Y. K. Gun'ko, J. J. Boland, P. Niraj, G. Duesberg, S. Krishnamurthy, R. Goodhue, J. Hutchison, V. Scardaci, A. C. Ferrari, and J. N. Coleman, "High-yield production of graphene by liquid-phase exfoliation of graphite," *Nat. Nanotechnol.*, vol. 3, no. 9, pp. 563–568, 2008.

[2]   M. Lotya, Y. Hernandez, P. J. King, R. J. Smith, V. Nicolosi, L. S. Karlsson, F. M. Blighe, S. De, Z. M. Wang, I. T. McGovern, G. S. Duesberg, and J. N. Coleman, "Liquid Phase Production of Graphene by Exfoliation of Graphite in Surfactant/Water Solutions," *J. Am. Chem. Soc.*, vol. 131, no. 10, pp. 3611–3620, 2009.

[3]   L. Guardia, M. J. Fernandez-Merino, J. I. Paredes, P. Solis-Fernandez, S. Villar-Rodil, A. Martinez-Alonso, and J. M. D. Tascon, "High-throughput production of pristine graphene in an aqueous dispersion assisted by non-ionic surfactants," *Carbon N. Y.*, vol. 49, no. 5, pp. 1653–1662, 2011.

[4]   J. W. T. Seo, A. A. Green, A. L. Antaris, and M. C. Hersam, "High-Concentration Aqueous Dispersions of Graphene Using Nonionic, Biocompatible Block Copolymers," *J. Phys. Chem. Lett.*, vol. 2, no. 9, pp. 1004–1008, 2011.

[5]   V. Palermo, "Not a molecule, not a polymer, not a substrate... the many faces of graphene as a chemical platform," *Chem. Commun.*, vol. 49, no. 28, pp. 2848–2857, 2013.

[6]   X. S. Li, W. W. Cai, L. Colombo, and R. S. Ruoff, "Evolution of Graphene Growth on Ni and Cu by Carbon Isotope Labeling," *Nano Lett.*, vol. 9, no. 12, pp. 4268–4272, 2009.

[7]   K. R. Paton, E. Varrla, C. Backes, R. J. Smith, U. Khan, A. O'Neill, C. Boland, M. Lotya, O. M. Istrate, P. King, T. Higgins, S. Barwich, P. May, P. Puczkarski, I. Ahmed, M. Moebius, H. Pettersson, E. Long, J. Coelho, S. E. O'Brien, E. K. McGuire, B. M. Sanchez, G. S. Duesberg, N. McEvoy, T. J. Pennycook, C. Downing, A. Crossley, V. Nicolosi, and J. N. Coleman, "Scalable production of large quantities of defect-free few-layer graphene by shear exfoliation in liquids," *Nat Mater*, vol. 13, no. 6, pp. 624–630, 2014.

[8]   P. Samorì, I. A. Kinloch, X. Feng, and V. Palermo, "Graphene-based nanocomposites for structural and functional applications: using 2-dimensional materials in a 3-dimensional world," *2D Mater.*, vol. 2, no. 3, p. 30205, 2015.

[9]   Z. Y. Xia, S. Pezzini, E. Treossi, G. Giambastiani, F. Corticelli, V. Morandi, A. Zanelli,

V. Bellani, and V. Palermo, "The Exfoliation of Graphene in Liquids by Electrochemical, Chemical, and Sonication-Assisted Techniques: A Nanoscale Study (Adv. Funct. Mater. 37/2013)," *Adv. Funct. Mater.*, vol. 23, no. 37, pp. 4684–4693, 2013.

[10] Y. Zhao, Y. Xie, Z. Liu, X. Wang, Y. Chai, and F. Yan, "Two-Dimensional Material Membranes: An Emerging Platform for Controllable Mass Transport Applications," *Small*, vol. 10, no. 22, pp. 4521–4542, 2014.

[11] Z. Y. Xia, S. Pezzini, E. Treossi, G. Giambastiani, F. Corticelli, V. Morandi, A. Zanelli, V. Bellani, and V. Palermo, "The Exfoliation of Graphene in Liquids by Electrochemical, Chemical, and Sonication-Assisted Techniques: A Nanoscale Study," *Adv. Funct. Mater.*, vol. 23, no. 37, pp. 4684–4693, 2013.

[12] A. Schlierf, H. F. Yang, E. Gebremedhn, E. Treossi, L. Ortolani, L. P. Chen, A. Minoia, V. Morandi, P. Samori, C. Casiraghi, D. Beljonne, and V. Palermo, "Nanoscale insight into the exfoliation mechanism of graphene with organic dyes: effect of charge, dipole and molecular structure," *Nanoscale*, vol. 5, no. 10, pp. 4205–4216, 2013.

[13] K. Parvez, R. J. Li, S. R. Puniredd, Y. Hernandez, F. Hinkel, S. H. Wang, X. L. Feng, and K. Mullen, "Electrochemically Exfoliated Graphene as Solution-Processable, Highly Conductive Electrodes for Organic Electronics," *ACS Nano*, vol. 7, no. 4, pp. 3598–3606, 2013.

[14] A. Schlierf, P. Samori, and V. Palermo, "Graphene-organic composites for electronics: optical and electronic interactions in vacuum, liquids and thin solid films," *J. Mater. Chem. C*, p. DOI: 10.1039/C3TC32153C, 2014.

[15] A. Schlierf, K. Cha, M. G. Schwab, P. Samori, and V. Palermo, "Exfoliation of graphene with an industrial dye: teaching an old dog new tricks," *2D Mater.*, vol. 1, no. 3, p. 35006, 2014.

[16] H. Yang, F. Withers, E. Gebremedhn, E. Lewis, L. Britnell, A. Felten, V. Palermo, S. Haigh, D. Beljonne, and C. Casiraghi, "Dielectric nanosheets made by liquid-phase exfoliation in water and their use in graphene-based electronics," *2D Mater.*, vol. 1, no. 1, p. 11012, 2014.

[17] I. McCulloch, M. Heeney, C. Bailey, K. Genevicius, I. MacDonald, M. Shkunov, D. Sparrowe, S. Tierney, R. Wagner, W. Zhang, M. L. Chabinyc, R. J. Kline, M. D. McGehee, and M. F. Toney, "Liquid-crystalline semiconducting polymers with high charge-carrier mobility," *Nat Mater*, vol. 5, no. 4, pp. 328–333, 2006.

[18] M. El Gemayel, S. Haar, F. Liscio, A. Schlierf, G. Melinte, S. Milita, O. Ersen, A.

Ciesielski, V. Palermo, and P. Samorì, "Leveraging the Ambipolar Transport in Polymeric Field-Effect Transistors via Blending with Liquid-Phase Exfoliated Graphene," *Adv. Mater.*, vol. 26, no. 28, pp. 4814–4819, 2014.

[19] S. M. Zhang, Y. L. Guo, H. X. Xi, C. A. Di, J. Yu, K. Zheng, R. G. Liu, X. W. Zhan, and Y. Q. Liu, "Effect of substituents on electronic properties, thin film structure and device performance of dithienothiophene-phenylene cooligomers," *Thin Solid Films*, vol. 517, no. 9, pp. 2968–2973, 2009.

[20] R. Dabirian, V. Palermo, A. Liscio, E. Schwartz, M. B. J. Otten, C. E. Finlayson, E. Treossi, R. H. Friend, G. Calestani, K. Mullen, R. J. M. Nolte, A. E. Rowan, and P. Samori, "The Relationship between Nanoscale Architecture and Charge Transport in Conjugated Nanocrystals Bridged by Multichromophoric Polymers," *J. Am. Chem. Soc.*, vol. 131, no. 20, pp. 7055–7063, 2009.

[21] G. De Luca, A. Liscio, F. Nolde, L. M. Scolaro, V. Palermo, K. Müllen, and P. Samorì, "Self-assembly of discotic molecules into mesoscopic crystals by solvent-vapour annealing," *Soft Matter*, vol. 4, no. 10, pp. 2064–2070, 2008.

[22] G. De Luca, A. Liscio, M. Melucci, T. Schnitzler, W. Pisula, C. G. Clark, L. M. Scolaro, V. Palermo, K. Müllen, and P. Samorì, "Phase separation and affinity between a fluorinated perylene diimide dye and an alkyl-substituted hexa-peri-hexabenzocoronene," *J. Mater. Chem.*, vol. 20, no. 1, pp. 71–82, 2010.

[23] C. E. Finlayson, R. H. Friend, M. B. J. Otten, E. Schwartz, J. J. L. M. Cornelissen, R. L. M. Nolte, A. E. Rowan, P. Samorì, V. Palermo, A. Liscio, K. Peneva, K. Müllen, S. Trapani, and D. Beljonne, "Electronic Transport Properties or Ensembles of Perylene-Substituted Poly-isocyanopeptide Arrays," *Adv. Funct. Mater.*, vol. 18, no. 24, pp. 3947–3955, 2008.

[24] V. Palermo, M. Buchanan, A. Bezinger, and R. A. Wolkow, "Lateral diffusion of titanium disilicide as a route to contacting hybrid Si/organic nanostructures," *Appl. Phys. Lett.*, vol. 81, no. 19, pp. 3636–3638, 2002.

[25] V. Palermo, A. Liscio, D. Gentilini, F. Nolde, K. Mullen, and P. Samori, "Scanning probe microscopy investigation of self-organized perylenetetracarboxdiimide nanostructures at surfaces: Structural and electronic properties," *Small*, vol. 3, no. 1, pp. 161–167, 2007.

[26] N. V Kozhemyakina, J. M. Englert, G. A. Yang, E. Spiecker, C. D. Schmidt, F. Hauke, and A. Hirsch, "Non-Covalent Chemistry of Graphene: Electronic Communication with Dendronized Perylene Bisimides," *Adv. Mater.*, vol. 22, no. 48, pp. 5483–5487, 2010.

[27] T. Weil, T. Vosch, J. Hofkens, K. Peneva, and K. Müllen, "The Rylene Colorant Family—Tailored Nanoemitters for Photonics Research and Applications," *Angew. Chemie Int. Ed.*, vol. 49, no. 48, pp. 9068–9093, 2010.

[28] V. Palermo and P. Samorì, "Molecular self-assembly across multiple length scales," *Angew. Chem.-Int. Ed.*, vol. 46, no. 24, pp. 4428–4432, 2007.

[29] H. Yang, Y. Hernandez, A. Schlierf, A. Felten, A. Eckmann, S. Johal, P. Louette, J. J. Pireaux, X. Feng, K. Muellen, V. Palermo, and C. Casiraghi, "A simple method for graphene production based on exfoliation of graphite in water using 1-pyrenesulfonic acid sodium salt," *Carbon N. Y.*, vol. 53, pp. 357–365, 2013.

[30] Q. Liu, Z. F. Liu, X. Y. Zhong, L. Y. Yang, N. Zhang, G. L. Pan, S. G. Yin, Y. Chen, and J. Wei, "Polymer Photovoltaic Cells Based on Solution-Processable Graphene and P3HT," *Adv. Funct. Mater.*, vol. 19, no. 6, pp. 894–904, 2009.

[31] F. Würthner, "Perylene bisimide dyes as versatile building blocks for functional supramolecular architectures," *Chem. Comm.*, no. 14, pp. 1564–1579, 2004.

[32] Z. Y. Xia, G. Giambastiani, C. Christodoulou, M. V Nardi, N. Koch, E. Treossi, V. Bellani, S. Pezzini, F. Corticelli, V. Morandi, A. Zanelli, and V. Palermo, "Synergic Exfoliation of Graphene with Organic Molecules and Inorganic Ions for the Electrochemical Production of Flexible Electrodes," *Chempluschem*, vol. 79, no. 3, pp. 439–446, 2014.

[33] K. Balakrishnan, A. Datar, T. Naddo, J. Huang, R. Oitker, M. Yen, J. Zhao, and L. Zang, "Effect of Side-Chain Substituents on Self-Assembly of Perylene Diimide Molecules: Morphology Control," *J. Am. Chem. Soc.*, vol. 128, no. 22, pp. 7390–7398, 2006.

[34] F. F. Fateley W. G., McDevitt N.T., Bentley, *F. F. Appl Spectrosc.* 1971.

[35] M. E. Eren B., Hug D., Marot L., Pawlak R., Kisiel M., Steiner R., Zumbuhl D. M., "Beilstein Journal of Nanotechnology," vol. 3, p. 852, 2012.

[36] A. C. Ferrari, J. C. Meyer, V. Scardaci, C. Casiraghi, M. Lazzeri, F. Mauri, S. Piscanec, D. Jiang, K. S. Novoselov, S. Roth, and A. K. Geim, "Raman spectrum of graphene and graphene layers," *Phys. Rev. Lett.*, vol. 97, no. 18, p. #187401, 2006.

[37] C. Backes, C. D. Schmidt, K. Rosenlehner, F. Hauke, J. N. Coleman, and A. Hirsch, "Nanotube Surfactant Design: The Versatility of Water-Soluble Perylene Bisimides," *Adv. Mater.*, vol. 22, no. 7, pp. 788–802, 2010.

[38] E. Varrla, C. Backes, K. R. Paton, A. Harvey, Z. Gholamvand, J. McCauley, and J. N.

Coleman, "Large-Scale Production of Size-Controlled MoS2 Nanosheets by Shear Exfoliation," *Chem. Mater.*, vol. 27, no. 3, pp. 1129–1139, 2015.

[39]   R. J. Smith, P. J. King, C. Wirtz, G. S. Duesberg, and J. N. Coleman, "Lateral size selection of surfactant-stabilised graphene flakes using size exclusion chromatography," *Chem. Phys. Lett.*, vol. 531, pp. 169–172, 2012.

[40]   A. Liscio, M. Bonini, E. Treossi, E. Orgiu, M. Kastler, F. Dotz, V. Palermo, and P. Samori, "Improving charge transport in poly(3-hexylthiophene) transistors via blending with an alkyl-substituted phenylene-thiophene-thiophene-phenylene molecule," *J. Polym. Sci. Part B-Polymer Phys.*, vol. 50, no. 9, pp. 642–649, 2012.

[41]   M. El Gemayel, A. Narita, L. F. Dössel, R. S. Sundaram, A. Kiersnowski, W. Pisula, M. R. Hansen, A. C. Ferrari, E. Orgiu, X. Feng, K. Müllen, and P. Samorì, "Graphene nanoribbon blends with P3HT for organic electronics," *Nanoscale*, vol. 6, no. 12, pp. 6301–6314, 2014.

[42]   L. Gong, R. J. Young, I. A. Kinloch, I. Riaz, R. Jalil, and K. S. Novoselov, "Optimizing the Reinforcement of Polymer-Based Nanocomposites by Graphene," *ACS Nano*, vol. 6, no. 3, pp. 2086–2095, 2012.

[43]   D. C. Giancoli, *Physics Principle with Applications*. 1998.

[44]   C. S. Boland, U. Khan, C. Backes, A. O'Neill, J. McCauley, S. Duane, R. Shanker, Y. Liu, I. Jurewicz, A. B. Dalton, and J. N. Coleman, "Sensitive, High-Strain, High-Rate Bodily Motion Sensors Based on Graphene-Rubber Composites," *ACS Nano*, vol. 8, no. 9, pp. 8819–8830, 2014.

[45]   L. Steve, *Characterization and Failure Analysis of Plastics*. 2003.

[46]   "Swelling Measurements of Crosslinked Polymers," *Cambridge Polymer Group*. [Online]. Available: http://www.campoly.com/files/4113/7122/7757/005_New_Swelling_measurements.pdf.

[47]   R. K. S. Chanda Manas, *Plastics Technology Handbook*, 3rd ed. 1997.

[48]   T. L.R.G, "The Equilibrium Swelling of Cross-Linked Amorphous Polymers," *Proc. R. Soc. A*, no. 200, p. 1061, 1950.

[49]   K. Kouroupis-Agalou, A. Liscio, E. Treossi, L. Ortolani, V. Morandi, N. M. Pugno, and V. Palermo, "Fragmentation and exfoliation of 2-dimensional materials: a statistical approach," *Nanoscale*, vol. 6, no. 11, pp. 5926–5933, 2014.

[50] E. Treossi, M. Melucci, A. Liscio, M. Gazzano, P. Samorì, and V. Palermo, "High-Contrast Visualization of Graphene Oxide on Dye-Sensitized Glass, Quartz, and Silicon by Fluorescence Quenching," *J. Am. Chem. Soc.*, vol. 131, no. 43, pp. 15576–15577, 2009.

[51] A. Liscio, V. Palermo, O. Fenwick, S. Braun, K. Mullen, M. Fahlman, F. Cacialli, and P. Samori, "Local Surface Potential of pi-Conjugated Nanostructures by Kelvin Probe Force Microscopy: Effect of the Sampling Depth," *Small*, vol. 7, no. 5, pp. 634–639, 2011.

[52] M. El Gemayel, S. Haar, F. Liscio, A. Schlierf, G. Melinte, S. Milita, O. Ersen, A. Ciesielski, V. Palermo, and P. Samori, "Leveraging the Ambipolar Transport in Polymeric Field-Effect Transistors via Blending with Liquid-Phase Exfoliated Graphene," *Adv. Mater.*, vol. 26, no. 28, p. 4814, 2014.

[53] G. De Luca, A. Liscio, P. Maccagnani, F. Nolde, V. Palermo, K. Mullen, and P. Samori, "Nucleation-governed reversible self-assembly of an organic semiconductor at surfaces: Long-range mass transport forming giant functional fibers," *Adv. Funct. Mater.*, vol. 17, no. 18, pp. 3791–3798, 2007.

[54] V. Palermo, A. Liscio, M. Palma, M. Surin, R. Lazzaroni, and P. Samori, "Exploring nanoscale electrical and electronic properties of organic and polymeric functional materials by atomic force microscopy based approaches," *Chem. Commun.*, vol. 32, pp. 3326–3337, 2007.

[55] Avanzare, "No Title," *www.avanzare.es*.

[56] M. Peplow, "Graphene booms in factories but lacks a killer app," *Nature*, vol. 522, no. 7556, pp. 268–269, 2015.

Chapter 6
Summary and Conclusions

6.1. Summary

The field of graphene, due to its huge success, is often a "land grab", where the new papers claim every week the production of high performance materials produced by different research groups. Therefore, there was a strong need for methods to evaluate the exfoliation of 2D materials, which essentially we tried to understand how these materials are produced at nanoscale level. Hence, this work touches upon an interesting fundamental question: *what is the intrinsic shape and size distribution of 2D nanomaterials and how these parameters can affect the large-scale production of 2D-based composite materials in the future*.

In this dissertation, we firstly developed a new method to evaluate the exfoliation results of Graphene and other 2D materials (Graphene Oxide, Boron Nitride).This was essential to understand the fundamental processes behind the production of 2D materials. Additionally, that helped us to understand the production development of 2D-based composite materials and bio-compatible materials, such as gelatin fibers. We evaluated the processed 2D nanomaterials with commonly used characterization techniques used in the scientific and industrial world, which are the Atomic Force Microscope. Furthermore, we developed this method by using Fluorescence Optical Microscopy (FOM), Scanning Electron Microscopy (SEM) and Atomic Force Microscopy (AFM). Based on AFM analysis of thousands samples, the exfoliation of 2D nanomaterials, like the distributions recognized in the fields of biology, astronomy and mineralogy. Finally, we demonstrated a new way to produce stable graphene solutions in low boiling point solvents and how the exfoliated material can interpret into polymer surface such as Polyvinylchloride (PVC) and natural rubber.

Overall, the uniqueness of this work is that we developed a new method that has not been studied before and gives the opportunity to materials scientists that are researching on the growing field of Graphene and other 2D materials to have a method in order to control, quantify and evaluate the exfoliation results of nanomaterials that are produced through the most well-known methods of liquid phase exfoliation and ball milling, both of which are applied in scientific and industrial level. Thus, the results presented in this work may offer insight into the polymer composites where the size and shape of nanosheets can be rationally optimized.

6.1.1 Making Composite Materials; why size is important

Graphene-based composite materials are the only application commercialized on a large scale until now. Although these products already exist in the market, their mechanical performance is not comparable to the one of a single graphene sheet. The main reason for this is that it is not yet fully understood how 2D-based composites are functioning at the nanoscale level, and especially how to achieve ultimate performance when they are embedded in the produced composite materials. Based on the technological demands, the number of these products is constantly increasing. The next figure provides a schematic comparison of how the size of the graphene sheets at nanoscale can affect the performance of macroscale materials. In order to understand if graphene and 2D materials (GRMs) in general can really find competitive applications at industrial level, we need a strong combination of processing techniques, prototyping, characterization and modelling.
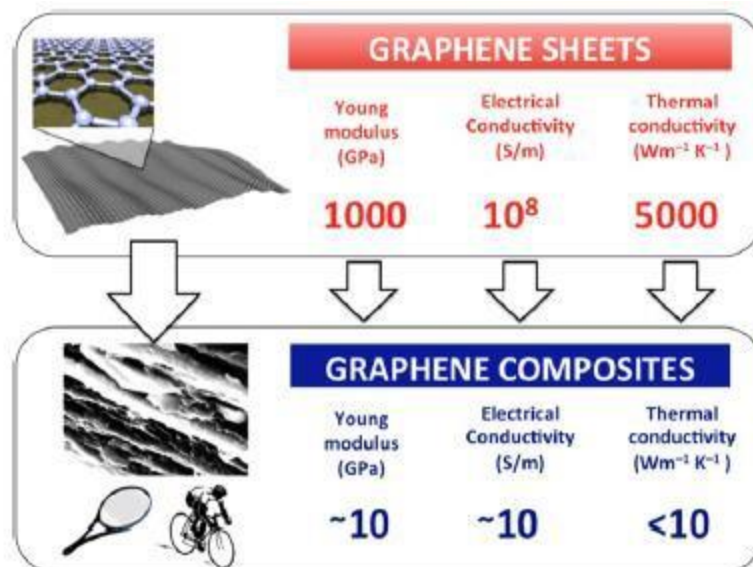

Fig. 1: A schematic representation of the different in performance between single, 'ideal' graphene sheets and graphene-based macroscopic composites suitable for commercial applications. The numbers reported will vary depending on the material measured and should be consider and order-of-magnitude estimate. For a more detailed description of different properties, see reference and references therein[1].

6.1.2 Towards 2D-based composite materials production

The amount of graphene required for the fabrication of composite materials in the large scale is generally high, therefore tons of the starting material are required. In general, the cost for using graphene in composites needs to be sufficiently lower than for other applications and the quality of the final material can be lower if it is compared to the high-quality graphene produced in the lab. Although graphene has been proven to improve the mechanical and electrical properties in many graphene-polymer composites and nanocomposites, full exploitation requires also the cost and scaling factors to be competitive compared to established carbonaceous materials. Until now, it is not considered that even with few percentages of graphene the final cost will be greatly increased. That explains why GRM composites will be firstly used in commercial applications with high added-value such as sport accessories, aerospace and biomedical devices.

Another issue is that these new composite materials will need to comply with processing steps of the current technology, thus requiring efficient ways to process graphene into polymer granules and liquid master batches. In solution, graphene can only be stabilized with organic solvents or surfactants through supramolecular interactions. Normally, when molecules are used along with graphene these molecules are easily attached to its surface. As a result, they can reduce the interaction with the polymer matrix and the beneficial effects of graphene additives. A possible solution to this could be the use of molecules that are already well-established for the large-scale compounding of polymers such as industrial colorants or additives for polymer composites. Nevertheless, the same molecules should be used to successfully solubilize other 2D materials for electronic applications. In general, nanocomposites can offer a variety of tunable properties to an extend degree through their incorporation with other 2D materials. The fact that nanocomposites can give control to the structure and properties of the final material, can give new possibilities to a range of properties of new materials.

6.2 Bibliography

[1]   A. C. Ferrari, F. Bonaccorso, V. Fal'ko, K. S. Novoselov, S. Roche, P. Boggild, S. Borini, F. H. L. Koppens, V. Palermo, N. Pugno, J. A. Garrido, R. Sordan, A. Bianco, L. Ballerini, M. Prato, E. Lidorikis, J. Kivioja, C. Marinelli, T. Ryhanen, A. Morpurgo, J. N. Coleman, V. Nicolosi, L. Colombo, A. Fert, M. Garcia-Hernandez, A. Bachtold, G. F. Schneider, F. Guinea, C. Dekker, M. Barbone, Z. Sun, C. Galiotis, A. N. Grigorenko, G. Konstantatos, A. Kis, M. Katsnelson, L. Vandersypen, A. Loiseau, V. Morandi, D. Neumaier, E. Treossi, V. Pellegrini, M. Polini, A. Tredicucci, G. M. Williams, B. Hee Hong, J.-H. Ahn, J. Min Kim, H. Zirath, B. J. van Wees, H. van der Zant, L. Occhipinti, A. Di Matteo, I. A. Kinloch, T. Seyller, E. Quesnel, X. Feng, K. Teo, N. Rupesinghe, P. Hakonen, S. R. T. Neil, Q. Tannock, T. Lofwander, and J. Kinaret, "Science and technology roadmap for graphene, related two-dimensional crystals, and hybrid systems," *Nanoscale*, vol. 7, no. 11, pp. 4598–4810, 2015.

6.3 Funding

6.4 Contributors

Consiglio Nazionale delle Ricerche

Dr. Vincenzo Palermo
Dr. Andrea Liscio
Dr. Emanuele Treossi
Dr. Vittorio Morandi
Franco Corticelli

ALMA MATER STUDIORUM UNIVERSITÀ DI BOLOGNA

Prof. Loris Giorgini
Prof. Adriana Bigi
Dr. Massimo Gazzano
Dr. Simone Ligi

CNRS – UNIVERSITÉ DE STRASBOURG

Prof. Paolo Samori
Prof. Emanuele Orgiu
Dr. Artur Ciesielski
Dr Mohamed el Garah
Wassima Rekab

UNIVERSITY OF TRENTO - Italy

Prof. Nicola M. Pugno

UNIVERSITY OF CAMBRIDGE

Prof. Andrea Ferrari
Dr. Matteo Bruna
Dr. Silvia Milana
Lucia Lombardi

UMONS Université de Mons

Dr. David Beljonne
Dr. Elias Gebremedhn

ΠΑΝΕΠΙΣΤΗΜΙΟ ΠΑΤΡΩΝ UNIVERSITY OF PATRAS

Prof. Costas Galiotis
Prof. Konstantinos Papagelis
Dr. George Anagnostopoulos
Dr. John Parthenios

CSIC CONSEJO SUPERIOR DE INVESTIGACIONES CIENTÍFICAS

Dr. Xavier Diez Betriu

6.5 Publications

1. G. Anagnostopoulos, K. Kouroupis-Agalou, E. Treossi, V. Palermo, J. Parthenios, K. Papagelis, C. Galiotis, "Straing engineering in highly wrinkled CVD-Graphene/Epoxy systems", under submission, 2016.

2. A. Liscio, K. Kouroupis-Agalou, X. D. Betriu, A. Kovtun, E. Treossi, N. M. Pugno, G. D. Luca, V. Palermo, "Scale-dependent fragmentation mechanism of two-dimensional materials, under submission, 2016.

3. K. Kouroupis-Agalou, E. Gebremedhn, A. Ciesielski, E. Orgiu, P. Samori, D. Beljonne, V. Palermo, "Tunable solubility of few-layers graphene in organic solvents by use of aromatic surfactants, under submission, 2016.

4. S. Panzavolta, B. Bracci, C. Gualdani, M. L. Focarete, E. Treossi, K. Kouroupis-Agalou, K. Rubini, F. Bosia, L. Brely, N. M. Pugno, V. Palermo, A. Bigi, "Structural reinforcement and failure analysis in composite nano fibers of graphene oxide and gelatin", *Carbon, 2014, 78, 566-577.*

5. K. Kouroupis-Agalou, A. Liscio, E. Treossi, L. Ortolani, V. Morandi, N. M. Pugno, V. Palermo, "*Fragmentation and exfoliation of 2-dimensional materials; a statistical approach", Nanoscale, 2014, 6, 5926-5933.*

6. E.L. Papadopoulou, M. Varda, K. Kouroupis-Agalou , M. Androulidaki, E. Chikoidze, P. Galtier, G. Huyberechts, E. Aperathitis, "*Undoped and Al-doped ZnO films with tuned properties grown by pulsed laser deposition*", ***Thin Solid Films***, *2008, 516,* 8141-8145.

6.6 Conference Presentations and Posters

Sept 2015   **Poster:** "Graphene-PVC composites through exfoliation in low boiling point solvents with Perylenediimides", GraphITA 2015, Bologna, Italy.

Aug 2015   **Talk :** "Exfoliation and fragmentation of 2D materials; a multi-scale statistical approach, MCM 2015, Eger, Hungary.

Oct 2014   **Talk:** "Processing and controlling 2D-based composite materials production", G.E.N.I.U.S meeting, CNR, Bologna, Italy.

Jul 2014   **Talk:** "Graphene Oxide nanosheets and Gelatin: composite films and nanofibers with improved mechanical properties", National conference of the Italian Biomaterials Society, Palermo, Italy.

May 2014   **Talk:** "Fragmentation and exfoliation of low-dimensional materials; a statistical approach", E-MRS 2014, Lille, France.

May 2014   **Talk:** "Large scale exfoliation of Boron nitride Nanosheets", E-MRS 2014, Lille, France.

May 2014   **Poster:** "Fragmentation and exfoliation of low-dimensional materials; a statistical approach", Graphene 2014, Toulouse, France.

Mar 2014   **Poster:** "How quasi-2D materials break; a statistical analysis of fragmentation and exfoliation products", Chemontubes 2014 Riva del Garda, Italy.

Sep 2013   **Talk:** "Large scale exfoliation of Boron Nitride Nanosheets", FEMS Euromat 2013, Seville, Spain.

Jun 2013   **Poster:** "Large scale exfoliation of Boron Nitride Nanosheets for Polymer Composites", Graphene Week 2013, Chemnitz, Germany.

Jan 2013   **Talk:** "Uncovering 2D nanosheets by exfoliation techniques for material composites and coatings", CNR, Bologna, Italy.

Jan 2013   **Talk:** "Exfoliating BN nanosheets by different techniques for composite materials", Department of Electrical Engineering, University of Cambridge, U.K.

Aug 2012   **Talk:** "Comparison of exfoliation techniques and nanoscale characterization of BN", G.E.N.I.U.S meeting, University of Strasbourg, France.

May 2012   **Talk:** "First experiments on graphene-based composites, characterization at nanoscale by SPM", G.E.N.I.U.S meeting, University of Mons, Belgium.

May 2012   **Poster:** "Studies of Isocyanate oligomer mixed with Graphene Oxide", Graphene 2012, Brussels, Belgium.

6.7 Schools and Workshops

Jul 2015   "Scanning Probe Microscopy and Spectroscopy for Materials Science" workshop, University of Bologna, Italy.

Jul 2014   1st Annual School on "Sustainable Industrial Chemistry", University of Bologna, Italy.

Dec 2013   "Science through Scanning Probe Microscopy" workshop, CNR, Bologna, Italy.

Apr 2013   "Graphene Workshop 2013", University of Nova Gorica, Slovenia.

Mar 2013   "Complementary skills" workshop, University College London (UCL), U.K.

Jan 2013   Secondment: Training and measuring with Raman spectroscopy, University of Cambridge, U.K.

Sep 2012   Summer school on "Photochemistry: Techniques and applications", CNR, Bologna, Italy.

Jul 2012   "Scanning Electron Microscopy techniques" workshop by PHENOM, University of Bologna, Italy.

Jun 2012   "Research to Business", 7th International Industrial Research Expo, Bologna, Italy.

May 2012   "Graphene modeling and experiment" workshop, University of Mons, Belgium.

Feb 2012   "Advanced XRD applications", University of Bologna, Italy.

Jan 2012   "International Expotech on automotive Materials", Modena, Italy.

Dec 2011   "Scanning Probe Microscopy techniques", CNR, Bologna, Italy.